USING RUTHENIUM TO MODIFY SURFACE PROPERTIES OF AUSTENITIC STAINLESS STEEL FOR IMPROVED CORROSION RESISTANCE

Fortunate Moyo

A thesis submitted to the Faculty of Engineering and the Built Environment, University of Witwatersrand, Johannesburg in fulfilment of the requirements for the degree of Doctor of Philosophy

Johannesburg, 2017

Declaration

I, Fortunate Moyo, declare that this thesis is my own unaided work. It is being submitted to the degree of Doctor of Philosophy to the University of the Witwatersrand, Johannesburg. It has not been submitted before for any other degree or examination in any other University.

Fmoyo

27th day of September 2017

Abstract

Chromium oxide provides an inexpensive and practical means of increasing the corrosion resistance of austenitic stainless steel in most environments. However, the oxide is prone to dissolve in reducing acids and in chloride containing solutions, which compromises the durability and effective operation of structures made of austenitic stainless steel.

This research project explored the use of thin ruthenium surface alloys produced by ion implantation, RF sputtering and pulsed electrodeposition (PED) to improve the corrosion resistance of AISI 304L austenitic stainless steel in reducing acids and chloride solutions via a technique known as cathodic modification. The properties of the alloyed 304L stainless steel were evaluated using a number of tools including X-ray diffraction (XRD), field emission scanning electron microscope (FESEM), potentiodynamic polarisation, and electrochemical impedance spectroscopy (EIS).

Preliminary tests in 1 M sulphuric acid showed that the ruthenium surface alloys sufficiently raised the corrosion potential of 304L stainless steel to ranges where the stability of chromium oxide is guaranteed. Surface alloys produced by RF sputtering and PED were associated with the best corrosion resistance, and protection efficiencies of at least 85%, but they spalled during corrosion exposure rendering them unsuitable for corrosion application. The corrosion of the ruthenium implanted surface alloys exhibited a strong dependence on the surface roughness of the stainless steel, with the least corrosion rates achieved on rough 304L stainless steel samples implanted with 10^{16} Ru/cm^2 at 50 keV.

Corrosion characterisation of these ruthenium implanted surface alloys was studied in various corrosive media including sulphuric acid, sodium chloride, magnesium chloride and simulated fuel cell solutions. Their corrosion rates in sulphuric acid decreased with increase in acid concentration, and exhibited non-Arrhenius behaviour in the acid solutions; corrosion rates were unaffected by increasing exposure temperature from 25 to 50°C. In 3.5 wt% sodium chloride, addition of ruthenium via ion implantation changed pit morphology from

elongated to circular, indicating a diminished tendency for pits to initiate at manganese sulphide stringers. Corrosion rates of the ruthenium implanted stainless steels in the simulated fuel cell solutions were at least 69% lower than the target corrosion rate for use in polymer electrode membrane fuel cells (PEMFCs), thus presenting a possible practical application of ruthenium surface alloyed austenitic stainless steel.

Dedications

To my parents Kendu and Saziso Moyo for the support, patience and love.

To my sisters Patience, Sanelisiwe and Makhosazana.

To my nephews Michael and Alexander Chinwada.

Acknowledgements

The support of the DST-NRF Centre of Excellence in Strong Materials (CoE-SM) towards this research is hereby acknowledged. I am grateful to the entire administrative staff of the CoE-SM for their generous assistance. I would also like to acknowledge the financial aid contributed by the University of the Witwatersrand Postgraduate Merit Award.

Impala Platinum Limited (Refineries) is thanked for supplying the ruthenium nitrosyl salt used in this work, and in particular Sifiso Sibiya for his tireless effort to secure the salt. I am sincerely grateful to Anglo Platinum for providing ruthenium powder.

Many thanks to iThemba LABS North for generously allowing me access to their ion implanter, most importantly to Tony Miller for his assistance. Necsa, and in particular Tshepho Ntsoane, is also thanked for their Bruker D8 Discovery.

Completion of this work would not have been possible without the constructive guidance and expertise of my supervisors Dr Josias van der Merwe and Dr Daniel Wamwangi. Their generous support and insightful mentorship is greatly appreciated. I extend my profound gratitude to the technical staff at the School of Chemical and Metallurgical Engineering for their invaluable assistance, and to all who directly or indirectly contributed to the success of this work.

Great thanks to my fellow students, especially Jaquiline Kurasha, Yonela Mgwebi and Thuli Mkhaliphi for unyielding encouragement, and robust thought provoking debates. I will forever be indebted to my family for allowing me the freedom to pursue my dreams. Their unconditional love and support made this journey much easier.

Lastly, I give glory and honour to God, through whom all things are possible.

Table of contents

DECLARATION ..... **I**

ABSTRACT ..... **II**

DEDICATIONS ..... **IV**

ACKNOWLEDGEMENTS ..... **V**

LIST OF FIGURES ..... **IX**

LIST OF TABLES ..... **XIX**

LIST OF ABBREVIATIONS ..... **XXIII**

CHAPTER 1 INTRODUCTION **1**

1.1 BACKGROUND AND MOTIVATION 1
1.2 RESEARCH PROBLEMS 3
1.3 RESEARCH AIMS AND OBJECTIVES 5
1.4 HYPOTHESES 6
1.5 DELIMITATION OF STUDY 7
1.6 SIGNIFICANCE OF STUDY 7
1.7 DEFINITION OF TERMS 8
1.8 OUTLINE OF THESIS 8

CHAPTER 2 LITERATURE REVIEW **10**

2.1 PRINCIPLES OF CORROSION 10
2.1.1 Corrosion thermodynamics *12*
2.1.2 Corrosion kinetics *12*
2.1.3 Polarisation *13*
2.2 CORROSION OF STAINLESS STEELS 14
2.2.1 Corrosion of 304 austenitic stainless steel *17*
2.3 CATHODIC MODIFICATION 23
2.3.1 Requirements for cathodic modification *24*
2.3.2 Mechanism of cathodic modification *25*
2.3.3 Cathodic modification with ruthenium *26*
2.4 SURFACE ALLOYING 31
2.4.1 Classes of surface alloys *31*
2.4.2 Corrosion control by surface alloying *34*
2.4.3 Surface alloying strategies *37*
2.5 CORROSION MEASURING TECHNIQUES 49
2.5.1 Potentiodynamic polarisation *50*
2.5.2 Electrochemical impedance spectroscopy *54*
2.5.3 Statistical consideration of corrosion measurements *59*

CHAPTER 3 MATERIALS AND EXPERIMENTAL PROCEDURES **61**

3.1 INTRODUCTION 61
3.2 MATERIALS 61
3.2.1 Substrate *61*
3.2.2 Ruthenium targets *62*
3.2.3 Ruthenium plating bath *62*

3.3 SYNTHESIS OF SURFACE ALLOYS 63
3.3.1 Ion implantation *63*
3.3.2 RF sputtering *64*
3.3.3 Pulsed electrodeposition *65*
3.4 DESIGN OF EXPERIMENTS 66
3.5 ALLOY CHARACTERISATION 67
3.5.1 Physico-chemical characterisation *67*
3.5.2 Electrochemical characterisation *70*
3.5.3 Non-electrochemical corrosion characterisation *75*

CHAPTER 4 MATERIALS CHARACTERISATION 76

4.1 INTRODUCTION 76
4.2 RESULTS 76
4.2.1 Chemical composition *76*
4.1.2 Microstructural analysis *77*
4.2.3 Mechanical properties *80*
4.2.4 Effect of surface preparation *81*
4.2.5 Corrosion characterisation *86*
4.3 DISCUSSION 95
4.4 SUMMARY 99

CHAPTER 5 ALLOY SYNTHESIS 101

5.1 INTRODUCTION 101
5.2 RESULTS: ION IMPLANTATION 102
5.2.1 SRIM simulation *102*
5.2.2 Design of experiments *104*
5.2.3 Effect of surface roughness *122*
5.2.4 Effect of dose *127*
5.3 RESULTS: RF SPUTTERING 136
5.3.1 SRIM simulation *136*
5.3.2 Determination of parameters *137*
5.3.3 Effect of deposition time *144*
5.3.4 Improving adhesion *152*
5.3.5 Effects of potential *163*
5.4 RESULTS: PULSED ELECTRODEPOSITION 165
5.4.1 Design of experiments *165*
5.4.2 Effect of T_{off} *177*
5.4.3 Effect of surface roughness *181*
5.4.4 Effect of plating time *183*
5.4.5 Long term exposure *185*
5.5 DISCUSSION 189
5.5.1 Ion implantation *190*
5.5.2 RF sputtering *193*
5.5.3 Pulsed electrodeposition *196*
5.5.4 Comparison *199*
5.6 SUMMARY 201

CHAPTER 6 CORROSION CHARACTERISATION 203

6.1 INTRODUCTION 203

6.2 RESULTS: CORROSION IN REDUCING ACIDS 203
6.2.1 Sulphuric acid *204*
6.2.2 Hydrochloric acid *221*
6.3 RESULTS: CORROSION IN CHLORIDE SOLUTIONS 231
6.3.1 Sodium chloride *232*
6.3.2 Magnesium chloride *240*
6.4 RESULTS: CORROSION IN SIMULATED FUEL CELL SOLUTION 242
6.5 DISCUSSION 247
6.5.1 Corrosion in sulphuric acid *248*
6.5.2 Corrosion in hydrochloric acid *251*
6.5.3 Corrosion in sodium chloride *252*
6.5.4 Corrosion in magnesium chloride *254*
6.5.5 Corrosion in simulated fuel solutions *255*
6.5.6 Comparison *256*
6.6 SUMMARY 258

CHAPTER 7 CONCLUSIONS AND RECOMMENDATIONS 259

7.1 INTRODUCTION 259
7.2 CONCLUSIONS 259
7.2.1 General conclusions *259*
7.2.2 Research highlights *260*
7.3 VALIDATION OF HYPOTHESES 261
7.4 RECOMMENDATIONS 262

BIBLIOGRAPHY 264

APPENDICES 291

APPENDIX A: PUBLICATIONS FROM THIS AND RELATED WORK 291
A.1 Peer reviewed articles *291*
A.2 Articles submitted or in preparation *291*
A.3 Scientific conferences *291*
APPENDIX B 293
B.1 Equivalent weight *293*
B.2 Density of supplied 304L stainless steel *294*
B.3 Corrosion current density *295*
APPENDIX C 296
APPENDIX D 297
D.1 Ruthenium composition on ruthenium implanted 304L stainless steel *297*
D.2 Thickness of ruthenium films deposited by PED *299*
APPENDIX E 301
E.1 Analytical instruments *301*
E.2 Electrochemical cell *302*
E.3 RF sputtering sample holder *303*

List of figures

Figure 1- 1 *(a) Compound annual growth rate of major metals: 1980 - 2014, (b) Stainless steel production by grade: 2004 – 2016.* 3
Figure 1- 2 *Analysis of 62 articles on cathodic modification. (a) Percentage of articles on cathodic modification with ruthenium and other PGMs, (b) Relative frequency of reports on ruthenium alloyed stainless steel alloys, (c) Comparison of studies on cathodic modification by bulk and surface alloying.* 5
Figure 1- 3 *Global demand for ruthenium compared to that for palladium and platinum: 2010-2016* 7

Figure 2- 1 *Schematic diagram combining the anodic and cathodic reactions for a corroding system* 11
Figure 2- 2 *Evans plot for a metal dissolving in acid* 13
Figure 2- 3 *Typical polarisation curves for stainless steel alloys showing (a) potential ranges of dissolving species, (b) passivity breakdown possibilities* 16
Figure 2- 4 *Hydrogen overpotential for iron based alloys measured in 1 N sulphuric acid at 303 K and different current densities* 19
Figure 2- 5 *Conventional polycrystalline 304 stainless steel after 30 days of immersion in 0.5 M hydrochloric acid at room temperature* 19
Figure 2- 6 *Effects of concentration and temperature on the corrosion rate of annealed type 304 stainless steel in deaerated sulphuric acid* 20
Figure 2- 7 *Micrograph of 304L stainless steel exposed to 2.5 M sodium chloride at +400 mV vs SCE for 10 minutes* 22
Figure 2- 8 *Autocatalytic processes occurring in a pit* 22
Figure 2- 9 *Pioneers of cathodic alloying (a) Philip Monnartz, (b) Nikon Danilovich Tomashov* 23
Figure 2- 10 *Hypothetical polarisation curve showing the influence of cathodic modification* 24
Figure 2- 11 *Effects of ruthenium on the polarisation characteristics of FeCr stainless steel in sulphuric acid* 28
Figure 2- 12 *Nyquist plot for Fe22Cr9Ni3Mo duplex stainless steel alloyed with (1) 0%, (2) 0.14%, (3) 0.22% and (4) 0.28% ruthenium immersed in 2 M hydrochloric acid* 30
Figure 2- 13 *Cyclic potentiodynamic polarisation curves for 2209 duplex stainless steel containing (1) 0% Ru and (2) 0.3% Ru in 0.6 M sodium chloride* 31
Figure 2- 14 *Schematic of two possible surface alloys for a binary alloy system A/B* 32
Figure 2- 15 *Silver film electrodeposited on copper foil showing aspects of mechanical and abrupt interface* 33
Figure 2- 16 *Typical features of an ion implanter.* 38
Figure 2- 17 *Schematic showing implantation profile as predicted by the Gaussian distribution.* 39
Figure 2- 18 *Skewness of implantation profiles resulting from different m_{ion}:m_{sub} ratios (a) Magnesium implanted with chromium at 15, 20, and 40 keV, (b) Nitrogen implanted in 304 stainless steel at 28 kV and different temperatures* 40
Figure 2- 19 *Schematic illustrating the process of sputtering.* 42
Figure 2- 20 *RF sputtering* 42
Figure 2- 21 *Effects of RF power on (a) deposition rate of ZnO:Al films on glass, (b) film thickness and residual stress of Ga-doped ZnO* 44
Figure 2- 22 *Dependence of film stress on sputtering gas pressure. (a) Molybdenum films produced by cathode sputter deposition using argon, (b) SiO_2 film produced by RF diode puttering using argon at 300 W* 45
Figure 2- 23 *Typical experimental set-up for electroplating.* 46

Figure 2- 24 *Concentration profiles of the diffusion layer near the cathode during DC electroplating* 47
Figure 2- 25 *Cu-Mn film deposited on PVD Cu seeded silicon wafer attached on RDE. Deposition was achieved by (a) DC, (b) PC plating* 48
Figure 2- 26 *(a) Typical current waveform used in pulse electrodeposition, (b) concentration profile of diffusion layer near the cathode during pulsed electrodeposition* 49
Figure 2- 27 *Potentiodynamic curves for (a) 304LN2 stainless steel exposed to 1, 3 and 6 M nitric acid at 25 °C, (b) 316L stainless steel in sulphuric acid with small chloride and fluoride additions measured between 0.25 and 1.05 V vs SHE* 51
Figure 2- 28 *Approaches for quantitatively analysing potentiodynamic polarisation curves, (a) Tafel, (b) LPR* 52
Figure 2- 29 *Misestimating i_{corr} from a small-range or nonlinear Tafel behaviour. Polarization curve obtained when Zn was exposed to aerated 0.01 M $NaHCO_3$ at 60°C and pH 8.1* 52
Figure 2- 30 *Electrical circuits analogues of a charge transfer controlled corrosion reaction (a) showing impedances of the corrosion system, (b) differentiating faradaic and non-faradaic components* 55
Figure 2- 31 *Graphical presentation of EIS data. (a) Nyquist plot, (b) Bode plots.* 56
Figure 2- 32 *Nyquist plots typical of corrosion systems (a) under diffusion control, (b) under both charge transfer and diffusion control* 57
Figure 2- 33 *Proposed models of ECs of coated aluminium LY12 alloy in 3.5% sodium chloride, (a) immediately after exposure, (b) after 50 minutes of exposure* 58

Figure 3- 1 *Apparatus used for RF sputtering.* 64
Figure 3- 2 *Set up used in pulsed electrodeposition.* 66
Figure 3- 3 *Typical current waveform used in pulsed electrodeposition.* 66
Figure 3- 4 *Potentiostat used for electrochemical characterisation.* 70
Figure 3- 5 *Reproducibility of the corrosion measurements* 73
Figure 3- 6 *Schematics of the corrosion cells with the sample in (a) a horizontal, (b) a vertical orientation.* 74
Figure 3- 7 *Effect of sample orientation on potentiodynamic polarisation curves of 304L in 1 M sulphuric acid.* 74
Figure 3- 8 *Assembled corrosion cell (a) photograph, (b) cross section* 75

Figure 4- 1 *Microstructure of the 304L stainless steel as revealed by (a) oxalic acid using optical microscope, (b) marble's solution, (c) sodium hydroxide using FESEM.* 78
Figure 4- 2 *EDS analysis of the stringers observed in Figure 4-1(c).* 79
Figure 4- 3 *Typical XRD pattern of 304L stainless steel.* 79
Figure 4- 4 *Typical stress-strain curve for the 304L stainless steel.* 80
Figure 4- 5 *Stereoscope images of failed specimen showing (a) necking, (b) cup and cone typical of ductile fracture.* 80
Figure 4- 6 *Influence of surface preparation on surface roughness.* 82
Figure 4- 7 *Effect of surface finish on precision and accuracy of measured corrosion rate of 304L stainless steel in 1 M sulphuric acid* 82
Figure 4- 8 *Effect of surface preparation on the Bragg angle of peaks (111) and (200) peaks.* 83
Figure 4- 9 *Strain vs $\sin^2\psi$ plots for (a) as received (b) ground to 240 grit, (c) polished 304L stainless steel.* 85
Figure 4- 10 *Residual stresses in 304L stainless steel samples as a function of surface preparation.* 86

Figure 4- 11 *Potentiodynamic polarisation curve for 304L stainless steel exposed to 1 M sulphuric acid at room temperature*..... 87
Figure 4- 12 *Nyquist plots of 304L stainless steel in 1 M sulphuric acid at (a) potential ranges 1 and 2 in Figure 4-11, (b) OCP*..... 88
Figure 4- 13 *Chronoamperometric measurements on 304L stainless steel exposed to 1 M sulphuric acid over 12 hours* 90
Figure 4- 14 *Typical corrosion surfaces obtained when 304L stainless steel was exposed to 1 M sulphuric acid, and examined by FESEM-SE.*..... 91
Figure 4- 15 *EDS analysis of the corrosion products deposited on 304L stainless steel exposed to 1 M sulphuric acid.* 92
Figure 4- 16 *Potentiodynamic polarisation curve for 304L stainless steel exposed to 3.5 wt%* 93
Figure 4- 17 *Current-time curves obtained when 304L stainless steel was exposed to 3.5 wt% sodium chloride at (a) 0 V, (b) 350 mV vs Ag/AgCl.* 94
Figure 4- 18 *Morphology of pits formed on 304L stainless steel exposed to 3.5 wt% sodium chloride, as examined by (a) FESEM-SE, (b) FESEM-BSD.* 95
Figure 4- 19 *Features of the pits grown in 3.5 wt%. (a) Interior of the pits as examined by FESEM-BSD, (b) cross section viewed with an optical microscope*..... 95

Figure 5- 1 Flow diagram illustrating the surface alloy synthesis and corrosion characterisation process. *101*
Figure 5- 2 Concentration distribution of ruthenium implanted into 304L stainless steel simulated at (a) 50 keV, and (b) 160 keV. *102*
Figure 5- 3 SRIM simulation of vacancies produced due to ruthenium implantation into 304L stainless steel at (a) 50 keV, and (b) 160 keV. *103*
Figure 5- 4 Simulated sputtering yield of 304L stainless steel implanted with ruthenium ions as a function of implantation energy..... *103*
Figure 5- 5 Typical XRD patterns of ruthenium implanted 304L stainless steel...... *105*
Figure 5- 6 Effect of implantation dose on Bragg angle. Samples prepared at 160 keV on (a) polished and (b) rough surfaces. *106*
Figure 5- 7 Effect of implantation dose on Bragg angle. Samples prepared at 50 keV on (a) polished and (b) rough surfaces. *106*
Figure 5- 8 Effect of surface preparation on Bragg angle. Samples implanted at 160 keV, with (a) 10^{12} Ru/cm^2, and (b) 10^{14} Ru/cm^2. ..... *107*
Figure 5- 9 Effect of surface preparation on Bragg angle. Samples implanted at 50 keV, (a) 10^{12} Ru/cm^2, and (b), 10^{14} Ru/cm^2. ..... *107*
Figure 5- 10 Effect of implantation energy on Bragg angle. Samples prepared on rough samples at (a) 10^{12} Ru/cm^2, and (b) 10^{14} Ru/cm^2. ..... *108*
Figure 5- 11 Effect of implantation energy on Bragg angle. Samples prepared on polished samples at (a) 10^{12} Ru/cm^2, and (b) 10^{14} Ru/cm^2. ..... *108*
Figure 5- 12 Influence of dose, energy and surface finish on (a) corrosion potential, and (b) corrosion rate of ruthenium implanted 304L stainless steel in 1 M sulphuric acid. *110*
Figure 5- 13 FESEM-SE images of the 304L stainless steel implanted at 50 keV, and exposed to 1 M sulphuric acid. *113*
Figure 5- 14 FESEM-SE images of the 304L stainless steel implanted at 160 keV, and exposed to 1 M sulphuric acid. *113*

Figure 5- 15 Polished samples magnified 1500x. Samples implanted at 160 keV and doses of (a) 10^{12} Ru/cm^2 and (b) 10^{14} Ru/cm^2. 114
Figure 5- 16 EDS analysis of agglomerates formed on some of the ruthenium implanted 304L stainless steels. 115
Figure 5- 17 FESEM-SE images of the samples with deposits after cleaning, magnified 500 and 10000x. Samples were prepared at (a) 160keV, 10^{12} Ru/cm^2, rough, (b) 50keV, 10^{12} Ru/cm^2, polished, (c) 160keV, 10^{14} Ru/cm^2, rough, (d) 50keV, 10^{14} Ru/cm^2, rough. 116
Figure 5- 18 Normal probability plot showing the effects of the main factors A-energy, B-dose and C-surface roughness and their interactions. 117
Figure 5- 19 Effect of (a) energy (A), and (b) surface roughness (C) on the corrosion rate of ruthenium implanted 304L stainless steel in 1 M sulphuric acid. 119
Figure 5- 20 Interaction graphs for the effects of (a) energy and surface (AC), and (b) dose and surface roughness (BC) on the corrosion rate of ruthenium implanted 304L stainless steel in 1 M sulphuric acid. 120
Figure 5- 21 Combinations of the conditions that can give the lowest corrosion rates of ruthenium implanted 304L stainless steel in 1 M sulphuric acid. 121
Figure 5- 22 Strain vs $\sin^2\psi$ plots for ruthenium implanted 304L stainless steel. The surfaces were initially (a) ground to 240 grit, (b) ground to 1200 grit, and (c) polished with 6 μm alumina powder.. 123
Figure 5- 23 Residual stresses in ruthenium implanted 304L stainless steel as a function of pre-implantation surface finish. 124
Figure 5- 24 Effect of implantation energy on surface roughness of initially polished 304L stainless steel: (a) polished sample before implantation, (b) after implantation at 50 keV, and (c) after implantation at 160 keV 125
Figure 5- 25 Effect of implantation energy on surface roughness of initially ground 304L stainless steel: (a) rough sample before implantation, (b) after implantation at 50 keV, and (c) after implantation at 160 keV 125
Figure 5- 26 Energy dependence of mean sputtered depth on ruthenium implanted 304L stainless steel. 126
Figure 5- 27 Effect of surface preparation on corrosion potential, and corrosion rates of ruthenium implanted 304L stainless steel in 1 M sulphuric acid. 127
Figure 5- 28 Influence of implantation dose on Bragg angle of ruthenium implanted 304L stainless steel. Samples were rough, and implantation energy was 50 keV 128
Figure 5- 29 Effect of implantation dose on surface roughness of initially polished 304L stainless steel: (a) polished sample before implantation, (b) after implantation with 10^{12} Ru/cm^2, and (c) after implantation with 10^{16} Ru/cm^2 130
Figure 5- 30 Effect of implantation dose on surface roughness of initially polished 304L stainless steel: (a) rough sample before implantation, (b) after implantation with 10^{12} Ru/cm^2, and (c) after implantation with 10^{16} Ru/cm^2 130
Figure 5- 31 Dose dependence of mean sputtered depth on ruthenium implanted 304L stainless steel. 131

Figure 5- 32 Influence of implantation dose on (a) corrosion potential, and (b) corrosion rate of ruthenium implanted 304L stainless steel in 1 M sulphuric acid 132
Figure 5- 33 Effect of sample orientation on the Bragg angle of ruthenium implanted 304L stainless steel 133
Figure 5- 34 Effect of sample orientation on potentiodynamic polarisation curves ruthenium implanted 304L stainless steel in 1 M sulphuric acid..... 134
Figure 5- 35 FESEM images of the ruthenium implanted 304L stainless steel exposure to 1 M sulphuric acid showing effect of sample orientation on corrosion. 135
Figure 5- 36 Variation of (a) ruthenium sputter yield, and (b) energy of sputtered ruthenium atoms as a function of argon incident energy..... 137
Figure 5- 37 Influence of deposition power on XRD patterns of 304L stainless steel coated with ruthenium films..... 138
Figure 5- 38 EDS analysis of the RF sputtered films. Beam voltage used was (a) 5 kV, and (b) 10 kV..... 139
Figure 5- 39 Influence of deposition power and time on the types of defects observed on the ruthenium films produced by RF sputtering 140
Figure 5- 40 AFM images of ruthenium films produced at 30 and 100 W. 141
Figure 5- 41 FESEM-SE images of the ruthenium coated 304L stainless steel after 12 hours of exposure to 1 M sulphuric acid..... 143
Figure 5- 42 Influence of deposition time on the thickness of ruthenium films deposited on 304L stainless steel by RF sputtering 144
Figure 5- 43 FESEM and AFM of ruthenium films deposited on 304L stainless steel at 30 W and different deposition times. 145
Figure 5- 44 Influence of deposition time on the Bragg angle of ruthenium coated 304L stainless steel 146
Figure 5- 45 Influence of deposition and exposure time on (a) corrosion potential, and (b) corrosion rate of ruthenium coated 304L stainless steel in 1 M sulphuric acid..... 147
Figure 5- 46 Bode phase plots for ruthenium coated 304L stainless steel in 1 M sulphuric acid (a) immediately upon exposure, and (b) after 48 hours of exposure. 149
Figure 5- 47 FESEM-SE images of ruthenium coated 304L stainless steel before and after 48 hours of exposure to 1 M sulphuric acid. 150
Figure 5- 48 FESEM-BS images showing remnants of the ruthenium films on 304L stainless steel after 48 hours of exposure to 1 M sulphuric acid..... 151
Figure 5- 49 Metal loss from ruthenium sputter coated 304L stainless steel as a function of deposition time after 48 hours exposure in 1 M sulphuric acid. 151
Figure 5- 50 Influence of (a) surface roughness, (b) annealing, (c) pulsing pressure, and (d) titanium seeding on the Bragg angle of ruthenium sputter coated 304L stainless steel. 154
Figure 5- 51 Variation of OCP of RF sputtered ruthenium films with exposure time in 1 M sulphuric acid 155

Figure 5- 52 Nyquist plots of the ruthenium sputter coated 304L stainless steel after 48hours of exposure in 1 M sulphuric acid and measured at OCP 156
Figure 5- 53 Resistance of the ruthenium sputtered films as a function of preparation technique 157
Figure 5- 54 Bode phase plots of the ruthenium films after exposure to 1 M sulphuric acid for (a) 1 hour, and (b) 48 hours 158
Figure 5- 55 FESEM post corrosion examination of the RF sputtered films after exposure to 1 M sulphuric acid for 48 hours: (a) polished,(b) rough, (c) pulsed pressure, and (d) titanium seeding 158
Figure 5- 56 Variation of OCP of RF sputtered films with exposure time in 1 M sulphuric acid post annealing 160
Figure 5- 57 Bode phase plots of the ruthenium films post annealing, after exposure to 1 M sulphuric acid for (a) 1 hour, and (b) 48 hours. 161
Figure 5- 58 FESEM post corrosion examination of annealed RF sputtered films deposited on 304L stainless steel after exposure to 1 M sulphuric acid for 48 hours. 162
Figure 5- 59 FESEM post corrosion examination of RF sputtered ruthenium films deposited by pulsed pressure and on titanium seed after exposure to 1 M sulphuric acid 162
Figure 5- 60 Effect of potential on the Bode phase plots for ruthenium coated 304L stainless steel exposed to 1 M sulphuric acid 163
Figure 5- 61 Effect of potential on resistance of ruthenium sputtered films after 2 hours of exposure in 1 M sulphuric acid 164
Figure 5- 62 Effect of potential on the adhesion of ruthenium sputtered films. Films were held in 1 M sulphuric acid at (a) -100 mV, (b) 200 mV, (c) 500 mV and (d) 800 mV. 164
Figure 5- 63 Influence of T_{on} and T_{off} on surface morphology of ruthenium films deposited on polished 304L stainless steel samples, i_p = 1.2 A (≈ 0.4 A/cm^2). ... 166
Figure 5- 64 Influence of T_{on} and T_{off} on surface morphology of ruthenium films deposited on polished 304L stainless steel samples, i_p = 2 A (≈ 0.7 A/cm^2). 167
Figure 5- 65 Influence of T_{on} and T_{off} on surface morphology of ruthenium films deposited on rough 304L stainless steel samples, i_p = 1.2 A (≈ 0.4 A/cm^2). 168
Figure 5- 66 Influence of T_{on} and T_{off} on surface morphology of ruthenium films deposited on rough 304L stainless steel samples, i_p = 2 A (≈ 0.7 A/cm^2). 169
Figure 5- 67 Influence of T_{off}, T_{on} and i_p on the corrosion rate of ruthenium coated 304L stainless steel in 1 M sulphuric acid. Surfaces were (a) polished and (b) rough. 171
Figure 5- 68 Images of ruthenium coated 304L stainless steel after exposure to 1 M sulphuric acid, showing effect of T_{off}. 172
Figure 5- 69 Normal probability plot of the main and interaction effects on the corrosion of ruthenium plated 304L stainless steel in 1 M sulphuric acid 174
Figure 5- 70 Effects of (a) T_{off} (B), (b) surface roughness (D), and (c) their interaction (BD) on the corrosion rate of ruthenium plated 304L stainless steel in 1 M sulphuric acid. 176

Figure 5- 71 Combinations of the conditions that can give the lowest corrosion rates of ruthenium plated 304L stainless steel in 1 M sulphuric acid. 177
Figure 5- 72 Effect of T_{off} on (a) temperature, and (b) pH of the ruthenium plating bath..... 178
Figure 5- 73 Variation of the ruthenium concentration with T_{off} as measured by ICP 179
Figure 5- 74 Influence of T_{off} on (a) Bragg angle, and (b) strain induced in ruthenium plated 304L stainless steel..... 180
Figure 5- 75 Variation of corrosion rate of ruthenium plated 304L with T_{off}. Total deposition time was 1800s, and samples were exposed to 1 M sulphuric acid. . 181
Figure 5- 76 Influence of surface roughness on film morphology..... 182
Figure 5- 77 Variation of corrosion rate of ruthenium plated 304L with T_{off}. Total deposition time was 1800 s, and samples were exposed to 1 M sulphuric acid . 183
Figure 5- 78 FESEM-SE images showing the influence of T_{off} and deposition on the morphology of ruthenum prepared by PED..... 184
Figure 5- 79 Effect of deposition time and T_{off} on the corrosion rate of ruthenium 304L stainless steel exposed to 1 M sulphuric acid. 185
Figure 5- 80 Adhesion of ruthenium films deposited on 304L stainless steel by PED..... 186
Figure 5- 81 Variation of corrosion potential of ruthenium plated 304L stainless steel with exposure time in 1 M sulphuric acid..... 187
Figure 5- 82(a) Bode phase plots, and (b) Nyquist plots of ruthenium plated 304L stainless steel in 1M sulphuric acid. 188
Figure 5- 83 FESEM-SE images of the corroded ruthenium plated 304L stainless steel after 1 and 48 hours in 1 M sulphuric acid. 189
Figure 5- 84 Schematic illustrating the possible dependence of sputtering on surface finish of the 304L stainless steel substrate. 192
Figure 5- 85 Effect of protrusions on current distribution 197
Figure 5- 86 Stress state in ruthenium films when substrate stresses were (a) compressive, and (b) tensile. 198
Figure 5- 87 Protection efficiency of ruthenium surface alloys 199
Figure 5- 88 Effects of ruthenium surface alloying on the corrosion potential of 304L stainless steel. 200

Figure 6- 1 *Samples used in corrosion characterisation: (a) unmodified, (b) ruthenium implanted 304L stainless steel. 203*
Figure 6- 2 *Potentiodynamic polarisation curves of unmodified and ruthenium implanted 304L stainless steel in 1 M sulphuric acid 204*
Figure 6- 3 *OCP-time curve of (a) unmodified, (b) ruthenium implanted 304L stainless steel in sulphuric acid of different concentrations 206*
Figure 6- 4 *Variation of OCP with sulphuric acid concentration for (a) unmodified, (b) ruthenium implanted 304L stainless steel. 207*
Figure 6- 5 *Effect of sulphuric acid concentration on the potentiodynamic polarisation curve obtained on ruthenium implanted 304L stainless steel after 2 hours of exposure. 208*
Figure 6- 6 *Influence of sulphuric acid concentration on corrosion rate of (a) unmodified, (b) ruthenium implanted 304L stainless steel. 209*

Figure 6- 7 *Influence of sulphuric acid concentration on (a) Nyquist, (b) Bode phase plots measured on ruthenium implanted 304L stainless steel.* 210
Figure 6- 8 *Influence of sulphuric acid concentration on the thickness of films grown on ruthenium implanted 304L stainless steel* 211
Figure 6- 9 *FESEM-SE images of the ruthenium implanted 304L stainless steel after 2 hours exposure at OCP in (a) 0.5 M, (b) 1 M, (c) 2 M, (d) 4 M sulphuric acid.* 212
Figure 6- 10 *Effect of exposure time and concentration on (a) OCP and E_{corr}, (b) corrosion rate of ruthenium implanted 304L stainless steel in 0.5 and 4 M sulphuric acid.* 213
Figure 6- 11 *OCP-time curve of ruthenium implanted 304L stainless steel in sulphuric acid of different concentrations at 50°C.* 214
Figure 6- 12 *OCP of (a) unmodified, and (b) ruthenium implanted 304L stainless steel in sulphuric acid of different concentrations at 25 and 50°C.* 215
Figure 6- 13 *Effect of temperature on the corrosion rate of (a) unmodified, (b) ruthenium implanted 304L stainless steel exposed to sulphuric acid.* 216
Figure 6- 14 *Typical FESEM-SE images of ruthenium implanted after exposure to sulphuric acid at 50°C. Acid concentration was (a) 1 M, (b) 4 M.* 217
Figure 6- 15 *Effect of agitation on the potentiodynamic polarisation curves for unmodified and ruthenium implanted 304L stainless steel in 1 M sulphuric acid.* 218
Figure 6- 16 *Influence of agitation on OCP-time curves for unmodified and ruthenium implanted 304L stainless steel in 1 M sulphuric acid over 3 hours.* 218
Figure 6- 17 *Effect of agitation on OCP-time curve for ruthenium implanted 304L stainless steel in 1 M sulphuric acid over 12 hours.* 219
Figure 6- 18 *Potentiodynamic polarisation curve of ruthenium 304L stainless steel exposed to 1 M sulphuric acid with ≈ 2750 ppm sodium chloride* 220
Figure 6- 19 *Potentiodynamic polarisation curves of unmodified and ruthenium implanted 304L stainless steel in 1 M hydrochloric acid* 221
Figure 6- 20 *OCP-time curves for (a) unmodified, (b) ruthenium implanted 304L stainless steel in hydrochloric acid of different concentrations* 223
Figure 6- 21 *Effects of hydrochloric acid concentration on the potentiodynamic polarisation curves obtained on (a) unmodified, (b) ruthenium implanted 304L stainless steel after 2 hours of exposure.* 225
Figure 6- 22 *Influence of concentration on (a) E_{corr}, (b) corrosion rates of unmodified and ruthenium implanted 304L stainless steel exposed to hydrochloric acid.* 226
Figure 6- 23 *FESEM images of unmodified and ruthenium implanted 304L stainless steel after 2 hours exposure in hydrochloric acid.* 227
Figure 6- 24 *Effect of temperature on the potentiodynamic polarisation curves for ruthenium implanted 304L stainless steel after 2 hours of exposure in (a) 1 M, (b) 2 M hydrochloric acid.* 229
Figure 6- 25 *Influence of temperature and concentration on the corrosion rates of (a) unmodified, (b) ruthenium implanted 304L stainless steel.* 230
Figure 6- 26 *FESEM images of unmodified and ruthenium implanted after 2 hours exposure at OCP in hydrochloric acid of different concentrations at 50°C.* 231
Figure 6- 27 *Potentiodynamic polarisation curves of unmodified and ruthenium implanted 304L stainless steel in 3.5 wt% sodium chloride* 232
Figure 6- 28 *Influence of sodium chloride concentration on polarisation curves of ruthenium implanted 304L stainless steel* 233
Figure 6- 29 *Effect of sodium chloride concentration and exposure temperature on (a) E_{corr}, (b) E_{pit} of unmodified and ruthenium implanted 304L stainless steel* 234
Figure 6- 30 *FESEM images of ruthenium implanted 304L stainless steel after exposure in (a) 1 wt%, (b) 3.5 wt%, and (c) 5 wt% sodium chloride at 25°C.* 235
Figure 6- 31 *Potentiodynamic polarisation curves of ruthenium implanted 304L stainless steel in different concentrations of sodium chloride at 50°C.* 236

Figure 6- 32 *Effect of temperature on E_{pit} of ruthenium implanted 304L stainless steel in different concentrations of sodium chloride.* 237
Figure 6- 33 *FESEEM images of ruthenium implanted 304L stainless after exposure in (a) 1 wt%, (b) 3.5 wt%, (c) 5 wt% sodium chloride at 50°C.* 237
Figure 6- 34 *Effect of temperature and sodium chloride concentration on pit density on ruthenium implanted 304L stainless steel.* 238
Figure 6- 35 *Effect of pH on the potentiodynamic polarisation curves for ruthenium implanted 304L stainless steel exposed to 3.5 wt% sodium chloride*..... 239
Figure 6- 36 *Variation of (a) E_{corr} and E_{pit}, and (b) dissolved iron with pH of 3.5 wt% sodium chloride.*..... 240
Figure 6- 37 *Potentiodynamic polarisation curves for unmodified and ruthenium implanted 304L stainless steel in 3.5 wt% magnesium chloride.*..... 241
Figure 6- 38 *Effect of temperature on the polarisation of ruthenium implanted 304L stainless steel in 3.5 wt% magnesium chloride.*..... 242
Figure 6- 39 *FESEM image of ruthenium implanted 304L stainless steel after 2 hours exposure in 3.5 wt% magnesium chloride at (a) 25, (b) 50°C.*..... 242
Figure 6- 40 *OCP-time curves for ruthenium implanted 304L stainless steel in simulated fuel cell solutions* 243
Figure 6- 41 *Potentiodynamic polarisation curves for ruthenium implanted 304L stainless steel in simulated fuel cell solutions after 2 hours exposure.* 244
Figure 6- 42 *Comparison of corrosion rates for ruthenium implanted 304L stainless steel in simulated fuel cell solutions*..... 245
Figure 6- 43 *Time variation of current density at 645 mV for ruthenium implanted 304L stainless steel exposed for 24 hours in (a) Electrolyte 1, (b) Electrolyte 2*..... 246
Figure 6- 44 *Effect of stirring on current density of ruthenium implanted 304L stainless steel at 645 mV in Electrolyte 1.* 247
Figure 6- 45 *Schematic illustrating possible effect of sulphuric acid concentration on ruthenium implanted 304L stainless steel.*..... 249
Figure 6- 46 *Schematic illustrating the typical effect of sulphuric acid concentration on the corrosion of 304 stainless steels* 250
Figure 6- 47 *Schematic illustrating pit initiation on the matrix close to a manganese sulphide inclusion* 254
Figure 6- 48 *Schematic diagram of a PEMFC* 256
Figure 6- 49 *Effect of ruthenium implantation on E_{pit} of 304L stainless steel in sodium and magnesium chloride solutions*..... 258

Figure B- 1 *Determination of polarisation resistance from potentiodynamic polarisation curves.* 295

Figure C- 1 *A copy of the assay certificate for the ruthenium nitrosyl salt used in this study.* 296

Figure D- 1*(a) Annular dark field STEM micrograph of the rough ruthenium implanted 304L stainless steel, (b) EDS line scan of the sample in (a)* 297
Figure D- 2 *Typical AES survey of ruthenium implanted 304L stainless steel (a) before, (b) after 1 minute sputtering at a rate of 15 nm/min.*..... 298
Figure D- 3 *Influence of Toff on the thickness of ruthenium films deposited on 304L stainless steel by PED.*..... 299
Figure D- 4 *FESEM images of the ruthenium film deposited on 304L stainless steel by PED in (a) SE mode, (b) BSD mode* 300

Figure E- 1 *Some of the analytical instruments used in this project. (a) Bruker D2 Phaser, (b) Veeco Dimension 3100 AFM, (c) Lecia DM6000 M optical microscope, (d) Carl Zeiss Sigma FESEM, (e) Agilent 240FS atomic adsorption spectroscope*..... 301
Figure E- 2 *Drawing of the cell used in electrochemical corrosion tests*..... 302
Figure E- 3 *Assembled and exploded views of the sample holder used in RF sputtering.* 303

List of tables

Table 2- 1 *Conductivity and diffusion coefficients of selected ions at infinite dilution in water at 25°C* 20
Table 2- 2 *Comparison of results for the corrosion of ruthenium alloyed stainless steels as reported by different investigators in sulphuric acid* 29
Table 2- 3 *Elements and techniques used to improve corrosion resistance of austenitic stainless steel alloys.* 35
Table 2- 4 *Technologies for surface alloying* 37
Table 2- 5 *Passive electrical elements used to construct equivalent circuits and their likely physical meanings* 59

Table 3- 1 *Chemical composition of the ruthenium nitrosyl salt* 62
Table 3- 2 *Etchants used for metallographic characterisation* 68

Table 4- 1 *Composition of 304L stainless steel as received* 77
Table 4- 2 *Mechanical properties of 304L stainless steel* 81
Table 4- 3 *Variation of Bragg angle and strain with surface preparation.* 83
Table 4- 4 *Electrochemical parameters obtained from EIS tests* 88
Table 4- 5 *Effect of molybdenum on PREN of supplied 304L stainless steel.* 96
Table 4- 6 *Corrosion parameters for 304L stainless steel after exposure to 1 M sulphuric acid and 3.5 wt% sodium chloride* 99

Table 5- 1 *Experimental conditions used for the 2^3 factorial DOE.* 104
Table 5- 2 *Corrosion rate (mm/y) results from the 2^3 DOE* 111
Table 5- 3 *Analysis of the effect of the parameters energy (A), dose (B) and surface roughness (C) and their interactions on the corrosion of ruthenium implanted 304L stainless steel in 1 M sulphuric acid* 118
Table 5- 4 *Dose dependence of lattice parameter and strain in ruthenium implanted 304L stainless steel* 128
Table 5- 5 *Effect of sample orientation on the ruthenium distribution and average corrosion rate of rough ruthenium implanted 304L stainless steel* 135
Table 5- 6 *Corrosion parameters of 304L stainless steel sputter coated with ruthenium* 142
Table 5- 7 *Experimental conditions used for the 2^4 factorial DOE.* 165
Table 5- 8 *Corrosion rate (mm/y) results from the 2^4 DOE* 170
Table 5- 9 *Effect of Ton (A), Toff (B), ip (C), and surface roughness (D) and their interactions on corrosion of ruthenium plated 304L in 1 M sulphuric acid* 173
Table 5- 10 *Synthesis conditions for ruthenium plated 304L stainless steel by PED.* 185
Table 5- 11 *Synthesis condition for ion implanted 304L stainless steel.* 193

Table 6- 1 *Electrochemical parameters obtained from EIS tests* 211
Table 6- 2 *Electrochemical parameters obtained from potentiodynamic polarisation of ruthenium implanted 304L stainless steel in different solutions.* 221

Table B- 1 *Determination of the equivalent weight of the supplied 304L stainless steel. *based on 1g of the alloy.* 293
Table B- 2 *Calculation of the actual density of the supplied 304L stainless steel. *based on 100g.* 294

List of symbols

A	surface area (cm^2)
B	Stern-Geary constant (V)
C	capacitance (F)
C_o	cation concentration in bulk solution (M)
C_s	cation concentration at electrode surface (M)
d	mean sputtered depth (m)
D	thickness (m), diffusivity (m^2/s)
E	potential (V), energy of incident ion (eV)
E^o	equilibrium potential (V)
E_{corr}	corrosion potential (V)
E_{crit}	critical potential (V)
E_{max}	maximum energy of ion (eV)
E_{pass}	passivation potential (V)
E_{pit}	pitting potential (V)
E_{trans}	transpassive potential (V)
E_w	equivalent weight
F	Faraday constant (96 489 A/mol)
G	Gibbs free energy (J/mol)
I_a	anodic current (A)
i_{app}	applied current density (A/cm^2)
I_c	cathodic current (A)
i_{corr}	corrosion current density (A/cm^2)
I_{corr}	corrosion current (A)
i_{crit}	critical current density (A/cm^2)
i_L	limiting current density (A/cm^2)
I_o	exchange current (A)
i_o	exchange current density (A/cm^2)
i_p	plating current density (A/cm^2)
i_{pass}	passivation current density (A/cm^2)
I_t	time-varying current (A)

K_1	constant (3.25×10^{-3} mm.g/μA.cm.y)
L	inductance (H)
m_{ion}	mass of implanted ion (amu)
m_{sub}	mass of substrate atoms (amu)
n	number of electrons, number of samples in a data set
N	atomic density
P_R	projected range/ implantation depth (m)
q	elementary charge (1.6×10^{-19} C)
Q	constant phase element (F.cm)
R	ideal gas constant (8.314 J/K.mol), resistance (Ω)
R_p	polarisation resistance ($\Omega.cm^2$)
R_s	solution resistance (Ω.cm)
S	entropy (J/K)
t	time (s)
T	absolute temperature (K), temperature (°C)
T_{off}	pulse off time (s)
T_{on}	pulse length (s)
V_t	time-varying potential (V)
W	Warburg resistance ($\Omega.s^{-½}$)
$wt\%$	weight percentage
x_i	i^{th} value in a data set
$\bar{x}$	arithmetic mean
Z	impedance (Ω)
β_a	anodic Tafel slope (V/decade)
β_c	cathodic Tafel slope (V/decade)
δ_N	width of diffusion layer (m)
δ_P	width of pulsating layer (m)
δ_S	width of stationary layer (m)
ε	relative dielectric constant (F/m)
ε_o	dielectric constant of free space (8.85×10^{-12} F/m)
η	overvoltage/ overpotential (V)

η_a	anodic overvoltage (V)
η_c	cathodic overvoltage (V)
η_{conc}	concentration overpotential (V)
ρ	density (g/cm^3)
τ	critical T_{on} to reach $C_s = 0$ (s)
θ	phase difference (°)
ω	angular frequency (rad/s)

List of Abbreviations

AC	alternating current (A)
AES	auger electron spectroscopy
AISI	American Iron and Steel Institute
ASTM	American Society for Testing and Materials
CPE	constant phase element
CPT	critical pitting temperature (°C)
CR	corrosion rate (mm/y)
DC	direct current (A)
EC(s)	Equivalent circuit(s)
EIS	electrochemical impedance spectroscopy
ImZ	imaginary impedance
ISSF	International Stainless Steel Forum
LPR	linear polarisation resistance
OCP	open circuit potential (V)
PED	pulse(d) electrodeposition
PGMs	platinum group metals
PREN	pitting resistance equivalent number
ReZ	real impedance
RF	radio frequency
SCC	stress corrosion cracking
SD	standard deviation
SDE	standard deviation error
SHE	standard hydrogen electrode

Chapter 1
Introduction

1.1 Background and motivation

Austenitic stainless steels are one of the most important classes of alloys ever produced. First patented in 1912 (Pasel 1918), they contain chromium and nickel as major constituents. Nickel promotes the stability of the austenite phase at room temperature and affords austenitic stainless steels a unique set of properties. They are mostly corrosion resistant, have good weldability and formability, good impact resistance down to -183°C and can resist scaling at temperatures as high as 1100°C (Dillion 1986; Kumar et al. 2002). These properties make austenitic stainless steels indispensable in many applications such as in fuel processing, pharmaceutical and food handling industries.

Corrosion resistance of austenitic stainless steels is based on passivity. Tomashov (1964) defined passivity as a state of increased corrosion resistance of metals or alloys caused by the selective control of the anodic process. In austenitic stainless steels, selective oxidation of chromium forms a passive layer of chromium oxide that is typically 1-5 nm thick (Olsson et al. 2003; Sudesh et al. 2006), adherent, compact, self-healing and protective in many corrosive environments. Passivity therefore provides an inexpensive and practical means of corrosion control on austenitic stainless steel structures. However, the chromium oxide layer is prone to dissolution in reducing acidic media such as dilute sulphuric acid, and in solutions containing chloride species. This limits the application spectrum of austenitic stainless steels, and compromises the durability and effective operation of structures made of these alloys.

World-over, the use of stainless steel alloys increases at a rate of more than 5% per annum, and far outweighs consumption of other engineering materials as illustrated in Figure 1-1(a) (ISSF 2015). Austenitic stainless steels are the most recognised type of stainless steel, and account for more than 70% of the annual stainless steel production worldwide (Figure 1-1(b)). Corrosion of metallic

structures costs industrialised countries an estimated 3% of the gross domestic product (GDP) annually, and up to 5.2% of the GDP for developing economies (Schumuki 2002; Lieser & Xu 2010). The South African economy, for instance, loses at least R130 billion per annum to corrosion, which is equivalent to about 4.5% of the GDP (Mintek 2011; Statistics South Africa 2016). As such, any measures that can promote passivity and improve the corrosion resistance of austenitic stainless steel in reducing acid and chloride containing solutions are worth contemplation.

Cathodic modification is one way by which passivity of austenitic stainless steels in reducing acidic media and those containing chloride species may be stimulated and sustained. Cathodic modification, also known as cathodic alloying, is a technique that involves introducing active cathodes such as platinum group metals (PGMs) into a stainless steel alloy matrix. These cathodes reduce cathodic polarisation by making the cathodic process kinetically easier, and substantially shift the stainless steel's corrosion potential to more noble values where a stable chromium oxide layer can easily form (Tomashov 1964; McGill 1990; Potgieter et al. 1990), and corrosion rates are marginal.

Philip Monnartz first observed this phenomenon in 1911 on iron-chromium alloys either wound or alloyed with platinum (Monnartz 1911). More than three decades later, a Russian scientist named Nikon Tomashov and his colleagues developed the concept of cathodic modification, extending it to titanium and chromium alloyed with palladium, ruthenium and iridium (Kolotyrkin 1977; Streicher 1977; Tomashov et al. 1984). They reported spontaneous passivation of these alloys in acidic media, and recorded improvements in corrosion resistance by a factor of up to 100.

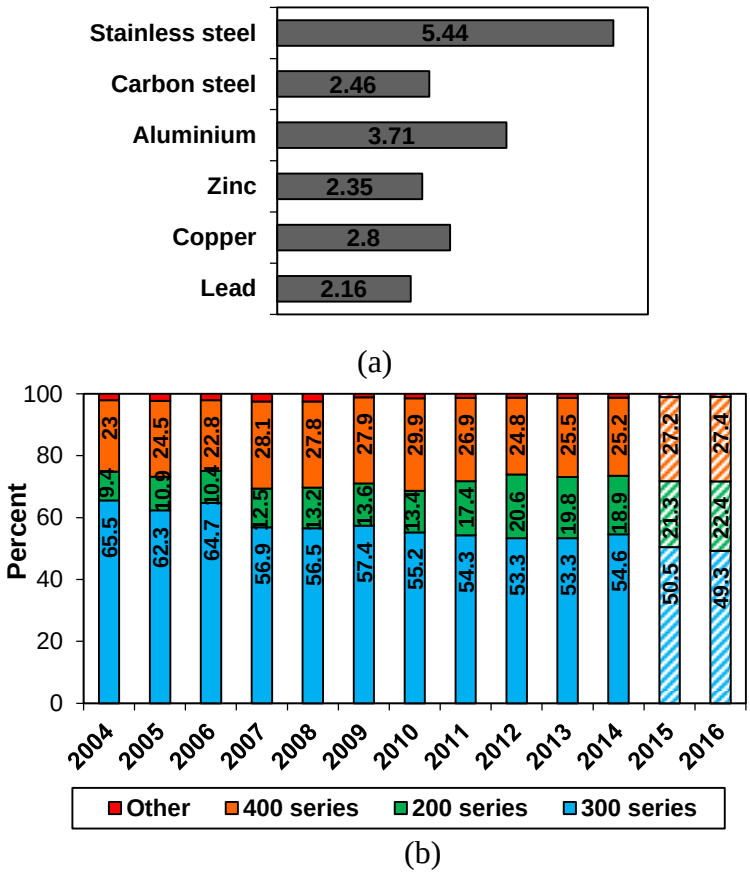

Figure 1- 1 *(a) Compound annual growth rate of major metals: 1980 - 2014, and (b) Stainless steel production by grade: 2004 – 2016* (adapted from ISSF 2015). 300 and 200 series are austenitic stainless steels. *2015 and 2016 are estimates.*

1.2 Research problems

The relatively high cost of most PGMs has prompted increased research interest on ruthenium, and examination of 62 journal articles in Figure 1-2(a) confirmed this. Numerous researchers have established that additions of ruthenium can significantly improve the stability of stainless steel alloys in reducing acidic media and chloride containing solutions (Tjong 1990a; Potgieter et al. 1996; Olubambi et al. 2009; Sherif et al. 2009a; Sherif 2012). Considerable success has been achieved on duplex, ferritic and super ferritic stainless steels, with Mintek commercialising a variant modelled on super ferritic stainless steel and known as Ruthalloy (Wolff 1999). However, as revealed in Figure 1-2(b), the effect of ruthenium on austenitic stainless steels has been largely overlooked. This, despite the synergistic effect of ruthenium and nickel noted by some researchers

(Potgieter & Kincer 1991; Lekala et al. 2012), and the fact that austenitic stainless steels are the most commonly used form of stainless steel.

Figure 1-2(c) shows that cathodic modification of stainless steel alloys is frequently achieved by bulk alloying. Ruthenium melts at very high temperatures of 2330°C, and its melting is not only energy intensive, but also requires an inert atmosphere to prevent the oxidation of ruthenium at temperatures above 800°C. A further drawback of this approach to cathodic modification is that bulk alloying uses substantial amounts of ruthenium, rendering such cathodically modified stainless steel alloys quite expensive and inaccessible for wider application. This is demonstrated by the fact that despite impressively low corrosion rates, Ruthalloy is largely unknown decades after its commercialisation. Surface alloying is undoubtedly a more economical way of introducing ruthenium to austenitic stainless steel alloys. Despite the practical and economic benefits inherent surface alloys of ruthenium, this approach to cathodic modification remains inadequately explored.

Up to now, surface alloying of austenitic stainless steel with ruthenium has been done mostly by laser surface alloying (Lekala et al. 2012; Van der Merwe & Tharandt 2015) using ruthenium enriched metal powders. While this approach has been considerably successful, poor alloying has been observed in most cases, with uneven distribution of ruthenium in the alloyed layer. This has led to inconsistent and unpredictable corrosion behaviour. For instance, higher corrosion rates were recorded on alloys that have higher ruthenium content, which is contrary to expectation. Tjong et al. (1997) observed similar compositional variability when ferritic Fe-40Cr stainless steel was laser surface alloyed with ruthenium powder. As such, it is necessary to explore alternative approaches of surface alloying austenitic stainless steel with ruthenium.

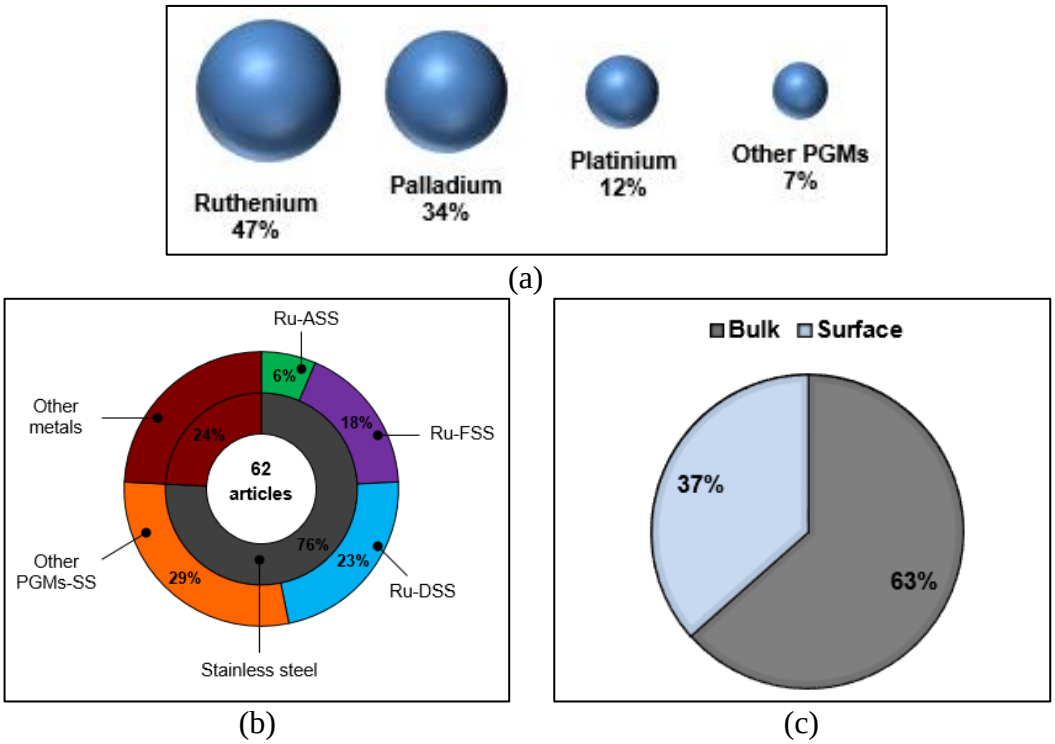

Figure 1- 2 *Analysis of 62 articles on cathodic modification. (a) Percentage of articles on cathodic modification with ruthenium and other PGMs, (b) Relative frequency of reports on ruthenium alloyed stainless steel alloys. SS=stainless steel, A=austenitic, F=ferritic and D=duplex, and (c) Comparison of studies on cathodic modification by bulk and surface alloying.*

1.3 Research aims and objectives

The aim of this research project, therefore, was to modify the surface properties of austenitic stainless steel using ruthenium for improved corrosion resistance in reducing acidic and chloride media. Focus was on employing non-thermal surface alloying strategies to ensure an even distribution of ruthenium and therefore predictable corrosion behaviour.

Specific objectives of the study were:

1. To synthesise ruthenium alloys on 304L austenitic stainless steel using three techniques, namely radio frequency (RF) magnetron sputtering, ion implantation and pulsed electrodeposition (PED).

2. To determine the physicochemical properties of the modified surfaces, and the influence of synthesis parameters on these using methods such as X-ray diffraction (XRD) and scanning electron microscope (SEM).

3. To use design of experiments (DOE), and similar statistical tools to optimise synthesis parameters for each technique with the view of producing surface alloys with maximum corrosion resistance.

4. To characterise and compare the corrosion behaviour of the surface alloys in reducing acidic media and chloride media using, among other methods, potentiodynamic polarisation and electrochemical impedance spectroscopy (EIS).

5. To recommend possible applications for the ruthenium alloyed 304L stainless steel.

1.4 Hypotheses

1. Corrosion is a surface dependent degradation mode. As such, the corrosion resistance of austenitic stainless steel in chloride and reducing acidic media can be increased by only enriching the surface with ruthenium.

2. Since cathodic modification provides sites that kinetically favour the cathodic process, the corrosion resistance of the surface alloys on austenitic stainless steel will not be compromised by discontinuities in the films prepared by RF magnetron sputtering or PED.

3. During synthesis of the surface alloys, the initial interaction between ruthenium and the austenitic stainless steel is on the surface. Hence, the nature of surface preparation would play an important role on the properties of the ruthenium surface alloys and therefore influence their corrosion behaviour.

1.5 Delimitation of study

In addition to corrosion resistance, it is often desirable that surface alloys bear good wear resistance properties. Although ruthenium is a known hardener that can possibly impart appreciable wear resistance to austenitic stainless steel, this study did not consider the wear resistance of the proposed surface alloys. Austenitic stainless steels and in particular 304 types are soft alloys rarely used in environments where wear is the predominant mode of failure.

1.6 Significance of study

Practical and economic benefits inherent to ruthenium surface alloys are not a widely explored subject. The present work therefore presented an opportunity to expand current knowledge to include the corrosion behaviour of austenitic stainless steel surface alloyed with ruthenium using RF magnetron, ion implantation and PED.

The platinum industry generates about 17% of South Africa's export revenue and, inevitably, 15-20 tonnes of ruthenium annually. Ruthenium is brittle even at temperatures as high as 1500°C and very difficult to fabricate, thus it has limited usefulness. Its global demand is diminutive as illustrated in Figure 1-3, and its potential as a revenue earner for South Africa is therefore not fully exploited. The results of this study are expected to expand the potential of this metal and stimulate further research into possible industrial applications.

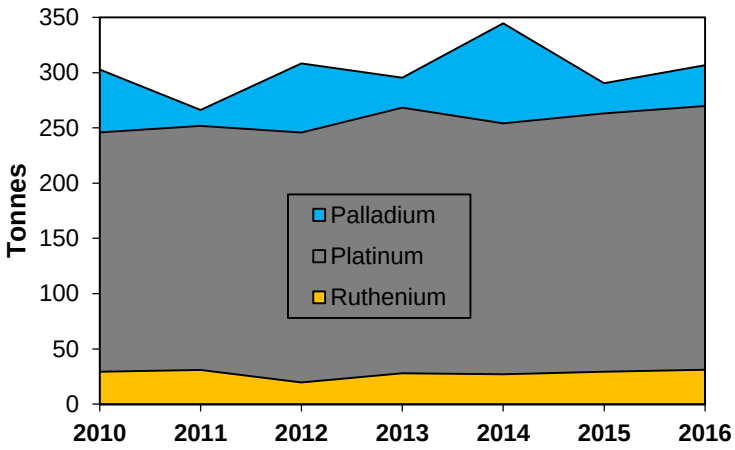

Figure 1- 3 *Global demand for ruthenium compared to that for palladium and*

platinum: 2010-2016 (adapted from Johnson Matthey 2016).

1.7 Definition of terms

Reducing acid: These are acids whose cathodic activity is characterised by the evolution of hydrogen according to Equation 1-1.

$$2H^+ + 2\bar{e} \rightarrow H_2 \qquad \textit{Equation 1-1}$$

Chloride solutions: Refers to aqueous solutions that consist of chloride (Cl^-) ions as the predominant anion. This definition encompasses hydrochloric acid although it is a reducing acid.

Noble: This is the positive direction of an electrode potential denoting increasingly oxidising conditions.

Cathodic efficiency: Represents the kinetic easiness of a cathodic reaction and not faradaic efficiency (Tomashov 1964).

1.8 Outline of thesis

In the present chapter, a description of the research problem was given as well as the motivation and objectives of the study. The thesis comprises six other chapters whose contents are summarised in the following paragraphs.

Chapter 2 presents a review of relevant literature and seeks to align the present study with existing research. The principles of corrosion, cathodic modification and the proposed surface alloying techniques are discussed in detail.

Chapter 3 focuses on the experiments done to achieve the objectives of the study. In addition, explanations on how the collected data were analysed for interpretation is given.

Chapter 4 contains the results obtained in characterising the as-received 304L stainless steel used in the study. In order to appreciate the impact of the proposed ruthenium surface alloys, and therefore qualify the success of this study, it was essential to gain an intimate knowledge of stainless steel.

Chapter 5 is dedicated to presenting the results obtained during the synthesis of the surface alloys. Attempts were made to optimise synthesis specifications to ensure the best and reproducible corrosion behaviour in dilute sulphuric acid.

Chapter 6 records the corrosion behaviour of the surface alloys produced by the proposed techniques in different reducing acids and chloride solutions. The effects of concentration, temperature, pH and exposure time were considered.

Chapter 7 concludes the study by summarising the findings, contesting the hypotheses proposed in Chapter 1 and recommending opportunities for further research.

A bibliography of quoted references and resources consulted in this study is presented at the end of the thesis. Work published from this study is listed in the Appendices section. Images of the equipment used in the experiments described in Chapter 3 as well as some experimental data are also recorded in the Appendices.

Chapter 2
Literature review

2.1 Principles of corrosion

ISO 8044:2015 describes corrosion as the physical interaction between a metal and its environment, which results in changes of the metal properties, and which may lead to significant functional impairment of the metal, the environment or the technical system of which they form a part. It is essentially a surface degradation mode and may be minimised by altering the surface properties of the metal. Corrosion of metals in aqueous solutions is an electrochemical process involving the coupling of at least one anodic reaction coupled with at least one cathodic reaction. The anodic reaction is always the oxidation of the metal as illustrated by Equation 2-1, where *M* is the corroding metal, while the cathodic reaction involves the reduction of some species in the environment. Typical cathodic reactions are presented in Equations 2-2 and 2-3.

$$M \rightarrow M^{n+} + n\bar{e} \qquad \textbf{\textit{Equation 2-1}}$$

$$2H^{+} + 2\bar{e} \rightarrow H_2 \qquad \textbf{\textit{Equation 2-2}}$$

$$O_2 + 2H_2O + 4\bar{e} \rightarrow 4OH^{-} \qquad \textbf{\textit{Equation 2-3}}$$

The flow of electrons as either the anodic or the cathodic reaction predominates, gives rise to current. Anodic current flow, i_a, induces a positive potential, whereas cathodic current flow, i_c, is associated with negative potential shift (Bagotsky 2006). This is illustrated in the schematic in Figure 2-1. For electrical neutrality, the Mixed-potential theory requires that the anodic and cathodic reactions occur at the same rate, i.e. i_a is equal to i_c, and there is no net flow of current. The requirement is satisfied at only a single point marked *X* in Figure 2-1. In corrosion reactions, the current and potential at this point are identified as I_{corr} and E_{corr} respectively. It should be noted that though the balancing of different reactions

(e.g. Equations 2-1 and 2-2), brings about the zero net current during a corrosion reaction, a true equilibrium is not established as neither reaction is equilibrated.

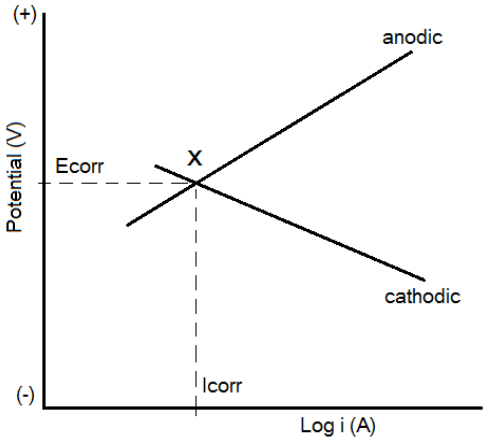

Figure 2- 1 *Schematic diagram combining the anodic and cathodic reactions for a corroding system.*

E_{corr} in Figure 2-1 is corrosion potential, also referred to as open circuit potential (OCP). It is a thermodynamic parameter, which represents the tendency of a corrosion reaction to occur; it represents the electromotive or driving force of the corrosion reaction (Warner 1943). The parameter I_{corr} is the corrosion current. When normalised by the area of the exposed surface, it is termed corrosion current density, i_{corr}, and is directly proportional to the corrosion rate, CR as given in Equation 2-4. In the equation, K_1 is a constant with a value of 3.27 x 10^{-3} mm.g/μA.cm.y, ρ is density of the corroding metal, and E_w is equivalent weight, defined as the mass of metal that will be oxidised by the passage of 1 Faraday of electric charge (ASTM G102-89(2010)).

$$CR = K_1 \frac{i_{corr}}{\rho} E_W \qquad \textbf{\textit{Equation 2-4}}$$

To study corrosion systems, it is common practise to maintain the metal at potentials other than E_{corr}. In this state, the metal is said to be polarised. The concepts of corrosion thermodynamics, kinetics and polarisation are discussed further in the subsequent subsections.

2.1.1 Corrosion thermodynamics

Corrosion is a result of the second law of thermodynamics. The law states that any isolated system will spontaneously progress in the direction of increasing disorder or entropy (dS > 0) i.e. a system will react to minimise its Gibbs free energy, ΔG. The inherent tendency of a metal to corrode in an aqueous solution can therefore be described in terms of ΔG by Equation 2-5, where E is the corrosion potential measured with respect to a standard reference electrode, F is the Faraday constant and n is the number of electrons exchanged during the corrosion reaction. When ΔG for the corrosion reaction is positive, it is presumed that the possibility of the reaction occurring is low if not nil. By the same vein, the more negative the value of ΔG, the greater the possibility for the corrosion reaction to occur.

$$\Delta G = -nFE \qquad \textbf{\textit{Equation 2-5}}$$

However, ΔG alone does not provide an indication of whether the corrosion reaction will actually occur, nor the rate at which it will progress (Fontana 1986; Bagotsky 2006). An example of this is the phenomenon of passivity. Passivity occurs when the corrosion reaction is hindered despite a marked thermodynamic tendency to occur. The value of ΔG for reactive metals such as chromium and titanium under oxidising conditions is very negative, indicating that the corrosion of these would occur spontaneously. The metals do react rapidly initially, but form insoluble passive oxide films, which significantly hinder the corrosion reaction. This suggests that it is not sufficient to account for corrosion from a thermodynamics viewpoint alone.

2.1.2 Corrosion kinetics

When the anodic and cathodic reactions in Figure 2-1 represent the backward and forward reactions of the same reaction, a true equilibrium is achieved. Under these conditions, the net current is zero, and the potential and current at which this occurs are termed the equilibrium potential, $E°$, and exchange current, I_o, or exchange current density, i_o, when normalised by exposure area respectively. The

exchange current density is the rate of oxidation and reduction reactions at equilibrium, and it plays a significant role in the rate of corrosion reactions.

Figure 2-2 depicts the dissolution of a metal in a reducing acidic medium. Increasing the exchange current density for the hydrogen reaction i_{oH}, for example by increasing temperature or altering the properties of the metal surface, would cause an increase in the corrosion current density from i_{corr1} to i_{corr2}, and simultaneously increase the value of E_{corr}. As shown in Equation 2-4, i_{corr} is a function of corrosion rate: the higher the value of i_{corr}, the higher the corrosion rate. By adjusting i_o of a corrosion reaction, it is therefore possible to control the rate of corrosion.

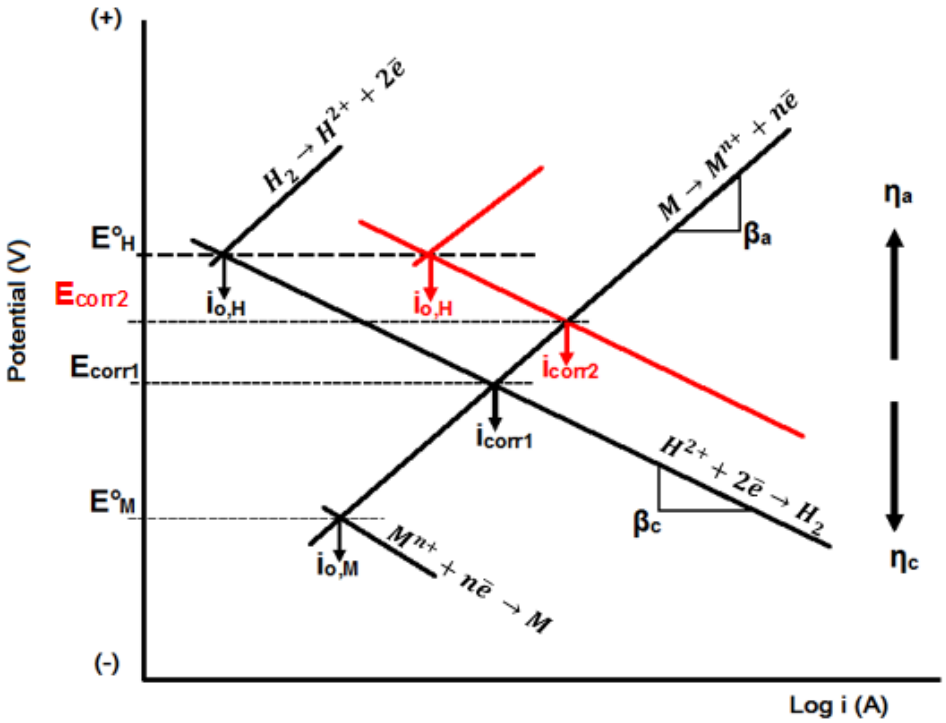

Figure 2- 2 *Evans plot for a metal dissolving in acid.*

2.1.3 Polarisation

The value of i_{corr} cannot be measured directly as there is no net current flow at E_{corr}, neither can it be established theoretically. To determine i_{corr}, the potential of the corroding metal in a given environment is deviated from E_{corr} by imposing an external voltage. This deviation is called polarisation and the magnitude of

polarisation is called overvoltage, denoted by η in Figure 2-2. Overvoltage can be either anodic (η_a) or cathodic (η_c). For a corrosion reaction characterised by a single charge transfer controlled cathodic reaction and a single charge transfer controlled anodic reaction, i_{corr} is related to overvoltage by Bulter-Volmer relationship in Equation 2-6 (Frankel 2008). β_a and β_c are the anodic and cathodic Tafel slopes respectively, determined as shown in Figure 2-2, and i_{app} is the applied current density.

$$i_{app} = i_{corr}(\exp[\frac{2.3\eta_a}{\beta_a}] - \exp[\frac{-2.3\eta_c}{\beta_c}]) \qquad \textit{Equation 2-6}$$

From Equation 2-6, it can be shown that slow corrosion reactions are associated with high overvoltage, while low overvoltage values are typical of fast reactions.

2.2 Corrosion of stainless steels

All stainless steel alloys depend on passivity for corrosion resistance. This passivity is due to the presence of a chromium oxide film no thicker than 5 nm. Although thin, the film is sufficiently protective to render stainless steel alloys corrosion resistant in most environments, including concentrated nitric acid, where corrosion rates less than 0.01 mm/y have been reported (Whillock & Worthing 2010). However, the chromium oxide film is susceptible to dissolution in reducing acidic and chloride solutions.

In essence, the passive film consists of mixed oxides of iron and chromium. It is not a rigid structure but constantly evolves, its thickness and composition changing depending on environmental factors such as solution type, pH, and temperature as well as alloy composition. Increasing chromium composition from 12 to 25% in ferritic stainless steel, for instance, resulted in the formation of a more resistant passive film in 1 M sulphuric acid, with release of less soluble products (Bojinov et al. 1999). Abreu et al. (2006) showed that air formed passive films on AISI 304L and 316L austenitic stainless steels were 3 and 1.5 nm thick respectively. The difference in thickness was attributed to the differences in nickel composition of the two alloys. Moreover, the air formed film had a higher Cr:Fe,

implying passive films mainly composed of chromium oxide, while the films electrochemically formed in 0.1 M sodium hydroxide were predominately composed of iron oxides. Chromium tends to form an insoluble interlinked chromium oxide network (Schumuki 2002), and the higher the concentration of chromium the lower the rate of metal dissolution.

The stability of passive films is strongly dependent on the potential of the environment. Figure 2-3(a) indicates the potential ranges of the species that typically make up the passive films on stainless steel. At low anodic potentials, corrosion products consist predominately of chromium (II), and at more noble potentials (E > -50 mV vs SHE or > -200 mV vs Ag/AgCl), dissolution produces chromium (III), iron (II) and (III). Trivalent chromium is responsible for passivity via the formation of chromium oxide. As the potential increases above 800 mV vs SHE (≈ 600 mV vs Ag/AgCl), chromium (III) is oxidised to soluble hexavalent species, namely CrO_4^{2-} and $Cr_2O_7^{2-}$, resulting in an increased fraction of iron oxides in the film. In acidic solutions, iron oxides are prone to chemical dissolution, and are therefore not protective.

In typical potentiodynamic polarisation curves for stainless steels, passivity manifests as a decrease in current density at a critical potential, E_{crit} (Figure 2-3(b)). Below this potential, stainless steel undergoes active dissolution as indicated by the increase in current density. The ease with which passivity is initiated is indicated by the value of critical current density, i_{crit}; the lower the value, the easier it is for the metal to passivate in the environment of exposure. Above E_{crit}, the passive film grows on the surface, and increasingly retards corrosion.

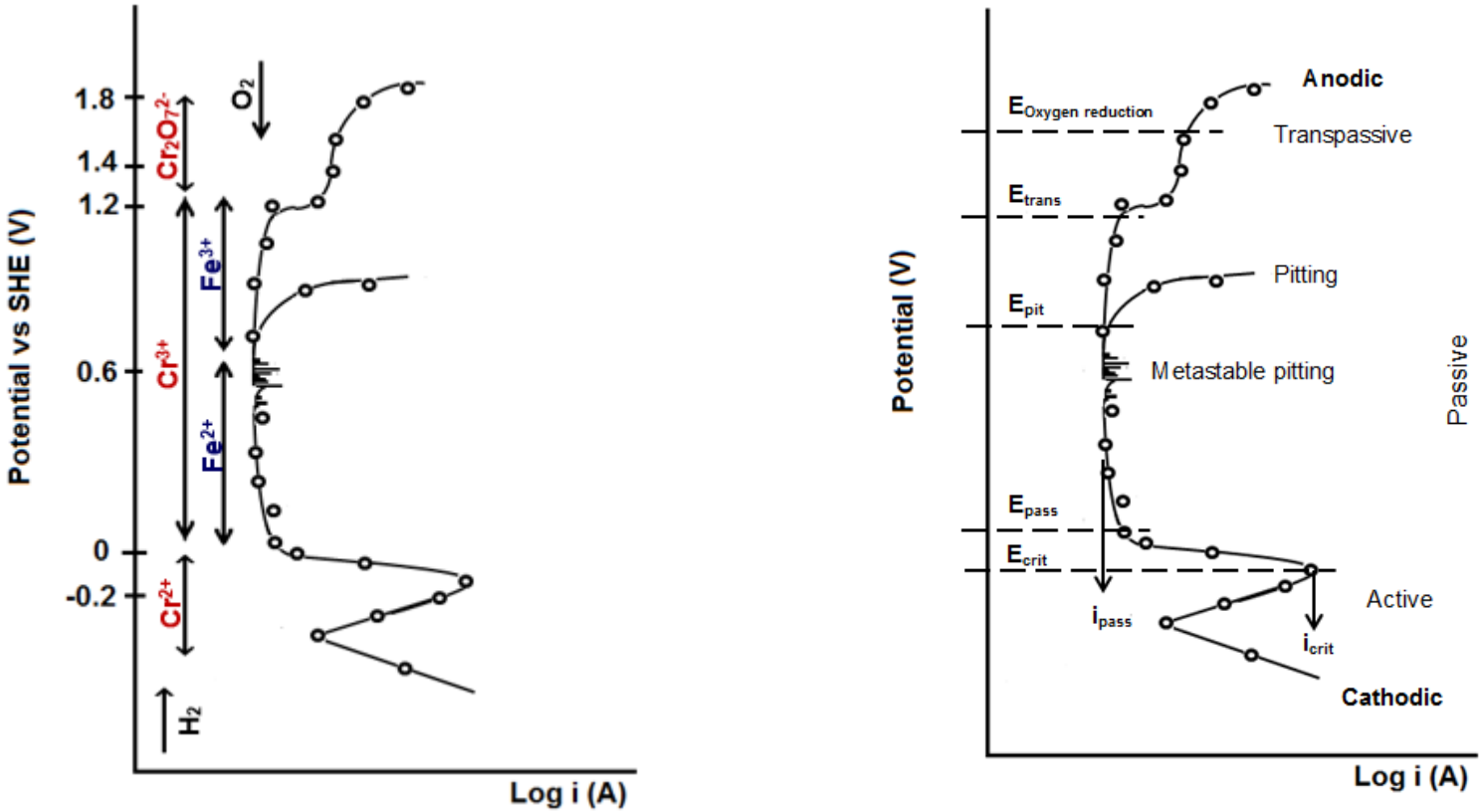

Figure 2- 3 *Typical polarisation curves for stainless steel alloys showing (a) potential ranges of dissolving species, and (b) passivity breakdown possibilities (adapted from Haupt & Strehblow 1995; Schmuki 2002).*

Passivity is established above passivation potential E_{pass}, where the entire surface is presumably covered with the passive layer. In the passive region, current density is independent of potential and metal dissolution is significantly inhibited. At very positive potentials, particularly those close to oxygen evolution potentials, depassivation occurs and the metal dissolves uniformly over the entire surface. This transpassive behaviour is identifiable by a sudden increase in current density at high anodic polarisation. When transpassive-like behaviour occurs at potentials way below oxygen reduction potentials, it is indicative of pitting. In such cases, current transients may be observed, pointing to metastable pitting.

2.2.1 Corrosion of 304 austenitic stainless steel

Type 304 stainless steels are solid solution alloys in which iron, chromium, nickel and carbon are completely miscible. Solid solution alloys usually exhibit better corrosion resistance than multiphase alloys such as duplex stainless steel, which are susceptible to galvanic coupling and compromised corrosion resistance. Nonetheless, 304 stainless steels cannot provide serviceable performance in reducing acids and tend to experience pitting corrosion in chloride environments.

Corrosion in reducing acids

Corrosion of metals in reducing acidic media is supported by the cathodic evolution of hydrogen as per Equation 2-2. The reaction is proposed to occur via three consecutive steps listed in Equations 2-7 to 2-9 (Bagotsky 2006).

$H^+ + \bar{e} \rightarrow H_{ads}$ *(Discharge/ Volmer step)* ***Equation 2-7***

$2H_{ads} \rightarrow H_2$ *(Recombination/ Tafel step)* ***Equation 2-8***

$H^+ + H_{ads} + \bar{e} \rightarrow H_2$ *(Evolution/ Heyrovskȳ step)* ***Equation 2-9***

Any of these steps can be rate determining, and it depends on the hydrogen overvoltage of the corroding metal. For metals such as platinum group metals (PGMs) that have low hydrogen overvoltage and possess high adsorption capacity

for hydrogen, the recombination step is rate determining, whereas for metals such as mercury and lead, that have high hydrogen overpotentials (Bagotsky 2006), and are almost incapable of adsorbing hydrogen, the discharge step is rate determining. As stated in Section 2.1.3, high hydrogen overvoltage is associated with slow rates of reaction.

At high overvoltage, the equilibrium in Equation 2-2 would lie to the left, and the corresponding corrosion potential would lie mostly in the active region of the polarisation curves in Figure 2-3, where non-protective chromium (II) species are thermodynamically stable. While chromium does not significantly affect the hydrogen overpotential of iron (Ezaki et al. 1993), Figure 2-4 shows that alloying with nickel results in a substantial increase in hydrogen overpotential. As such, austenitic stainless steels will corrode unabated in reducing acids.

Austenitic stainless steels are incompatible with hydrochloric acid at all concentrations. Corrosion of 304 grade stainless steel in this acid is characterised by the absence of passivation and is associated with steady anodic dissolution. Passivation in hydrochloric acid is hindered by the combined effect of chloride and hydrogen ions, leading to a marked increase in rates of dissolution. Hydrochloric acid is also known to support pitting corrosion of 304 austenitic stainless steel as shown in Figure 2-5. This form of corrosion is mostly associated with chloride ions and is discussed further in succeeding subsections.

Figure 2-6 summarises the corrosive nature of sulphuric acid and its dependence on concentration. At concentrations less than 25 wt% (≈ 2.5 M), sulphuric acid predominately contains water which facilitates its dissolution into hydrogen, bisulphate and sulphate ions (Dillion 1986; Richardson 2010). These acid solutions are inherently reducing and will rapidly corrode stainless steel at all temperatures. However, 304 stainless steel alloys exhibit increased tolerance for concentrations greater than 70 wt% (≈12 M). At these concentrations, sulphuric acid solutions are essentially free of water, with a large concentration of undissociated sulphuric acid molecules. Sulphate ions do not initiate pitting and 304 stainless steel is unlikely to experience pitting corrosion in sulphuric acid.

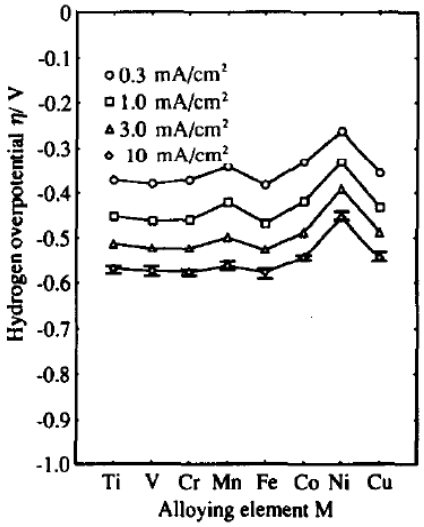

Figure 2- 4 *Hydrogen overpotential for iron based alloys measured in 1 N sulphuric acid at 303 K and different current densities (Ezaki et al. 1993).*

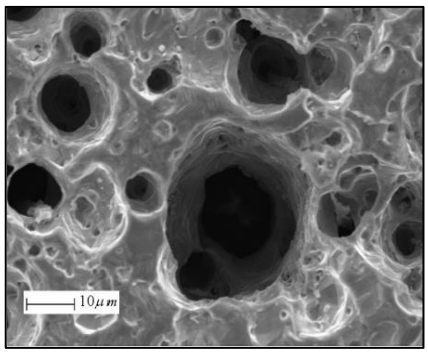

Figure 2- 5 *Conventional polycrystalline 304 stainless steel after 30 days of immersion in 0.5 M hydrochloric acid at room temperature (Wang et al. 2013).*

Other reducing acids in which the corrosion resistance of 304 stainless steel is compromised include phosphoric, formic and acetic acids. Low concentrations of phosphoric acid are particularly harmful, and despite good laboratory data, 304 type stainless steel have been observed to perform poorly in service environments containing this acid (Dillion 1986). Organic acids are generally weaker than inorganic because they are only slightly ionised. However, corrosion rates as high as 1.3 mm/y have been associated with type 304 stainless steel in 50 wt% acetic acid and 80 wt% formic acid (Fontana 1986).

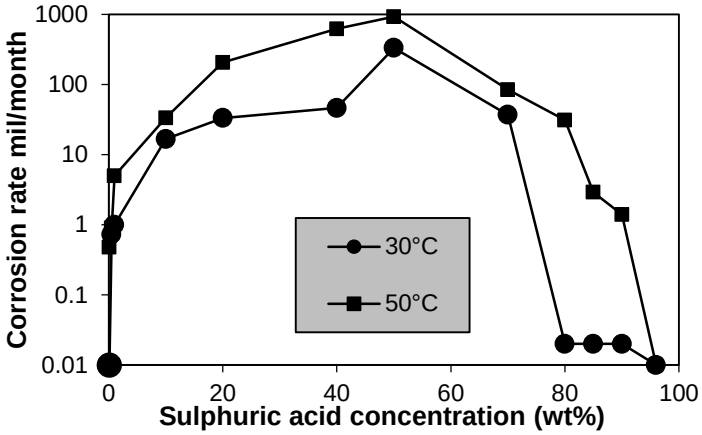

Figure 2- 6 *Effects of concentration and temperature on the corrosion rate of annealed type 304 stainless steel in deaerated sulphuric acid. Corrosion rates calculated from losses of weight (adapted from Phelps & Vreeland 1957).*

Corrosion in chloride environments

Corrosion of austenitic stainless steel in chloride solutions is primarily due to the chloride ions. These ions are small and have high diffusivity as illustrated in Table 2-1, enabling them to penetrate through the passive chromium oxide film on stainless steel with ease (Galvele 1981; Ibrahim et al. 2009).

Table 2- 1 *Conductivity and diffusion coefficients of selected ions at infinite dilution in water at 25°C (Roberge 2000; Revie & Uhlig 2008).*

Species	**Conductivity ($S.cm^2.mol^{-1}$)**	**Diffusivity x 10^5 ($cm^2.s^{-1}$)**
H^+	349.8	9.30
OH	197.6	5.25
Cl^-	76.3	2.03
HSO_4^-	50.0	1.33
SO_4^{2-}	160.0	1.06
O_2	-	2.26
H_2O	-	2.44

Several theories have been forwarded to describe how the chloride ions penetrate the passive film on stainless steel alloys. The Oxide-film theory postulates that chloride ions collodially disperse in the passive film and increase the film's permeability by preventing its repair (Revie & Uhlig 2008). The inability of

stainless steel alloys to repassivate is due to localised acidification of the metal surface as per Equation 2-10, which breaches the integrity of the passive films at localised areas.

$$Fe^{2+} + 6H_2O \rightarrow Fe(H_2O)_6^{2+}$$ ***Equation 2-10***

According to the Adsorption theory, chloride ions are preferentially adsorbed onto the metal surface in competition with dissolved oxygen (Table 2-1), and once in contact with the metal surface, hydrolyse the metal ions as presented in Equation 2-10. The result is an increased exchange current density for the iron oxidation reaction, and consequently the ease with which the iron ions enter the solution (Schmuki 2002; Revie & Uhlig 2008).

Cathodic activity in chloride solutions depends on the nature of the chloride. Corrosion in neutral chloride solutions such as sodium chloride is supported by the reduction of oxygen according to Equation 2-3. Hydroxide ions thus produced may react with iron (II) ions produced anodically, to form a film of ferrous hydroxide. The film is, in most cases, adherent and may provide an effective diffusion barrier resulting in retarded corrosion rates.

Cathodic activity in acidic non-oxidising chlorides such as ferrous chloride and magnesium chloride occurs by combined hydrogen evolution and oxygen reduction (Dillion 1986; Revie & Uhlig 2008). The increased demand for electrons resulting from the increased total reduction rate implies high anodic reaction rates. Corrosion in this type of chloride solutions is therefore characterised by high rates. Oxidising chlorides can either be corrosive or be passivators. They can sufficiently polarise a corroding system to noble potentials. A typical example of an oxidising chloride is ferric chloride, in which the cathodic activity involves the reduction of ferric ions as in Equation 2-11.

$$Fe^{3+} + \bar{e} \rightarrow Fe^{2+}$$ ***Equation 2-11***

Figure 2- 7 *Micrograph (*350x*) of 304L stainless steel exposed to 2.5 M sodium chloride at +400 mV vs SCE for 10 minutes (Ibrahim et al. 2009).*

Corrosion of 304 austenitic stainless steel in chloride solutions is characterised by pitting. This is a form of extremely localised and insidious attack, which leads to the perforation of the metal as shown in Figures 2-5 and 2-7. Pitting in chloride solutions is autocatalytic; initial dissolution conditions are established which stimulate further dissolution (Schmuki 2002). The dissolution of the metal within the pit tends to produce an excess of cations. To maintain electrical neutrality, chloride ions migrate from the solution into the pits where they hydrolyse the metal (Equation 2-10), causing a significant drop in pH. The low pH prevents repassivation of the metal, thus propagating pit growth. This is illustrated in Figure 2-8. In addition to pitting, 304 stainless steels are particularly susceptible to stress corrosion cracking (SCC) in magnesium chloride.

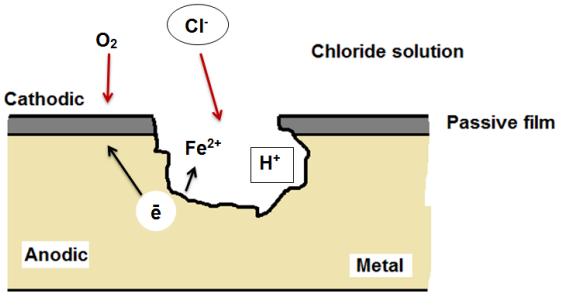

Figure 2- 8 *Autocatalytic processes occurring in a pit (adapted from Fontana 1986).*

2.3 Cathodic modification

In 1948, Nikon Danilovich Tomashov (Figure 2-9(b)) and co-workers proposed, and developed the concept of cathodic modification. They postulated that in order to achieve the transition of a system into a passive state, and consequently lower its corrosion, it is necessary, if one rules out the possibility of pit formation or transpassive corrosion, to seek increased cathodic efficiency (Tomashov 1964). Since then, numerous researchers have contributed to the development of the concept.

In South Africa, Mintek and the University of the Witwatersrand have been at the forefront of research on cathodic modification, with much focus on alloying stainless steel with ruthenium. The research, in corroboration with local platinum producers, led to the commercialisation of a variant of these alloys under the trade name Ruthalloy, which is based on the super ferritic stainless steel Fe29Cr4Mo and has additions of 0.2 wt% ruthenium. Although the alloy showed remarkable corrosion resistance in aggressive media, its use has only been limited to pump components such as impellers.

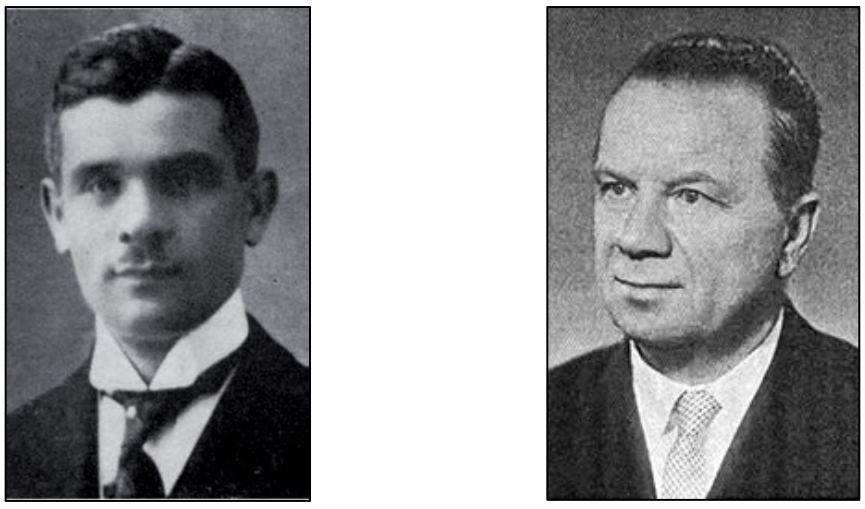

(a) (b)

Figure 2- 9 *Pioneers of cathodic alloying (a) Philip Monnartz (Simcoe 2015) and (b) Nikon Danilovich Tomashov (Kolotyrkin 1977).*

2.3.1 Requirements for cathodic modification

Passivity can be induced in an alloy by addition of metals having high cathodic exchange current density, such as PGMs, if the passive region of the alloy extends to potentials that are more negative than the redox potential of the environment (Potigieter et al. 1990). This is the fundamental principle of cathodic modification, and is illustrated in Figure 2-10.

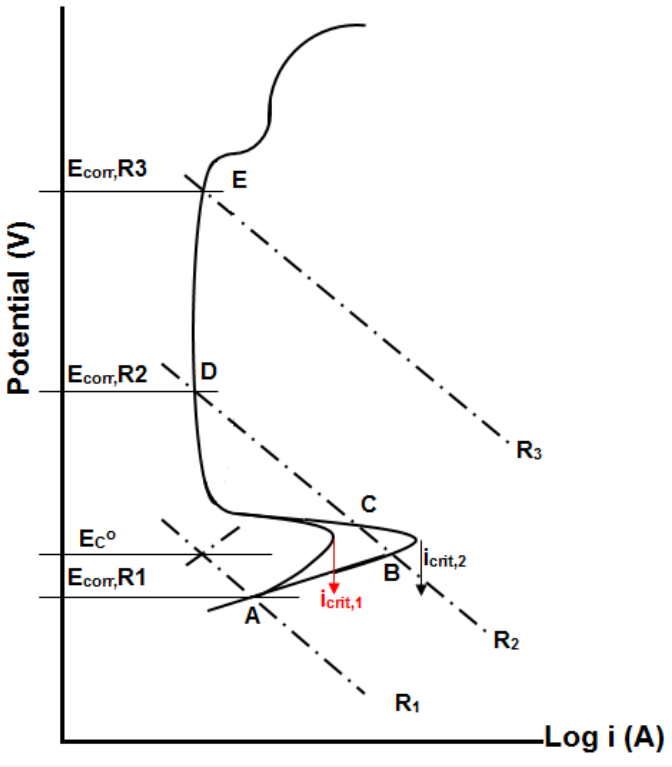

Figure 2- 10 *Hypothetical polarisation curve showing the influence of cathodic modification (adapted from Tomashov 1964; Potgieter et al. 1990). R_n depicts the cathodic process at different efficiencies: R_2 is faster than R_1.*

Case 1

The cathodic efficiency of R_1 is small, and the cathodic curve intersects the anodic curve at point *A* in the active region (see Figure 2-3). In this case, E_{pass} of the alloy is nobler than the potential of the environment E_C°. Under such conditions, passivation will not be established and the alloy will undergo *active* corrosion.

Case 2

The cathodic efficiency of R_2 is relatively higher than that of R_1. In this case, the success of cathodic modification will depend on the size of i_{crit}. Where i_{crit} is less than the current of the cathodic reaction R_2, for example i_{crit1}, then the anodic and cathodic curves will intersect at point *D*, in the passive region. The system in such a case will be in a state of *spontaneous stable passivity*. When such a system is disturbed, it will spontaneously return to a passive state. Corrosion rates of this system are marginal and equivalent to i_{pass}.

However, where i_{crit} is greater than the current of the cathodic reaction such as i_{crit2}, then the anodic and cathodic curves will intersect at points *B*, *C* and *D*. These conditions present two possibilities: *passive or active.* At noble potentials, the system will passivate, but actively corrode at lower potentials. The corrosion behaviour of such a system is unpredictable and undesirable.

Case 3

In the third case, the cathodic efficiency of R_3 is very high such that the anodic and cathodic curves intersect at point *E* in the *transpassive or the pit formation regions*. These conditions have detrimental consequences, either resulting in increased dissolution rates or pitting corrosion.

Based on this, the requirements for successful cathodic modification may therefore be summarised as:

1. A wide passive region i.e. E_{pass} must be sufficiently negative and E_{trans} be sufficiently positive.
2. A sufficiently low value of i_{crit}.

2.3.2 Mechanism of cathodic modification

Cathodic modification presumably inhibits corrosion in two ways. Firstly, the active cathodes reduce cathodic overpotential thereby increasing the efficiency of the cathodic process. PGMs, for example, catalyse hydrogen evolution from reducing acidic solutions (Equation 2-2), thereby increasing the efficiency of the

process. Secondly, the alloying elements act as blocking agents that decrease the anodic dissolution of the metal by blocking the active sites in the crystal lattice of the host metal (Tomashov et al. 1984).

During exposure, selective dissolution of the base alloy leads to surface enrichment of the active cathodes (Pickering 1983), thus increasing their availability for corrosion processes. The rate at which the active cathodes accumulate on the surface, and therefore facilitate improved cathodic efficiency naturally depends on their concentration. Tomashov et al. (1970) exposed palladium alloyed Fe25Cr6Ni stainless steel to 10% sulphuric acid at 100°C. The corrosion potential of the stainless steel with 0.1% palladium could not reach E_{crit} (Figure 2-3(b)) and the alloy remained active. Partial passivation was observed on the alloy with 0.2% palladium, and this was attributed to increased rate of palladium enrichment on the surface. Increasing palladium content to 0.5% caused a shift in potential into the passive region, resulting in spontaneous passivation. It follows therefore that increasing the concentration of active cathodes in a metal matrix would induce passivity, yet care should be taken not to exceed transpassive or pit formation potentials.

In stainless steel alloys, PGMs decrease the dissolution of chromium and iron, and increase the likelihood of forming a stable passive layer. Myburg and co-workers (1998) used auger electron spectroscopy (AES) to study the composition of the passive film on Fe22Cr9Ni3Mo duplex stainless steel alloyed with 0.3 wt% ruthenium and exposed to 1 M sulphuric acid. Their results revealed that the presence of ruthenium increased the surface concentration of chromium. Delport and Roux (1986) reported similar observations when they subjected high chrome stainless steel (Fe40Cr) alloyed with small additions of palladium to a heat treatment regime.

2.3.3 Cathodic modification with ruthenium

Ruthenium has generated a lot of interest as a metal of choice in cathodic modification of stainless steels because it is by far the cheapest of the PGMs. In addition, ruthenium forms alloys with most metals, except gold, lead and silver,

and has better corrosion resistance in hydrochloric acid than rhodium, palladium and platinum (Llopis et al. 1966). Potgieter (1991) attributed these observations to several factors some of which are:

1. Ruthenium has lower hydrogen overpotential than most PGMs. This enables ruthenium to reduce the overvoltage for cathodic evolution of hydrogen of stainless steel more efficiently. In fact, the effectiveness of PGMs in improving corrosion resistance in sulphuric acid and hydrochloric acid decreases in the order:

   Ir > Rh > **Ru** > Pd > Os

2. Ruthenium can adsorb oxygen, form oxides and thus enter the composition of the hydroxide or oxide layer formed on the surface of the stainless steel. This increases resistance against the action of chloride ions. Palladium, for instance, remains a separate metallic phase in the surface layer and does not impart pitting resistance.

In reducing acids

The influence of ruthenium on the corrosion of stainless steel alloys in sulphuric acid is summarised in Figure 2-11. Ruthenium increases the efficiency of the cathodic process by lowering hydrogen overvoltage and consequently shifting the corrosion potential towards the passive region. In addition to this, ruthenium can reduce i_{crit}, increasing the ease with which passivation is achieved. This is desirable to establish stable spontaneous passivity. An effect that is perhaps unique to ruthenium is its ability to reduce i_{pass} to significantly low values. When the corrosion potential is in the passive regime (point *D* in Figure 2-10), corrosion rates are equivalent to i_{pass}: hence, the lower the value of i_{pass} the lower the corrosion rate.

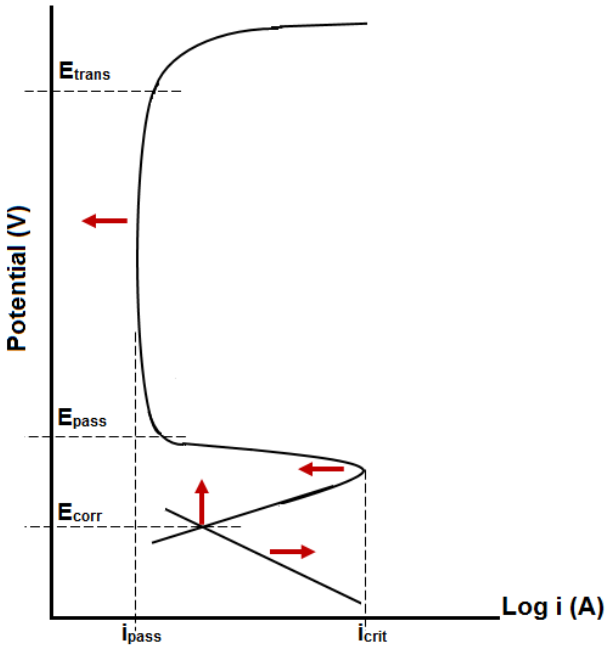

Figure 2- 11 *Effects of ruthenium on the polarisation characteristics of FeCr stainless steel in sulphuric acid (adapted from Potgieter 1991).*

Table 2-2 shows the effect of ruthenium on a variety of stainless steel alloys exposed to sulphuric acid. These data confirm that the presence of ruthenium in stainless steel does indeed reduced corrosion rates and i_{crit} values in sulphuric acid regardless of the test temperature, indicating an increased ease of passivation. The observations made by these investigators are consistent with the schematic in Figure 2-11. Increase in temperature generally resulted in increased attack of the ruthenium alloyed stainless steel, and the effect was apparently less detrimental at lower concentrations of the acid.

Work done by Sherif and colleagues (2009a) showed that introducing ruthenium into a duplex stainless steel alloys increased corrosion resistance in 2 M hydrochloric acid. The increase in the radii of the Nyquist semicircles shown in Figure 2-12 either is related to the thickening or increased stability of the passive film formed on the duplex stainless steel, pointing to higher corrosion resistance.

Table 2- 2 *Comparison of results for the corrosion of ruthenium alloyed stainless steels as reported by different investigators in sulphuric acid. # denotes information not supplied by the authors.*

Alloy	**Corrosion rate (mm/y)**	**i_{crit} (A/cm²)**	**Acid concentration**	**Temperature (˚C)**	**Reference**
Fe22Cr9Ni3Mo	0.752	1.20E-4	10%	Room temperature	Sherif 2011
Fe22Cr9Ni3Mo-0.14Ru	0.672	9.20E-5			
Fe22Cr9Ni3Mo-0.28Ru	0.431	7.50E-5			
Fe29Cr2Ni4Mo-0.05Ru	0.0967	#	1 M	25	Olubambi et al. 2009
Fe29Cr2Ni4Mo-0.20Ru	0.0524	#			
Fe22Cr9Ni3Mo	#	2.50E-3	40%	55	Potgieter et al. 1995
Fe22Cr9Ni3Mo-0.22Ru	#	3.00E-4			
Fe22Cr9Ni3Mo-0.28Ru	#	2.00E-5			
Fe29Cr14Ni3Mo	0.2900	#	50%	25	Potgieter & Brookes 1995
Fe29Cr14Ni3Mo-0.28Ru	0	#			
Fe29Cr14Ni3Mo	1.2420	#		55	
Fe29Cr14Ni3Mo-0.28Ru	0.0276	#			
Fe29Cr14Ni3Mo	405.1	#		90	
Fe29Cr14Ni3Mo-0.28Ru	0.695	#			
Fe21Cr1Ni	0.098	4.29E-2	1 M	25	Olaseinde et al. 2012
Fe21Cr1Ni-0.15Ru	3.19E-5	6.79E-5			
Fe21Cr1Ni	1.29E-3	2.04E-3		80	
Fe21Cr1Ni-0.15Ru	3.61E-3	2.30E-4			

However, the presence of inductive loops at low frequencies points to adsorption processes at the metal-electrolyte interfaces, which could be the adsorption of H^+ and Cl^-, both of which have detrimental consequences such as dissolution of the passive film, and pit formation. Prolonged tests could have given results that are more conclusive in this regard.

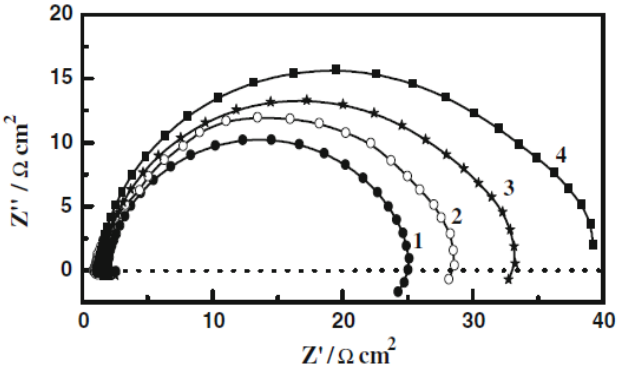

Figure 2- 12 *Nyquist plot for Fe22Cr9Ni3Mo duplex stainless steel alloyed with (1) 0%, (2) 0.14%, (3) 0.22% and (4) 0.28% ruthenium immersed in 2 M hydrochloric acid for 1 hour (Sherif et al. 2009a).*

In chloride environments

The primary mechanism of corrosion attack in chloride media is pitting (Section 2.2.1). There exists a characteristic potential, E_{pit} (Figure 2-3) above which pitting will definitely occur. The degree of pitting resistance can therefore be inferred from values of E_{pit}, and elements that can shift E_{pit} to nobler values have beneficial effects on pitting resistance. Although cathodic modification by ruthenium and other PGMs has been largely discussed with reference to acids, Sherif et al. (2009b) reported increased E_{pit} on stainless steels alloyed with ruthenium and exposed to chloride solutions.

Increasing ruthenium from 0 to 0.28% shifted E_{pit} of 22Cr9Ni3Mo duplex stainless steel in 3.5 wt% sodium chloride from 5 mV to 150 mV vs Ag/AgCl. This shows a reduced tendency to pitting with additions of ruthenium. In some cases, the probability of pit initiation was reduced to zero by alloying with ruthenium. Similar observations were made in a separate study, the results of which are presented in Figure 2-13. The absence of a hysteresis loop on the cyclic

polarisation curve for duplex stainless steel with 0.3% ruthenium indicates that pitting did not occur in 0.6 M sodium chloride.

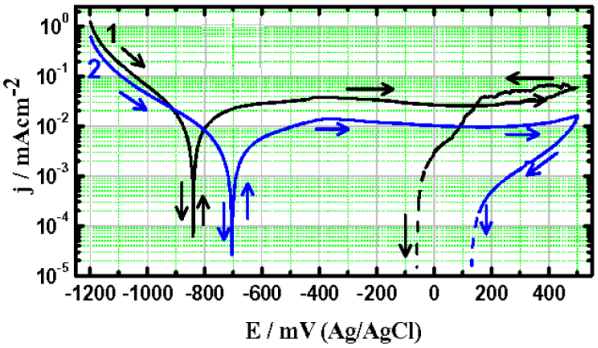

Figure 2- 13 *Cyclic potentiodynamic polarisation curves for 2209 duplex stainless steel containing (1) 0% Ru and (2) 0.3% Ru in 0.6 M sodium chloride (Sherif 2012).*

2.4 Surface alloying

Surface alloying involves altering the surface properties of a metal independent of the bulk properties. It allows for the modification of relatively inexpensive substrates with small amounts of more expensive alloying elements. Since surface alloying can be limited only to those surfaces exposed to corrosion attack, it is more cost effective than bulk alloying. With some surface alloying processes such as ion implantation, it is possible to form any alloy regardless of their miscibility: for example implanting alumina with iridium and silver for biomaterials (Jagielski et al. 2006). In addition, surface alloying makes it possible to exceed the solubility limit of the alloying elements. For instance, steel can be alloyed with up to 1 wt% nitrogen by traditional metallurgical processes, whereas up to 15 wt% nitrogen can be introduced by surface alloying (Flis & Kuczynska 2004).

2.4.1 Classes of surface alloys

Considering a binary system of *A/B*, where *A* are the atoms of the alloying element and *B* are those of the substrate, two types of surface alloys are possible. These are illustrated schematically in Figure 2-14.

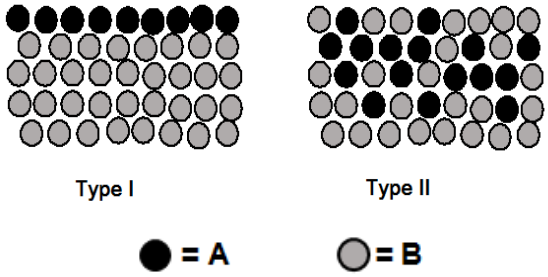

Figure 2- 14 *Schematic of two possible surface alloys for a binary alloy system A/B (adapted from Hoster 2013).*

Type I surface alloys

Type I surface alloys involve placing the alloying element on the topmost surface layer of the substrate, which eliminates the need for relieving strain effects that occur when an atom is introduced into the lattice structure of the host alloy. Thin films and coatings are examples of this type of surface alloys. Thin films are materials created ab inito by the random process of nucleation and/or growth of individual condensing atoms on a substrate (Canli 2010).

The usefulness of thin films hinges on their ability to adhere onto the substrate. ASTM D907-15 defines adhesion as the state in which interfacial forces, which may consist of valence forces, interlocking forces or both, hold two surfaces together. This implies that adhesion of thin films and coatings is influenced by the structure of the interfacial region. Ohring (2002) described four types of interfaces: abrupt, compound, diffusion and mechanical interfaces. Abrupt interfaces arise when there is no interaction between the atoms of the film and those of the substrate. This is typical of eutectic alloy systems (Okamoto et al. 2004), and immiscible systems such as cadmium/iron, gold/carbon and silver/copper shown in Figure 2-15.

Adhesion may be achieved by interlocking of the film into cavities, pores and asperities of the substrate, creating a mechanical interface. Increasing interfacial contact, for example by roughening the surface of the substrate, has the effect of enhancing the adhesive strength of this type of interface. Fracture propagation on a rough interface is relatively more difficult as the fracture must frequently change direction or pass through stronger regions (Mattox 1973). However, care must be

taken that there are no voids between the contacting surfaces as this may have a negative influence on adhesion (Figure 2-15).

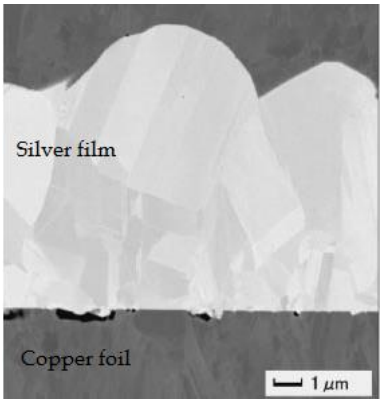

Figure 2- 15 *Silver film electrodeposited on copper foil showing aspects of mechanical and abrupt interface (Okamoto et al. 2004).*

Elements or metals that are mutually soluble in all proportions will form a diffusion interface, thus promoting good adhesion. The mobility of the atoms across the interface is very important and may lower adhesion strength. Where atomic mobility is sufficiently different and the diffusion rate of one type of atom is faster in one direction, then voids may form at the interfacial zone due to the Kirkendall effect (Mattox 1973). The presence of voids at the interface is not conducive to good adhesion because it allows for easy propagation of fractures.

At times, the interacting film and substrate atoms result in chemical reactions and the formation of compounds or intermetallics resulting in a compound interface. This is typical in cases whereby there is little diffusion between the reactive atoms. Fabrication of oxygen-active Type I surface alloys on oxide substrate results in the formation of an oxide interface. The formation of compounds is usually accompanied by volumetric changes, which generate high stresses (Ohring 2002). As such, the adhesive strength of a compound interface depends largely on the size of these interfacial compounds. If they were thin, adhesion would be generally good, but poorer if thicker layers form, since the formation of thicker interfacial compounds results in the development of high residual stresses (Mattox 1998). The formation of micro-cracked brittle intermetallics in the interfacial zone can also lead to poor adhesion.

Type II surface alloys

The main advantage of this type of surface alloys over Type I is that there is no risk of de-adhesion and therefore compromised performance of the modified surface. In Type II surface alloys, the alloying element atoms are incorporated into the subsurface of the substrate as illustrated in Figure 2-14.

Depending on the type of fabrication process, this may result in volume expansion of the initial lattice structure, precipitation of new phases or compounds, amorphisation of near surface layers and the introduction of defects and defect clusters. The usefulness of Type II surface alloys is therefore related to the nature of the fabrication process. For instance, conventional plasma nitriding results in the formation of a nitride layer very close to the surface, which slows down further ingress of nitrogen. On the other hand, plasma ion implantation uses high energy to pump nitrogen well into the surface at rates that do not allow sufficient time for significant nitride precipitation near the surface (Collins et al. 1994). The presence of high nitride concentration at the surface of austenitic stainless steel alloys may be ideal for wear resistance, but not necessarily so for corrosion resistance due to chromium depletion in nitride formation.

2.4.2 Corrosion control by surface alloying

Corrosion is essentially a surface dependent degradation mode. As such, surface alloying may significantly reduce the corrosion of metallic structures. In corrosion applications, Type I surface alloys function by providing a physical barrier to isolate the metal from the corrosive environment thus interrupting the electrochemical reactions discussed in Section 2.1. If the surface alloy is more electropositive with respect to the substrate, it should be free of pores, or similar through-thickness defects to avoid a high cathode:anode area ratio, which can lead to localized corrosion of the substrate (Walsh et al. 2008). Some surface alloys such as zinc in galvanised steel and magnesium on steel offer sacrificial protection.

Surface alloying of austenitic stainless steels

Table 2-3 summarises some of the surface alloys used to retard the corrosion of austenitic stainless steel alloys.

Table 2- 3 *Elements and techniques used to improve corrosion resistance of austenitic stainless steel alloys.*

Stainless steel alloy	**Alloying element**	**Application technique**	**Test environment**	**Reference**
304L	N	ion implantation	NaOH and NaCl	Abreu et al. 2008
304	Ti, O_2	reactive magnetron sputtering	HNO_3	Padhy et al. 2011a
304	-	laser surface melting	H_2SO_4 with KCN	Yang et al. 2008
304	Zn, Al	thermal spraying	sea water	Kim & Woo 2010
304L	Ce	dip coating	NaCl	Zand et al. 2012
316L	Ti, Al, N	DC magnetron sputtering	simulated body fluid	Subramanian et al. 2010
316L	Ti, N	cathodic arc and ion implantation	NaCl	Escalada et al. 2013
304L	Ce	ion implantation	NaOH	Abreu et al. 2002a

Numerous researches have studied surface alloying of austenitic stainless steels with nitrogen (Flis et al. 2004; Cano et al. 2006; Fossati et al. 2006; Padhy et al. 2010). Using nitrogen is reasonable due to its ability to stabilise the austenite phase, improve wear resistance and pitting resistance according to the pitting resistance equivalent (PREN) in Equation 2-12. The improvement in wear resistance is due to the precipitation of chromium nitride particularly at temperatures above 500°C. However, nitride precipitation depletes chromium in the matrix and compromises corrosion resistance.

$$PREN = \%Cr + 3.3(\%Mo) + 30(\%N) \qquad \textbf{\textit{Equation 2-12}}$$

Elements such as yttrium, titanium, cerium and lanthanum have a high affinity for oxygen and form stable passivating oxides that can retard anodic dissolution. This

is similar to the effect of chromium in stainless steel. Titanium and cerium based surface alloys have been analysed in oxidising acids, neutral chlorides such as sodium chloride and in alkaline solutions (Chou et al. 2001; Ibrahim et al. 2002; Abreu et al. 2002b; Padhy et al. 2011a; 2011b), yet this has not been done in reducing acidic media. It is possible that, like chromium oxide, the oxides of cerium and titanium are unstable under these conditions.

The use of base metals such as zinc, nickel and molybdenum for surface alloying austenitic stainless steels seems attractive from a cost point of view. This has prompted research into these surface alloys (Wang et al. 1994; Saidi et al. 2015). However, these base metals have significantly higher hydrogen overpotentials (Ezaki et al. 1993; Roberge 2000), and cannot be successfully applied in reducing acidic media. In addition, the effectiveness of molybdenum is debatable. From Equation 2-12, molybdenum plays a significant role in the pitting resistance of stainless steel. However, hexavalent molybdenum oxide dissolves at potential well below oxygen evolution and molybdenum (VI) oxide in particular is soluble in acidic electrolytes (Olsson et al. 2003). The presence of molybdenum (VI) may destabilise the passive film on stainless steel and compromise corrosion resistance of the alloy.

Surface cathodic modification

The interest in surface cathodic modification is prompted by efforts to make cathodically modified stainless steels alloys more cost effective and accessible for wider application. Potgieter et al. (1992) prepared two ruthenium alloyed 2209 duplex stainless steels; one produced by vapour deposition and the other by vacuum smelting. The results showed that while the bulk alloyed sample recorded the lowest i_{pass} and i_{corr}, the corrosion performance of the two alloyed samples was very alike. Tomashov and colleagues (1980) also reported similar conclusions on titanium, chromium and stainless steel alloys surface and bulk alloyed with palladium and exposed to hydrochloric and sulphuric acid solutions at different temperatures. Several researchers have since contributed to the subject to cathodic surface alloying extending interest to other surface alloying techniques such as ion

implantation (Tjong & Chu 2007), and laser surface alloying (Tjong et al. 1997; Lekala et al. 2012; Van der Merwe & Tharandt 2015).

2.4.3 Surface alloying strategies

Surface alloying can involve an overlay or a surface modification process. In an overlay process, the alloying material is added to the surface such that the substrate is covered and undetectable on the surface, whereas a surface modification process changes the properties of the surface and the substrate remains detectable on the surface (Mattox 1998). Table 2-4 shows a number of common techniques used to fabricate surface alloys.

Table 2- 4 *Technologies for surface alloying (adapted from Mattox 1998).*

Overlay processes	**Surface modification processes**
Magnetron sputtering	Ion implantation
Electroplating	Shot peening
Thermal spraying	Anodizing
Cladding	Nitriding
Chemical vapour deposition	Carburizing

Ion implantation

Ion implantation is a low temperature technique, which offers the ability to alloy any element into the near surface region of any metal regardless of their miscibility. It modifies only the subsurface regions that are less than 1 μm from the surface (Suda et al. 2002), alloying it and imparting improved properties to the substrate. Although ion implantation was initially used for doping semiconductors for electronic application, the technique has attracted considerable interest in the field of corrosion in recent years. The frequent use of ion implantation in corrosion application is demonstrated in Table 2-3. Nitrogen ion implantation in particular has received the most attention, and was demonstrated to give stainless steel alloys appreciable resistance in nitric acid, chloride and alkaline solutions (Lei & Zhu 2005; Cano et al. 2006; Abreu eta al. 2008; Padhy et al. 2010). Not as

much has been done on ion implantation of PGMs, with Tjong and colleagues (1989; 2007) working on ruthenium implantation of high chromium stainless steel alloys.

The schematic in Figure 2-16 shows the basic components of an ion implanter; namely an ion source, which may be solid or gaseous, a magnetic separator, accelerator and the substrate. Plasma is generated via any of the following means; helicon plasma source, capacitatively coupled plasma source, metal vapour arc or DC glow discharge. Plasma thus formed is drawn out of the ion source chamber using an extraction voltage, and propelled at energies of up to 50 keV to the mass separator. The magnetic field of the separator is adjusted to preferentially bend the beam of the desired ions: heavier ions will not bend, while lighter ions will be strongly pulled by the magnet and will crush into the walls of the separator. The ion beam, consisting of only the desired ions is then accelerated with high energy towards the substrate. Accelerator energy is adjustable and determines the depth to which the ions will be implanted into the substrate.

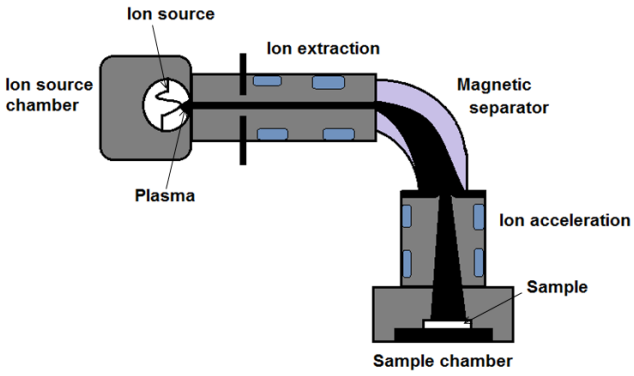

Figure 2- 16 *Typical features of an ion implanter*.

Interaction between the implanted ions and the host atoms is assumed to be elastic, and the maximum transferable energy during a collision, E_{max}, is obtained by energy and momentum conservation as expressed by Equation 2-13 (Mattox 1998). Parameters m_{ion} and m_{sub} are the masses of the implanted ions and the atoms of the substrate respectively, while E is the energy of the incident ions.

Heavy ions transfer much more energy to the substrate, and are more likely to generate more defects and damage than lighter ions.

$$E_{\max} = \frac{4m_{ion}m_{sub}}{m_{ion} + m_{sub}} E$$ ***Equation 2-13***

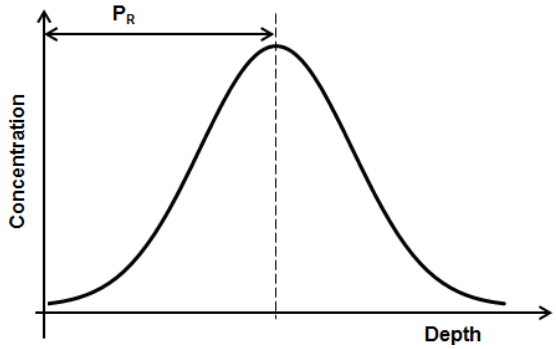

Figure 2- 17 *Schematic showing implantation profile as predicted by the Gaussian distribution.*

The average depth of the implanted ions is called the projected range P_R or implantation depth (Figure 2-17). Implantation depth depends, initially, on m_{ion}:m_{sub} ratio. When m_{ion} is greater than m_{sub}, then implantation depth is smaller and ions concentrate closer to the surface. The distribution of the implanted ions in the substrate is assumed to have a Gaussian distribution as shown in Figure 2-17. However, the difference in the values of m_{ion} and m_{sub} introduces skewness to the expected Gaussian implantation profile as illustrated in Figure 2-18.

From the profiles, it can be seen that heavy ions skew the distribution profile towards the surface while lighter ions skew it further away, and that implantation depth also increases with increase in implantation energy. The latter was demonstrated by Xu et al. (2013). They implanted chromium in magnesium using energies of 15, 20 and 40 keV, and the implantation depth at 40 keV was almost 100 nm but a little over 30 nm at 15 keV. Surface concentration of the implanted ions decreases with increase in implantation energy; at high energies, the ions are projected deeper into the surface.

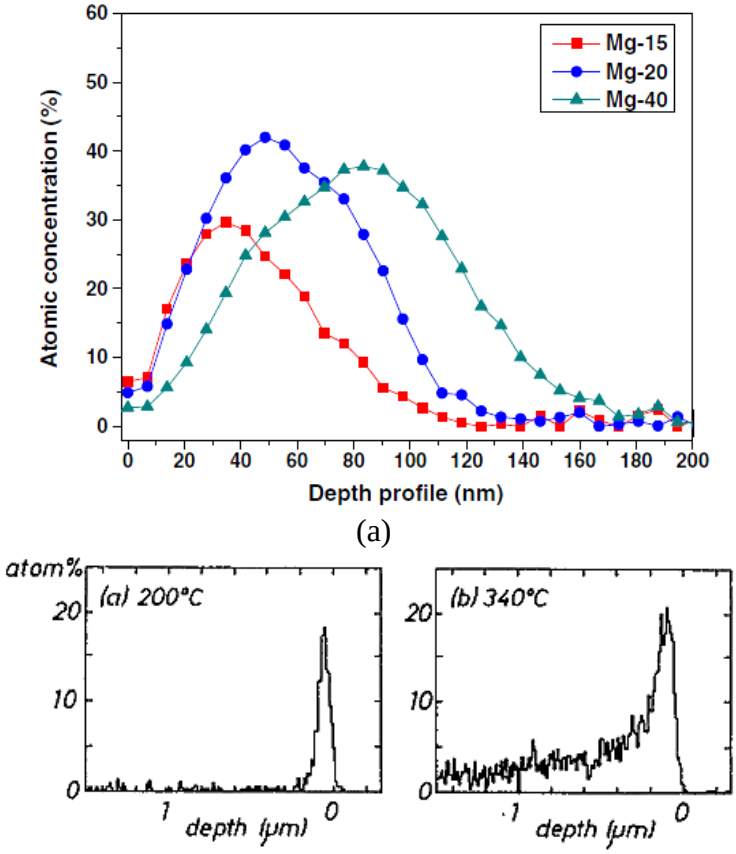

Figure 2- 18 *Skewness of implantation profiles resulting from different m_{ion}:m_{sub} ratios (a) Magnesium implanted with chromium at 15, 20, and 40 keV (Xu et al. 2013), (b) Nitrogen implanted in 304 stainless steel at 28 kV and different temperatures (Collins et al. 1991).*

Implanted ions are stopped at random positions, and often not in lattice sites. Implanted ions can cause scattering of the substrate atoms resulting in vacancies, defects and a distorted lattice. An ion implanted into long-range polycrystalline substrates may undergo channelling. During channelling, the ions are projected between favourably oriented crystal planes where they experience almost no interaction with the atoms of the substrate. Channelling results in incalculable penetration depths, at times several magnitudes more than with random positioning. Damaging or amorphisation of the surface can limit channelling.

Sputtering or ejection of atom from the substrate surface is also a possible result of ion-substrate interaction. Burkin and Armini (1994) showed that sputtering limits the concentration of implanted ions in the substrate; that at some point, the

rate of ion implantation equals the rate at which material, including implanted ions, is lost by sputtering. To improve efficiency and achieve near 100% implantation, the authors suggest using a sacrificial coating layer, which will be sputtered preferentially.

RF magnetron sputtering

Sputtering is a non-thermal, non-equilibrium process that involves the physical vaporisation of atoms from a surface by momentum transfer from bombarding energetic atomic sized particles (Mattox 1998). Arthur Wright (1877) was the first to report sputter deposition. He used sputtering to deposit 174 and 183 nm thick gold and platinum films on glass using a rather crude electrical apparatus with an induction coil, a battery source and evacuated with the aid of multiple pumps. Since then, significant progress has been made, with the advent of magnetron sputtering in the 1970s (Clark 1971; Chapin 1979) rendering it the preferred coating technique in the microelectronics industry. Several authors (Subramaniam et al. 2010; Padhy et al. 2011; Saidi et al. 2015), have shown that sputter deposited surface alloys can impart satisfactory corrosion resistance to base metals in a variety of corrosive agents.

Film deposition by sputtering is illustrated in Figure 2-19. A sputtering gas, typically an inert gas such as argon or xenon, is ionized by use of a breakdown or striking voltage to create plasma. The positively charged ions of the plasma are attracted to the negatively charged target, which is the source of the desired alloying element. They bombard the target, and collide elastically with its atoms, imparting energy of which the magnitude can be estimated by Equation 2-13. The energy transferred is sufficient to eject or dislodge the atoms from the surface of the target and sputter them towards the substrate, where they condense to form a thin film.

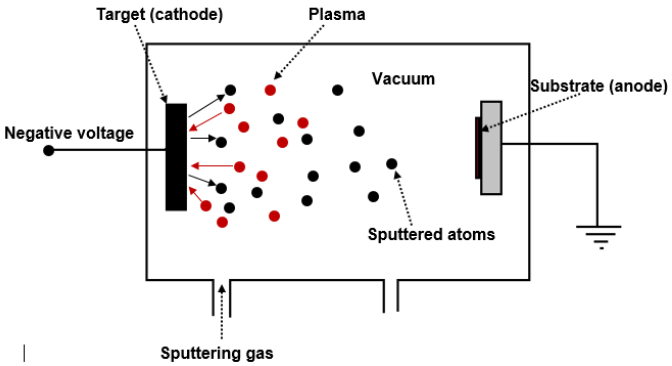

Figure 2- 19 *Schematic illustrating the process of sputtering.*

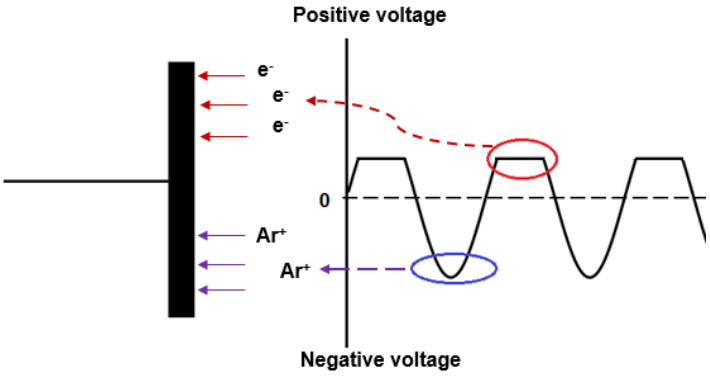

Figure 2- 20 *RF sputtering (adapted from Alfonso et al. 2012).*

Radio frequency (RF) sputtering, shown in Figure 2-20, utilizes alternating current at a pre-set frequency, usually 13.56 MHz to create the plasma. At each half cycle, the potential is such that ions in the plasma are accelerated to the target to cause sputtering, while on the alternate half cycles, electrons reach the surface to maintain charge neutrality. This makes it possible to use either electrically conductive or nonconductive targets. During ion bombardment, secondary electrons are emitted from the target. Magnetron sputtering uses a magnetic field to confine these secondary electrons near the target such that ionisation of the sputtering gas occurs closer to the target, resulting in higher ionisation efficiency, higher sputtering rates and consequently higher deposition rates (Kelly & Arnel 2000). It is for this reason, coupled with its capacity to produce dense films, that

RF magnetron sputtering has generated much interest (Banerjee et al. 2010; Saad & Kassis 2012).

Sputter deposition parameters have a significant effect on the properties of the films. Increasing sputtering power for instance, has the effect of increasing the energy of the plasma ions and therefore the sputter yield. This is seen by a general increase in deposition rate and film thickness as a function of RF power in Figure 2-21. However, at very high energies, sputter yield may decrease (Mattox 1998) as the sputtering ions tend to lose much of their energy far below the surface of the target. Chaoumead et al. (2012) demonstrated this when they deposited titanium-doped indium oxide on glass using RF magnetron sputtering. Deposition powers greater than 300 W were accompanied with reduced deposition rate.

High RF powers are associated with high residual stresses. Films produced by sputtering will naturally be stressed, owing to particle bombardment by sputtered atoms and working gas molecules. The energy of the bombarding particles, and hence the magnitude of residual stress is expected to increase with increase in sputtering power. In separate studies, Cuthrell et al. (1988) and Bhatt et al. (2007) showed that film residual stress is also a function of sputtering gas pressure. The results, presented in Figure 2-22 showed that at low deposition pressures, film stresses are largely compressive, but change to tensile with increase in pressure. At much higher pressure, the nature of film stresses becomes increasingly compressive. It is therefore possible to control film residual stresses by manipulating sputtering gas pressure. Films having tensile residual stresses are likely to fail by cracking, while those under compressive stresses will experience buckling.

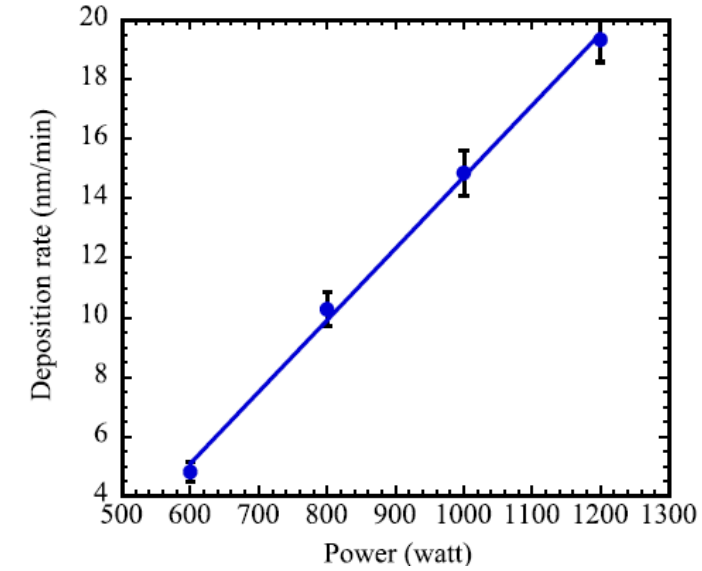

(a)

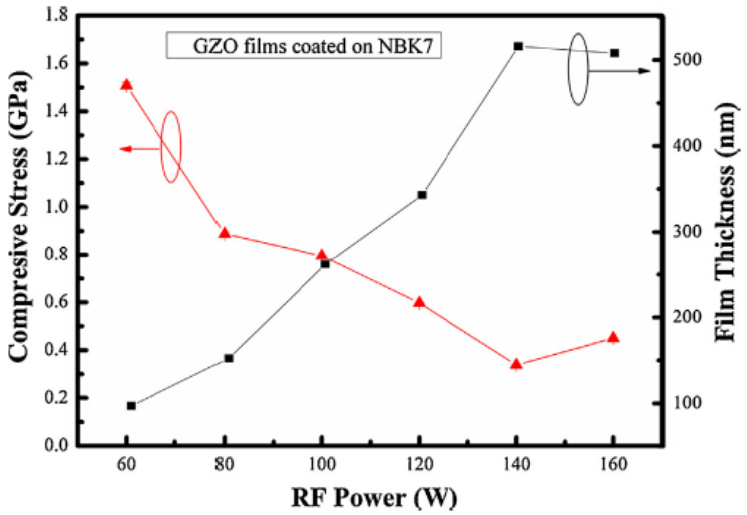

(b)

Figure 2- 21 *Effects of RF power on (a) deposition rate of ZnO:Al films on glass (Spadoni & Addonizio 2015), and (b) film thickness and residual stress of Ga-doped ZnO (Tien et al. 2015).*

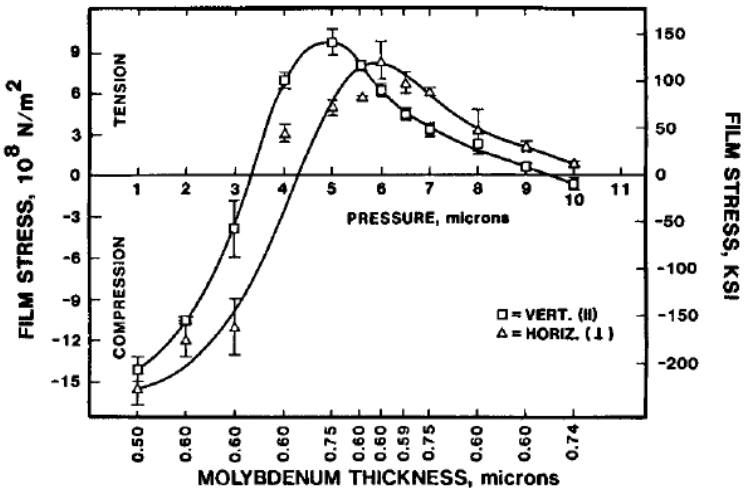

(a)

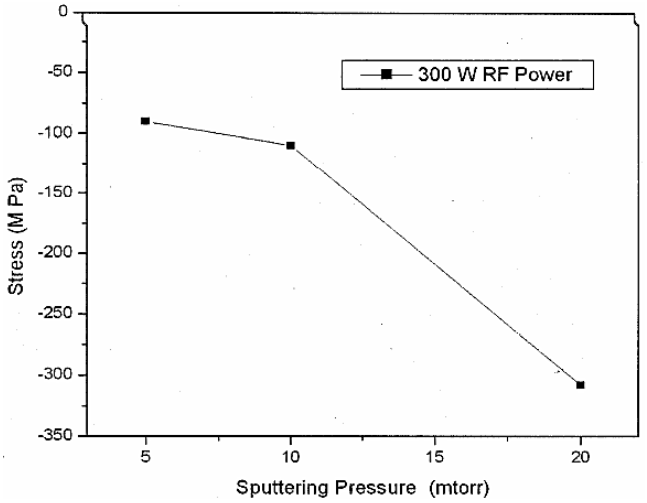

(b)

Figure 2- 22 *Dependence of film stress on sputtering gas pressure. (a) Molybdenum films produced by cathode sputter deposition using argon (Cuthrell et al. 1998)*, and (b) SiO_2 film produced by RF diode puttering using argon at 300 W (Bhatt et al. 2007). *1 μ = 1.333 Pa*

Pulsed electrodeposition

Electrodeposition, also referred to as electroplating, is a low energy process of producing coherent metallic coatings on conductive substrates from a solution containing cations of the desired metal. It involves passing electric current through the solution in a set up similar to the one shown in Figure 2-23, and reducing the metal cations as per Equation 2-14, where *M* is the metal is to be deposited.

$M^{n+} + n\bar{e} \rightarrow M$ **Equation 2-14**

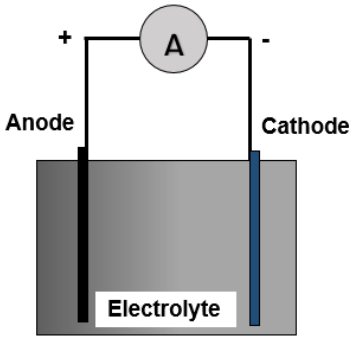

Figure 2- 23 *Typical experimental set-up for electroplating.*

This technique is relatively inexpensive, easy to scale up and can be used on articles with complex geometry. Variety of metallic surface alloys can be prepared using electrodeposition with high chemical purity, and these include films of nickel, copper, cobalt and zinc (Kim & Weil 1989; Tóth-Kádár et al. 1996; Quemper et al. 2000; Yousseff et al. 2004; Tury et al. 2007). The versatility of electrodeposition has seen its application in car parts such as engine cylinder and wheel rims, bath taps, jewellery, catalysts used in photovoltaic devices. Gao et al. (2009) electroplated 316 austenitic steel with palladium for corrosion protection.

Electrodeposition is traditionally carried out using direct current (DC). Figure 2-24 shows the concentration profile of the plating electrolyte near the cathode. During electrodeposition, the diffusion layer becomes depleted of the metal cations and enriched with anions. The anions impede cation migration from the bulk electrolyte, and the failure to replenish the diffusion layer with the metal cations creates a concentration gradient between the bulk and the electrode surface. The width of the diffusion layer (δ_N) grows with time to a thickness limited by the hydrodynamic movement of the bulk solution (Ibl 1980; Chandarasekar & Pushpavanam 2008), which may be induced by stirring or convection effects. Assuming uniform current distribution across the cathode, the build-up of the concentration gradient results in a potential drop called

concentration overpotential, η_{conc} and described by the Nernst expression in Equation 2-15.

$$\eta_{conc} = \frac{RT}{nF} In \frac{C_s}{C_o} \qquad \textbf{Equation 2-15}$$

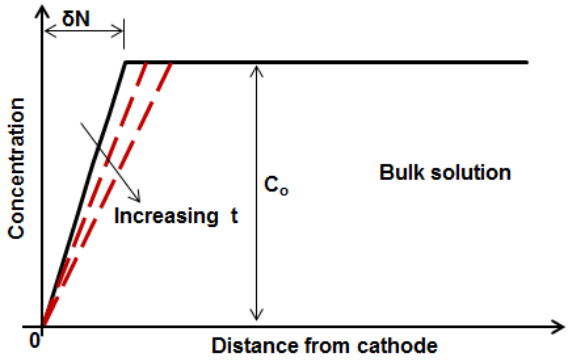

Figure 2- 24 *Typical concentration profiles of the diffusion layer near the cathode during DC electroplating. C_o = cation concentration in the bulk, δ_N = width of diffusion layer, and t = deposition time.*

In Equation 2-15, C_s is the cation concentration at the electrode surface, C_o is the cation concentration in bulk electrolyte, and the other symbols have their usual meanings. The reduction in η_{conc} means that high-energy input is required to maintain the plating current and sustain the electrodeposition process. When the surface cation concentration drops to zero, a critical current is reached below which no plating occurs, as there is no sufficient energy for deposition. This current, known as the limiting current density, i_L is described by Equation 2-16 (Qu et al. 2003), and is an inverse function of δ_N.

$$i_L = \frac{nFDC_o}{\delta_N} \qquad \textbf{Equation 2-16}$$

The conditions discussed in the preceding paragraphs result in limited rate of metal deposition and the production of powdery films, similar to those shown in Figure 2-25(a). Severe mass transport limitation and vigorous hydrogen evolution associated with DC plating are attributed for the quality of these deposits (Chandarasekar & Pushpavanam 2008; Joi et al. 2013).

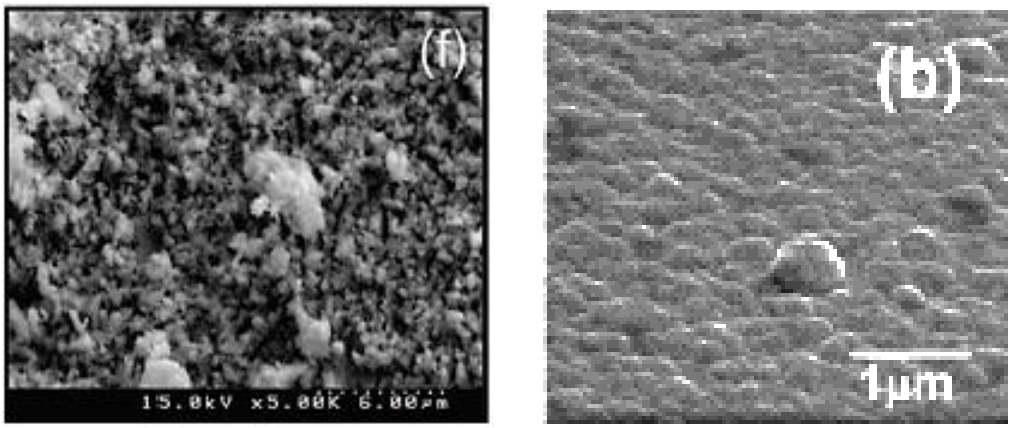

(a) (b)

Figure 2- 25 *Cu-Mn film deposited on PVD Cu seeded silicon wafer attached on RDE. Deposition was achieved by (a) DC, and (b) PC plating (Joi et al. 2013).*

Pulsed electrodeposition (PED) presents an alternative to DC plating. It involves interrupting the plating current at predetermined intervals shown as T_{off} in Figure 2-26(a), during which the current may or may not drop to zero (Ibl et al. 1978). The momentary interruption allows for the discharge of the diffusion layer, and for the migration of cations from the bulk solution. This results in a constantly high η_{conc}. High η_{conc} can greatly influence nucleation rates, as more energy is available for the formation of nuclei (Ibl 1980; Qu et al. 2003). The interruption also allows for desorption of hydrogen resulting in films with lower residual stresses.

Pulsing the current has the notable effect of thinning the diffusion layer in Equation 2-16 as shown in Figure 2-26(b). In the figure, the dotted lines depict the replenishment process during T_{off}. The diffusion layer in the case of PED consists two layers: a pulsating or stirred layer of width δ_p and a stationary layer whose thickness is δ_s (Ibl 1980). The concentration gradient depends on the length of T_{off}, and approaches zero as T_{off} increases. As with DC plating, i_L for PED is expressed by Equation 2-16. The pulse length, T_{on} required for cation surface concentration to reach zero and to reach i_L is τ, and may be predicted by Equation 2-17.

$$\tau = \frac{(nF)^2 C_o D}{2 i_p} \qquad \textbf{\textit{Equation 2-17}}$$

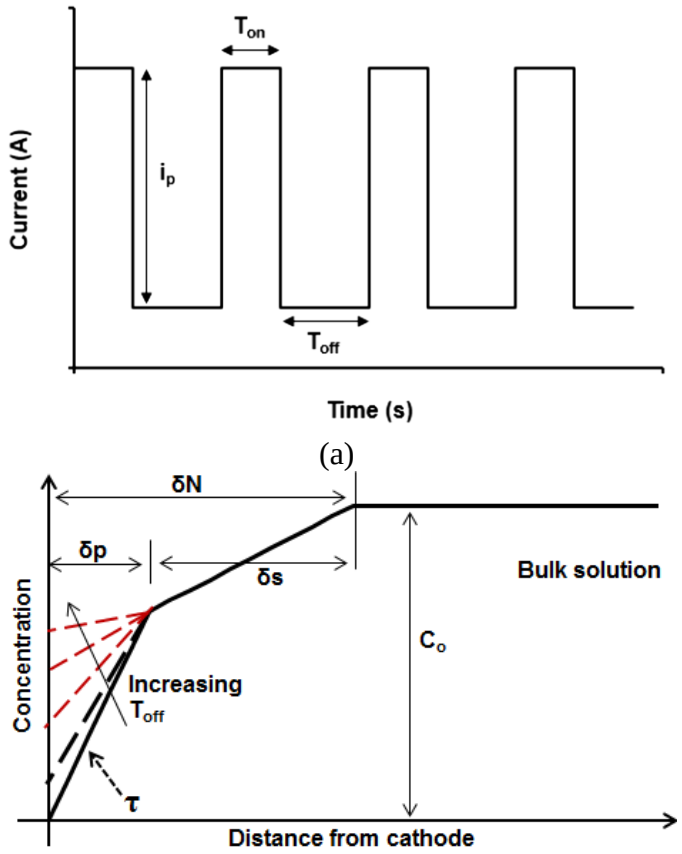

Figure 2- 26 *(a) Typical current waveform used in pulse electrodeposition, and (b) concentration profile of diffusion layer near the cathode during pulsed electrodeposition (adapted from Ibl 1980). T_{on} = length of time current is on, T_{off} = length of time current is off, and i_p = peak current.*

2.5 Corrosion measuring techniques

Given that corrosion of metals is an electrochemical process, it is plausible that the majority of techniques for determining corrosion behaviour are electrochemical in nature. The advantages of electrochemical approaches to studying corrosion are a relatively short measuring time, high accuracy and the possibility for continuous monitoring (Lorenz & Mansfeld 1981). Corrosion study using electrochemical methods is often carried out using potentiostats interfaced with computers and suites of data acquisition software, and involves polarising the test sample away from the equilibrium potential (Section 2.1). Polarisation may induce a set of electrochemical reactions that would otherwise not occur, but which contribute to the overall corrosion reaction and compromise accuracy.

Alternatives to electrochemical methods are non-electrochemical methods, such as weight loss and solution analysis. These are valuable where corrosion products are non-adherent and when knowledge of the corroding system at equilibrium is of importance. They however require relatively long exposure periods for the results to be meaningful. In addition, they are poorly reproducible and often not sensitive enough to give more than qualitative information (Jüttner 1990).

Two methods were used extensively in this study. These are potentiodynamic polarisation and electrochemical impedance spectroscopy (EIS), discussed broadly in the subsequent subsections.

2.5.1 Potentiodynamic polarisation

This method involves polarising the test sample at a predetermined rate, called the scan rate, and monitoring the current density as a function of potential. Data obtained this way is typically presented in a semi-logarithmic plot similar to the ones shown in Figures 2-11 and 2-27. Qualitative analysis of these curves entails evaluating theirs shapes and how they evolved with changes in the properties of the corrosive environment. For example, in Figure 2.27(a), increasing acid concentration from 1 M to 6 M shifted the curve to lower current densities and more noble potentials. The implication is increased corrosion resistance. Similarly, the current fluctuations in Figure 2-27(b) indicate susceptibility to pitting.

Quantitative analysis of potentiodynamic polarisation is done by using either the Tafel method or linear polarisation resistance (LPR), appropriately known as the Stern-Geary method. The kinetics of a corrosion system are expressed by the Bulter-Volmer relationship given in Equation 2-5, and the values of Tafel slopes β_a and β_c can be determined from potentiodynamic curves at potentials between ±20 to ±50 mV from E_{corr}, as shown in Figure 2-28(a). In this region, the anodic and cathodic branches of the polarisation curves exhibit linearity, the gradients of which are equivalent to β_a and β_c respectively. Extrapolating these slopes to E_{corr} allows for the approximation of i_{corr}. As stated previously (Section 2.1), i_{corr} is directly proportional to corrosion rate.

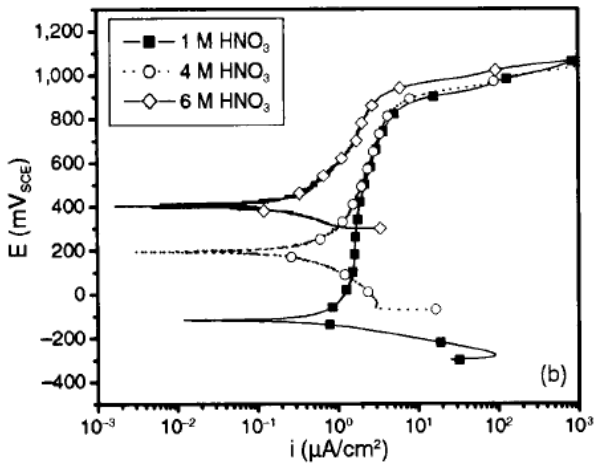

(a)

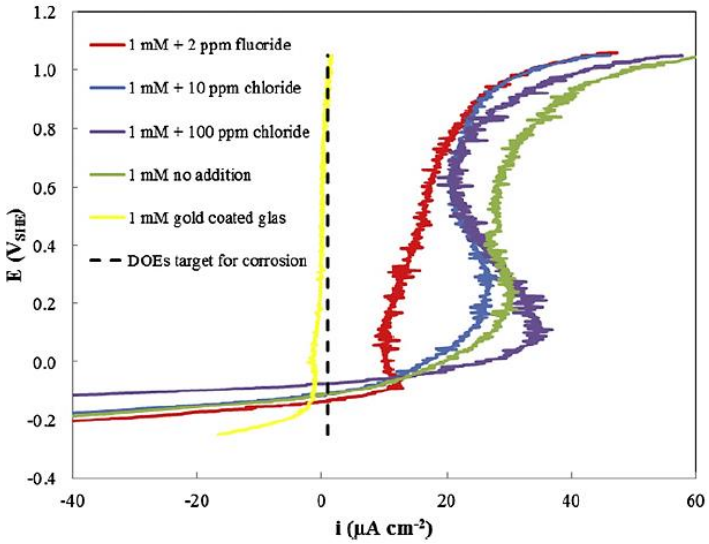

(b)

Figure 2- 27 *Potentiodynamic curves for (a) 304LN2 stainless steel exposed to 1, 3 and 6 M nitric acid at 25 °C (Girja et al. 2012), and (b) 316L stainless steel in sulphuric acid with small chloride and fluoride additions measured between 0.25 and 1.05 V vs SHE in (Lædre et al. 2012).*

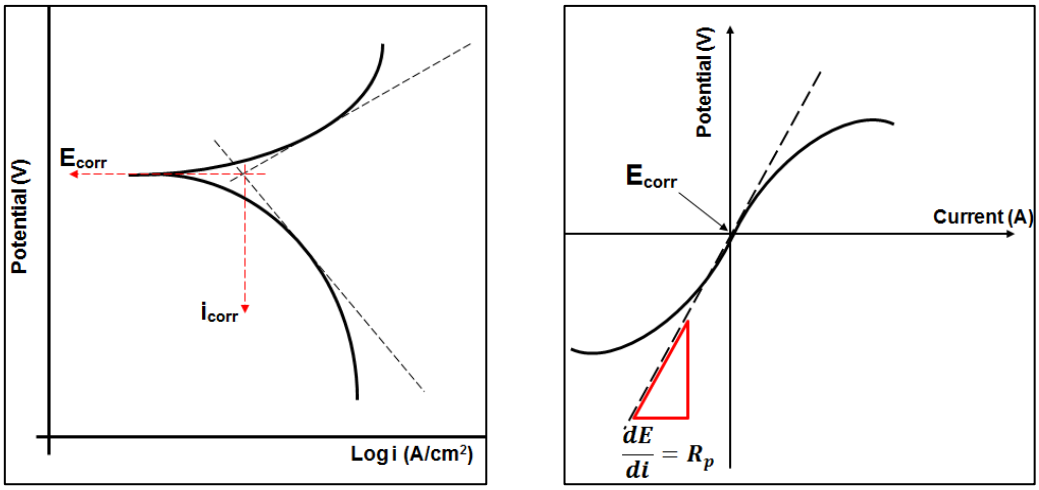

(a) (b)

Figure 2- 28 *Approaches for quantitatively analysing potentiodynamic polarisation curves, (a) Tafel and (b) LPR. Tafel method uses semi-logarithmic plots of current and potential, while LPR uses linear plots.*

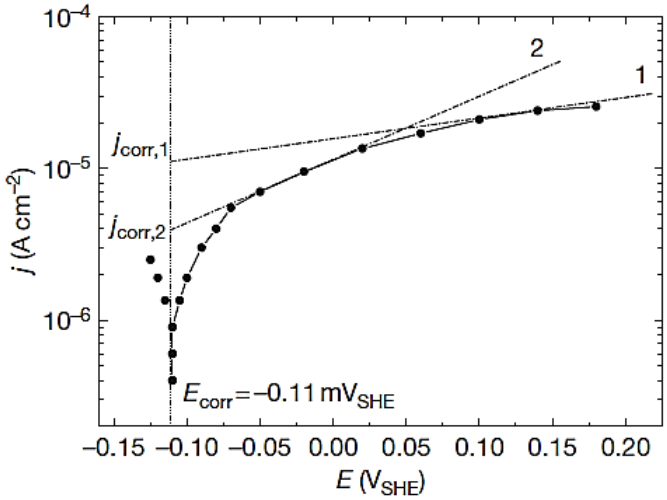

Figure 2- 29 *Misestimating i_{corr} from a small-range or nonlinear Tafel behaviour. Polarization curve obtained when Zn was exposed to aerated 0.01 M $NaHCO_3$ at 60°C and pH 8.1 (Lefrou et al. 2010).*

The use of the Tafel approach requires that linearity in the Tafel region extend to more than one decade of current (Flitt & Schweinsberg 2005a; Lefrou et al. 2010). Where Tafel behaviour is not large enough or is ambiguous, the use of the Tafel method may lead to erroneous approximation of i_{corr}. This is demonstrated in Figure 2-29 where the anodic Tafel region occupies less than one decade of current, presenting high chances of misestimating the value of i_{corr}. Another

limitation of the Tafel approach of estimating the value of i_{corr} is that it assumes that the corrosion reaction is single-step and charge transfer controlled. For corrosion reactions influenced by mass transport, poor solution resistance, or by more than one reduction reaction occurring at similar rates, deviation in Tafel behaviour may be observed (Stern & Geary 1957). In such cases, it is often difficult to obtain Tafel slopes with plausible accuracy.

Stern and Geary (1957) proposed an alternative method of estimating i_{corr} from polarisation measurements: LPR. The method, described by the expression in Equation 2-18, relates the slope of the polarisation curve in the zero current region (Figure 2-28(b)) to i_{corr} and Tafel slopes β_a and β_c. This relation holds for polarisation within the ±10 mV E_{corr} range. In this range, the slope is equal to polarisation resistance, R_p. The value of R_p is mainly influenced by i_{corr} and is relatively independent to β_a and β_c (Walsh et al. 2008). This is the greatest advantage of the LPR approach as it allows for interpretation of i_{corr} without determining the Tafel slopes. Rearranging Equation 2-18 gives Equation 2-19, where B is a proportionality constant defined by Equation 2-20.

$$\frac{dE}{di_{E\to 0}} = \frac{-\beta_a |\beta_c|}{2.3 i_{corr}(\beta_a + |\beta_c|)} = R_p \qquad \textbf{Equation 2-18}$$

$$i_{corr} = \frac{B}{R_p} \qquad \textbf{Equation 2-19}$$

$$B = \frac{\beta_a |\beta_c|}{2.3(\beta_a + |\beta_c|)} \qquad \textbf{Equation 2-20}$$

The value of B may be determined experimentally by linearizing Equation 2-19 or calculated from Equation 2-20 using documented values of Tafel slopes. This makes LPR easier to use, and applicable to most cases without the need for extensive polarisation (Üneri 1969). However, values of i_{corr} determined by LPR are subject to error when the anodic process is dominated by the oxidation of some species other than the test metal, or when the ohmic resistance of the test solution is too high (Scully 2000).

The use of either Tafel slopes or LPR for determining i_{corr} assumes uniform corrosion (ASTM G102-89(2010)). They misestimate corrosion rates when the metal corrodes by pitting.

2.5.2 Electrochemical impedance spectroscopy

EIS is a non-intrusive method of studying corrosion behaviour of metals. It is particularly sensitive to localised corrosion and useful for detecting defects on Type I surface alloys. It involves applying a time-varying potential (AC) and monitoring current response. In this technique, corrosion resistance is described by impedance, *Z*, which is defined as the ability to resist flow of AC. *Z* bears ohmic like characteristics as expressed in Equation 2-21, where ω is angular frequency, *t* is time and Φ is the phase difference between applied voltage and current response. When Φ is zero, *Z* is real or faradaic and represents a pure resistor, and when Φ is 90°, its value is imaginary or non-faradaic and represents a capacitor.

$$Z = \frac{V_t}{I_t} = \frac{V\sin(wt)}{I\sin(wt+\phi)} \qquad \textbf{\textit{Equation 2-21}}$$

A simple case of an electrode exposed to a corrosive solution without any mass transfer reaction is depicted in Figure 2-30. In Figure 2-30(a), the corroding system is presented as the solution resistance, R_s in series with an interfacial resistance *Z*. However, interfacial resistance consists of a faradic current due to metal dissolution and a non-faradaic current due to periodic changes in the amounts of a charge in the electric double layer near the surface (Macdonald 1992; Bagotsky 2006; Orazem & Tribollet 2008). R_p in Figure 2-30(b) is polarisation resistance defined by Equation 2-18, and may be used to determine corrosion rate.

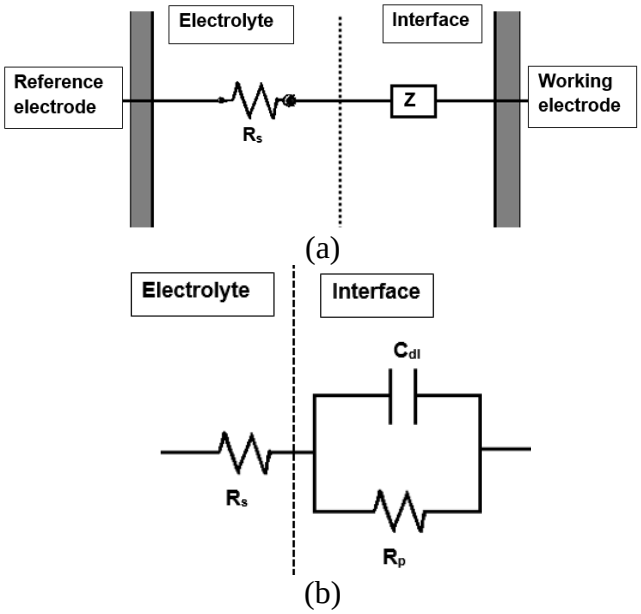

Figure 2- 30 *Electrical circuits analogues of a charge transfer controlled corrosion reaction showing (a) showing impedances of the corrosion system, and (b) differentiating faradaic and non-faradaic components (adapted from Orazem & Tribollet 2008).*

EIS data is typically presented on a complex plane or Nyquist format. In this graphical presentation shown in Figure 2-12 and 2-31(a), imaginary impedance *ImZ*, is plotted as a function of the real component of impedance *ReZ*. EIS models the corrosion process into bulk and electrode related effects. Bulk effects are associated with the high end of the frequency range, and include solution resistance as well as dielectric effects resulting from the dissolution and recombination of charges in the electrolyte. Electrode effects involve activities near the electrode, such as pitting and adsorption of reaction species and is characterised by the response at the low frequency end (Macdonald 1992). From this description and the Nyquist plot in Figure 2-31(a), the following conditions may be derived:

$$Z_{w\to\infty} = R_s \qquad \textbf{\textit{Equation 2-22}}$$

$$Z_{w\to 0} = R_s + R_p \qquad \textbf{\textit{Equation 2-23}}$$

In cases where solution resistance is negligible, for example in highly conductive solutions such as sulphuric acid and sodium chloride, then the value of R_p may be

approximated from the low frequency end of the Nyquist plot according to Equation 2-23 by assuming that R_s is zero.

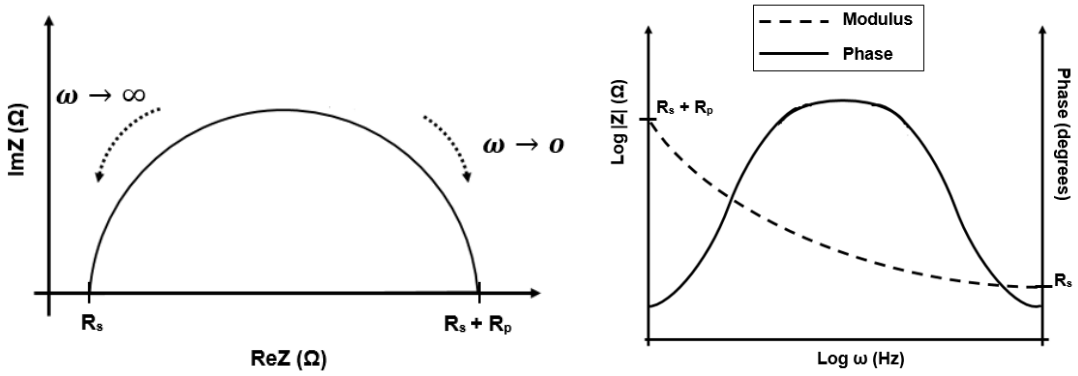

(a) (b)

Figure 2- 31 *Graphical presentation of EIS data. (a) Nyquist plot and (b) Bode plots.*

Although Nyquist plots are typically semi-circular as presented in Figure 2-31(a), their shapes evolve depending on the kinetics and diffusional characteristics of the corrosion reaction. Semi-circular plots are typical of charge transfer limited processes, and the larger the radius, the higher the corrosion resistance. A depressed Nyquist semicircle may be due to the roughness of the electrode-electrolyte interface or to inhomogeneous distribution of defects at grain boundaries (Abouzari et al. 2009). Multiple semicircles are often an indication of more than one processes occurring on the surface, for example corrosion occurring on a defective coated metal.

Straight-line Nyquist plots (Figure 2-32(a)) represent diffusion-limited processes. On the other hand, reactions influenced by both charge transfer and diffusion will be characteristically semi-circular at high frequencies and linear at low frequencies as given in Figure 2-32(b). According to Wang (2006), the linear part in Figure 2-32(b) constitutes a larger portion of the Nyquist plot for reactions with very fast electron transfer, while slow electron transfer processes are characterised by a larger semi-circular region.

The limitation of Nyquist plots is that the frequency dimension of the data is obscure, and much information is lost. As such, Nyquist plots are usually

accompanied with Bode plots shown in Figure 2-31(b). These present the modulus of impedance and phase angle as a function of frequency on a logarithmic scale. As with the Nyquist plot, the value of impedance at low frequency is equivalent to the sum of R_s and R_p as defined by Equation 2-23, where the value of R_p may be used to determine corrosion rate.

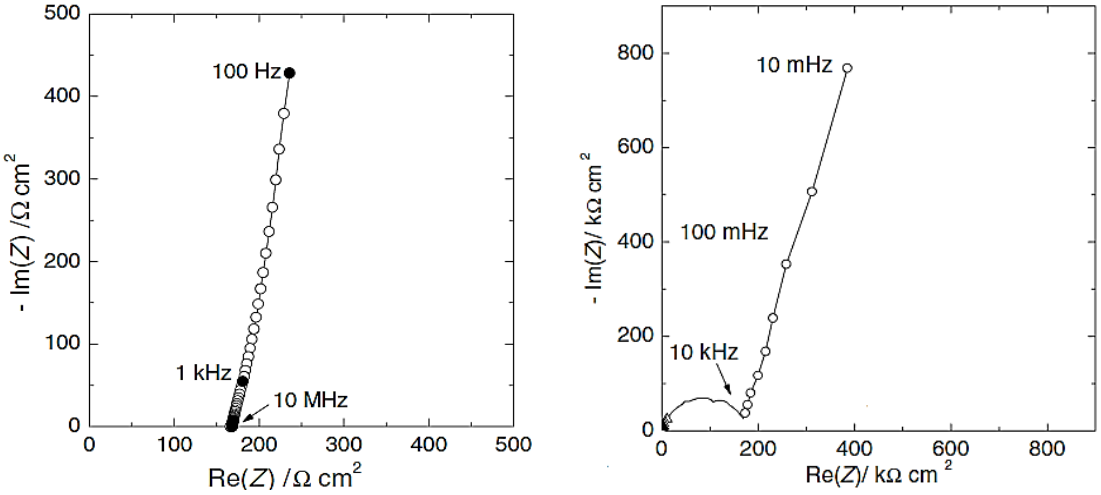

Figure 2- 32 *Nyquist plots typical of corrosion systems (a) under diffusion control and, (b) under both charge transfer and diffusion control (Abreu et al. 2004).*

For a corrosion resistant configuration, the phase angle tends towards |90°| at low frequencies, suggesting capacitive behaviour, and towards zero at high frequencies due to R_s (Orazem & Tribollet 2008). The value of capacitance, C is related to the thickness of the film or layer formed on a metal surface by Equation 2-24 (Gorji & Sanjabi 2012). In the equation, ε_o is the dielectric constant of free space (8.85 x10^{-12} F/m), ε is the relative dielectric constant of the corresponding medium, A is the surface area of the electrode, and d is the thickness of the oxide film. This makes it possible to study the evolution of oxide films with regards to structure and protection efficiency.

$$C = \frac{\varepsilon_o \varepsilon A}{d} \qquad \textbf{\textit{Equation 2-24}}$$

For a reactive configuration, the phase angle tends towards zero at both low and high frequencies, indicating that current and potential are in phase (Orazem &

Tribollet 2008). The Bode modulus plots are typically characterised by asymptotes at low and high frequencies, and the transition between these has a slope of about -1.

Quantitative analysis of EIS data may be done by use of equivalent circuits (ECs), an example of which is described in Figure 2-30(b). ECs are constructed using passive electrical elements, i.e. elements that do not generate current or potential. Typical elements and their physical meanings are presented in Table 2-5, and are used in Figure 2-33 to depict the electrode surface of 2205 duplex stainless steel and 20Cr28Ni austenitic stainless steel in 0.1 M sodium chloride below and above the critical pitting temperature (CPT).

The use of ECs requires a thorough knowledge of the corroding system. It is susceptible to ambiguous interpretation and the possibility of degenerate circuits compounds this problem. Degenerate circuits are ECs that exhibit identical impedances over the entire axis of frequencies (Fletcher 1994), but may bear very distinct physical meaning. It is necessary therefore to validate a proposed EC, for example by changing a single component of the corroding system such as concentration or temperature and observing if expected changes occur to the impedance spectrum.

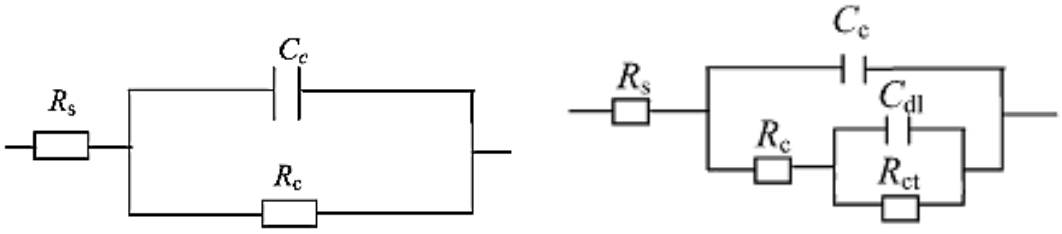

Figure 2- 33 *Proposed models of ECs of coated aluminium LY12 alloy in 3.5% sodium chloride, (a) immediately after exposure and, (b) after 50 minutes of exposure (Hu et al. 2003).*

Table 2- 5 *Passive electrical elements used to construct equivalent circuits and their likely physical meanings (Liu et al. 2003; Gorji & Sanjabi 2012).*

Symbol	Name	Physical meaning
	Resistance, R	R_s = solution resistance R_f = film resistance
	Capacitance, C	Interfacial capacitance due to the double layer for an ideal surface
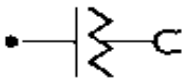	Constant phase element, Q	Interfacial capacitance due to the double layer for a real surface
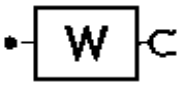	Warburg resistance, W	Diffusion or mass transport effect over an infinite diffusion length
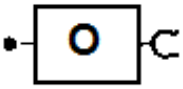	Cotangent hyperbolic, O	Diffusion or mass transport effect over finite diffusion length
	Inductance, L	At high frequency, due to non-uniform current distribution, inductance of cell cables etc. At low frequency, adsorption or desorption process e.g. hydrogen evolution

2.5.3 Statistical consideration of corrosion measurements

Corrosion is a property that does not easily lend itself to precise or concise presentation. Precision is defined, firstly, as the closeness between randomly selected measurements in a replicated experiment, and secondly as the agreement between the measured values and those obtained by other investigators (ASTM G16-95(2010)). The latter is termed reproducibility. Frankel (2008) pointed out that most corrosion rates are only reproducible to within a factor of 2 to 3, especially when the value of the Tafel slopes is assumed around 100 mV/dec.

To secure the statistical relevance of corrosion results, it is often necessary to test a large number of samples and using the mean of the results, calculated as per Equation 2-25 as the typical value of the data set. In Equation 2-25, $\bar{x}$ is the mean of the data set with n values. It is expected that more measurements give a more reliable mean, and may compensate for response variability as well as guard against random errors.

$$\bar{x} = \frac{\sum_{i=1}^{n} x_i}{n_i} \qquad \textbf{Equation 2-25}$$

$$SD = \sqrt{[\frac{1}{n}\sum_{i=1}^{n}(x_i - \bar{x})^2]} \qquad \textbf{Equation 2-26}$$

$$SDE = \frac{SD}{\sqrt{n_i}} \qquad \textbf{Equation 2-27}$$

Standard deviation (SD) and standard deviation error (SDE) as described by Equations 2-26 and 2-27 may be used as indicators of precision: the smaller these values, the more satisfactory the precision of the response variables. However, the use of these tools assumes that the collected data is normally distributed. To validate such assumptions, and therefore the use of the tools defined in Equations 2-26 and 2-27, randomisation of the sequence of test runs is often necessary (Mason et al. 1989). This also protects measurements against systematic errors and improves the accuracy of the measured values.

Chapter 3
Materials and experimental procedures

3.1 Introduction

Work in this study was divided into two parts: surface alloy synthesis and surface alloy characterisation. Alloy synthesis was done using ion implantation, RF sputtering and pulsed electrodeposition, while surface alloy characterisation mainly involved surface analysis, and corrosion characterisation. The present chapter describes the materials and experimental procedures used to achieve this. In addition, it explains how the collected data were analysed for interpretation.

3.2 Materials

3.2.1 Substrate

The substrate used in this study was AISI 304L austenitic stainless steel. It was supplied by MacSteel South Africa in the form of 6 mm thick plates. The chemical composition of the stainless steel was confirmed by spark analysis at Scrooby's Laboratory Services South Africa.

Smaller samples were sectioned from the supplied plate. Water with a cooling additive from ATM GmbH was continuously added to prevent overheating of the samples during sectioning. The samples were wet ground with silicon carbide paper from 80 grit to different surface finishes as required. Where polishing was necessary, 6 μm alumina paste as well as 1 and 3 μm diamond pastes were used. The samples were used without further annealing. They were first washed in detergent, rinsed with deionised water (resistivity > 1 MΩ.cm), and then degreased in ethanol, methanol or isopropanol prior to use.

3.2.2 Ruthenium targets

A 99.9 wt% ruthenium target was used for RF sputtering. The target, supplied by Good Fellow UK, was 76 mm in diameter and 3 mm thick. To facilitate mounting on the RF sputtering machine, a copper plate was bonded to the target using indium. Prior to film deposition, the target was cleaned by sputtering at 100 W for 5 minutes at a gas pressure of 13 Sccm. Power density was determined by Equation 3-1.

$$Power\ density = \frac{RF\ sputter\ power}{Eroded\ \ area} \qquad \textbf{\textit{Equation 3-1}}$$

Ruthenium powder supplied by Anglo Platinum South Africa was used to produce the ion source for ion implantation. The powder, 99.9% pure, was consolidated using spark plasma sintering at 1400°C and 30 MPa as described by Angerer et al. (2009). The consolidated solid was 20 mm in diameter and 2 mm thick.

3.2.3 Ruthenium plating bath

The electroplating bath was prepared using a ruthenium nitrosyl salt ($(NH_4)_2RuCl_6$) supplied by Impala Platinum Limited (Refineries) South Africa. A summary of the chemical composition of the salt was provided by the supplier and is given in Table 3-1.

Table 3- 1 *Chemical composition of the ruthenium nitrosyl salt. *Trace elements >2 ppm. A full assay is presented in Figure C-1.*

Major constituents	**wt %**	**Trace elements***	**ppm**
Metal content	24.07	Platinum	17
Ruthenium	99.90	Tin	4
		Rhodium	9
		Osmium	3
		Calcium	8
		Aluminium	3
		Chromium	4
		Iron	41
		Silicon	22

The bath was modelled on that proposed by Crosby (1981), but without pH adjustment since the films produced after adjusting pH using either potassium hydroxide or sodium hydroxide had poor adhesion and were not usable. It was made by dissolving about 25 g/l of the salt to achieve a ruthenium concentration of 6.2 g/l, and 40 g/l of oxalic acid in deionised water. The electrolyte was held at about 100°C for 24 hours, continuously stirred throughout the period, and then aged for 72 hours. After this, the solution was carefully filtered to remove any undissolved solids.

3.3 Synthesis of surface alloys

3.3.1 Ion implantation

Ion implantation was carried out in a Varian 350D implanter at iThemba LABS North, South Africa. The implantation process was initially simulated by the Stopping and Range of Ions in Matter (SRIM-2008) software to understand the effect of implantation energy on the sputter yield, projected range, substrate damage as well as the distribution of incident ruthenium ions. The simulation did not take into account the possibilities of channelling, but was sufficient for comparison purposes. Implantation parameters were chosen based on the limitations of the machine; energy was varied from 50 to 160 keV, while doses (fluence) used ranged from 10^{12} to 10^{16} Ru/cm^2.

All implantation was done at room temperature. During implantation, the substrates were tilted at 0 and 7° to vary the incidence angle of the ruthenium ions and hence minimise channelling effects. Some of the samples were annealed to minimise the effects of radiation damage. Annealing was done at 400°C under a nitrogen atmosphere for 1 hour in a Carbolite Type 301 tube furnace. Nitrogen gas was used to evacuate the tube before annealing, and gas flow was maintained during cooling to room temperature.

3.3.2 RF sputtering

Radio frequency (RF) sputtering was carried out using the apparatus shown in Figure 3-1 and housed at the School of Physics, University of the Witwatersrand. The sputtering chamber was evacuated using a pair of turbo pumps to a base pressure of between 1.5 $x10^{-5}$ and 3 $x10^{-5}$ mbar. The sputter gas used was argon, whose flowrate was varied between 10 to 23 Sccm to achieve working gas pressures in the range of 1 $x10^{-3}$ and 4 $x10^{-3}$ mbar. Stable argon plasma was obtained at 10 Sccm, hence this was chosen as the lower working pressure limit for this study.

Deposition power ranged from 15 to 200 W with a self-DC negative bias of about 169 and 250 V, and deposition times were varied between 1 and 30 minutes. All films were produced from the ruthenium target described in Section 3.2.2 at room temperature and zero bias. The target-substrate distance was maintained at 60 mm for all depositions, and the ruthenium target was continuously cooled with water whose conductivity was kept at less than 10 μS/cm.

Figure 3- 1 *Apparatus used for RF sputtering.*

Preliminary tests involved depositing the ruthenium films on (100) single crystal silicon wafers. Once satisfactory ruthenium films were obtained, deposition was done on the 304L stainless steel samples. A sample holder capable of taking 8 samples at a time was designed and manufactured at the University of the Witwatersrand. The holder, described in Figure E-3 and made of aluminium, had a shutter allowing a single sample to be exposed to the ruthenium plum at a time.

For some samples, a thin layer (≈ 2 nm) of titanium was deposited prior to ruthenium deposition. Titanium deposition was done according to Vasu et al. (2014). After deposition, some of the samples were annealed at 400°C under a nitrogen atmosphere for 2 hours in a Carbolite Type 301 tube furnace as describe in Section 3.3.1.

3.3.3 Pulsed electrodeposition

Samples used for pulsed electrodeposition (PED) were prepared by drilling 3 mm diameter holes used to suspend them in the plating solution. They were ground and polished as described in Section 3.2.1, after which they were masked using insulation tape on their edges and backside such that only the central area measuring about 3 cm^2 was exposed. This was done to minimise the edge effect, and to control the cathode-to-anode ratio so at to ensure uniform distribution of deposit thickness.

The masked samples were pre-treated by immersing them in 10% sulphuric acid with small quantities of ferric chloride at 80°C to remove native oxides. This was followed by a thorough rinse in deionised water, and the samples were immediately transferred to the plating bath prepared as described in Section 3.2.3.

Plating was carried out in a 3-electrode cell shown in Figure 3-2. The cell consisted of the stainless steel sample as the cathode, a graphite electrode with a surface area of about 28 cm^2 as the anode, and silver/silver chloride electrode/3 M potassium chloride (Ag/AgCl/3 M KCl) reference electrode. The distance between the cathode and the anode was maintained at about 50 mm. All plating was done at room temperature. After plating, the deposits were thoroughly rinsed in deionised water and ethanol, and then allowed to dry in air.

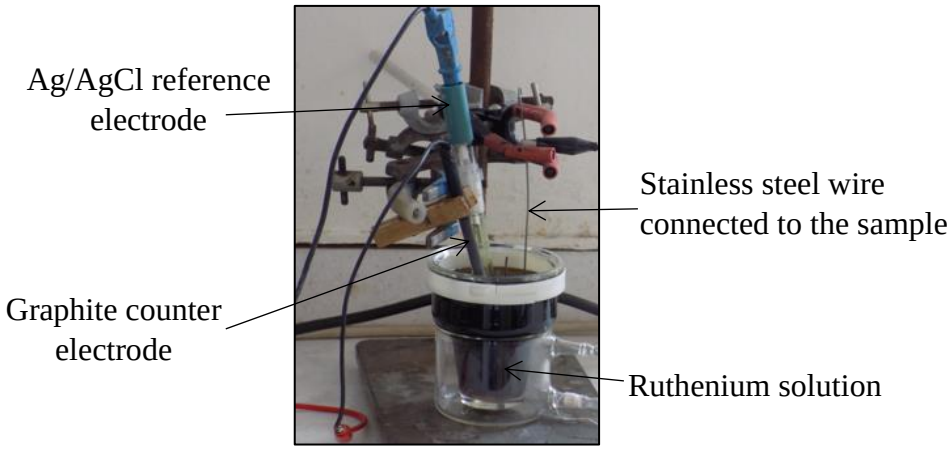

Figure 3- 2 *Set up used in pulsed electrodeposition.*

Electrodeposition was done chronopotentiometrically using a Metrohm PGSTAT302 Autolab potentiostat. The potentiostat generated a waveform similar to that presented in Figure 3-3. T_{off}, the time during which current was zero, was varied from 1 to 50 s, and T_{on} ranged from 3 to 10s. Plating current, i_p, used was 1.2 and 2 A to give a target current density of 0.40 and 0.67 A/cm^2 respectively. These values were chosen based on the limitations of the potentiostat, and suggestions made by previous researchers using DC plating (Reddy & Taimsalu 1971; Crosby 1981).

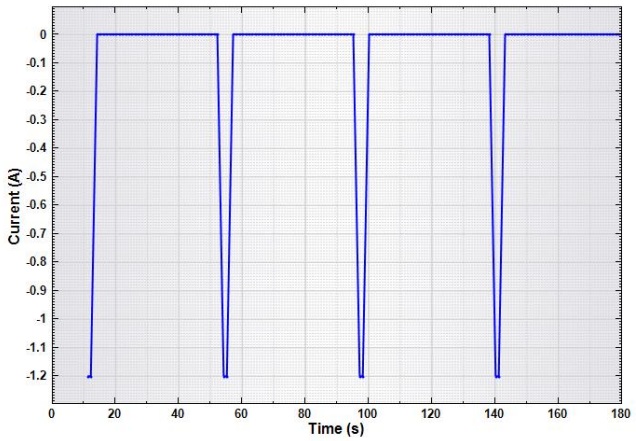

Figure 3- 3 *Typical current waveform used in pulsed electrodeposition.*

3.4 Design of experiments

It was important to reliably determine the significant synthesis parameters on the corrosion resistance of the proposed surface alloys without prolonging

experimentation time and increasing cost. A full 2^k factorial design of experiments (DOE) was chosen for this work. The DOE approach involves studying several parameters at two levels; high (coded +1) and low (coded -1). The effect of each parameter was estimated by the difference between the average response at high and low levels as expressed in Equation 3-2 (Barrentine 1999), where *Y* is the observed response, and *n* is the number of responses at the level (high or low).

$$Effect = \frac{1}{n}\sum_{i=1}^{i=n} Y_{+} - \frac{1}{n}\sum_{i=1}^{i=n} Y_{-} \qquad \textbf{\textit{Equation 3-2}}$$

The significance of the estimated effects was determined using a normal probability plot. This is a graph of the effects and their cumulative normal probabilities, P_i as approximated by Equation 3-3 (Hogg & Ledolter 1992). In the equation, *m* is the total number of effects, and *i* is the rank number when the effects are arranged in an ascending order. Effects that do not fit reasonably well on a straight line are significant, while those that fall on the straight line are normally distributed and are regarded insignificant.

$$P_i = \left(\frac{i - 0.5}{m}\right) \times 100 \qquad \textbf{\textit{Equation 3-3}}$$

Parameters studied varied from one synthesis technique to another. However, in all cases the response considered was the corrosion rate of the surface alloy in 1 M sulphuric acid at ≈ 25°C. The order of the experiments was randomised.

3.5 Alloy characterisation

3.5.1 Physico-chemical characterisation

Surface analysis

Surface analysis of the alloyed pre and post corrosion was done using field emission scanning electron microscope (FESEM), and atomic force microscope (AFM).

A Carl Zeiss Sigma FESEM with energy-dispersive X-ray spectroscopy (EDS) was used to study the surface morphology of the alloyed surface. The FESEM, capable of magnification as high as 1.3 million times, was used in both secondary

electron (SE) and backscattered electron (BSE) modes. Where necessary, the samples were coated with a thin gold-palladium coating to improve resolution at high magnification by minimising the space charge effects. An accelerating voltage of 10 and 20 kV was used for imaging and for EDS analysis respectively. In both instances, the working distance was maintained at about 8.5 mm. Line scans and mapping was also done to highlight elemental distribution.

Surface analysis by AFM was performed in the tapping mode. The AFM used was Veeco Dimension 3100 equipped with a Nanoscope V530r3sr3 data acquisition software. Measurements were done using scan sizes between 50 nm^2 and 1600 μm^2 at frequencies ranging from 2.5 Hz to 0.5 Hz. Analysis by AFM was limited to uncorroded samples only.

Microstructural analysis

Stainless steel samples for metallographic characterisation were hot mounted in black phenolic conductive resin at 6 kN for 8 minutes. They were prepared by grinding with successively finer abrasives as described in Section 3.2.1. The polished samples were then etched using the etchants listed in Table 3-2. All etchants were prepared using deionised water according to ASTM E407-07. Once etched, the samples were liberally rinsed in water and ethanol, dried with warm air, and then examined using both the optical microscope and FESEM. The optical microscope used was Lecia DM6000 M equipped with a digital camera and Lecia Application Suite (LAS) software.

Table 3- 2 *Etchants used for metallographic characterisation as per ASTM E407-07.*

Etchant	**Oxalic acid**	**Marbles solution**	**Sodium hydroxide**
Purpose	General structure of austenitic grains	Darkens austenitic grains	Darkens ferritic grains
Composition	10g oxalic acid 100ml water	10g copper sulphate 50ml hydrochloric acid 50ml water	40g sodium hydroxide 100ml water
Method of etching	Electrolytic at 6V for 10-60s	Immerse for 5-60s	Electrolytic at 5-10V for 5-20s

Metallographic characterisation was complimented by X-ray diffraction (XRD) measurements. These were done using a Bruker 2D Phaser with LynxEye detector, and Fe-filtered Co-Kα radiation with a wavelength of 0.179 nm. Unless stated otherwise, the XRD measurements were performed in the range 20° < 2θ < 140° 2θ using a step size of 0.026°at temporal resolution of 37s/step. Analysis of XRD was done using Diffrac.Eva V3.2 software with ICDD Powder Diffraction File (PDF) database.

Stress analysis

Stresses in the alloyed surfaces were studied by considering the shift in the Bragg position of XRD peaks. Using the data collected with the Bruker 2D Phaser as described in the preceding subsection, stress was inferred from strain approximated from Equation 3-4. In the equation, θ_1 is the Bragg angle of a peak as given in the relevant reference pattern or in the measured pattern of the untreated sample, and θ_2 is the Bragg angle of the same peak measured on the alloyed surface. This approach is semi-quantitative and sufficient for comparative study.

$$\varepsilon = \frac{\sin\theta_2}{\sin\theta_1} - 1 \qquad \textbf{\textit{Equation 3-4}}$$

Stress analysis was also done using the $Sin^2\psi$ method at rotation angles of 0, 45, 90, 180, 225 and 270°, and ψ ranging from 0 to 70°. Measurements were based on the shift in Bragg position of the stainless steel (311) peak at 2θ = 90.70°, and were carried out using Ni-filtered Cu-Kα radiation with a wavelength of 0.154 nm. The elastic constants used to determine stress were $S_1 = -1.77\text{x}10^{-6}$ MPa, $1/2S_2 = 7.49\text{x}10^{-6}$ MPa and Poisson's ratio of 0.31. Residual stress data were collected using Bruker D8 Discover equipped with 2D Hi-Star detector, and analysed using Leptos 6.02 software.

Mechanical properties

Typical tensile specimens with a gauge length of 25 mm were tested using a Tinius Oslen type DBBSTOL-50kN tensile tester. The machine was interfaced with a QMat Professional software. After fracture, the specimens were examined via a Nikon SMZ745 stereo microscope, with a 7.5x zoom magnification. The microscope was mounted with a high definition DS-Fi2 camera from Nikon and equipped with NIS-Elements version 4.00 imaging software.

It was assumed that the surface alloys were too thin to have a notable impact on the mechanical properties of the stainless steel. As such, mechanical characterisation was limited to unalloyed 304L stainless steel. To ensure statistical relevance, three specimens were tested.

3.5.2 Electrochemical characterisation

Corrosion performance of the alloyed surfaces was evaluated by potentiodynamic polarisation, chronoamperometry, potentiostatic measurements and electrochemical impedance spectroscopy (EIS). This was done in a three-electrode cell consisting the stainless steel sample as the working electrode, Ag/AgCl/3 M KCl reference electrode (≈ 199 mV vs SHE), and a large area graphite counter electrode. The tests were carried out in the Metrohm PGSTAT 302 Autolab shown in Figure 3-4. The potentiostat was equipped with Frequency Response Analyser (FRA) module, and interfaced with Nova 1.70 data acquisition software.

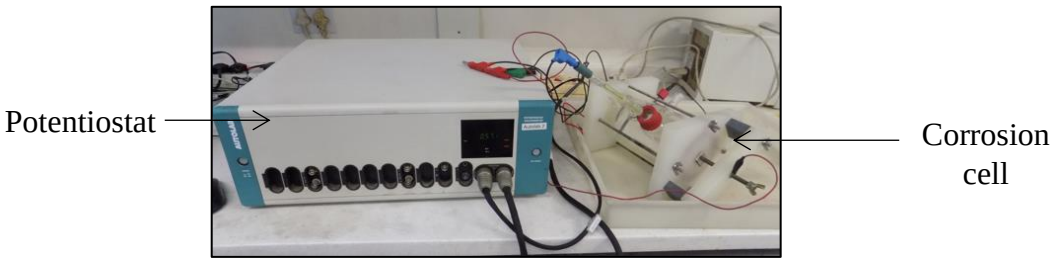

Figure 3- 4 *Potentiostat used for electrochemical characterisation.*

Corrosion tests were done in sulphuric and hydrochloric acid, sodium, ferric and magnesium chloride solutions. The chemicals used were analytical grade supplied

by Associated Chemical Enterprises (ACE), South Africa. They were diluted to the desired concentrations using deionised water. These solutions are highly conductive; hence, no potential drop (IR) compensation was done. Fresh solutions, and samples were used for every test, and untreated 304L stainless steel was used as a control.

Unless stated otherwise, all tests were done at 25 ± 1°C under natural aeration and static conditions. Where stirring was necessary, a battery powered stirrer with a fixed speed on 900 rpm was used. Temperature was controlled by means of an insulated water bath with a thermostat, and was continuously monitored by a mercury thermometer. The surface alloyed samples were used as fabricated, without further processing. This was done to preserve the integrity of the ruthenium alloys. Where possible, at least two samples were tested, and a fresh sample was used for each test.

Post corrosion examination of the corroded surfaces was done using FESEM, stereo and optical microscopy. Where necessary, the corroded samples were cleaned prior to examination in an ultrasonic bath using ethanol.

Potentiostatic measurements

Open circuit potential (OCP) measurements were done to assess the thermodynamic stability of the surface alloyed stainless steel samples. They were done at zero applied current. Variations of OCP were recorded for periods ranging from 120 seconds to 72 hours.

Potentiodynamic polarisation

Prior to potentiodynamic polarisation, the samples were held at OCP until $\frac{dE}{dt}$ was 1 μV/s, which was typically at least 120 seconds. Polarisation was done at a scan rate of 0.5 mV/s from potentials cathodic vs OCP to anodic potentials. Passivation tendencies were deduced from the shapes of the polarisation curves, while corrosion rate were determined by Stern-Geary method as summarised in Section

2.5.1, and described in ASTM G102-89(2010). In this study, the values of β_a and β_c were assumed 100 mV/decade (Frankel 2008), such that the value of B in Equation 2-19 was 0.022 V.

Chronoamperometry

Chronoamperometric tests were used to study localised corrosion on the alloyed samples. The technique was also used to understand the stability of passive films. Current-time curves were recorded at different potentials in the passive region over periods ranging from 30 minutes to 24 hours.

Electrochemical impedance spectroscopy

For EIS measurements, the electrochemical cell was placed in a grounded Faraday cage. The measurements were done using the FRA module in the Metrohm PGSTAT 302 Autolab, and voltage amplitude of 10 mV. Unless stated otherwise, all EIS measurements were done at OCP. Quantitative analysis was done by fitting equivalent circuits to the data, and a fit was accepted as satisfactory when the estimated error was less than 10% (0.1).

Precision of the potentiostat

Corrosion of 304L stainless steel in 1 M sulphuric acid was used to confirm the precision, repeatability and reproducibility of corrosion measurements recorded by the potentiostat. Twenty-five experiments were done under the same conditions, and corrosion rates determined by Stern-Geary method. Results in Figure 3-5 show that reproducibility of the corrosion measurements was good; measured average was in agreement with that found in literature (Akgün et al. 1995). The percent error, calculated by Equation 3-5 was 0.3% for corrosion rate measurements, and 1.9% for corrosion potential.

$$\%\ Error = \left| \frac{Expected\ \ value - Measured\ value}{Expected\ \ value} \right| \times 100 \qquad \textbf{Equation 3-5}$$

Precision of the corrosion measurements was evaluated by standard deviation of the average (SDE) as described by Equation 2-27 (ASTM G16-95(2010)). SDE for the corrosion rate measurements was 0.06 mm/y, while that for corrosion potential was 3.18 mV, indicating close agreement in randomly selected results.

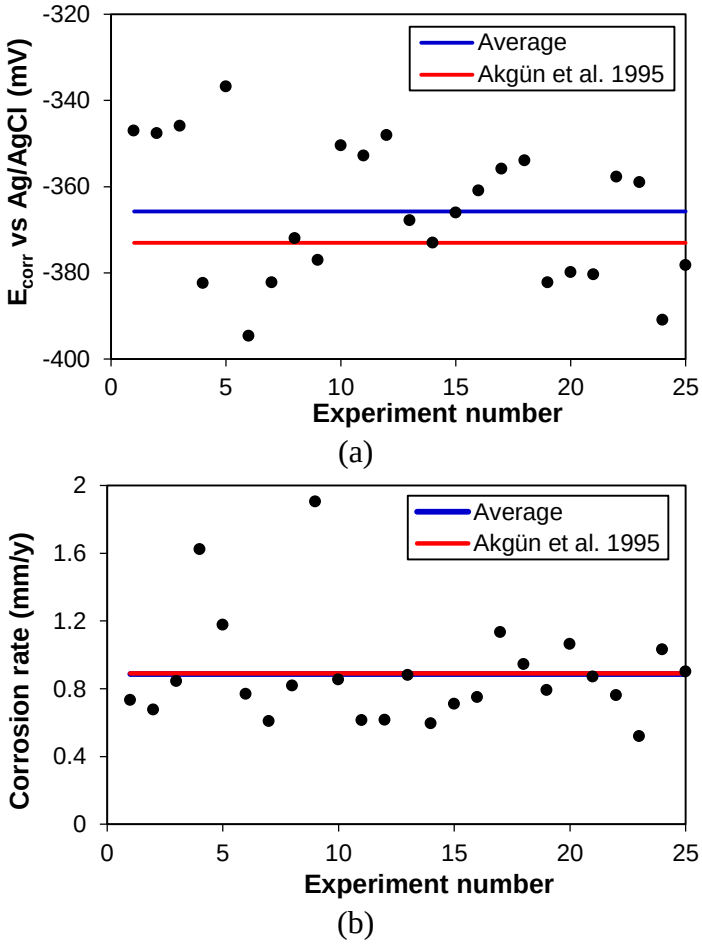

Figure 3- 5 *Reproducibility of the corrosion measurements. Average corrosion potential was -366 mV and corrosion rate was 0.89 mm/y.*

Given this analysis, it was assumed that the potentiostat used was precise in its measurements, and any deviations were due to the electrochemical behaviour of the samples.

Cell design

Two sample orientations were explored: a horizontal and vertical orientation as shown in Figure 3-6. Figure 3-7 presents the potentiodynamic polarisation curves obtained when 304L stainless steel was tested in 1 M sulphuric acid.

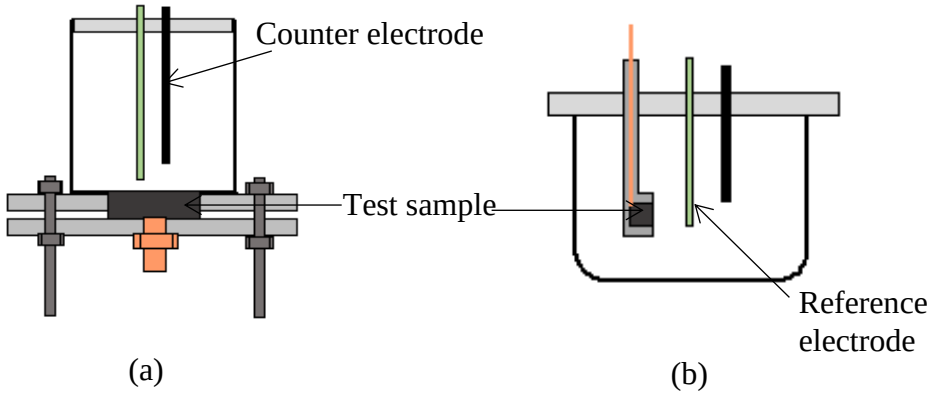

Figure 3- 6 *Schematics of the corrosion cells with the sample in (a) a horizontal and (b) a vertical orientation.*

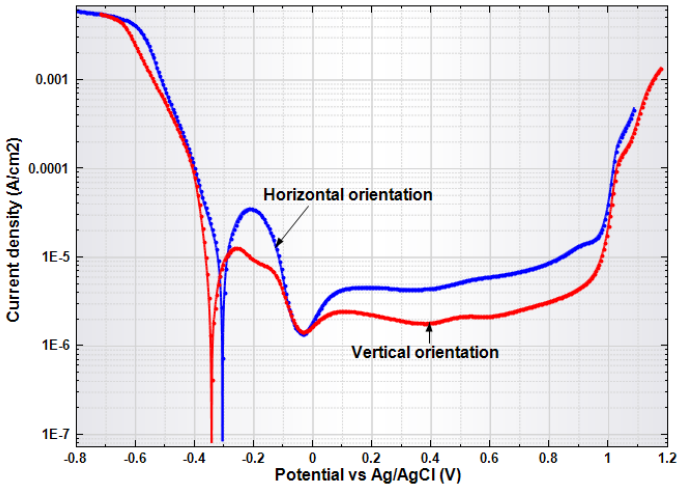

Figure 3- 7 *Effect of sample orientation on potentiodynamic polarisation curves of 304L in 1 M sulphuric acid.*

The curves obtained on the horizontally oriented samples exhibited high i_{crit} and i_{pass}, suggesting greater difficulty to passivate. This was consistent with the report by Hoyle and Taylor (1993) that particulate matter within the solution may deposit on a horizontal surface, and prevent the formation of a protective oxide film or disturb the film already formed. To ensure that the corrosion behaviour

recorded was due to the electrochemical reactions and not orientation of the sample, the vertical sample orientation was preferred for this work.

A horizontal electrochemical cell was designed at the University of the Witwatersrand, and manufactured by United Glass Blowers, South Africa. The cell, shown in detail in Figure 3-8, had an outer jacket through which water was circulated to control the temperature of the electrolyte.

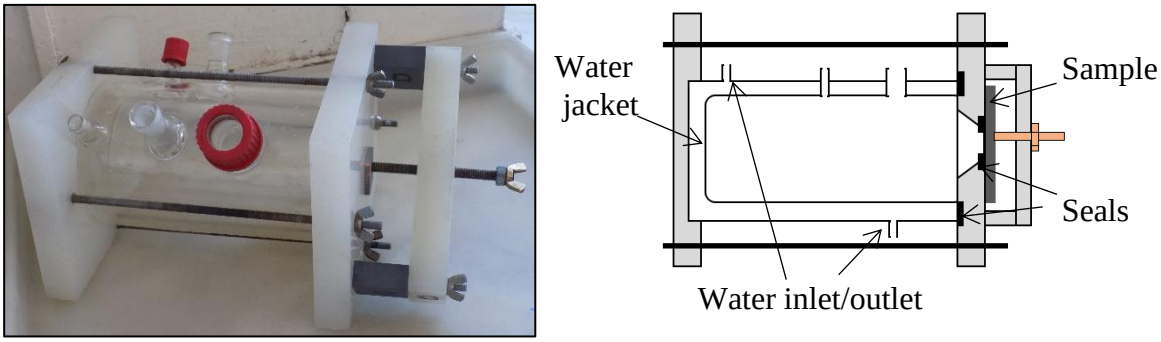

(a) (b)

Figure 3- 8 *Assembled corrosion cell (a) photograph, and (b) cross section.*

3.5.3 Non-electrochemical corrosion characterisation

Solution analysis

The chemical analysis of the corrosion solution was analysed by inductively coupled plasma mass spectroscopy (ICP-MS) and atomic absorption spectroscopy (AAS). Analysis by ICP-MS was done by Scrooby's Laboratory Services, while AAS was carried out at the University of the Witwatersrand using a 240FS AA from Agilent Technologies. Results obtained were used to corroborate the corrosion results obtained via electrochemical methods discussed in Section 3.5.2.

In most cases, chemical analysis was limited to iron, chromium and nickel; the major constituents of AISI 304L stainless steel. The solutions were aliquoted for at least 3 analyses to ensure repeatability. In all instants, fresh solution and deionised water were used as controls.

Chapter 4
Materials characterisation

4.1 Introduction

To appreciate the impact of this study, and hence qualify its success, the corrosion behaviour of pristine AISI 304L stainless steel was characterised in common electrolytes: sulphuric acid and sodium chloride. Chemical, mechanical as well as metallographic characterisation was also done, and the observed results compared to known and accepted values. This chapter presents the results of the characterisation exercise.

4.2 Results

4.2.1 Chemical composition

Table 4-1 presents the chemical composition of the AISI 304L stainless steel used in this work as verified by spark analysis. The results obtained were compared to the specifications listed in ASTM A240. In general, the composition of the supplied 304L stainless steel was within the limits specified in the ASTM A240. Molybdenum is not specified in ASTM A240, but was found to be in excess of 0.3 wt% in the supplied stainless steel alloy. This could imply that the pitting resistance of the present 304L stainless steel alloy was higher than that of the stainless steel specified in the ASTM standard.

Table 4- 1 *Composition of 304L stainless steel as received. A complete assay is presented in Table A-2.*

Element	Composition (wt%)	
	Supplied 304L	**ASTM A240**
Iron	70.60	Balance
Chromium	18.32	18-20
Nickel	8.20	8-12
Manganese	1.21	2 max
Silicon	0.44	1 max
Molybdenum	0.34	Not specified
Phosphorus	0.038	0.045 max
Carbon	0.03	0.03 max
Nitrogen	0.076	0.1 max
Sulphur	0.0062	0.03 max
Other	0.430	-

4.1.2 Microstructural analysis

The supplied 304L stainless steel was ground, polished and etched using oxalic acid, marbles solution and sodium hydroxide solution prepared as described in Table 3-2. Figure 4-1 shows the microstructures revealed by each etchant.

Both oxalic acid and marbles solution revealed a microstructure that was entirely austenitic. As observed from Figures 4-1(a) and (b), the stainless steel had a wide grain size distribution, which ranged from 69 to 384 μm. Twins were also observed from these micrographs. Etching with sodium hydroxide did not reveal any evidence of ferrite (Table 3-2), as can be seen in Figure 4-1(c). The micrographs were essentially featureless, except for elongated inclusions. EDS analysis of these inclusions or stringers (Figure 4-2) showed that they consisted of sulphur. Sulphur has low solubility in austenite and will exist as inclusions in the alloy (ASM Handbook 1985), possibly as manganese sulphide stringers.

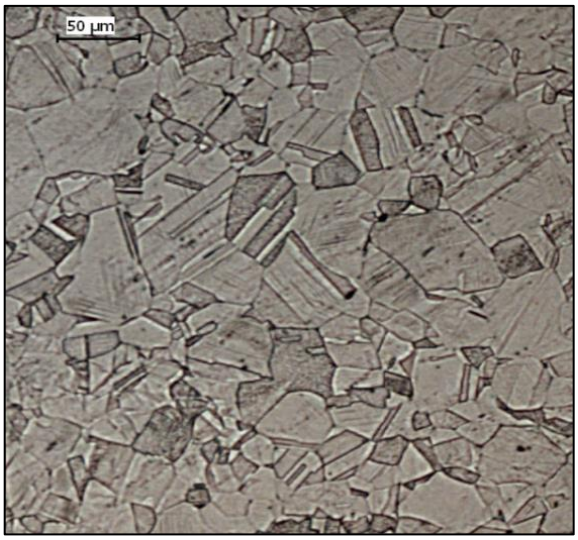

(a)

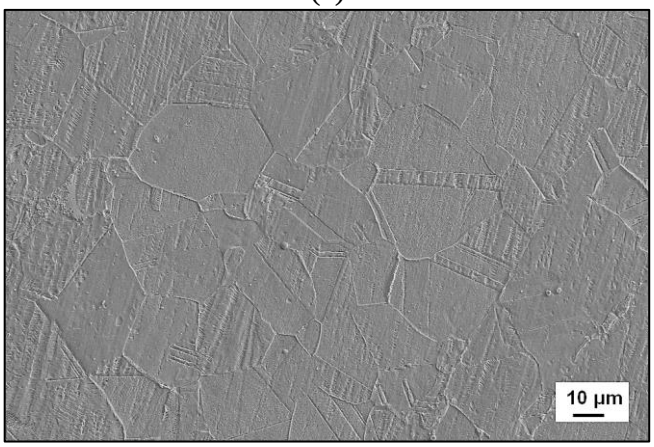

(b)

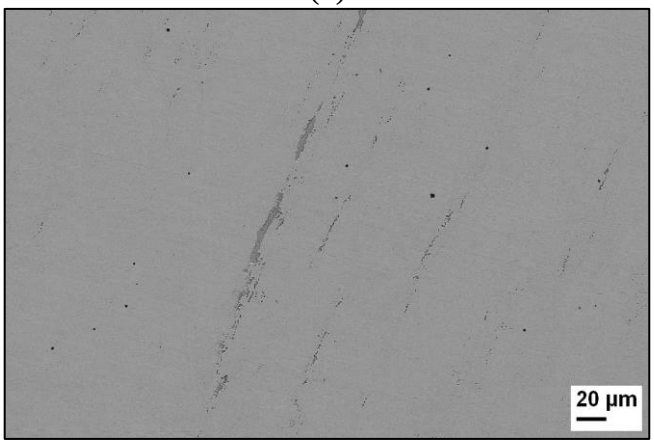

(c)

Figure 4- 1 *Microstructure of the 304L stainless steel as revealed by (a) oxalic acid using optical microscope, (b) marble's solution and (c) sodium hydroxide using FESEM.*

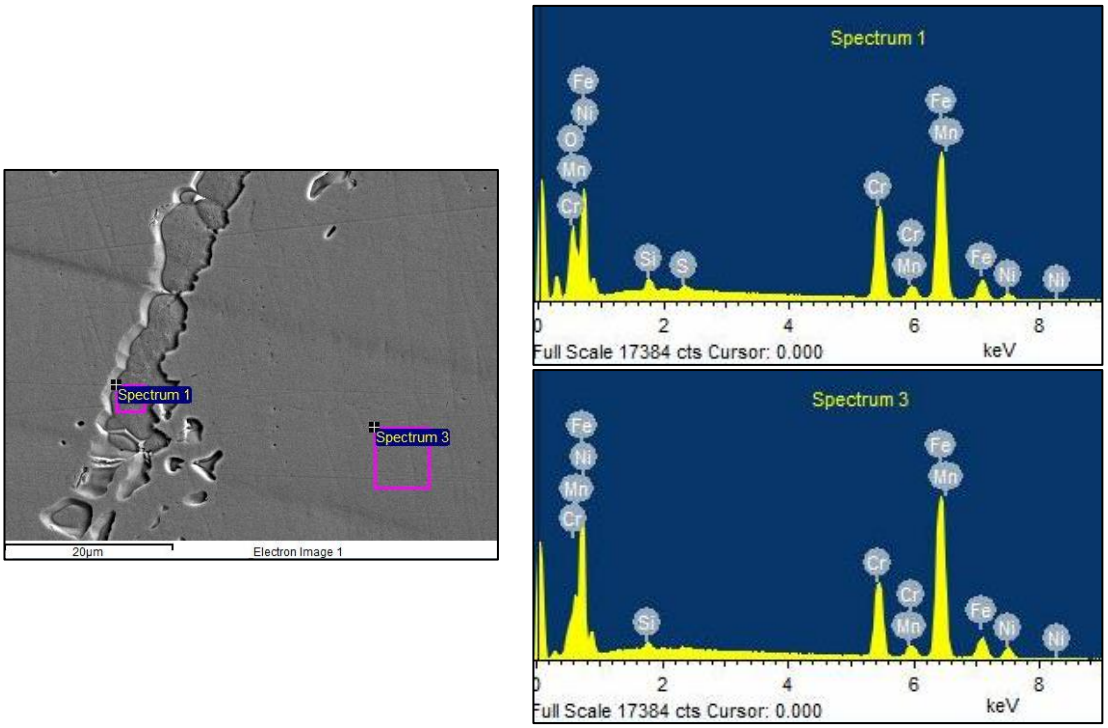

Figure 4- 2 *EDS analysis of the stringers observed in Figure 4-1(c).*

XRD analysis of the 304L stainless steel resulted in the spectrum in Figure 4-3. Peaks were detected at 2θ ≈ 51.05°, 59.60°, 89.48°, and 111.14°, and were matched to (111), (200), (220) and (311) of a face centred cubic (FCC) crystal structure according to PDF 04 002 1898. This indicates that the supplied stainless steel consisted entirely of austenite. These results are consistent with metallographic analysis in Figure 4-1(a) and (b).

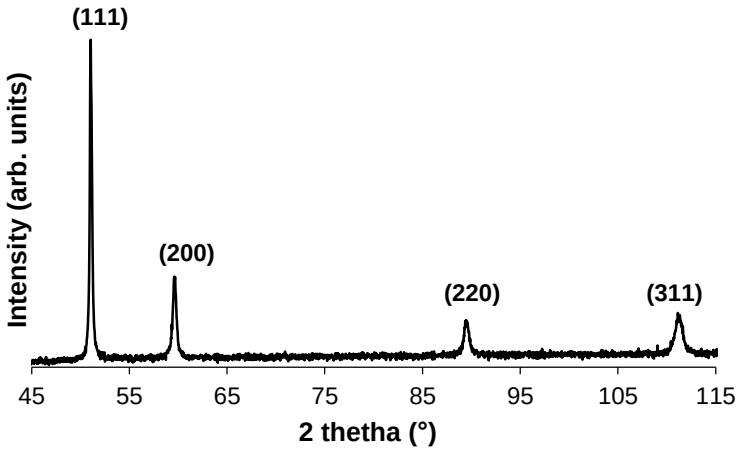

Figure 4- 3 *Typical XRD pattern of 304L stainless steel.*

4.2.3 Mechanical properties

The mechanical properties of the 304L stainless steel were investigated using tensile testing at room temperature. A typical stress-strain curve obtained from the tensile tests is presented in Figure 4-4. The curve exhibited continuous yielding, without a distinct transition from elastic to plastic deformation. This is consistent with ductile behaviour. Post-test examination of the failed specimens using a stereo microscope revealed that the fracture was preceded by appreciable necking and extensive shear lips, typical of ductile fracture. The images of the failed samples are presented in Figure 4-5.

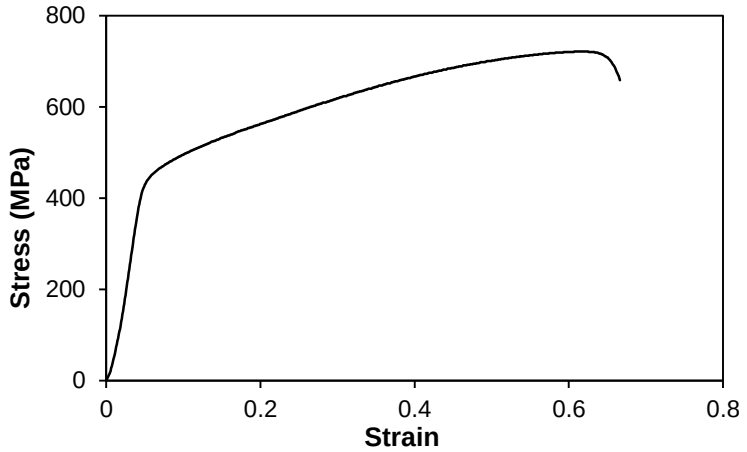

Figure 4- 4 *Typical stress-strain curve for the 304L stainless steel.*

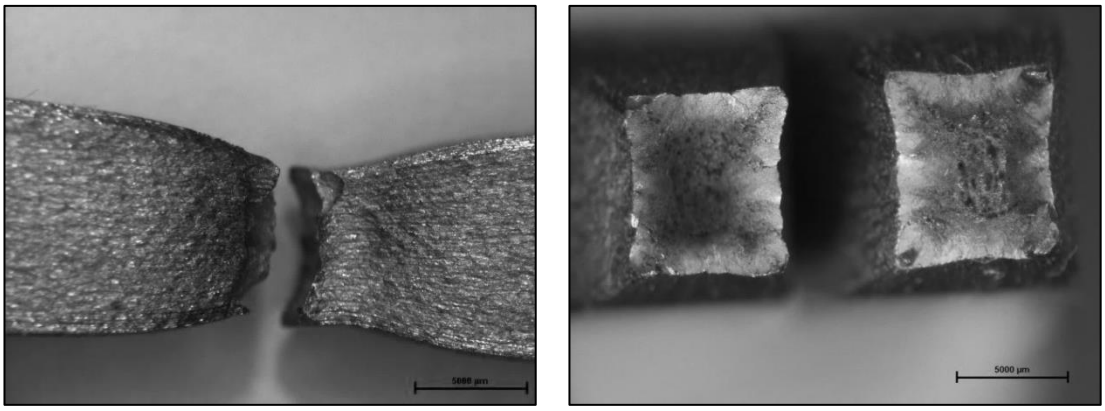

(a) (b)

Figure 4- 5 *Stereoscope images of failed specimen showing (a) necking and (b) cup and cone typical of ductile fracture.*

Table 4-2 summarises some of the properties derived from the stress-strain curves. The calculated values were well within the limits stated in literature.

Table 4- 2 *Mechanical properties of 304L stainless steel measured at room temperature.*

Property	**Calculated**	**Typical**
Tensile strength (MPa)	564.99 ± 16.00	550-590 (Lide 2005; Macsteel 2009)
0.2% Proof stress (MPa)	342.21 ± 1.45	200 min (EN 10088)
Elongation (% in 25mm)	74.15 ± 1.32	-
Young's modulus (GPa)	-	193-195 (Lide 2005)

4.2.4 Effect of surface preparation

304L stainless steel samples were prepared by progressively abrading their surfaces using silicon carbide as described in Section 3.2.1. The effect of surface preparation on corrosion rate and surface stress was studied.

Corrosion rate

An obvious effect of surface preparation was on surface roughness as shown in Figure 4-6. The consequence of this on corrosion rate is illustrated in Figure 4-7. Corrosion rates in 1 M sulphuric acid decreased from an average of 1.2 mm/y for the roughest sample (120 grit) to about 0.3 mm/y for the sample polished with 6 μm alumina powder.

Figure 4-7 also presents evidence that surface preparation had a significant effect on the precision and accuracy of the corrosion rate measurements. Apparently, the finer the surface finish of the 304L stainless steel samples, the better the precision of the measured values. Precision, in this case referred to the closeness of recorded measurements in replicated experiments, was indicated by the standard deviation error (SDE) as calculated by Equation 2-27. SDE for the roughest samples was 0.19 and polishing the stainless steel reduced SDE to ≈ 0.08,

implying better precision. This was attributed to improved surface homogeneity on the smoother surface.

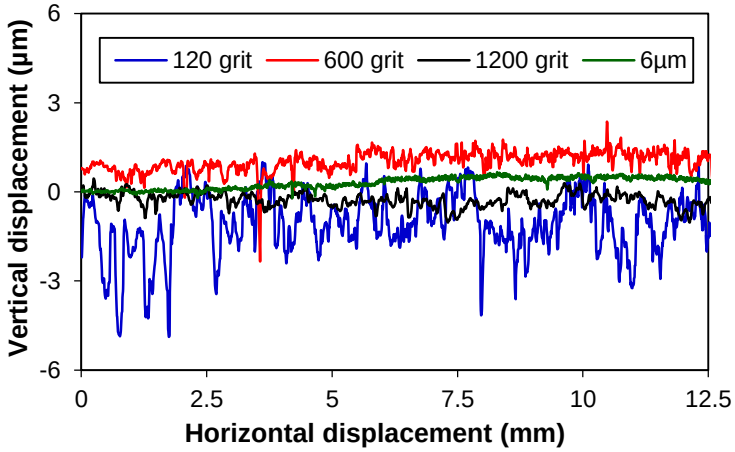

Figure 4- 6 *Influence of surface preparation on surface roughness.*

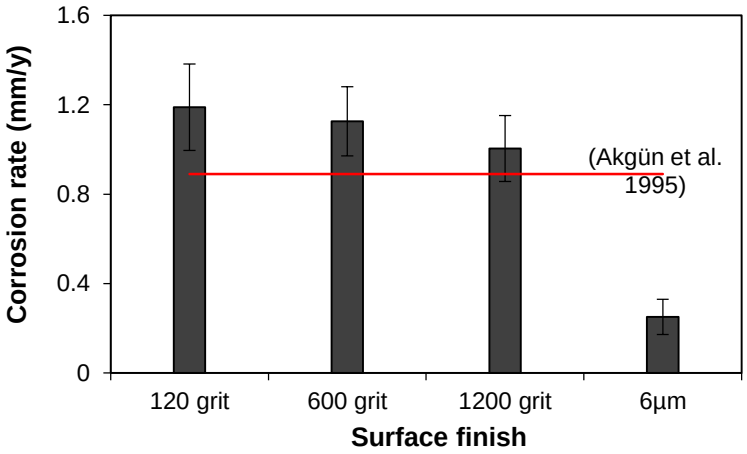

Figure 4- 7 *Effect of surface finish on precision and accuracy of measured corrosion rate of 304L stainless steel in 1 M sulphuric acid. At least 10 samples were tested for each condition.*

However, finely polishing the 304L stainless steel reduced the probability of accurately measuring corrosion rates to zero. Accuracy was defined as the ability to reproduce a known or documented value. As can be seen in Figure 4-7, measurements on the polished samples underestimated corrosion rate of 304L stainless steel in 1 M sulphuric acid by as much as 72%.

Surface stresses

Residual stresses generated during grinding and polishing of the 304L stainless steel samples were analysed using routine XRD and $Sin^2\psi$ technique.

Figure 4-8 presents the XRD diffractograms obtained on as received, ground (120 grit) and polished (6 µm) 304L stainless steel samples. For ease of analysis, only the (111) and (200) peaks are shown. As indicated in Figure 4-8 and Table 4-3, surface preparation shifted the peaks to lower Bragg angle. This is consistent with the generation of compressive stresses in the surface. The shift in the Bragg angle was most significant on the polished samples. Polishing reduced the Bragg by as much as 1.8% compared to 0.6% caused by grinding to 120 grit only. It is apparent that higher compressive stresses were generated during polishing.

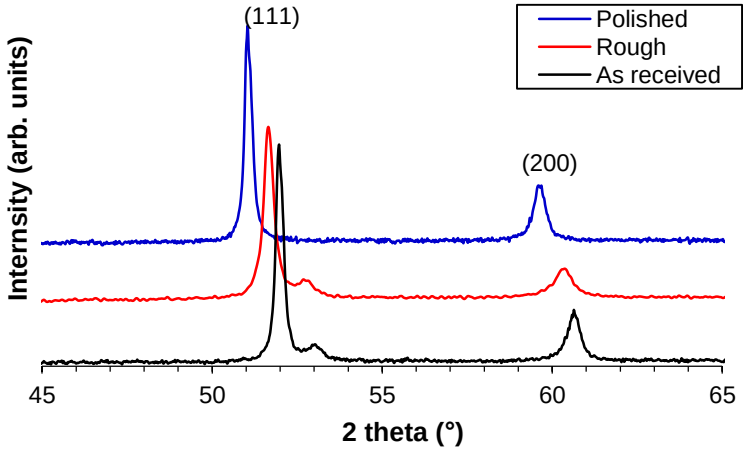

Figure 4- 8 *Effect of surface preparation on the Bragg angle of peaks (111) and (200) peaks.*

Table 4- 3 *Variation of Bragg angle and strain with surface preparation.*

Sample condition	**Bragg angle (°)**		**Strain**	
	(111)	**(200)**	**(111)**	**(200)**
As received	51.97	60.64	-	-
Rough (120 grit)	51.65	60.37	-0.004	-0.003
Polished (6 µm)	51.05	59.60	-0.013	-0.010

An extra peak was detected at ≈ 52.82° for the as received and rough 304L stainless steel samples (Figure 4-8). This peak was matched to (110) of a body

centred cubic (BCC) crystal structure, and suggested the presence of ferrite in the stainless steel; contradicting the findings in Figure 4-1. The peak, however, disappeared upon polishing.

The stresses generated because of surface preparation were further analysed with the $Sin^2\psi$ method. Figure 4-9 shows the typical ε vs $sin^2\psi$ plots obtained, while Figure 4-10 presents the residual stresses calculated from these plots. The ε vs $sin^2\psi$ plots measured on the as received 304L stainless steel samples exhibited oscillatory behaviour. Such behaviour indicates that the surface had inhomogeneous stress distribution. Surface preparation increased surface homogeneity and the ε vs $sin^2\psi$ plots (Figures 4.9(b) and (c)) became increasingly linear.

Least square lines fitted to the data obtained on the ground and polished samples had negative slopes. This is consistent with compressive residual stresses. Residual stresses are directly proportional to the gradient of ε vs $sin^2\psi$ plots (Noyan & Cohen 1987). A close examination of Figures 4-9(b) and (c) reveals that the magnitude of the gradient obtained on the polished samples was larger: ≈ 4.3 compared to 3.2 for the rough samples. The implication is that higher compressive stresses were generated during polishing. These results corroborate the findings recorded in Figure 4-8.

Residual stresses determined via the $Sin^2\psi$ method are given in Figure 4-10. The results show that the supplied stainless steel already had compressive residual stresses in the order of ≈ 100 MPa. Surface preparation increased compressive surface stresses to almost 340, and 575 MPa for the roughened and polished samples respectively.

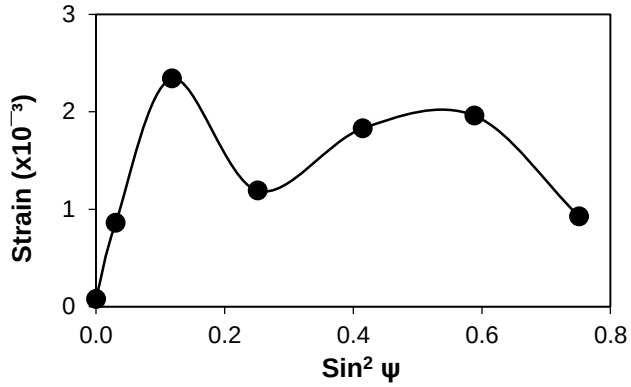

(a)

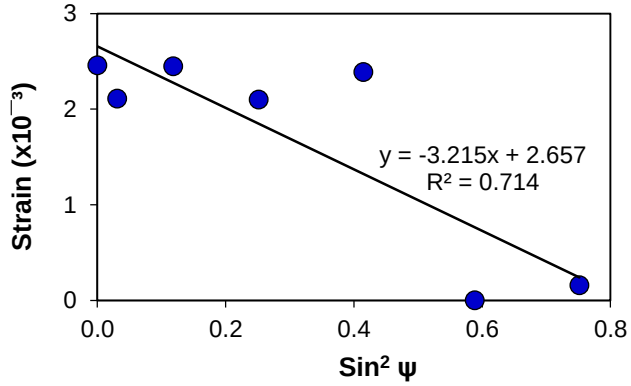

(b)

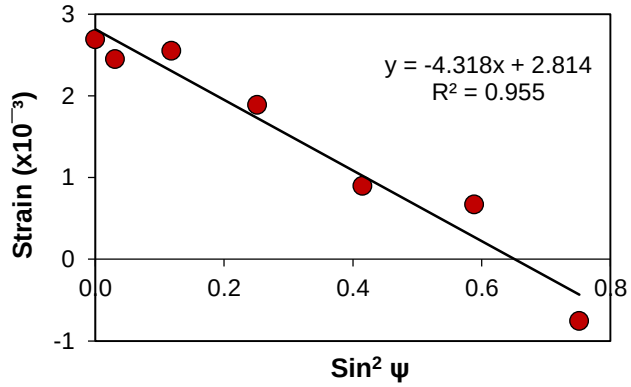

(c)

Figure 4- 9 *Strain vs sin²ψ plots for (a) as received (b) ground to 240 grit and (c) polished 304L stainless steel.*

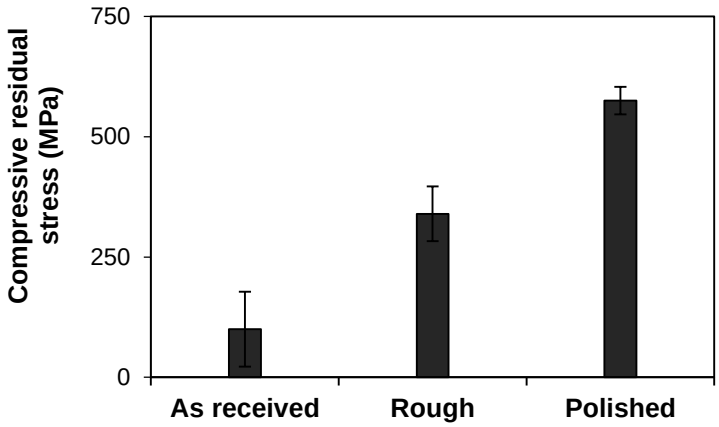

Figure 4- 10 *Residual stresses in 304L stainless steel samples as a function of surface preparation.*

4.2.5 Corrosion characterisation

Corrosion characterisation of the supplied 304L stainless steel was studied in 1 M sulphuric acid and in 3.5 wt% sodium chloride. Prior to corrosion, the conductivity of the solutions was measured by a probe-type conductivity meter. The conductivity of 3.5 wt% sodium chloride and 1 M sulphuric acid were found to be 55.4 ± 1.1 and 397.8 ± 2.4 mS/cm respectively.

Corrosion in sulphuric acid

Figure 4-11 shows the curve obtained when 304L stainless steel was potentiodynamically polarised in 1 M sulphuric acid. The curve exhibits features typical of active-passive metals: an anodic peak and a passive region as well as a transpassive region at potentials close to 1000 mV vs Ag/AgCl.

Examination of the passive region revealed that it was characterised by two current plateaux. The first plateau, labelled 1 in Figure 4-11 extended from E_{pass} to about 200 mV vs Ag/AgCl, while the second one was observed between 200 and 600 mV. Current density values recorded on the second plateau were as low as 0.91 μA/cm² compared to ≈ 1.26 μA/cm² at the lower potentials. Passivity is caused by the presence of a protective layer or film. Therefore, the variation of the current density in the passive region suggests a change in either the structure or the chemical composition of the protective layer. The passive layers formed above

200 mV seemed to be more protective than those produced at potentials < 200 mV.

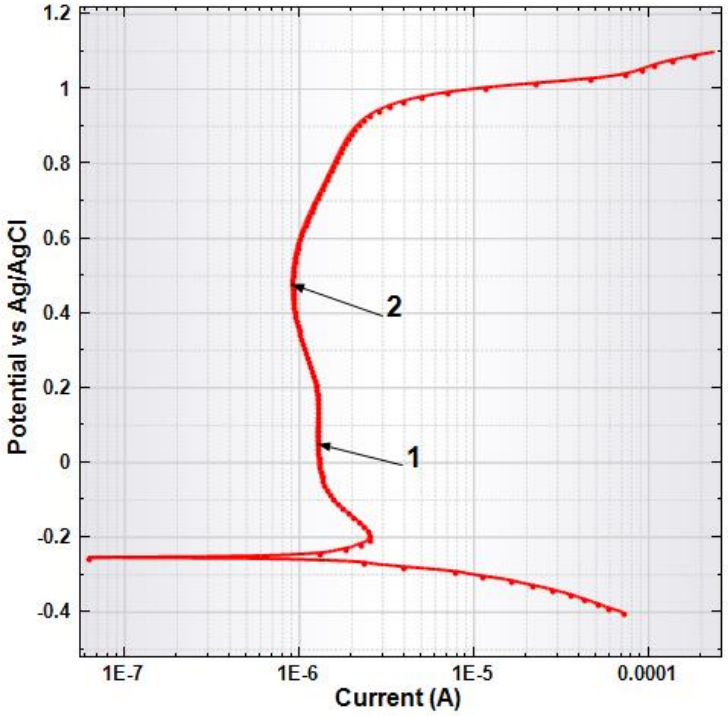

Figure 4- 11 *Potentiodynamic polarisation curve for 304L stainless steel exposed to 1 M sulphuric acid at room temperature.*

304L stainless steel samples were held at potentials in the ranges marked 1 and 2 in Figure 4-11 for 24 hours in 1 M sulphuric acid. After the exposure period, the corrosion solution was analysed by AAS for iron content. Solutions collected at potentials 200 mV vs Ag/AgCl had an iron content of ≈ 1.64 ± 0.02 mg/l, at least 23% more than the iron content in the solutions collected at higher potentials. This is consistent with the presumption that the films formed in these potentials had different protection capabilities. The iron content values recorded at these potentials were much lower than the 12 mg/l reported at OCP.

EIS was done above and below 200 mV vs Ag/AgCl. The Nyquist plots obtained are presented in Figure 4-12(a), where the solid lines are the fit obtained from simulations using the equivalent circuit in Figure 4-12(c). Data extracted from these simulations is presented in Table 4-3, where R_p was used to represent film resistance R_f. Curves in Figure 4-12(a) are semi-circular, suggesting that the

corrosion processes in these potentials; regions were charge transfer limited as opposed to mixed control at OCP (Figure 4-12(b)).

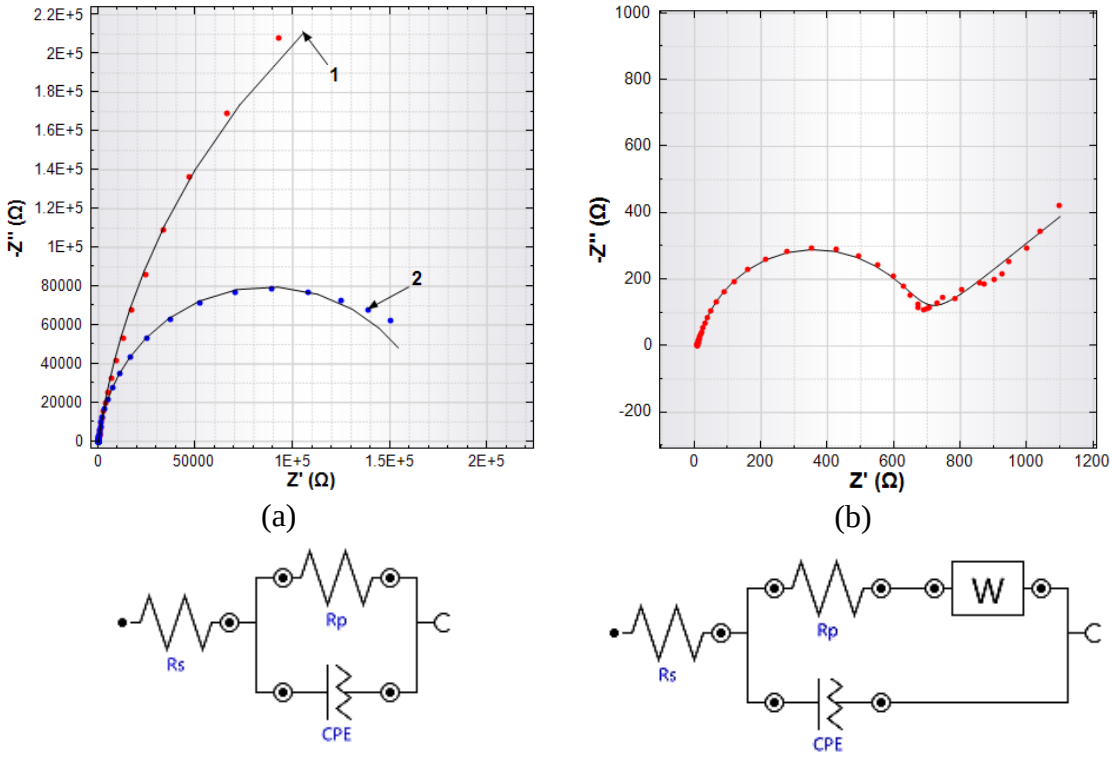

Figure 4- 12 *Nyquist plots of 304L stainless steel in 1 M sulphuric acid at (a) potential ranges 1 and 2 in Figure 4-11, and (b) OCP. Simulation of data in (a) and (b) was done using equivalent circuits in (c) and (d) respectively.*

Table 4- 4 *Electrochemical parameters obtained from EIS tests. *Estimated error in fitting equivalent circuit to data.*

Potential range	n	R_f (kΩ.cm²)	CPE (µF.cm)	C (µF)
< 200 mV (1)	0.913	726	47.8	67.1
	**0.11%*	*4.35%*	*0.47%*	
> 200 mV (2)	0.944	174	25.3	27.6
	0.13%	*1.11%*	*0.59%*	

The radii of the semicircles in Figure 4-12(a) are large, as shown by the R_f values in Table 4-4, and point to slow electron transfer processes and high corrosion resistance. Increasing potential to above 200 mV vs Ag/AgCl decreased the radius of the spectrum. This could be due to at least one of the following: (1) decrease in

corrosion resistance, (2) reduction in the thickness of the films formed at higher potentials or (3) faster electron transfer processes.

Current densities reported in Figure 4-11, and the iron content measured by AAS are inconsistent with reduced corrosion resistance. Therefore, it is unlikely that the decrease in the Nyquist radius with increase in potentials is due to reduced corrosion resistance. In addition, corrosion rates at these potentials are expected to be reduced by passivation.

CPE values in Table 4-4 were converted to capacitance using Equation 4-1, where *C* is capacitance (Hirschorn et al. 2010). From Equation 2-24, capacitance is inversely proportional to film thickness. This, and the results in Table 4-3 imply that the films formed at potentials > 200 mV vs Ag/AgCl were thicker than those formed at lower potentials; consistent with the expectation that passive film thickness on stainless steels increases with potential (Olefjord & Elfstrom 1982; Olsson & Landlot 2003). From Table 4-4, it can be seen that the *CPE* coefficient, *n*, approached 1 at higher potentials, suggesting increased surface homogeneity (Orazem & Tribollet 2008), which could also be responsible for increased protectiveness at these potentials.

$$C = CPE^{\frac{1}{n}} \times R_f^{\frac{1-n}{n}} \qquad \textbf{\textit{Equation 4-1}}$$

The decrease in the radius of the Nyquist curve in Figure 4-12(a) at higher potentials could be due to faster electron transfer processes. Figure 4-13(a) presents the log*i*-log*t* plots obtained potentiostatically at the two potential ranges. The area under these plots gives the total amount of charge needed for the formation of the passive films, while the slopes are indicative of the rate of passivation (Haruyama 1990; Flis & Kuczynska 2004).

It can be seen from Figure 4-13(a) that a larger electronic charge was associated with the formation of the passive film at potentials > 200 mV vs Ag/AgCl (marked 2 in Figure 4-11), confirming the findings of the EIS tests. At potentials > 200 mV, the gradient was initially about -0.45, and remained almost constant for the first 1000 s. At lower potentials, the gradient was initially -0.58, suggesting faster rates of passivation. Examination of the curve reveals that the

gradient changed dramatically after about 290 s from -0.58 to -1.36. Slopes larger than -1 are usually ascribed to the precipitation of salts (Flis & Kuczynska 2004). It is likely that the film responsible for passivation at potentials < 200 mV possibly contained iron sulphate.

After longer exposure times, the current densities stabilised at around 87 and 38 nA/cm² for the films grown below and above 200 mV vs Ag/AgCl respectively. This implies that the films produced at higher potentials were more protective, consistent with the current densities reported in Figure 4-11, and iron content results reported earlier.

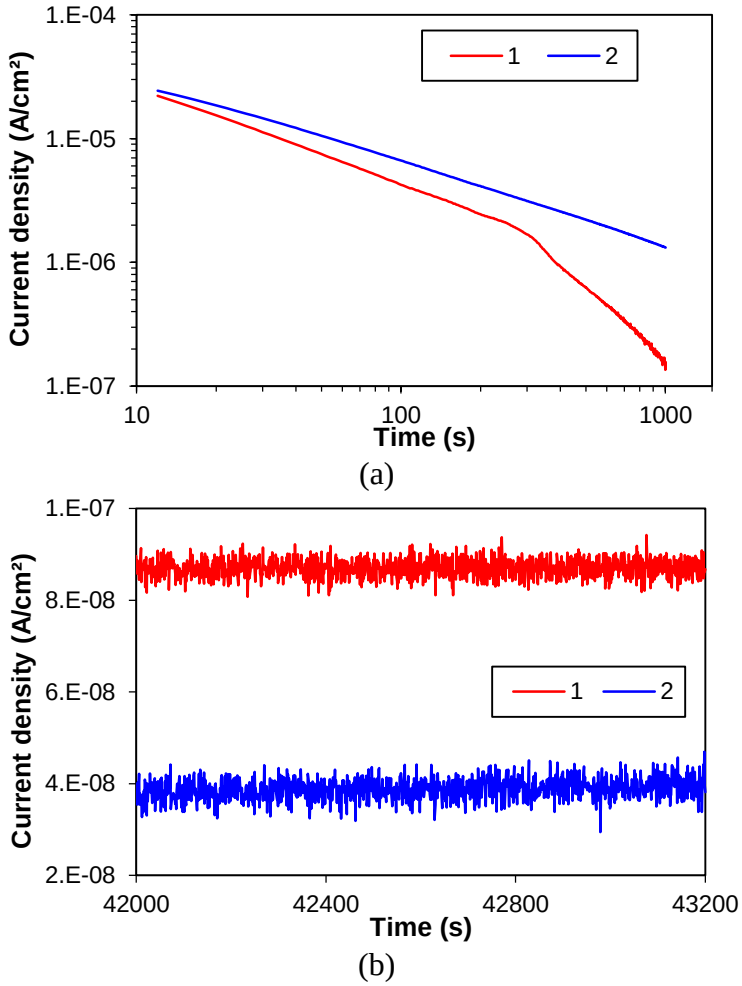

Figure 4- 13 *Chronoamperometric measurements on 304L stainless steel exposed to 1 M sulphuric acid over 12 hours at the potential ranges 1 and 2 in Figure 4-11. Graphs show measurements in the (a) first 1000 s, and (b) last 1000 s of the experiment.*

Figure 4-11 shows that the onset of transpassive corrosion was around 950 mV vs Ag/AgCl. This is consistent with the transpassive potentials reported in Figure 2-3 (≈ 1200 mV vs SHE). Transpassive behaviour was preceded by a gentle increase in current density. Transpassive corrosion is a usually ascribed to the oxidative dissolution of chromium oxide. The fact that the transition from passive to transpassive regions in Figure 4-11 is not abrupt, suggests the presence of more than just chromium oxide in the passive film. Passivation at these potentials is likely maintained by other oxides or similar species, which completely dissolve at ≈ 950 mV leading to transpassive corrosion. Several researchers (Haupt & Strehblow 1995; Olsson & Landolt 2003), showed that at higher potentials, the passive films formed on stainless steel consisted mainly of chromium (III) and iron (III) species.

Corrosion surfaces obtained when 304L was exposed to 1 M sulphuric acid are shown in Figure 4-14. The surface in Figure 4-14(a) was characterised by corrosion grooves. These grooves are typically initiated by the selective leaching of iron, and propagated by cathodically produced hydrogen bubbles that ascend, burst and rupture any protective films formed on the surface (Richardson 2010). Preferential dissolution of iron was also observed by Haupt & Strehblow (1995) on Fe-15Cr and Fe-20Cr stainless steels in sulphuric acid. In some instances, the corrosion surfaces exhibited signs of uniform corrosion. Figure 4-14(b) shows similar attack of the grain and the grain boundaries. However, the triple junctions where three grains meet were characterised by round regular shaped pits.

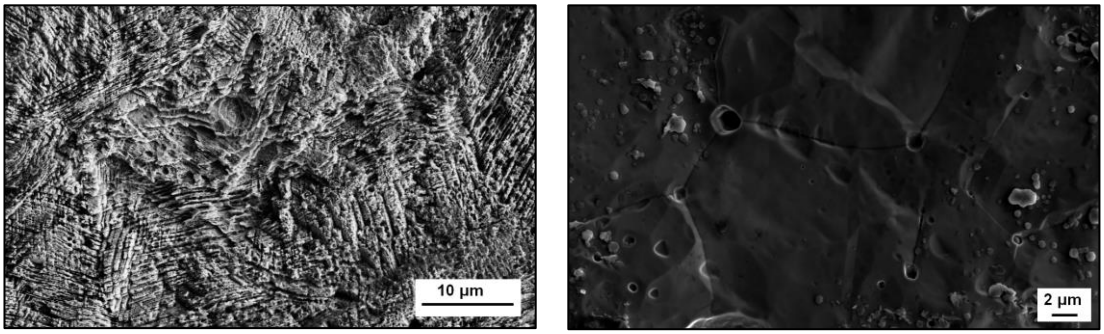

(a) (b)

Figure 4- 14 *Typical corrosion surfaces obtained when 304L stainless steel was exposed to 1 M sulphuric acid, and examined by FESEM-SE.*

Some of the stainless steel samples had corrosion products deposited on their surfaces. These products were carefully scrapped off, placed on carbon tape and analysed by EDS. The results, presented in Figure 4-15 show that the corrosion products consisted predominately iron, sulphur and oxygen. It is likely that these products were ferrous sulphates.

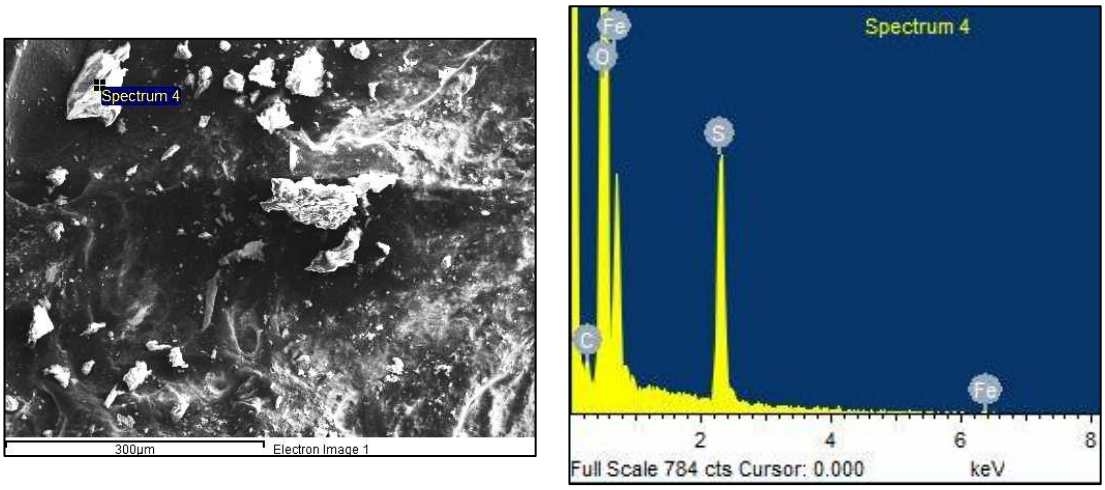

Figure 4- 15 *EDS analysis of the corrosion products deposited on 304L stainless steel exposed to 1 M sulphuric acid.*

Corrosion in sodium chloride solutions

Presented in Figure 4-16 is the potentiodynamic polarisation curve for 304L in 3.5 wt% sodium chloride. The curve exhibited typical active-passive behaviour, indicating that the stainless steel was able to passivate in the solution. However, the passive region was quite narrow, with the onset of transpassive corrosion at about 400 ± 23 mV vs Ag/AgCl. The E_{trans} potentials were way below the oxygen evolution potential, suggesting that 304L stainless steel experienced pitting under the test conditions. This is in agreement with the current transients observed between 0 and 400 mV, which are typically associated with incidents of localised corrosion (Schumki 2002).

Above 400 mV, the curve exhibited evidence of pseudo passivity at current densities of ≈ 5.5 mA/cm^2. In this region, current became independent of potential. The occurrence of pseudo passivity suggests a possible deposition and build-up of slightly protective corrosion products on the 304L stainless steel

surface. These products are typically thick, porous and could be iron hydroxide (Codd et al. 1970).

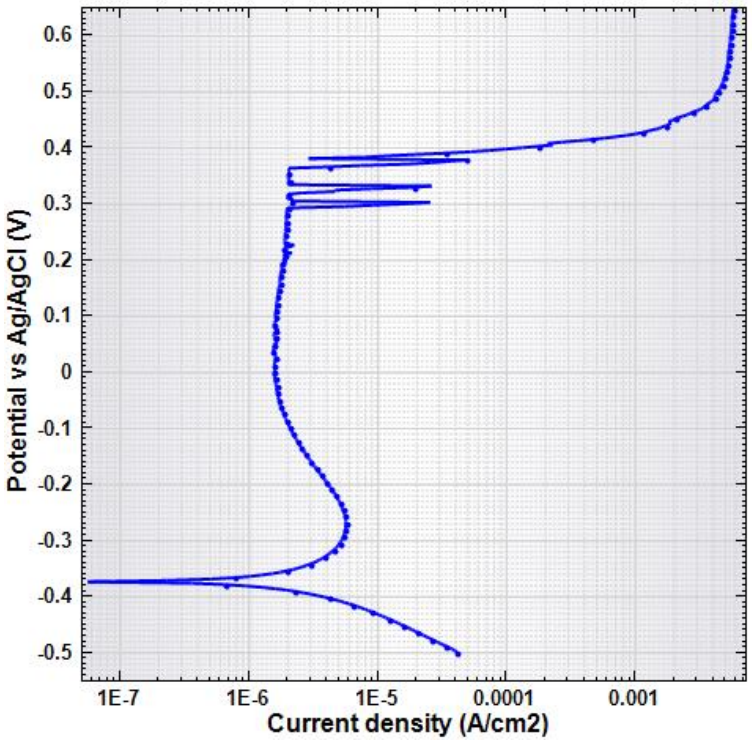

Figure 4- 16 *Potentiodynamic polarisation curve for 304L stainless steel exposed to 3.5 wt% at ≈ 25°C.*

Current-time curves measure potentiostatically at 0 and 350 mV are presented in Figure 4-17. The curve obtained at 0 V (Figure 4-17(a)) was characterised by abrupt peaks in current density. These perturbations are typical of metastable pitting, during which a number of pit growth events are initiated, but pits immediately repassivate, as conditions in the newly formed pits are insufficient for stable pit growth (Dawson & Ferreira 1986; Schumki 2002). Current densities at this potential were quite low; in fact, they were in the same order of magnitude as i_{pass}. This confirms that conditions favoured tendency to repassivate rather than to pit.

Current densities at 350 mV were much larger (≈ 782 μA/cm^2), indicating higher dissolution rates. At this potential, the strong oscillations recorded at 0 V were not observed. The current density increased steadily with time instead, suggesting stable pit growth and reduced tendency for the metal to repassivate.

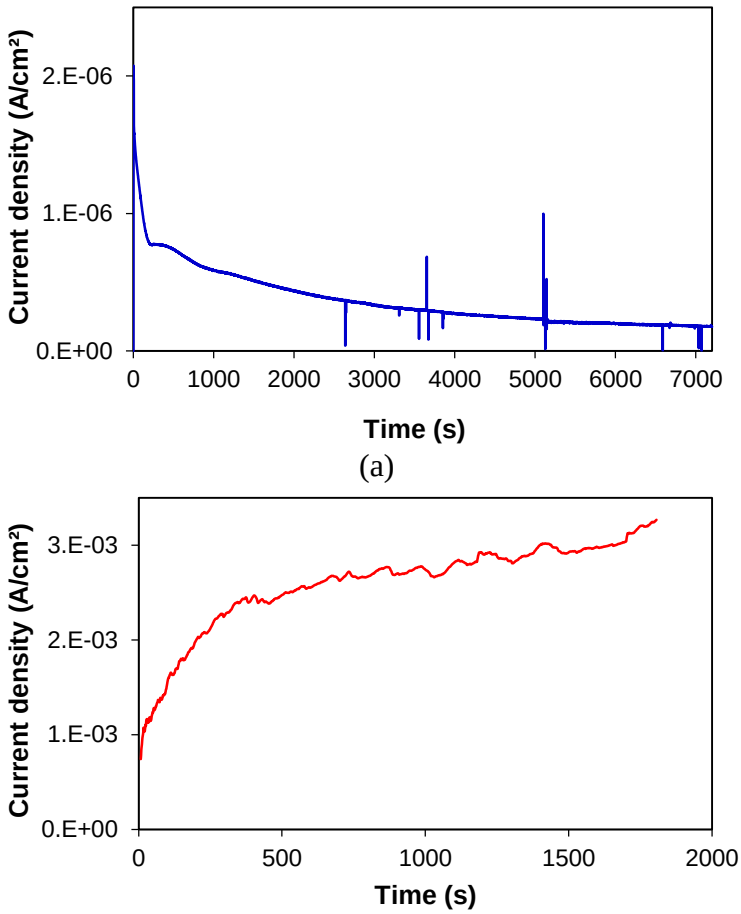

Figure 4- 17 *Current-time curves obtained when 304L stainless steel was exposed to 3.5 wt% sodium chloride at (a) 0 V, and (b) 350 mV vs Ag/AgCl.*

Post corrosion examination of the 304L stainless steel exposed to 3.5 wt% sodium chloride was done using the FESEM and optical microscope. The resulting images are illustrated in Figures 4-18 and 4-19, and revealed randomly oriented shallow pits. These pits were elongated and irregular in shape, and some had a lacy metal covering. Inside some pits, a semi-continuous network of undissolved stringers were observed (Figure 4-19(a)). The stringers were presumed to be the manganese sulphide inclusions reported in Figure 4-1(c). Cross section examination of the pits revealed that pitting progressed by undercut, and grew lengthwise. No visible films were observed on the samples.

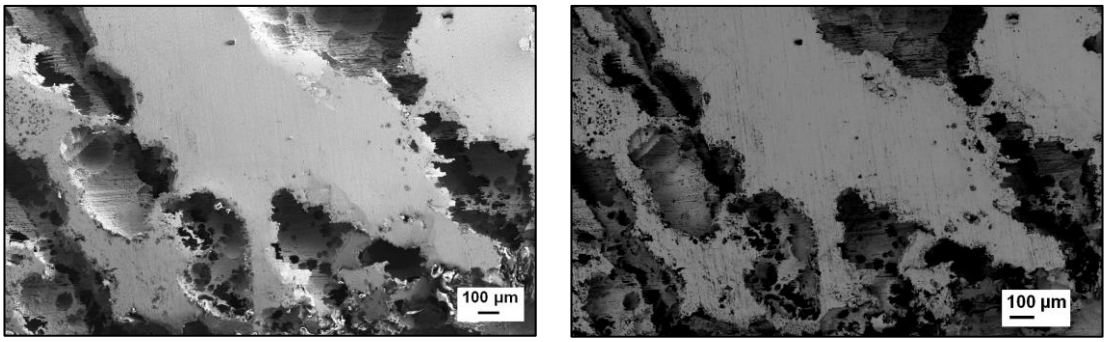

(a) (b)

Figure 4- 18 *Morphology of pits formed on 304L stainless steel exposed to 3.5 wt% sodium chloride, as examined by (a) FESEM-SE and (b) FESEM-BSD.*

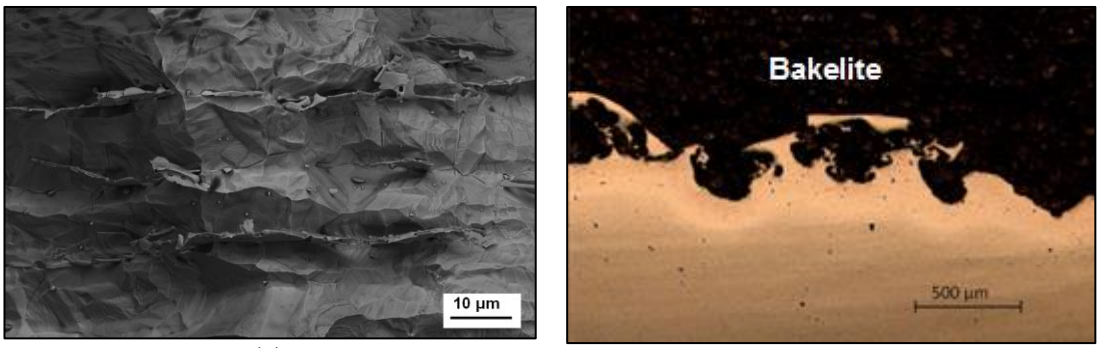

(a) (b)

Figure 4- 19 *Features of the pits grown in 3.5 wt%. (a) Interior of the pits as examined by FESEM-BSD and (b) cross section viewed with an optical microscope.*

4.3 Discussion

Chemical composition of the supplied 304L stainless steel was found to be consistent with ASTM A240. The stainless steel however had ≈ 0.3wt% molybdenum, an element known to have beneficial effects on pitting resistance (Mischler et al. 1991; Jargelius-Pettersson & Pound 1998; Olsson & Landolt 2003). The impact of the 0.34 wt% molybdenum on the pitting resistance of the supplied 304L stainless steel was determined by calculating its PREN by Equation 2-12, and comparing it to that of the alloy prescribed by ASTM A240 in Table 4-5.

Table 4- 5 *Effect of molybdenum on PREN of supplied 304L stainless steel.*

Alloy	Chromium (wt%)	Molybdenum (wt%)	Nitrogen (wt%)	PREN
Present 304L	18.32	0.34	0.076	21.72
ASTM A240	18.00	0	0.10	21.00

As can be seen in Table 4-5, the presence of 0.34 wt% molybdenum caused a marginal difference in the pitting resistance of the two alloys, and therefore it could be presumed that they were similar. By inference, their corrosion behaviour and mechanical properties were assumed comparable. This allowed for comparison of the results obtained in this work to those cited in literature, provided the chemical composition of the cited 304L stainless steel conformed to that prescribed by ASTM A240.

Metallographic analysis of the stainless steel showed an alloy composed entirely of austenite. Yet XRD measurements suggested the presence of ferrite. Retained ferrite in austenitic stainless steels was previously reported by some researchers, and was shown to reduce pitting resistance in chloride solutions (Manning et al. 1980; Ibrahim et al. 2009; Sadeghpour et al. 2013). The appearance of the ferrite peak seemed dependent on surface preparation. In Figure 4-8, the peak disappeared upon polishing, indicating a possible deviation in crystallographic orientation.

Close examination of the micrographs in Figure 4-1(a) and (b) showed evidence of twins. Twins in FCC metals are typically a consequence of annealing (Deiter 1986). This suggests that the supplied 304L was annealed, possibly after cold work. Annealing causes the formation of randomly orientated new crystallites, resulting in crystallographic texture. Since the chemical composition of the stainless steel was not altered, it is likely that polishing caused preferential orientation, and hence the disappearance of the (110) ferrite peak.

Surface preparation had a marked influence on the corrosion rate of 304L stainless steel; corrosion rates increased with increase in surface roughness. Li and Li (2006) attributed this trend to a decrease in electron work function. They showed

that rougher surfaces lose electrons with much more ease than smoother ones, resulting in higher corrosion rates.

The experiments to determine the effect of surface preparation on corrosion rates were done in 1 M sulphuric acid, in which the predominant cathodic reaction is the evolution of hydrogen by Equation 2-2. The rate of this reaction depends on the hydrogen overpotential of the surface. Roughening of a surface reduces its hydrogen overpotential, and improves the catalytic activity of a surface leading to faster hydrogen evolution (McGill 1990; Revie & Uhlig 2008). Consequently, the rate of the coupled anodic reaction will be faster resulting in enhanced corrosion. The trend observed in Figure 4-7 may also be attributed to the fact that film growth on stainless steel is easier on smooth surfaces than on rough ones because a much smaller film initiation network is required (Hoyle & Taylor 1993).

Results presented in Figure 4-7 indicated that increasing surface fineness improved precision of the measured corrosion rate values. For smoother more homogeneous surfaces, the anodic and cathodic reaction are likely to be distributed over all surface segments (Bagotsky 2006), and the corrosion rates thus measured will be consistently repeatable. However, polishing 304L stainless steel presented a zero probability of accurately estimating the corrosion rates. The best combination of precision and accuracy was obtained on samples ground to 1200 grit. As such, for corrosion test on unmodified 304L stainless steel in this work, surfaces were ground to 1200 grit to ensure repeatability and reproducibility.

Crystallographic orientation could have also played a significant role in the trend recorded in Figure 4-7. A study by Kumar et al. (2005) showed that: (1) the orientation of closely packed crystallographic planes parallel the surface improved passivation, and (2) changes in crystallographic orientation minimised corrosion by reducing sites favourable for corrosion attack. For FCC metals, the {111} planes are the most closely packed, and from Figures 4-2 and 4-7, the (111) reflection was the most intense.

Stresses induced during surface preparation were found to be compressive in nature. The compressive stresses reached a maximum value of ≈ 575 MPa. While

these values were in the same order of magnitude as the strength of the 304L stainless steel in tension (Table 4-2), they were consistent with those reported by Tomlism and Carroll (1990). Compressive stresses are generally beneficial to material performance.

The 304L stainless steel was exposed to 1 M sulphuric acid and 3.5 wt% sodium chloride. In both solutions, the supplied stainless steel exhibited typical active-passive behaviour. Passivation in these solutions is facilitated by water as a source of oxygen, and is established through the formation of chromium/iron oxides, ferrous sulphate or ferric/ferrous hydroxides (Codd et al. 1970; Fontana 1986; Stypula & Banas 1993; Schmuki 2002).

In sulphuric acid, chronoamperometric measurements suggested that the nature and protectiveness of the films produced on the stainless steel surface changed with potential and exposure time. This is consistent with previous reports (Olsson & Landlot 2003; Schmuki 2002), which emphasised that the composition and thickness of passive films vary with potential and exposure time. X-ray photoelectron spectroscopy (XPS) analysis by Haupt & Strehblow (1995) of passive films grown in 0.5 M sulphuric acid showed that iron (II) content increased with decrease in potential, while chromium (III) accumulated with increase in potential and exposure time. Chromium (III) species are more protective than iron (II) corrosion products.

In sodium chloride, metastable pitting was observed at potentials as low as 0 V vs Ag/AgCl. Pit initiation typically occur at surface inhomogeneities such as inclusions, precipitates, grain boundaries and dislocations (Schmuki 2002), and occurs via localised thinning of the passive film due to the intrusive chloride ions. At higher potentials (≈ 350-400 mV vs Ag/AgCl), pit growth occurred, indicated by an increase in current density in Figure 4-17(b). As can be seen in Figure 4-18, the pits were elongated in shape, and are likely to have initiated from the manganese sulphide stringers in Figures 4-1(c) and 4-19. Dissolution of manganese sulphide generates sulphur, which in turn promotes active dissolution of alloys via the formation of acidic species such as sulphuric acid and hydrogen sulphide (Wranglén 1974; Pardo et al. 2008).

Corrosion parameters obtained from potentiodynamic polarisation tests are presented in Table 4-6.

Table 4- 6 *Corrosion parameters for 304L stainless steel after exposure to 1 M sulphuric acid and 3.5 wt% sodium chloride. *Standard deviation error.*

Solution	E_{corr} (mV)	i_{corr} (µA/cm²)	E_{pit} (mV)	R_p (Ωcm²)	Dissolved iron (mg/l)
1 M sulphuric acid	-282 ± 16*	48 ± 18	-	669	12
3.5 wt% sodium chloride	-288 ± 55	132 ± 53	400 ± 23	2116	0.17

From Table 4-6, it is clear that the dissolution rates of the supplied stainless steel were higher in sulphuric acid than in sodium chloride. The conductivity of the acid used was ≈ 398 mS/cm, while that of the 3.5 wt% sodium chloride was only 55 mS/cm. Hence, it was expected that the corrosion rate of the stainless steel would be higher in sulphuric acid.

The observed results can also be attributed to the nature of cathodic reactions supported in each solution. In acids, the cathodic reaction is the evolution of hydrogen by Equation 2-2, which does not allow for the formation of any protective films. On the other hand, corrosion in sodium chloride is supported by the reduction of water and oxygen as described in Equation 2-3, which produces hydroxide ions that can facilitate the formation of adherent and frequently protective iron hydroxide. Similar observations were made by Sherif (2012) when 2209 duplex stainless steel was exposed to hydrochloric acid and to sodium chloride.

4.4 Summary

For the results of this work to be meaningful, it was essential that complete information on the supplied 304L stainless steel be known. This chapter therefore sought to present a thorough characterisation of the alloy prior to the proposed surface modifications.

Positive identification of the 304L stainless steel was successfully achieved via spark analysis and metallographic examination. The corrosion behaviour of the alloy was studied in sulphuric acid and sodium chloride, while microstructural properties were analysed by metallography and XRD. These were found to be reasonably consistent with documented limits. Therefore, any deviations from expected corrosion behaviour and microstructural on the modified 304L stainless steel could be confidently attributed to the proposed ruthenium surface alloys.

Chapter 5
Alloy synthesis

5.1 Introduction

Corrosion resistance of ruthenium-stainless steel alloys has been widely investigated in 1 M sulphuric acid, with previous researchers reporting corrosion rates of between 0.0052 and 0.85 mm/y at room temperature (Potgieter et al. 1992; Olubambi et al. 2009; Sherif 2011; Olaseinde et al. 2012). The objective of the study in this chapter was to produce ruthenium surface alloys that would reduce the corrosion rate of 304L stainless steel in 1 M sulphuric acid to less than 0.1 mm/y: equivalent to at least 88% improvement in corrosion resistance. This was achieved through a series of steps summarised in Figure 5-1. It was also important that the Type I surface alloys (Section 2.4.1) maintained their integrity during exposure to ensure long-term applicability.

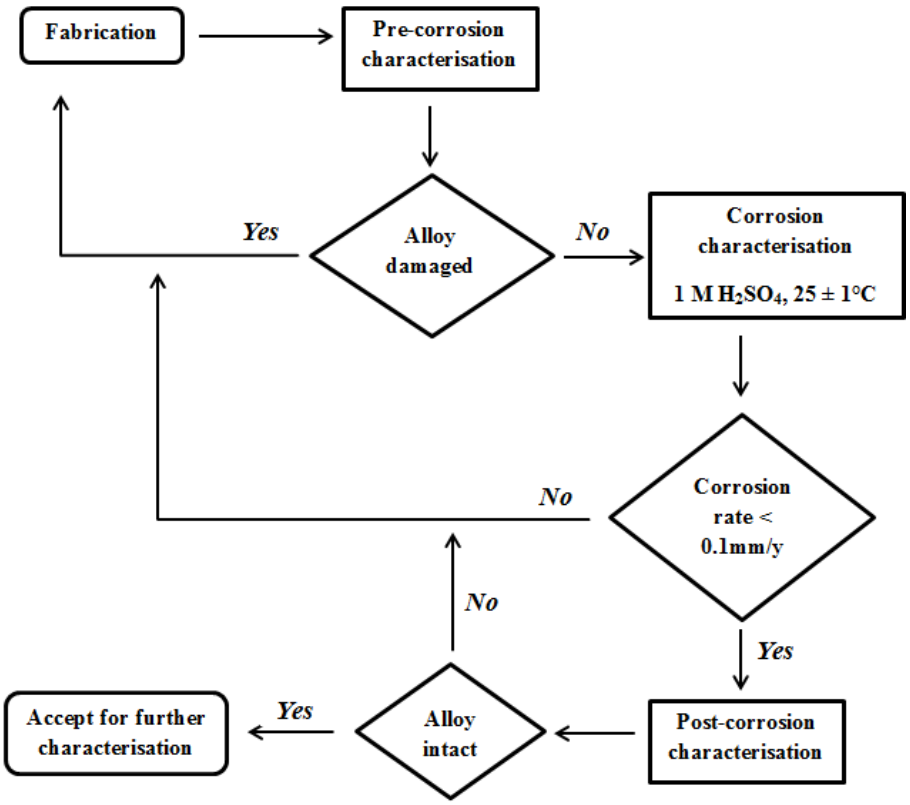

Figure 5- 1 *Flow diagram illustrating the surface alloy synthesis and corrosion characterisation process.*

5.2 Results: Ion implantation

This section of the chapter seeks to present, and describe the results of the synthesis of the ruthenium alloy via ion implantation.

5.2.1 SRIM simulation

Simulation of the ion implantation process using SRIM-2008 in the full cascade option produced the results in Figures 5-2 to 5-4. In all cases, simulation was done using 5000 ions.

Figure 5-2 shows that implantation depth increased with increase in implantation energy. The depth of the ruthenium peak concentration was about 13 nm at 50 keV, and increased to almost 34 nm at 160 keV. In addition, skewness at the lower implantation energy was more positive, indicating that the implanted ruthenium was closer to the surface than at the higher energy.

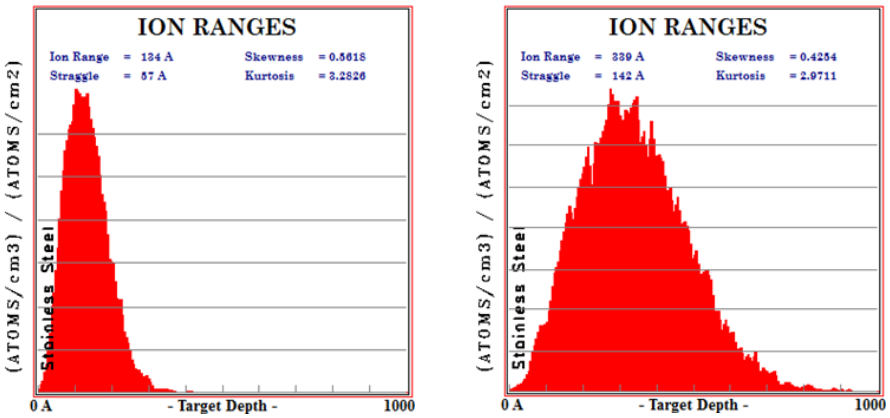

Figure 5- 2 *Concentration distribution of ruthenium implanted into 304L stainless steel simulated at (a) 50 keV, and (b) 160 keV. Angle of incidence = 0°.*

Lateral straggle, i.e. the width of the concentration distribution, was larger at 160 keV than at 50 keV. This suggests that the ruthenium ions implanted at the higher energy interacted more with the atoms of the stainless steel substrate. Results presented in Figure 5-3 support this, and demonstrate that the number of vacancies produced by the knock-on effect of implanted ruthenium ions was greater for higher implantation energy than for lower energy. The consequence is

a large volume of damage in the substrate implanted at 160 keV, which could negatively influence corrosion behaviour.

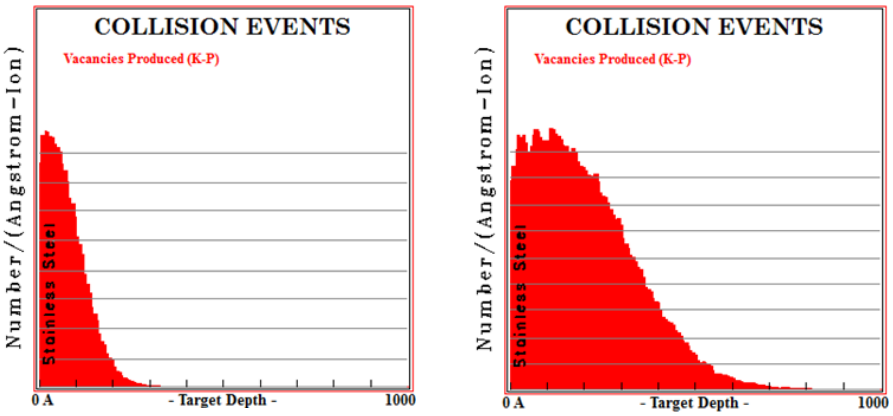

Figure 5- 3 *SRIM simulation of vacancies produced due to ruthenium implantation into 304L stainless steel at (a) 50 keV, and (b) 160 keV. Angle of incidence = 0°.*

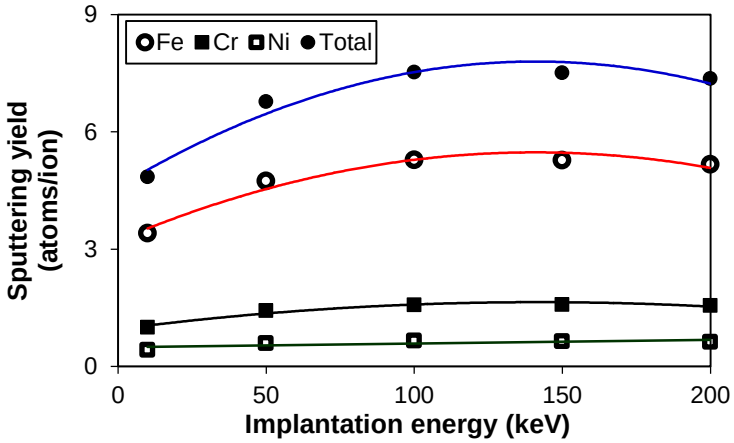

Figure 5- 4 *Simulated sputtering yield of 304L stainless steel implanted with ruthenium ions at a fixed incident angle of 0° as a function of implantation energy*

Figure 5-4 compares the sputtering yield of the major alloying elements of 304L stainless steel as a function of implantation energy. It can be seen that the sputtering yield of iron was greater than that of chromium and nickel; in fact, the sputtering yields of these metals followed the trend Fe > Cr > Ni. These results seem to suggest differential sputtering and a possible surface enrichment of nickel during ion implantation process.

From the same figure, it can be observed that while there was a change in sputtering yield with increase in implantation energy, the change was slight. For instance, about 6.8 atoms per ruthenium ion were sputtered at 50 keV and increasing implantation energy to 150 keV increased sputtering yield by just 11%. It is also apparent that increasing implantation energy beyond 100 keV resulted in a reduction in the sputtering yield. The sputtering yield at 100 keV and at 200 kev was similar: about 7.5 and 7.4 atoms per ruthenium ion respectively.

5.2.2 Design of experiments

A 2^3 factorial design for three independent parameters was done to study their effect on the corrosion resistance of ruthenium implanted 304L stainless steel. Table 5-1 lists the parameters studied, their ranges and levels. Roughness measurements were done via AFM.

Table 5- 1 *Experimental conditions used for the 2^3 factorial DOE. *Samples prepared using 6 μm alumina paste (Polished) or 120 grit silicon carbide paper (Rough)*

Symbol	Parameter	Unit	Low level (-1)	High level (+1)
A	Energy	keV	50	160
B	Dose	Ru/cm²	10^{12}	10^{14}
C	Surface roughness	-	Polished* ($R_a \approx 6$ nm)	Rough ($R_a \approx 131$ nm)

After ion implantation, the samples were characterised by XRD, FESEM and potentiodynamic polarization. The results of these tests are presented in the following subsections.

X-ray diffraction analysis

XRD patterns for the ruthenium implanted 304L stainless steel shown in Figure 5-5 are identical to that of the unmodified stainless steel presented in Figures 4-2 and 4-5. The absence of ruthenium peaks suggests that the amount of ruthenium implanted into the stainless steel alloy was lower than the detection limit of the

D2 Phaser used (≈ 4 vol%). In addition, there was no evidence of the precipitation of new phases, or intermetallic compounds, both of which have been associated with ion implantation process (Radjobov 1988; Collins et al. 1994; Pelletier et al. 1999; Riviere et al. 2002).

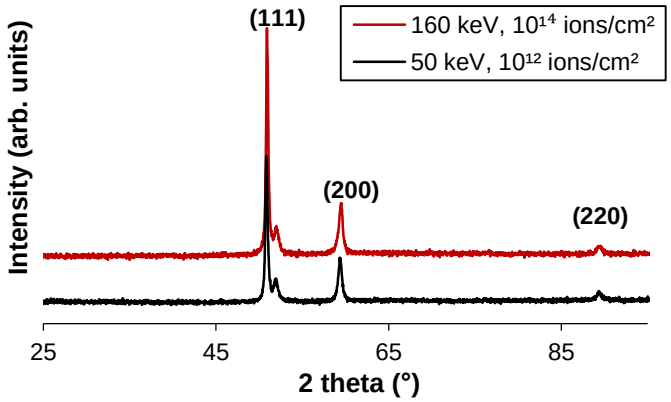

Figure 5- 5 *Typical XRD patterns of ruthenium implanted 304L stainless steel, referenced against PDF 04 002 1898 and PDF 00 006 0663. Co-Kα radiation.*

Figures 5-6 to 5-11 compare the XRD diffractograms of the unmodified 304L stainless steel with those of the ruthenium-implanted alloy. For clarity, only the (111) and (200) peaks are presented. It can be seen that in all cases, ruthenium implantation shifted the stainless steel peaks to lower Bragg angles. This is consistent with an increase in interplanar spacing, and indicative of compressive stresses in implanted steels (Equation 3-14), as well as the expansion of the lattice.

It is clear from Figures 5-6 and 5-7 that implantation at a high dose (10^{14} Ru/cm^2) caused a larger shift in the Bragg's angle. This is consistent with a larger volume expansion of the stainless steel lattice because of introducing a larger amount of ruthenium ions (Mändl et al. 2005; Dudognon et al. 2008). The largest change in Bragg angle was observed on the rough samples implanted at 50 keV. A 2.6% decrease in 2θ was measured on the sample implanted with 10^{14} Ru/cm^2, compared to about 2.2% on a similar sample implanted at the same energy but lower dose (Figure 5-7(b)).

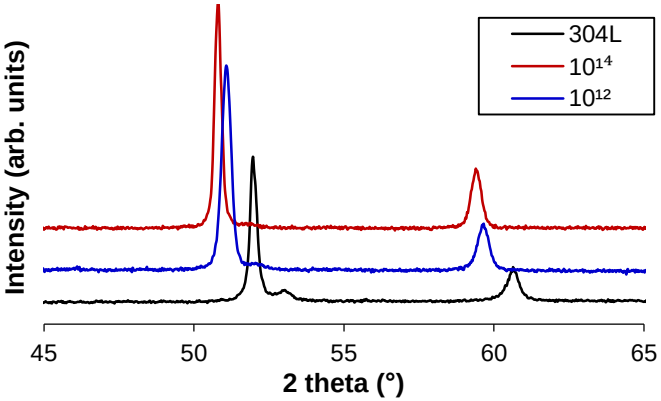

(a)

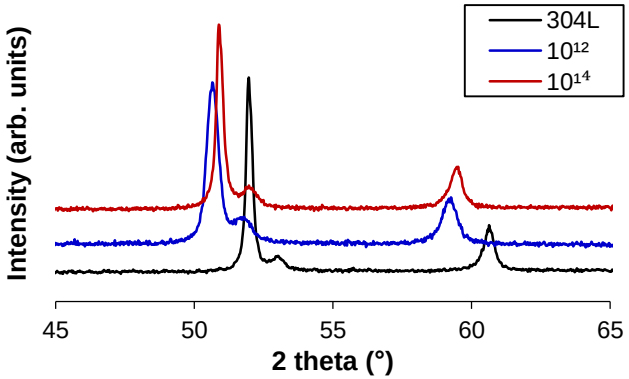

(b)

Figure 5- 6 *Effect of implantation dose on Bragg angle. Samples prepared at 160 keV on (a) polished and (b) rough surfaces.*

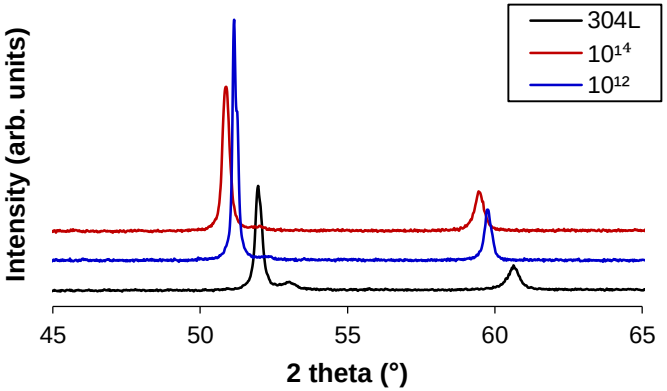

(a)

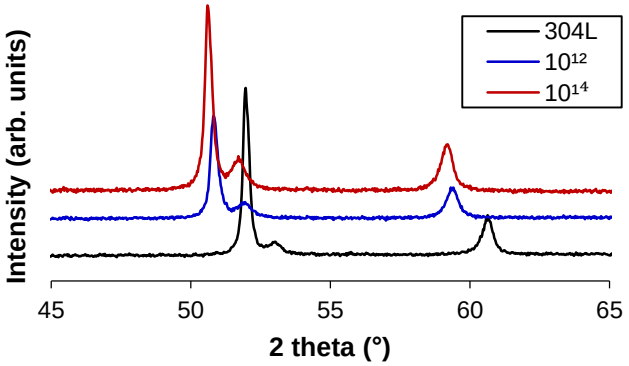

(b)

Figure 5- 7 *Effect of implantation dose on Bragg angle. Samples prepared at 50 keV on (a) polished and (b) rough surfaces.*

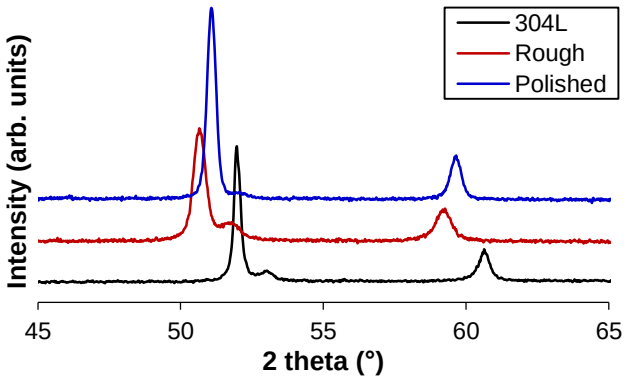

(a)

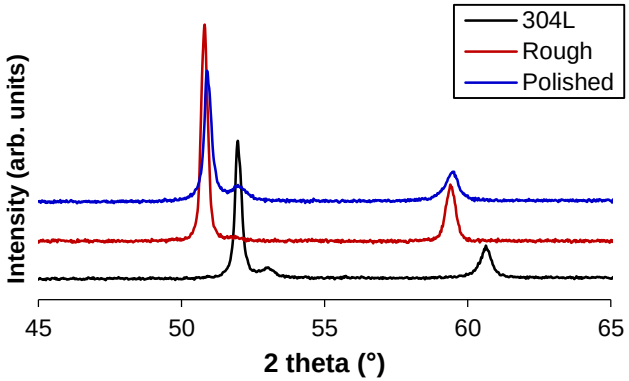

(b)

Figure 5- 8 *Effect of surface preparation on Bragg angle. Samples implanted at 160 keV, with (a) 10^{12} Ru/cm^2, and (b) 10^{14} Ru/cm^2.*

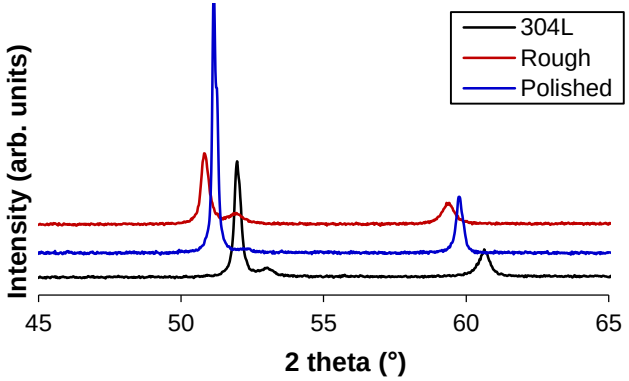

(a)

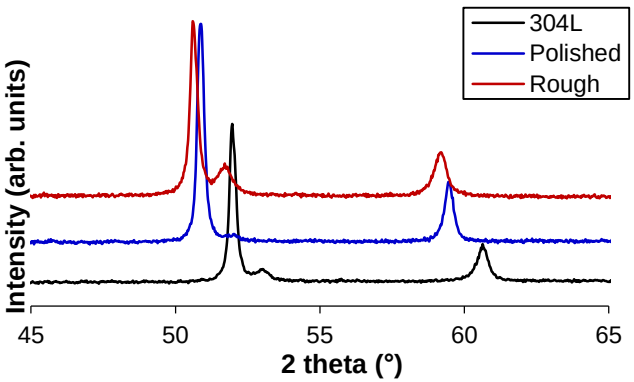

(b)

Figure 5- 9 *Effect of surface preparation on Bragg angle. Samples implanted at 50 keV, (a) 10^{12} Ru/cm^2, and (b), 10^{14} Ru/cm^2.*

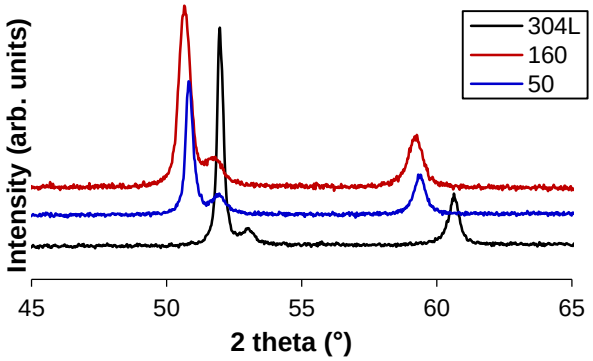

(a)

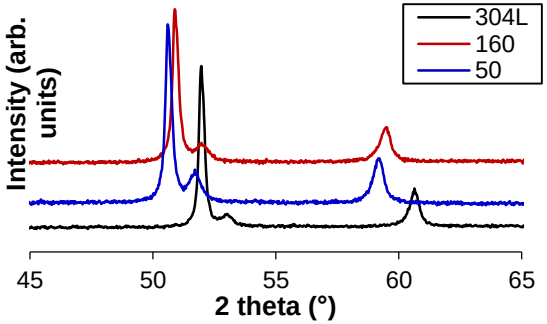

(b)

Figure 5- 10 *Effect of implantation energy on Bragg angle. Samples prepared on rough samples at (a) 10^{12} Ru/cm^2, and (b) 10^{14} Ru/cm^2.*

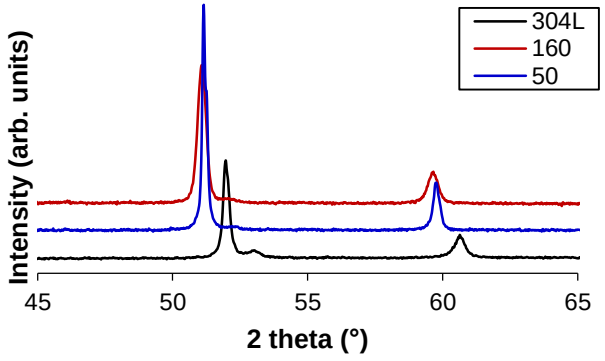

(a)

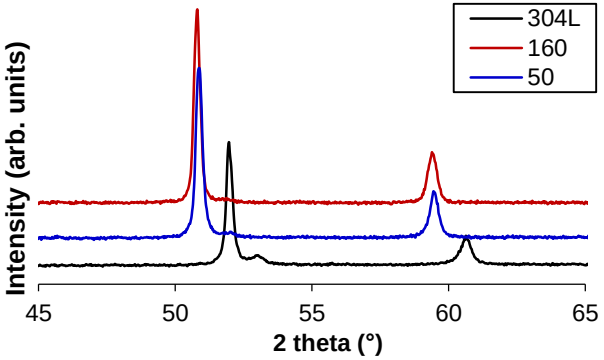

(b)

Figure 5- 11 *Effect of implantation energy on Bragg angle. Samples prepared on polished samples at (a) 10^{12} Ru/cm^2, and (b) 10^{14} Ru/cm^2.*

An anomaly was observed on the rough sample implanted at 160 keV. The results presented in Figure 5-6(a), show that the shift in the Bragg angle was larger at lower doses (10^{12} Ru/cm^2). This was not in agreement with the expectation that a higher ruthenium dose would cause a larger expansion of the lattice and consequently a larger decrease in Bragg angle.

In all the cases studied, ruthenium implantation into rough stainless steel surfaces resulted in larger shifts in the Bragg angle. These results are presented in Figures 5-8 and 5-9. Angular shift of the (111) peak was between 2.1 and 2.6% for the rough samples relative to unmodified 304L stainless steel, while the shift for the polished samples ranged from 1.6 to a maximum of 2.2%. These observations seem to suggest that more ruthenium was successfully implanted into the rough samples leading to a larger expansion of the lattice.

At high implantation energy and high dose (Figure 5-8(b)), the effect of surface finish on Bragg angle was indistinguishable. The angular position of the (111) peak measured on the rough and polished surfaces was 50.9° and 50.8° respectively. This implies that at high implantation energy and high dose, surface preparation had little or no effect on the induced stress or on the concentration of implanted ruthenium.

Figures 5-10 and 5-11 show the effect of implantation energy on the Bragg angle. The Bragg position of the (111) peak shifted more for the polished samples implanted with 10^{14} Ru/cm^2 regardless of implantation energy, consistent with the expectation that high implantation dose would cause larger lattice expansion. Increasing implantation energy from 50 to 160 keV resulted in a similar shift in Bragg angle regardless of surface finish. For instance, in Figure 5-11(b) the value of 2θ changed from ≈ 52° for 304L stainless steel to 50.9° and 50.8° for the rough and polished samples respectively.

However, the trend was not as straightforward for the rough samples. As can be seen in Figure 5-10, the effect of implantation energy on the angular position of the (111) and (200) peaks was dependent on the implantation dose. At the lower dose (10^{12} Ru/cm^2), the shift in Bragg angle was slightly larger for samples

prepared at 160 keV than at 50 keV. Increasing dose to 10^{14} Ru/cm^2, however caused a larger shift on samples implanted at 50 keV.

Corrosion characterisation

Corrosion rates of the implanted samples in 1 M sulphuric acid are presented in Table 5-2 and Figure 5-12.

Although the presence of ruthenium shifted the E_{corr} to nobler values, the effect was only slight (Figure 5-12(a)), given that the average E_{corr} of pristine 304L was -366 mV. The most marked change in E_{corr} was observed on the rough samples prepared at 50 keV, and 10^{14} Ru/cm^2; E_{corr} increased to ≈ -263 mV.

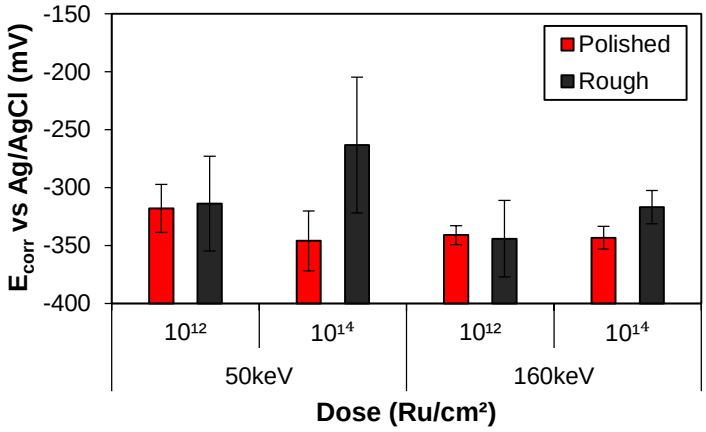

(a)

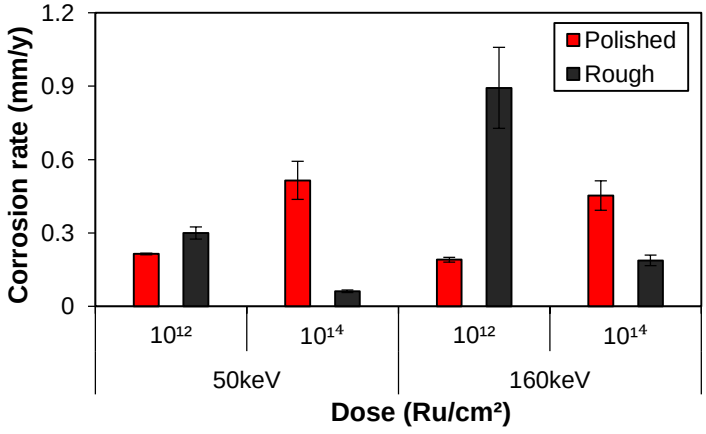

(b)

Figure 5- 12 *Influence of dose, energy and surface finish on (a) corrosion potential, and (b) corrosion rate of ruthenium implanted 304L stainless steel in 1 M sulphuric acid.*

Nonetheless, ruthenium implanted stainless steel reacted slower than pristine 304L stainless steel in most cases. From Table 5-2, it is evident that the highest average corrosion rate was obtained on the rough samples implanted at low dose (10^{12} Ru/cm^2) and high energy (160 keV). Corrosion rates in this case were as high as 1.4 mm/y, and averaged about 0.9 mm/y. This is equal to the corrosion rate of unmodified 304L stainless steel. It implies that implanting at high energy and low dose did not improve corrosion resistance at all, and is consistent with the observation in Figure 5-2 that high implantation energy distributed the ruthenium deeper in the stainless steel substrate, thus limiting its availability for corrosion protection.

Table 5- 2 *Corrosion rate (mm/y) results from the 2^3 DOE, calculated by LPR method and expressed to 3 d.p. *Bold italics present average corrosion rate.*

		A: Energy (keV)			
		(-1)		**(+1)**	
		C: Surface roughness		**C: Surface roughness**	
		(-1)	**(+1)**	**(-1)**	**(+1)**
B: Dose (Ru/cm²)	**(-1)**	0.226	0.179	0.085	0.782
		0.267	0.292	0.163	1.048
		0.270	0.552	0.339	1.354
		0.143	0.156	0.230	0.263
		0.169	0.320	0.138	1.020
		0.215*	***0.300***	***0.191***	***0.893***
	(+1)	0.943	0.028	0.805	0.407
		0.348	0.062	0.541	0.225
		0.313	0.014	0.181	0.015
		0.653	0.022	0.470	0.192
		0.318	0.183	0.269	0.099
		0.515	***0.062***	***0.453***	***0.188***

The slowest corrosion rate (average of 0.06 mm/y) was measured on the rough samples implanted at low energy and high dose. This observation was atypical, since rough surfaces are usually associated with higher corrosion rates (Melchers & Jeffery 2004; Li & Li 2006; Revie & Uhlig 2008). However, it concurred with the expectation that at low implantation energies, the ruthenium would be closer

to the surface and accessible for corrosion processes. In addition, corrosion resistance should increase with increase in ruthenium dose.

Figure 5-12(b) suggests that surface finish had a marked effect on corrosion resistance of the ruthenium implanted 304L stainless steel. For the polished samples, corrosion rates increased with increasing in implantation dose regardless of implantation energy. This response was contrary to predictions that higher doses would cause improved corrosion resistance. Furthermore, increasing implantation energy caused a slight decrease in corrosion rates. For rough samples though, corrosion rates decreased with increase in implantation dose, which was as expected. Lower corrosion rates were recorded for samples prepared at lower implantation energy.

Post corrosion examination of the corroded surfaces was done using FESEM. The images shown in Figures 5-13 and 5-14, indicate that round spongy-like agglomerates covered most of the rough samples. Figure 5-14 suggests that the density of these agglomerates increased with increase in implantation dose. Only one set of the polished samples displayed similar behaviour: the samples implanted at low energy and low dose (Figure 5-13), were covered by flat round button-like agglomerates.

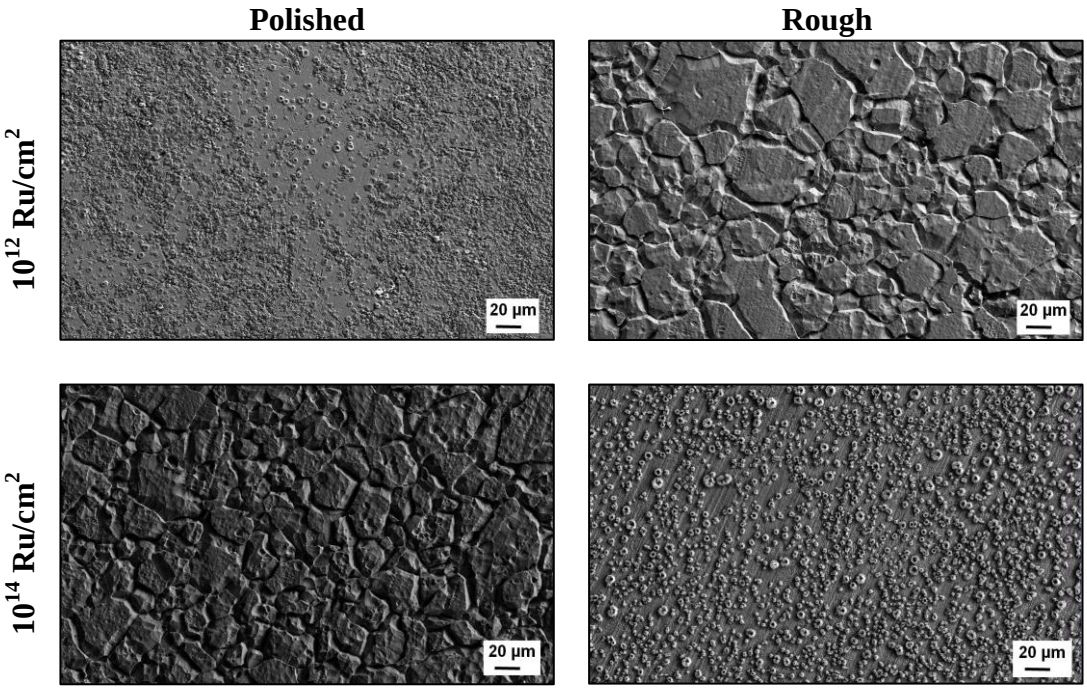

Figure 5- 13 *FESEM-SE images of the 304L stainless steel implanted at 50 keV, and exposed to 1 M sulphuric acid.*

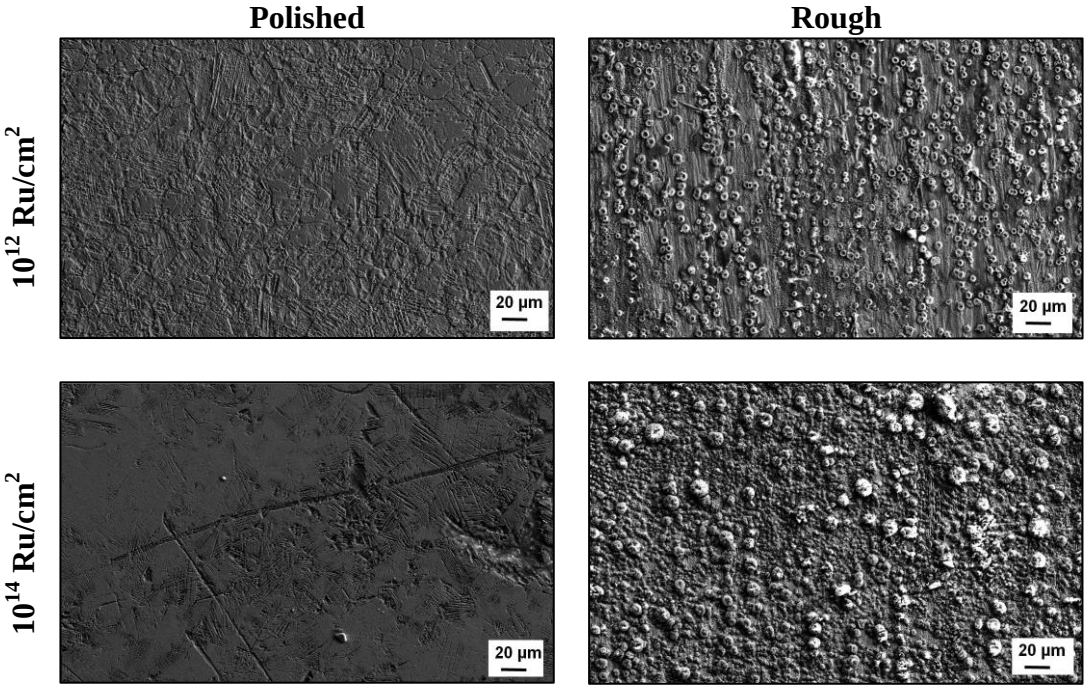

Figure 5- 14 *FESEM-SE images of the 304L stainless steel implanted at 160 keV, and exposed to 1 M sulphuric acid.*

Surfaces that did not develop these agglomerates showed evidence of intergranular corrosion, and selective leaching. At high implantation energy, and on polished samples (Figures 5-14 & 5-15), the samples underwent fine intergranular corrosion. The surfaces were characterised by shallower damage of the grains than on the grain boundaries. This suggests that the dissolution rate on the grains relative to that of the grain boundaries was slower, thus corroborating the lower corrosion rates reported in Figure 5-12(b).

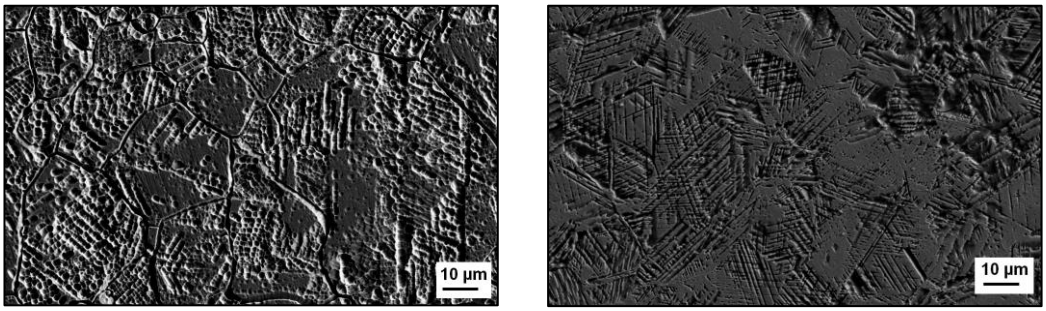

(a) (b)

Figure 5- 15 *Polished samples magnified 1500*x. *Samples implanted at 160 keV and doses of (a) 10^{12} Ru/cm^2 and (b) 10^{14} Ru/cm^2.*

At low implantation energy (50 keV), both polished and rough samples exhibited coarse, broad attack of the grain boundaries (Figure 5-13). In both cases, the corrosion rates were higher than observed for the samples showing fine intergranular corrosion. There was no apparent correlation between dose and type of intergranular attack, and selective leaching seemed predominant on polished samples implanted at high energy.

The agglomerates precipitated on some of the samples were analysed by EDS. Results presented in Figure 5-16 indicate that these agglomerates were rich in sulphur. It is likely therefore that these agglomerates were sulphates. Previous authors (Schumki 2002; Richardson 2010) have reported nucleation and growth of ferrous sulphates in sulphuric acid of all concentrations. Interestingly, the agglomerates on samples prepared at low energy (50 keV) had higher chromium content: they typically had between 6.6 to 7.8 wt% chromium compared to 2.9 to 6.5 wt% for samples prepared at 160 keV. It is possible that the chromium was present in the precipitates a chromium oxide.

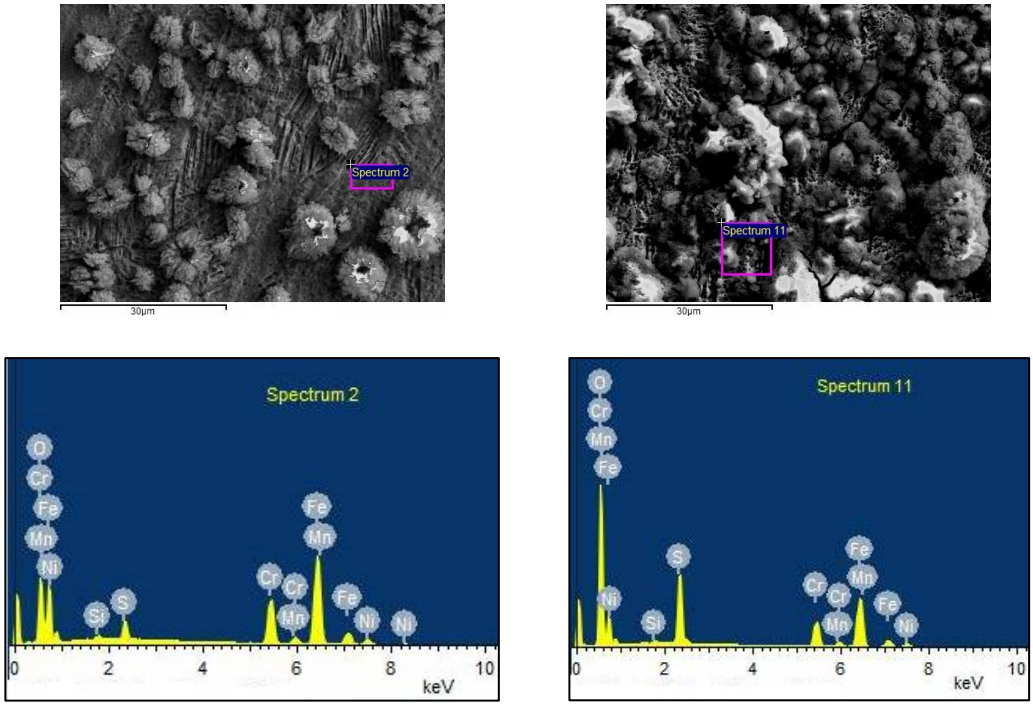

(a) (b)

Figure 5- 16 *EDS analysis of agglomerates formed on some of the ruthenium implanted 304L stainless steels.*

To assess the corrosion damage beneath the agglomerates, the samples were cleaned in ethanol using an ultrasonic cleaner, and three cleaning cycles each 5 minutes long. FESEM images of the clean surfaces are presented in Figure 5-17. The agglomerates formed on the rough sample implanted at 50 keV with 10^{14} Ru/cm^2 (Figure 5-17 (d)), were quite adherent as residue of the agglomerates remained attached on the surface even after thorough cleaning. These agglomerates formed films that could be responsible for the low corrosion rates reported in Table 5-2 and Figure 5-12(b). The composition of the agglomerates is presented in Figure 5-16.

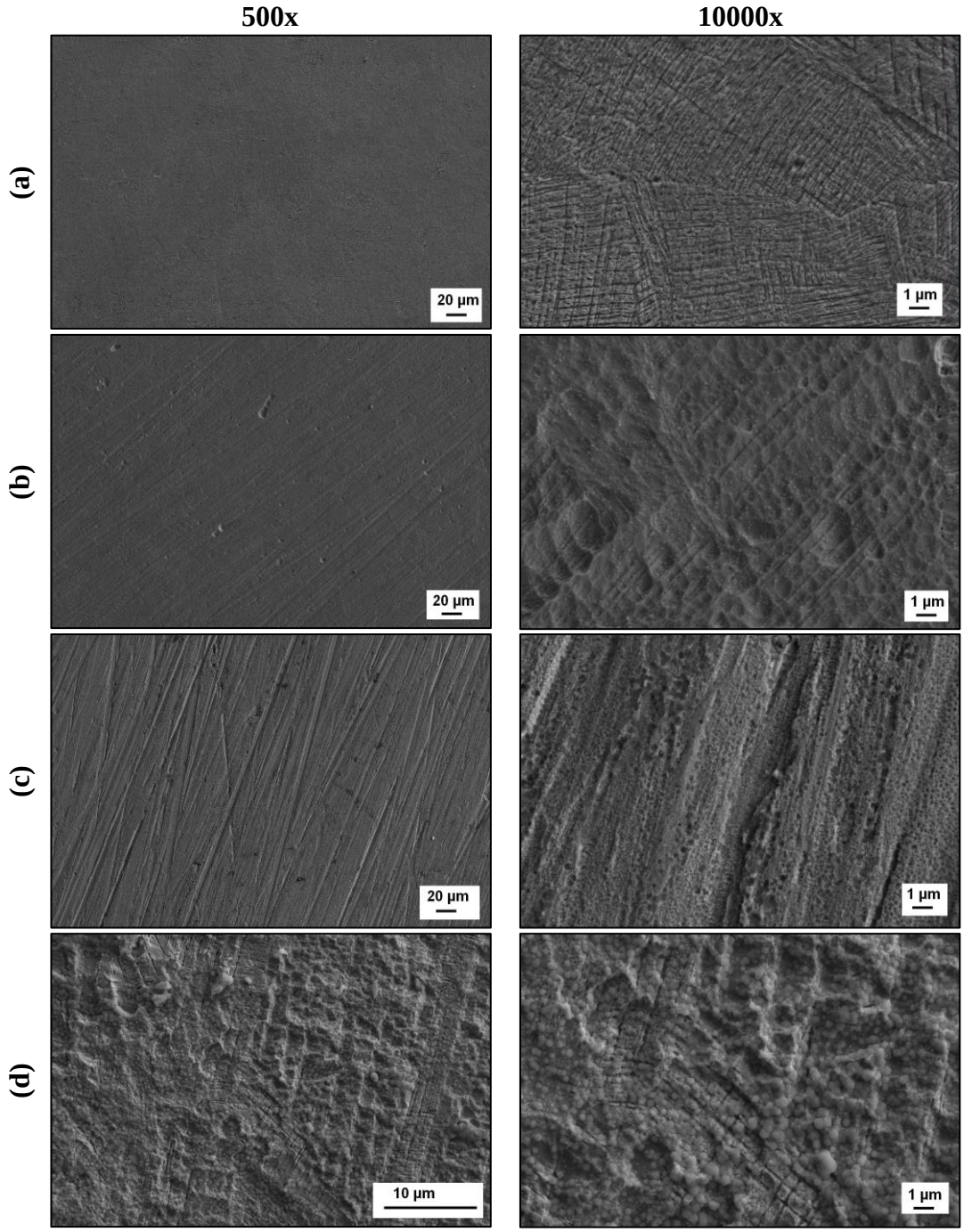

Figure 5- 17 *FESEM-SE images of the samples with deposits after cleaning, magnified 500 and 10000*x. *Samples were prepared at (a) 160keV, 10^{12} Ru/cm^2, rough, (b) 50keV, 10^{12} Ru/cm^2, polished, (c) 160keV, 10^{14} Ru/cm^2, rough, (d) 50keV, 10^{14} Ru/cm^2, rough.*

Statistical analysis

Table 5-3 presents the effects of implantation energy, dose, and surface roughness on the corrosion rate of ruthenium implanted 304L stainless steel in sulphuric acid. The effects were calculated as described in Section 3.3, and their significance plotted in Figure 5-18.

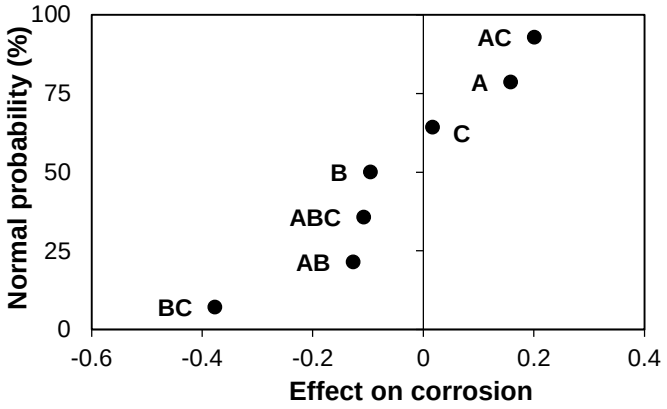

Figure 5- 18 *Normal probability plot showing the effects of the main factors A-energy, B-dose and C-surface roughness and their interactions.*

The probability plot in Figure 5-18 shows that the effects of implantation dose (B) as well as its interaction with energy (AB) and surface roughness (ABC) lay on a straight line. This means that these parameters were statistically unimportant for this study. Parameters that seemed to be of statistical significance were energy (A), surface roughness (C) and their interaction (AC) as well as that of dose and surface roughness (BC). As shown in Figure 5-18, the effects of these parameters did not fit reasonably well on a straight line.

Table 5- 3 *Analysis of the effect of the parameters energy (A), dose (B) and surface roughness (C) and their interactions on the corrosion of ruthenium implanted 304L stainless steel in 1 M sulphuric acid. *S^2 = variance, all values expressed to 3 d.p.*

Sample	**A**	**B**	**C**	**AB**	**AC**	**BC**	**ABC**	**$\bar{Y}$**	***S^2**
1	(+1)	(-1)	(+1)	(-1)	(+1)	(-1)	(-1)	0.893	0.165
2	(+1)	(+1)	(-1)	(+1)	(-1)	(-1)	(-1)	0.453	0.060
3	(-1)	(+1)	(-1)	(-1)	(+1)	(-1)	(+1)	0.515	0.078
4	(+1)	(+1)	(+1)	(+1)	(+1)	(+1)	(+1)	0.188	0.022
5	(+1)	(-1)	(-1)	(-1)	(-1)	(+1)	(+1)	0.191	0.010
6	(-1)	(-1)	(+1)	(+1)	(-1)	(-1)	(+1)	0.300	0.025
7	(-1)	(-1)	(-1)	(+1)	(+1)	(+1)	(-1)	0.215	0.003
8	(-1)	(+1)	(+1)	(-1)	(-1)	(+1)	(-1)	0.062	0.005
$\sum\bar{Y}_+$	1.725	1.218	1.443	1.155	1.811	0.655	1.193		
$\sum\bar{Y}_-$	1.092	1.599	1.374	1.661	1.006	2.161	1.623		
$\bar{Y}_+$	0.431	0.304	0.361	0.289	0.453	0.164	0.298		
$\bar{Y}_-$	0.273	0.400	0.343	0.415	0.251	0.540	0.406		
Effect	***0.158***	***-0.095***	***0.017***	***-0.126***	***0.201***	***-0.376***	***-0.107***		

Analysis of the effects of energy and surface roughness is presented in Figure 5-19. From Figure 5-19(a) it can be seen that increasing implantation energy from 50 keV (coded -1) to 160 keV (coded +1), caused an increase in corrosion rates. This is consistent with the expectation that at high implantation energy, the ruthenium would be distributed deep in the substrate making it less accessible for corrosion protection. In addition, higher implantation doses were associated with larger surface damage (Figure 5-3(b)), and therefore higher susceptibility to corrosion attack.

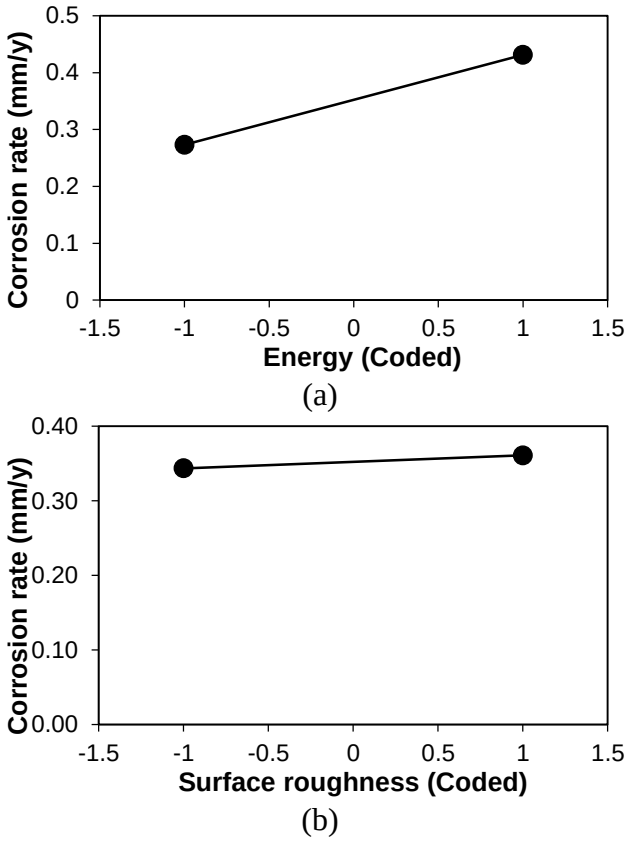

Figure 5- 19 *Effect of (a) energy (A), and (b) surface roughness (C) on the corrosion rate of ruthenium implanted 304L stainless steel in 1 M sulphuric acid.*

The effect of surface roughness on corrosion was very slight as can be observed in Figure 5-19(b). Increasing surface roughness only caused a 5% increase in corrosion rate. While the increase in corrosion rate with surface roughness was expected (Melchers & Jeffery 2004; Li & Li 2006), the increase was not as much as observed in Figure 4-7 where increasing surface roughness increased corrosion rates by at least 300%. These results point to (1) a possible smoothening effect caused by the ion

implantation process (Bunker & Armini 1994), and (2) the effectiveness of ruthenium in improving corrosion resistance.

Interactions AC and BC were disordinal in nature, as seen by the intersections of the graphs in Figure 5-20. This indicates that the effects of energy and dose on the corrosion resistance of ruthenium implanted 304L stainless steel were strongly dependent on surface finish of the substrate pre- ion implantation.

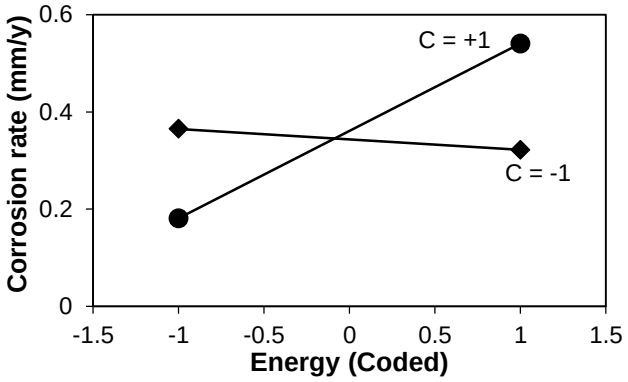

(a)

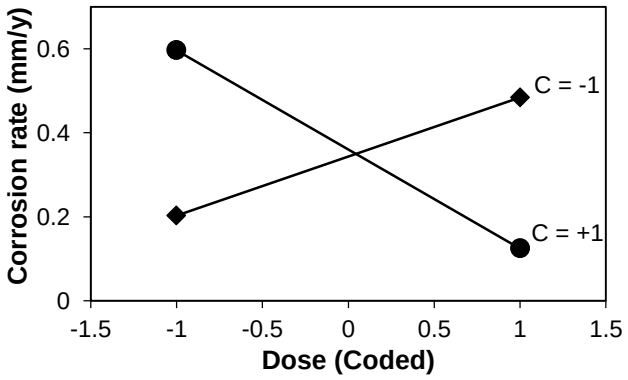

(b)

Figure 5- 20 *Interaction graphs for the effects of (a) energy and surface (AC), and (b) dose and surface roughness (BC) on the corrosion rate of ruthenium implanted 304L stainless steel in 1 M sulphuric acid.*

In Figure 5-20(a), increasing both implantation energy and surface roughness had the effect of increasing corrosion rates of the modified stainless steel. The results are in agreement with the following: (1) at high implantation energy, ruthenium distribution is deeper in the substrate, (2) rough surfaces are generally prone to high corrosion rates, and (3) high implantation energies are associated with larger surface damage. However, increasing implantation energy on polished surfaces caused a decrease in corrosion rates

in 1 M sulphuric acid. The decrease was marginal when compared to decreasing implantation energy on rough samples.

Simultaneously increasing dose and surface roughness led to decreased corrosion rates. As can be seen in Figure 5-20(b), increasing implantation dose from 10^{12} to 10^{14} Ru/cm^2 on rough surfaces (coded +1) increased corrosion resistance by a factor > 4.5. While it was expected that increasing implantation dose would increase ruthenium concentration in the surface layer and therefore improve corrosion resistance, a similar effect was not anticipated with increasing surface roughness. On polished surfaces, increasing implantation dose had the opposite effect. As shown in Figure 5-20(b), increasing dose on these surfaces increased corrosion rates by as much as 138%. This behaviour was contrary to expectation.

Interaction of effects takes precedence over the effect of individual main parameters (Barrentine 1999), i.e. in this study, the effects in Figure 5-20 were more important than those in Figure 5-19. The objective of this study was to reduce corrosion rates of 304L stainless steel. Looking at Figure 5-20, it can be concluded that low corrosion rates are achievable under two conditions: (1) low implantation energy, and rough surfaces (Figure 5-20(a)), and (2) high implantation dose, on rough surfaces (Figure 5-20(b)).

An extract of Table 5-3 presented in Figure 5-21 shows several combinations of these conditions. Sample number 8 satisfied the two conditions, and its average corrosion rate was ≈ 0.06 mm/y, which conforms to the target outlined in Figure 5-1. Therefore, further study was focused on understanding the effect of surface roughness and dose, as well as optimising these for best corrosion resistance.

Sample	A	B	C
1	(+1)	(-1)	(+1) ✓
2	(+1)	(+1) ✓	(-1)
3	(-1) ✓	(+1) ✓	(-1)
4	(+1)	(+1) ✓	(+1) ✓
5	(+1)	(-1)	(-1)
6	(-1) ✓	(-1)	(+1) ✓
7	(-1) ✓	(-1)	(-1)
8	(-1) ✓	(+1) ✓	(+1) ✓

Figure 5- 21 *Combinations of the conditions that can give the lowest corrosion rates of ruthenium implanted 304L stainless steel in 1 M sulphuric acid.*

5.2.3 Effect of surface roughness

Surface stresses

Ion implantation is associated with the generation of surface stresses, and for austenitic stainless steels with, stress induced transformations to form corrosion susceptible phases such as martensite and ferrite (Pelleiter et al. 1999; 2001; Picard et al. 2001; Dudognon et al. 2008; Padhy et al. 2010). In the present work, the effect of surfaces roughness on the stresses generated in 304L stainless steel during ruthenium implantation were studied using the $Sin^2\psi$ method. The results are presented in Figures 5-22 and 5-23.

It is immediately clear from Figure 5-22 that the slopes of the ε vs $\sin^2\psi$ plots for all the samples studied were negative, suggesting that the nature of the stresses generated were generally compressive. These results are consistent with the expectation that the impinging ruthenium ions would have a peening effect on the substrate surface, and are in agreement with those reported by previous researchers (Pane & Speriosu 1987). In addition, Figure 5-22 shows that the gradients became increasingly positive with reduction in surface roughness. This suggests that the stresses generated because of ion implantation became increasingly tensile with reduction in surface roughness shown in Figure 5-23.

Comparing the results in Figure 5-22 and Figure 5-23 with those reported in Figures 4-9 and 4-10, revealed several effects. (1) The ε vs $\sin^2\psi$ plots for the sample ground to 240 grit became linear after ion implantation, with R^2 values increasing from 0.71 to 0.99, and (2) the gradients of the ε vs $\sin^2\psi$ plots increased for the rough sample, but decreased for the polished samples after ion implantation. This implies that ion implantation induced different forms of stress depending on the surface finish of the sample, and that ion implantation caused less amorphisation of the rough surfaces. For rough surfaces, the process induced larger compressive stresses whereas it induced tensile stresses in the polished surfaces. The stresses induced on polished surfaces increased from $\approx$ -575 to -479 MPa after ruthenium implantation.

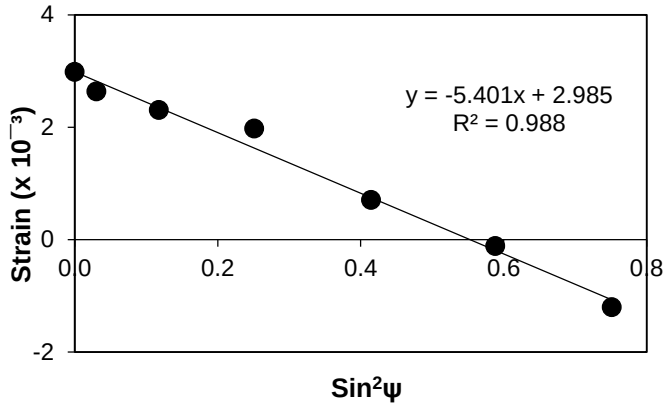

(a)

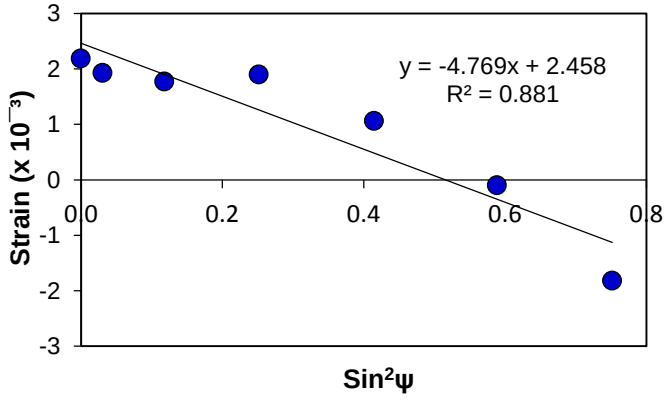

(b)

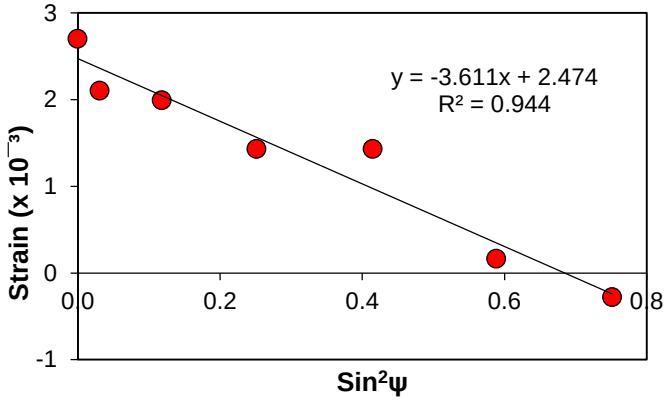

(c)

Figure 5- 22 *Strain vs $\sin^2\psi$ plots for ruthenium implanted 304L stainless steel. The surfaces were initially (a) ground to 240 grit, (b) ground to 1200 grit, and (c) polished with 6 μm alumina powder. Dose = 10^{14} Ru/cm^2, and energy = 50 keV.*

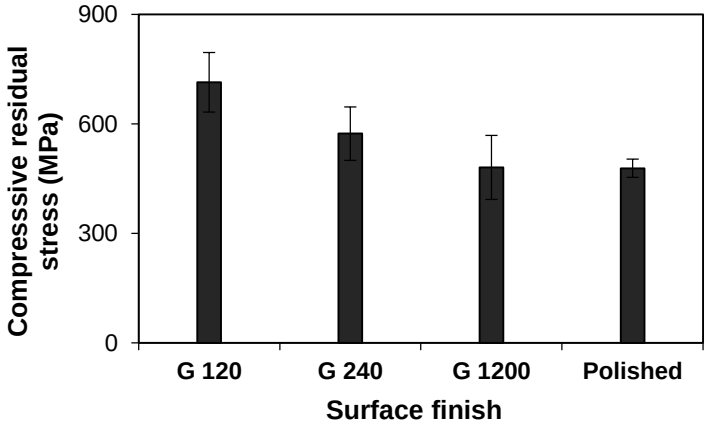

Figure 5- 23 *Residual stresses in ruthenium implanted 304L stainless steel as a function of pre-implantation surface finish.*

Surface sputtering

Figures 5-24 and 5-25 show the AFM analysis of 25 μm^2 304L surfaces before and after ruthenium implantation. The samples were prepared at 50 keV and 160 keV using a dose of 10^{12} Ru/cm^2.

As can be seen from these figures, the ion implantation process did influence the surface roughness of the stainless steel substrate. This was consistent with observations by other researchers (Braceras et al. 2007; Dudognon et al. 2008; Xu et al. 2013), and is a consequence of the removal of surface material by sputtering. It is apparent that ruthenium implantation increased the roughness of initially polished samples, but decreased the roughness of initially rough stainless steel samples. In addition, these effects were enhanced by increasing implantation energy from 50 keV to 160 keV. These observations suggest that the sputtered depth due to ruthenium implantation was dependent on both pre-implantation surface finish and implantation energy.

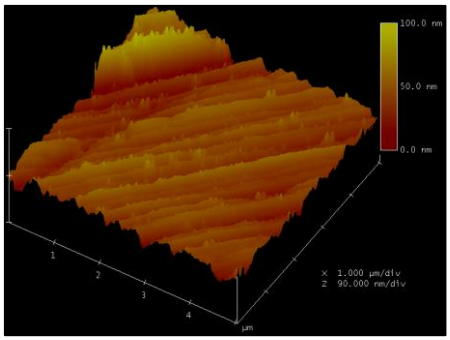

(a)

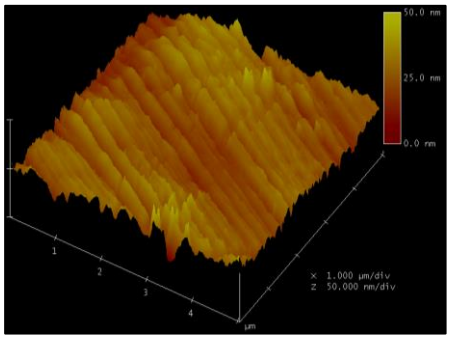

(b)

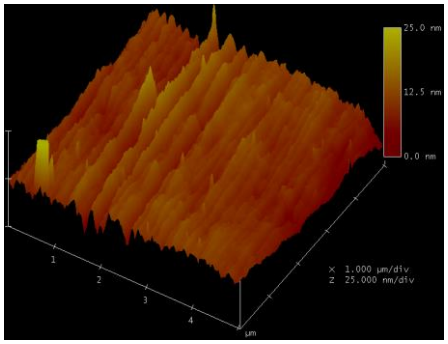

(c)

Figure 5- 24 *Effect of implantation energy on surface roughness of initially polished 304L stainless steel: (a) polished sample before implantation, (b) after implantation at 50 keV, and (c) after implantation at 160 keV. Implantation dose = 10^{12} Ru/cm^2.*

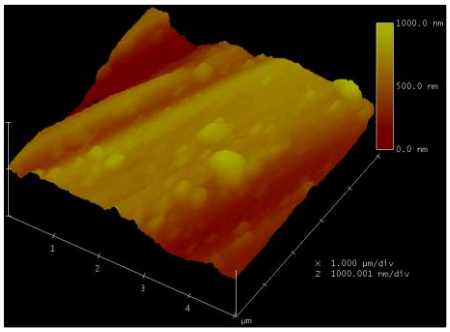

(a)

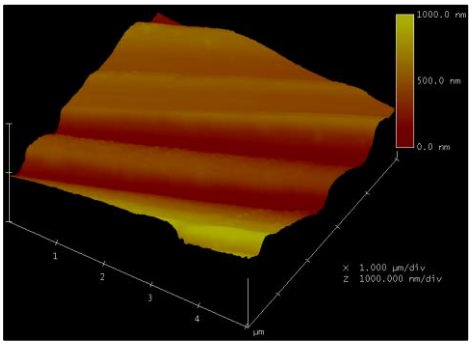

(b)

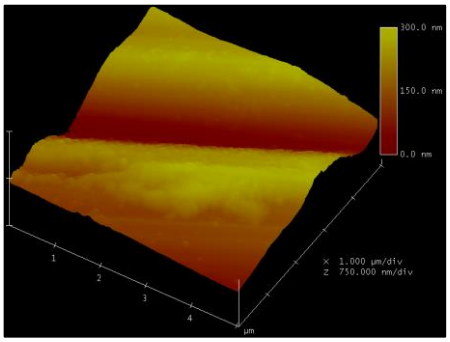

(c)

Figure 5- 25 *Effect of implantation energy on surface roughness of initially ground 304L stainless steel: (a) rough sample before implantation, (b) after implantation at 50 keV, and (c) after implantation at 160 keV. Implantation dose = 10^{12} Ru/cm^2.*

Sputtered depth can be related to sputtering yield (Y) by Equation 5-1 (Nunogaki et al. 1989), where A is the implanted area, N the atomic density of the implanted material, F the implanted dose, and d is the mean sputtered depth as defined by Equation 5-2. In Equation 5-2, d_i is the average depth in the analysed section.

$$Y = \frac{AdN}{F} \qquad \textbf{\textit{Equation 5-1}}$$

$$d = \frac{1}{n}\sum_{i=1}^{n} d_i \qquad \textbf{\textit{Equation 5-2}}$$

In this work, R_a values obtained via AFM analysis before and after ruthenium implantation were used to characterise d_i in Equation 5-2, and generate the graph in Figure 5-26. The graph confirms that sputtering yield was larger from rough surfaces; especially those implanted using high implantation energy. From Equation 2-13, it is clear that the maximum transferable energy during ion implantation is a direct function of the energy of the implanted ions. Thus, it was plausible to anticipate sputtering yield to increase with increase in implantation energy. However, the observed trend concerning surface roughness was contrary to expectation. Previous researchers (Mattox 1998; Smentkowski 2000) showed that sputter yield generally decreased with increase in the roughness of a target.

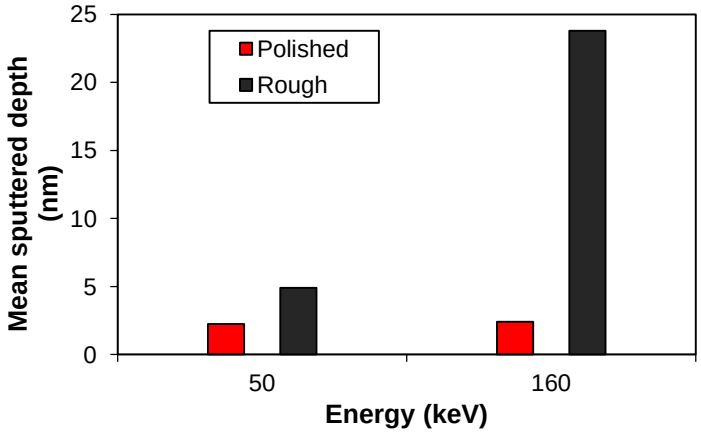

Figure 5- 26 *Energy dependence of mean sputtered depth on ruthenium implanted 304L stainless steel.*

Corrosion rates

Samples with different surfaces were prepared by ion implanting with 10^{14} Ru/cm^2 at 50 keV. These samples were exposed to 1 M sulphuric acid, and potentiodynamically polarised at 0.5 mV/s. Corrosion parameters extrapolated from the measured curves are presented in Figure 5-27.

The results obtained confirm the findings of the DOE study presented in Section 5.2.2, confirming that rough samples implanted as 50 keV and 10^{14} Ru/cm^2 performed better than polished samples prepared under the same conditions. They also showed that (1) increasing surface roughness beyond merely grinding e.g. sand blasting, did not necessarily effect change in corrosion performance, and (2) foregoing surface preparation pre implantation resulted in corrosion rates as high as those of unmodified 304L stainless steel.

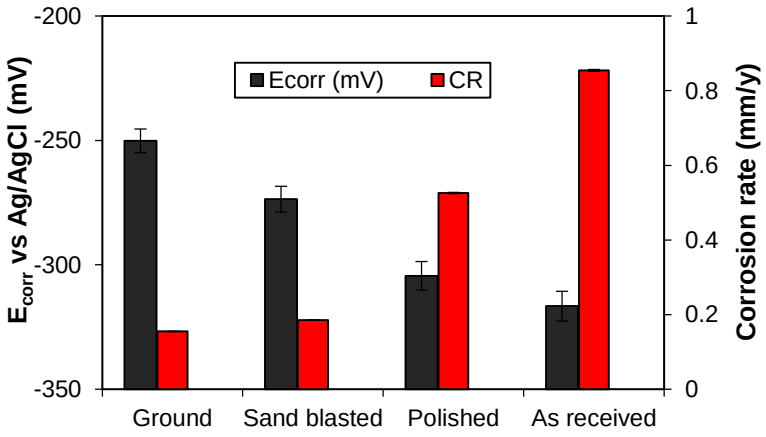

Figure 5- 27 *Effect of surface preparation on corrosion potential, and corrosion rates of ruthenium implanted 304L stainless steel in 1 M sulphuric acid.*

5.2.4 Effect of dose

Stress and concentration

Routine XRD measurements were done on rough samples (120 grit) implanted with doses ranging from 10^{12} to 10^{16} Ru/cm^2, and the results are presented in Figure 5-28 and Table 5-4. Strain in Table 5-4 was calculated with reference to as-received 304L stainless steel in Figure 4-8.

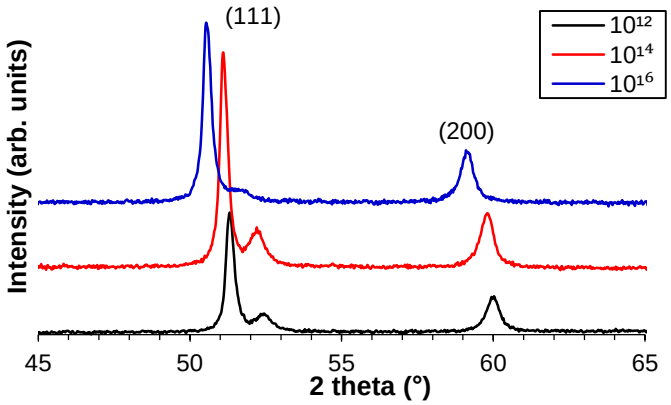

Figure 5- 28 *Influence of implantation dose on Bragg angle of ruthenium implanted 304L stainless steel. Samples were rough, and implantation energy was 50 keV. Only the (111) and (200) peaks are shown.*

Table 5- 4 *Dose dependence of lattice parameter and strain in ruthenium implanted 304L stainless steel. Values expressed to 4 s.f.*

Dose Ru/cm²	Peak	Bragg angle (°)	d spacing (Å)	Lattice parameter (Å)	Strain
As received 304L	111	51.97	2.043	3.538	-
	200	60.64	1.773	3.546	-
10^{12}	111	51.30	2.067	3.581	-0.01194
	200	60.02	1.789	3.579	-0.00925
10^{14}	111	51.09	2.075	3.595	-0.01573
	200	59.81	1.795	3.590	-0.01243
10^{16}	111	50.54	2.097	3.632	-0.02572
	200	59.10	1.815	3.630	-0.02313

As observed in Figure 5-28, increasing dose had the notable effect of shifting the Bragg angles of the (111) and (200) peaks to lower 2θ values. For instance, the (111) peak shifted from ≈ 51.3° for the samples implanted with 10^{12} Ru/cm^2 to ≈ 50.5° for those implanted with 10^{16} Ru/cm^2. This is consistent with (1) an increase in compressive surface stresses, and (2) an increase in the concentration of ruthenium in the lattice of the stainless steel. The ferrite (110) peak at 2θ ≈ 52° disappeared at the high (10^{16} Ru/cm^2), suggesting a deviation in crystallographic orientation. Dudognon and colleagues (2008) reported similar behaviour when 430 stainless steel was implanted with 3 x 10^{16} Ag/cm^2.

Strain induced by the implantation process was calculated from Equation 3-4, and presented in Table 5-4. The variation in strain suggests that residual stresses became increasingly compressive with increase in dose. Increasing implantation dose at constant energy entails increasing implantation time as shown in Equation 5-3, where I is the beam current, t the implantation time, A the beam scanning area and q the elementary charge (1.6 x 10^{-19} C). This means that for the higher ruthenium dose, more time was spent bombarding the stainless steel substrate, resulting in larger compressive surface stresses.

$$Dose = \frac{It}{qA} \qquad \textbf{\textit{Equation 5-3}}$$

As expected, lattice volume expansion increased with increase in ion implantation dose. The relative lattice expansion due to introducing ruthenium in the austenite lattice was in the range of 0.9 to 1.2%, and 2.4 to 2.7% for the samples implanted with 10^{12} and 10^{16} Ru/cm^2 respectively.

Surface sputtering

AFM images of 304L stainless steel before and after implantation at 10^{12} and 10^{16} Ru/cm^2 are presented in Figures 5-29 and 5-30.

Figures 5-29 and 5-30 suggest that at high dose (10^{16} Ru/cm^2), the surfaces became smoother for the initially rough surfaces, but did not seem to influence surface roughness of initially polished samples. The mean sputtered depth was calculated as per Equation 5-2, and presented in Figure 5-31. It is apparent that mean sputtered depth increased with increase in dose, implying that sputter yield increased with dose. This was consistent with results reported by Nunogaki et al. (1989).

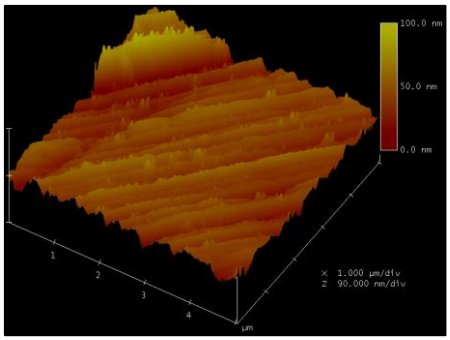

(a)

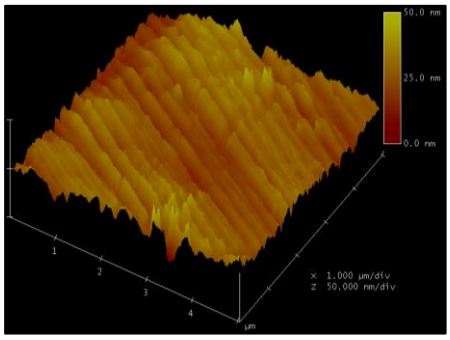

(b)

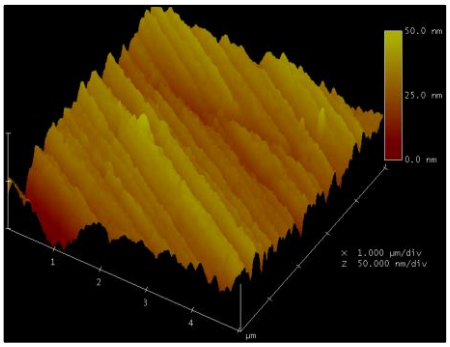

(c)

Figure 5- 29 *Effect of implantation dose on surface roughness of initially polished 304L stainless steel: (a) polished sample before implantation, (b) after implantation with 10^{12} Ru/cm^2, and (c) after implantation with 10^{16} Ru/cm^2. Implantation energy = 50keV.*

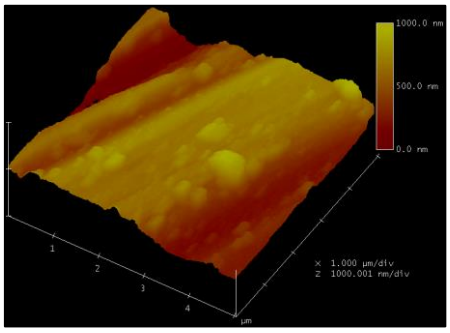

(a)

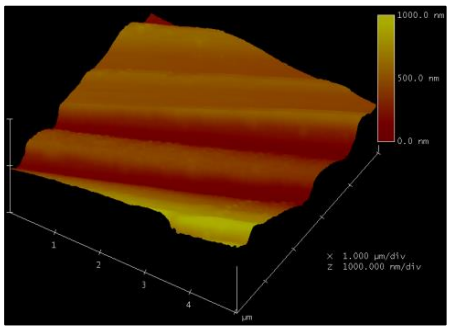

(b)

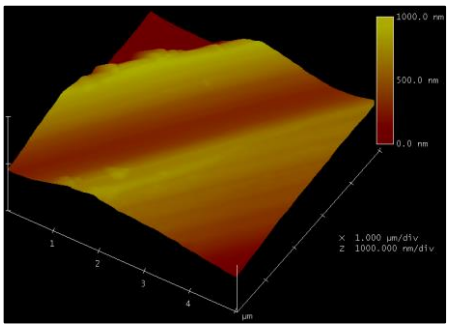

(c)

Figure 5- 30 *Effect of implantation dose on surface roughness of initially polished 304L stainless steel: (a) rough sample before implantation, (b) after implantation with 10^{12} Ru/cm^2, and (c) after implantation with 10^{16} Ru/cm^2. Implantation energy = 50keV.*

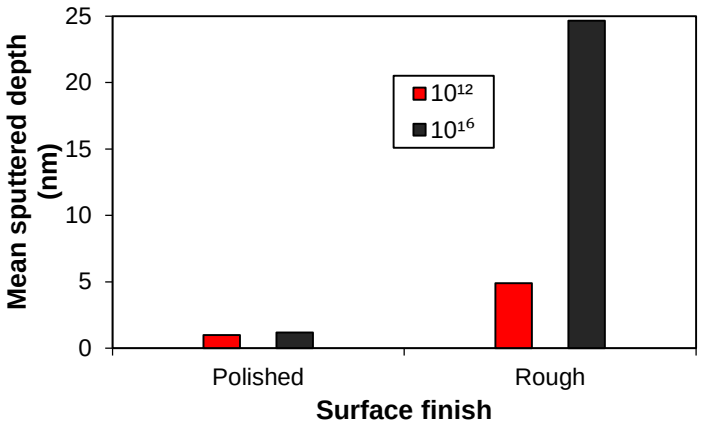

Figure 5- 31 *Dose dependence of mean sputtered depth on ruthenium implanted 304L stainless steel.*

Comparing Figure 5-29 to 5-31 with Figures 5-24 to 5-26 revealed that increasing dose had almost the same effects on sputter yield from rough surface as increasing implantation energy. In both cases, increasing dose and increasing energy caused an 80% and 79% change in surface roughness respectively. On the other hand, increasing dose seemed to cause higher sputter yield on polished surfaces than increasing implantation dose. Increasing implantation dose to 10^{16} Ru/cm^2 caused a 90% change in surface roughness, compared to ≈ 8% caused by increasing energy.

Corrosion rates

Ruthenium implanted 304L stainless steel samples were prepared at 50 keV, and different implantation doses, before being exposed to 1 M sulphuric acid. Corrosion rates estimated from potentiodynamic polarisation tests are presented in Figure 5-32.

It is clear that increasing implantation dose increased the corrosion resistance of the ruthenium implanted 304L stainless steel. Corrosion potential increased with dose, consistent with the principles of cathodic modification, and observations by other scholars (Potgieter & Brookes 1995; Olubambi et al. 2009; Sherif 2011). Corrosion rates decreased from an average of ≈ 0.24 mm/y on samples implanted with 10^{12} Ru/cm^2 to about 0.008 mm/y for samples prepared with 10^{16} Ru/cm^2. This was consistent with the expectation that increasing implantation dose would increase the amount of ruthenium accessible for participation in corrosion processes.

However, increasing dose from 10^{14} to 10^{16} Ru/cm^2 seemed to cause a small change in corrosion rate. In fact, such an increase in dose only caused about 12% decrease in corrosion rates. There is a limiting concentration associated with ion implantation, and the effect is most significant for heavy elements such as ruthenium and other PGMs that typically have large sputtering coefficients (Bunker & Armni 1994). This limiting concentration limit is reached when there is a steady state in which the rate of material removal by sputtering matches the rate of material addition by ion implantation. It is likely therefore, that increasing implantation dose beyond 10^{16} Ru/cm^2 would not be necessarily beneficial for corrosion resistance of 304L stainless steel.

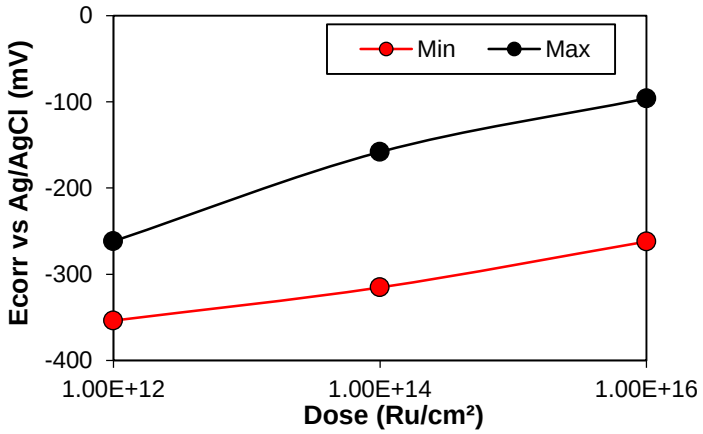

(a)

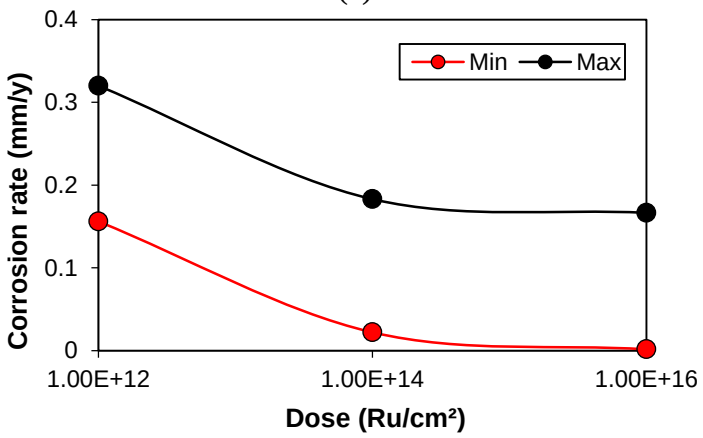

(b)

Figure 5- 32 *Influence of implantation dose on (a) corrosion potential, and (b) corrosion rate of ruthenium implanted 304L stainless steel in 1 M sulphuric acid. Samples were rough and implantation energy was 50 keV.*

One way of increasing the surface concentration of implanted elements without increasing dose or implantation costs is to tilt the substrate, and affecting beam

incidence angle. Titling the substrate would minimise the effects of channelling, reduce depth of penetration (Chang & Ameen 2011), and therefore increase the surface concentration of the ruthenium. For the present work, the 304L stainless steel substrate was tilted by 7°.

XRD measurements done post ion implantation are presented in Figure 5-33. It is immediately clear that tilting the 304L stainless steel sample by 7° had numerous effects on the diffractograms.

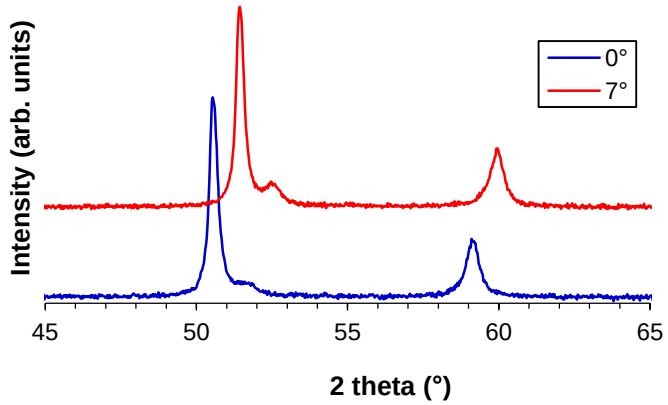

Figure 5- 33 *Effect of sample orientation on the Bragg angle of ruthenium implanted 304L stainless steel. Samples were rough, and implanted with 10^{16} Ru/cm^2 at 50 keV.*

Titling the stainless steel substrate increased the Bragg angle to higher values, from 2θ ≈ 50.5° for the sample oriented at 0°, to about 51.5°, which is approximately equal to that of unmodified 304L. This seems to suggest that either negligible stresses were induced in the substrate during ion implantation, or less ruthenium was successfully implanted into the surface resulting in only a slight change in the lattice volume. It is also likely that tilting the stainless steel aligned the incident angle of the ruthenium ions with the channelling direction, and increased P_R to values much greater than 13 nm predicted in Figure 5-2. In addition, tilting the stainless steel substrate led to the reappearance of the ferrite (100) at 2θ ≈ 52.8°.

Post XRD analysis, the samples were exposed to 1 M sulphuric acid, and polarised potentiodynamically. The results obtained are presented in Figures 5-34 and 5-35. Immediately clear from the potentiodynamic polarisation curves in Figure 5-34 was the absence of the anodic peak typical of 304L stainless steel in 1 M sulphuric acid (Figure 4-11). This is consistent with instant passivation associated with the presence of

ruthenium, similar to the behaviour noted by other scholars (Potgieter & Kincer 1991; Olubambi et al. 2009) on stainless steel with at least 0.1 wt% ruthenium. Changing the orientation to 7° shifted the curve downwards and to the right: indicative of increased tendency to corrode. Examination of the corroded surfaces in Figure 5-35 confirmed this. Images of the polished samples were added to show repeatability.

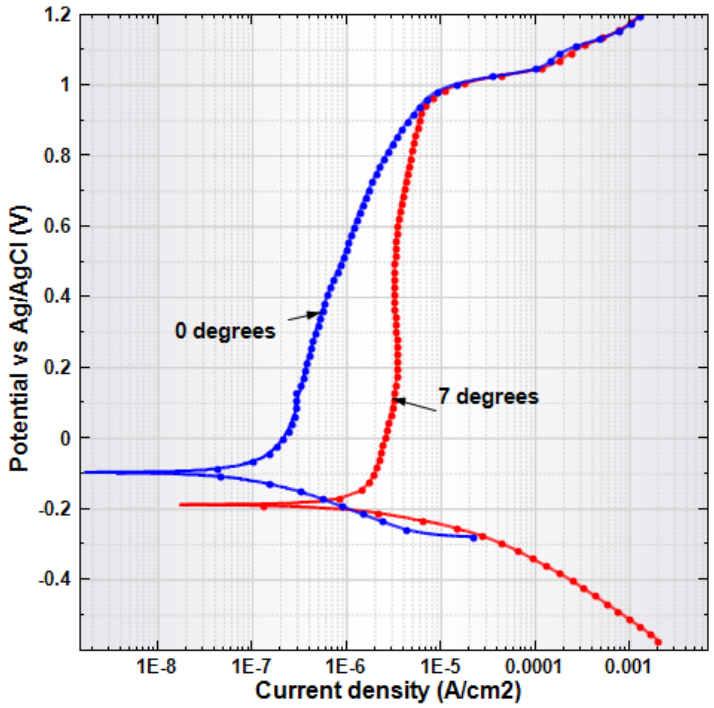

Figure 5- 34 *Effect of sample orientation on potentiodynamic polarisation curves ruthenium implanted 304L stainless steel in 1 M sulphuric acid. Samples were rough and implanted at 50 keV with* 10^{16} *Ru/cm*^{2}.

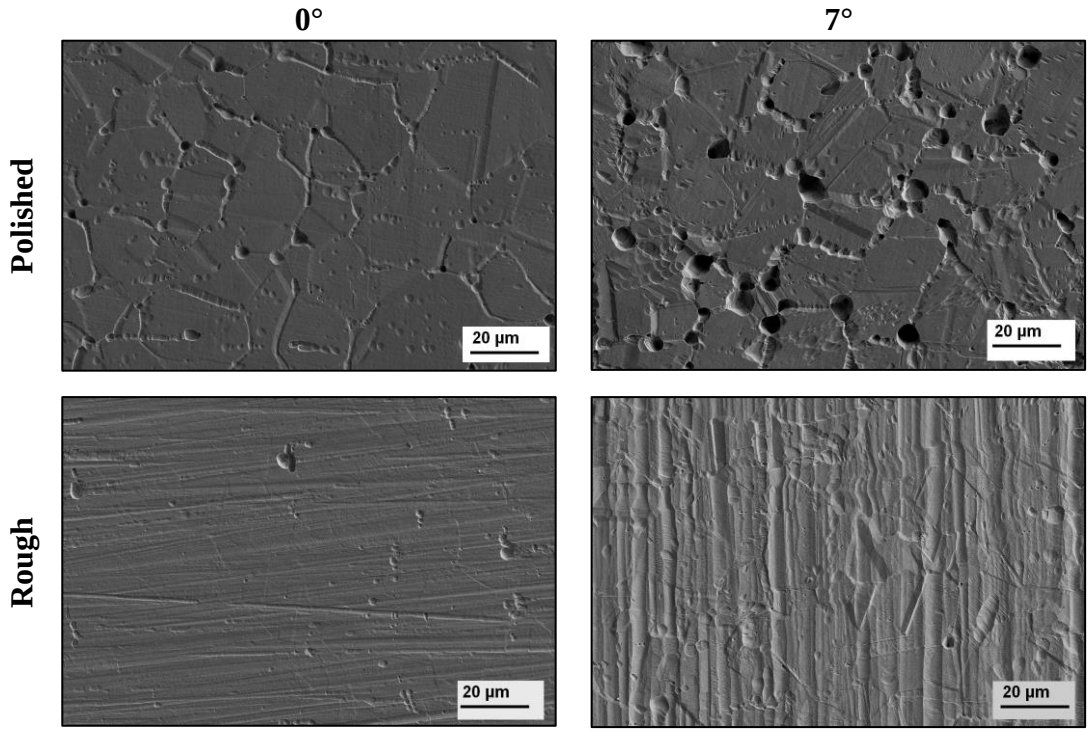

Figure 5- 35 *FESEM images of the ruthenium implanted 304L stainless steel exposure to 1 M sulphuric acid showing effect of sample orientation on corrosion.*

Corrosion rates extrapolated from the potentiodynamic curves in Figure 5-34 were compared with the ruthenium distribution as determined by SRIM simulation. The results obtained are presented in Table 5-5.

Table 5- 5 *Effect of sample orientation on the ruthenium distribution and average corrosion rate of rough ruthenium implanted 304L stainless steel. Ruthenium distribution was determined by SRIM simulation.*

Sample orientation	0°	7°
Ion range (A)	132	133
Lateral straggle (A)	59	58
Skewness	0.580	0.556
Kurtosis	3.212	3.176
Corrosion rate (mm/y)	0.009	0.084

Projected range for the 0 and 7° orientations was 13.2 and 13.3 nm respectively. A more positive skewness was reported on the sample with 0° orientation, confirming that the peak concentration of ruthenium was closer to the surface. Furthermore, Kurtosis value for this sample was more positive, pointing to a longer tail of the Gaussian distribution

in Figures 2-17 and 5-2, and hence more channelling. However, in all the cases, the changes were minimal. This seems to suggest that sample orientation had no influence on the distribution ruthenium in the rough 304L stainless steel. Despite this, corrosion rates of the samples oriented at 7° were higher than those with 0° orientation.

5.3 Results: RF sputtering

This section of the chapter seeks to present, and describe the results of the synthesis of ruthenium surface alloys via RF sputtering.

5.3.1 SRIM simulation

Sputtering of ruthenium by argon was simulated using SRIM-2008 in the full cascade option, and the results obtained are presented in Figure 5-36. Simulation was done using 5000 ions.

Sputter yield of ruthenium in Figure 5-36(a) was shown to increase with increase in the incident energy of the argon ions. This is consistent with the expectation that with higher energy, momentum, and therefore, energy transferred to the ruthenium atoms, as per Equation 2-13, would be larger. Figure 5-36(b) concurs this.

At higher energies, increasing incident energy did not seem to significantly affect ruthenium-sputtering yield. For instance, increasing energy from 0.5 to 1 keV caused a 53% increase in sputtering yield, while increasing energy from 8 to 10 keV only resulted in ≈ 5% increase. It is likely that at these high energies, the argon ions tended to penetrate into the ruthenium target, and deposit most of their energy deep into the target. Such a situation results in ion implantation and less sputtered material. The consequence is reduction in deposition rates, as observed by previous researchers (Chaoumead et al. 2012).

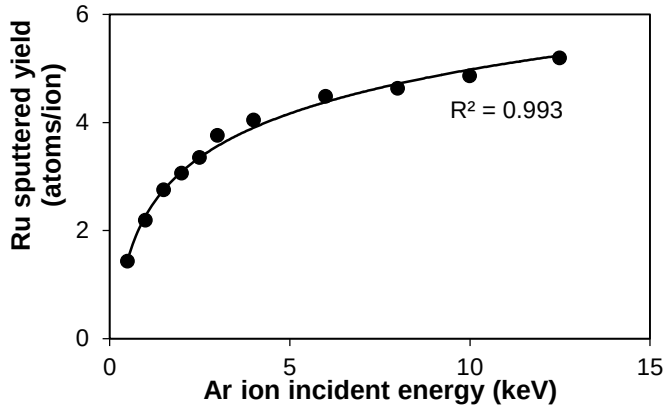

(a)

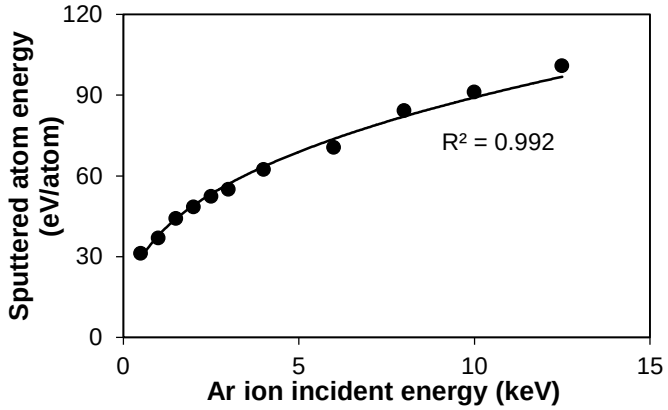

(b)

Figure 5- 36 *Variation of (a) ruthenium sputter yield, and (b) energy of sputtered ruthenium atoms as a function of argon incident energy. Results obtained from SRIM simulations.*

5.3.2 Determination of parameters

A one-factor-at-a-time approach was used to determine the influence of deposition power and deposition time on the corrosion resistance of 304L stainless steel sputter coated with ruthenium. Initial sputtering conditions were as follows: power was held at 30, 100 and 200 W, while time was limited at 3 and 5 minutes. All 304L samples were polished using 6 μm alumina powder as described in Section 3.2.1.

XRD measurements were done on the sputter coated 304L stainless steel, and typical diffractograms are presented in Figure 5-37. The Bragg position of the (111) and (200) reflexes corresponding to 304L stainless steel remained largely unaltered at $2\theta \approx 51°$ and 59° respectively, when deposition power was increased. This suggests that any stresses induced during sputtering were not transferred to the substrate. A peak was

observed at around 48°, and was found to match the (0022) reflection of a hexagonal close packed (HCP) crystal structure of ruthenium according to PDF 00 006 0663.

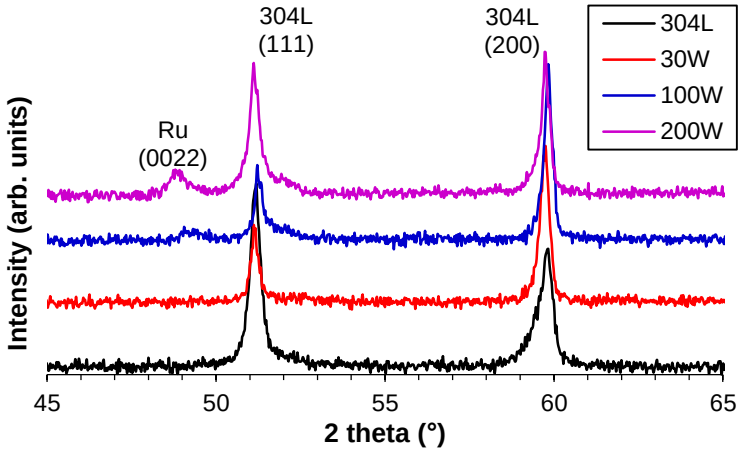

Figure 5- 37 *Influence of deposition power on XRD patterns of 304L stainless steel coated with ruthenium films, referenced against PDF 04 002 1898 and PDF 00 006 0663. Deposition time = 3 minutes.*

The (0022) ruthenium peak was observed on samples prepared at 100 and 200 W. This is consistent with the expectation that ruthenium sputter yield would be larger at higher powers (Figure 5-36(a)), and therefore more material would be available for sputter deposition on the stainless steel substrate. The presence of a single ruthenium (0022) peak suggested preferential film growth. Other researchers (Meng & Santos 1999; Vasu et al. 2014) also observed similar preferential growth of thin films, and could be due to the constraints presented by the thin size of the films. These peaks were however too small for meaningful grain size analysis.

As can be seen in Figure 5-37, the intensity of the (0022) peak was most prominent at sputtering power of 200 W. A closer examination of this peak revealed it shifted to lower Bragg angles with increase in deposition power. The shift indicates that higher compressive stresses were induced in the film during sputter deposition. Generation of compressive film stresses during RF sputter deposition have been reported by previous researchers (Meng & Santos 1999; Bhatt et al. 2007; Detor et al. 2009), and was attributed to the bombarding effect of ions and atoms impinging on the substrate.

Post deposition, the films were examined by FESEM and AFM, and the results obtained are presented in Figures 5-38 to 5-40. EDS analysis of the sputtered films in Figure 5-38

shows that they were made entirely of ruthenium. This was consistent with expectation, and the XRD measurements reported in Figure 5-37.

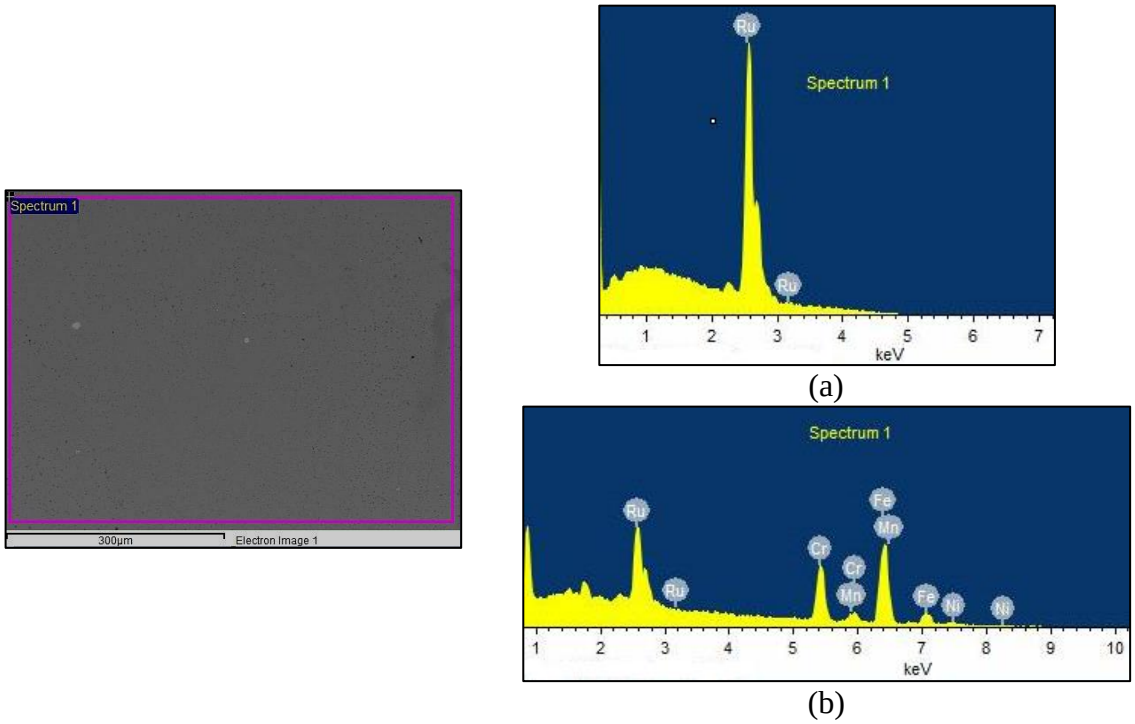

Figure 5- 38 *EDS analysis of the RF sputtered films. Beam voltage used was (a) 5 kV, and (b) 10 kV.*

Both Figures 5-39 and 5-40 show that the surface morphology of the ruthenium films was strongly dependent on deposition power and deposition time. Deposits made at 30 W were flat, continuous and mostly featureless regardless of deposition time. Particulates observed on some of these films, and illustrated more clearly in Figure 5-40 were made entirely of ruthenium, since EDS analysis in Figure 5-38 could not detect the presence of other elements in the film. Particulates have been associated with pressed powder targets (Mattox 1998). Nonetheless, these particulates were not expected to influence corrosion performance.

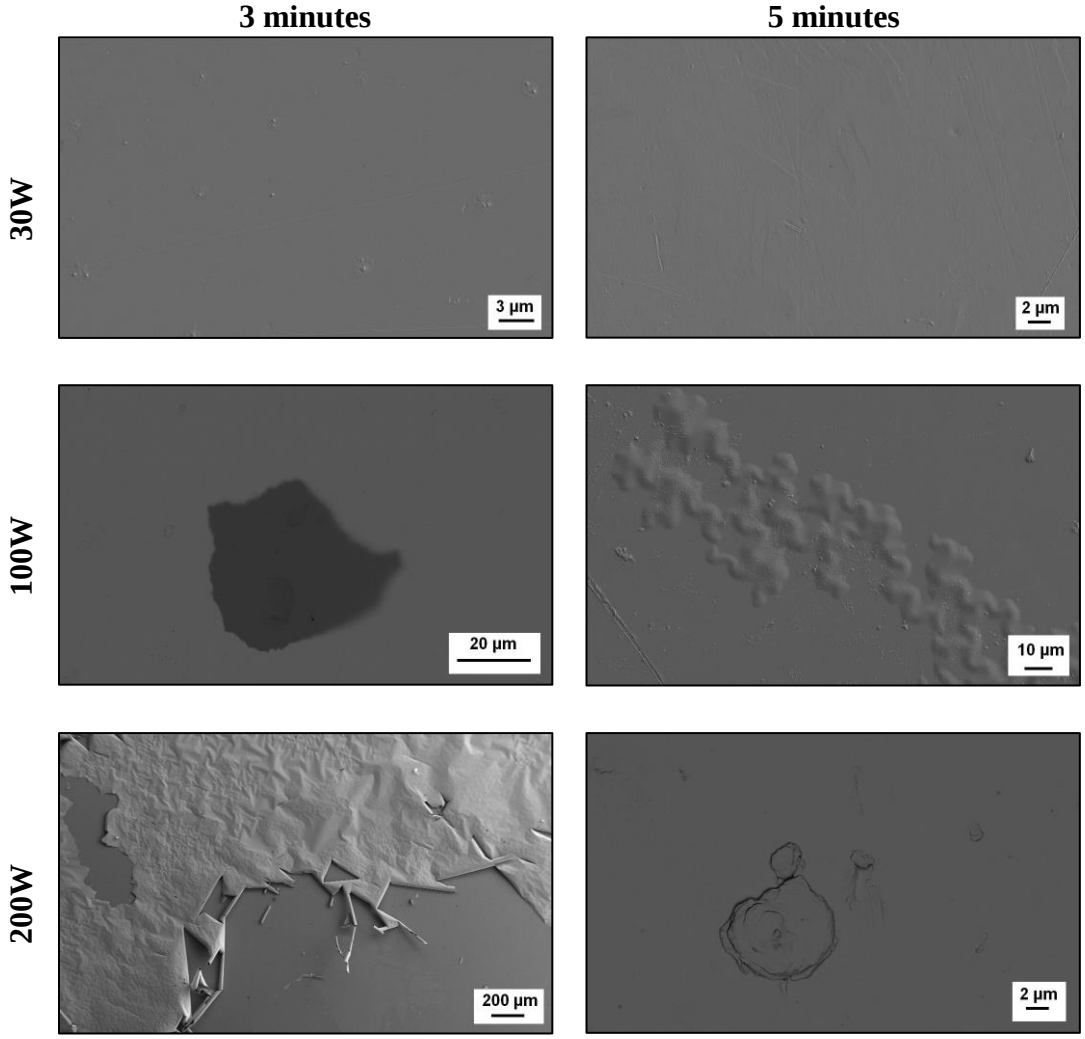

Figure 5- 39 *Influence of deposition power and time on the types of defects observed on the ruthenium films produced by RF sputtering, and viewed by FESEM.*

Increasing deposition power to 100 and 200 W led to the formation of a variety of defects. At 100 W and low deposition time, the films exhibited bare spots and film wrinkling. Bare spots suggest low surface coverage, which was not expected at 100 W since ruthenium sputter yield was shown to increase with deposition power in Figure 5-36. Though care was taken in sample preparation pre sputtering (Section 3.2), it is possible that these bare spots were due dust or artefacts on the surface.

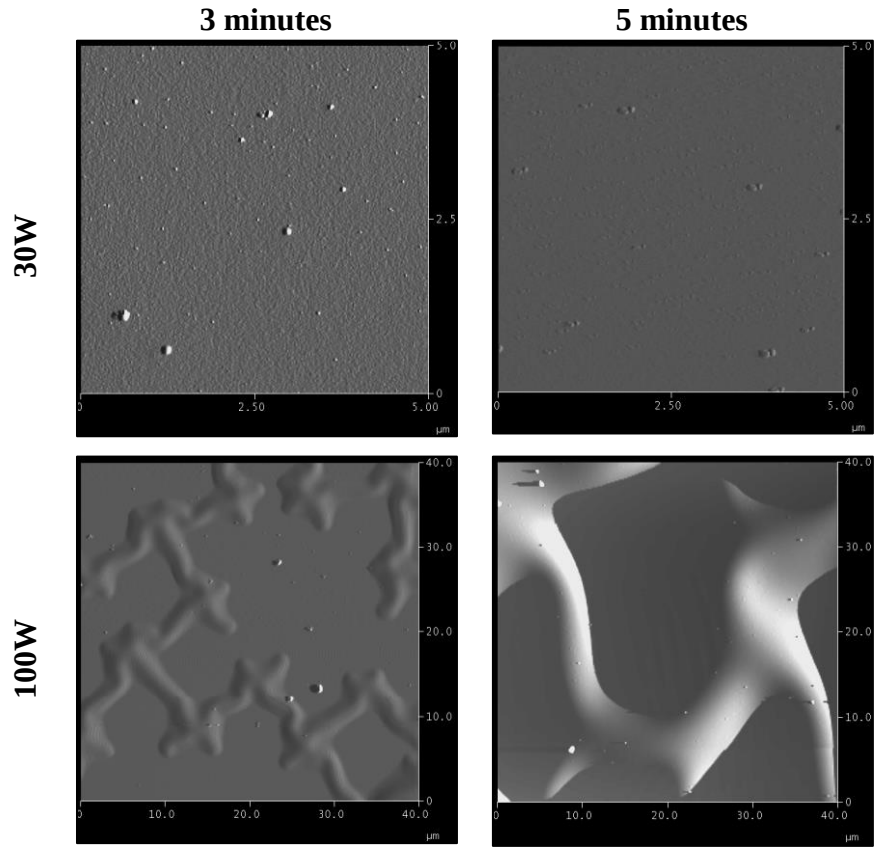

Figure 5- 40 *AFM images of ruthenium films produced at 30 and 100 W. Scan area was 40x40 μm^2.*

Film wrinkling on the other hand was consistent with the likely presence for compressive stresses in the films reported in Figure 5-37, and was in agreement with literature (Cuthrell et al. 1988; Ohring 2002). Film wrinkling is indicative of localised loss of adhesion, and in the case of the samples prepared at 100 W film wrinkling became more prominent with deposition time (Figures 5-39 & 5-40). This implies that the size of compressive stresses in the films possibly increased with increase in deposition time.

Films made at 200 W showed extensive flaking and peeling, proof of loss of adhesion to the 304L stainless steel substrate. It also points to the high compressive stresses induced during sputtering at high powers. High compressive stresses would be expected at high deposition power since atoms sputtered at high power have high energy (Figure 5-36(b)). In addition to wrinkling and peeling, films deposited for 5 minutes, had ruthenium droplets, most of which were flattened and round. By virtue of their poor

mechanical integrity, films deposited at 200 W were excluded from further corrosion testing.

The corrosion performance of the film sputtered at 30 and 100 W was studied in 1 M sulphuric acid, and the parameters extrapolated from the potentiodynamic polarisation tests are presented in Table 5-6.

Table 5- 6 *Corrosion parameters of 304L stainless steel sputter coated with ruthenium. Results derived from potentiodynamic polarisation in 1 M sulphuric acid.*

Deposition power (W)	Deposition time (mins)	E_{corr} vs Ag/AgCl (mV)	R_p (kΩ.cm)	i_{corr} (μA/cm²)	Corrosion rate (mm/y)
30	3	453	137.1	0.160	0.002
	5	418	11.0	1.998	0.021
100	3	441	18.1	1.218	0.013
	5	428	15.2	1.451	0.016

Values of E_{corr} obtained on the 304L stainless steel sputter coated with ruthenium were greater than 400 mV. This was several magnitudes greater than those recorded on unmodified 304L stainless steel in Figures 3-5 and 4-11, and is in the region where protective chromium III species are thermodynamically stable (Figure 2-3). The increase in E_{corr} to much nobler potentials is consistent with the principles of cathodic modification described in Figure 2-10. While there did not seem to be a correlation between E_{corr} and deposition power, Table 5-6 shows that corrosion potential decreased with increase in deposition time. The decrease in E_{corr} was however not significant enough to markedly influence corrosion rates.

Corrosion rates generally increased with deposition power and deposition time. Increasing deposition power was shown in Figure 5-39 to have a detrimental effect on the adhesion of the ruthenium films; hence, it was understandable to expect this trend in corrosion rate. Figure 5-40 suggested that higher compressive stresses were induced on films deposited for longer deposition times, which caused loss of adhesion. While there was no physical evidence to support this, it is likely that similar behaviour occurred on the films deposited at 30 W for 5 minutes. As can be seen in Figure 5-41, this film lost adhesion and delaminated during exposure to the sulphuric acid.

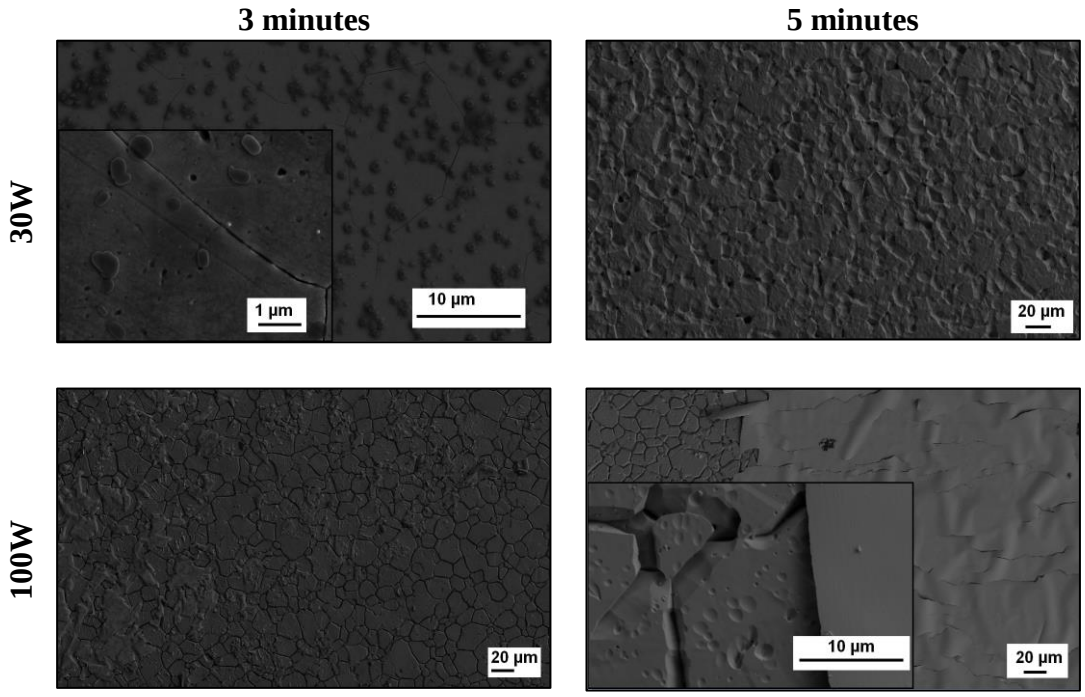

Figure 5- 41 *FESEM-SE images of the ruthenium coated 304L stainless steel after 12 hours of exposure to 1 M sulphuric acid.*

The films produced at 100 W and for 5 minutes, though largely fractured and damaged post corrosion exposure (Figure 5-41), remained on the substrate, affording the metal partial coverage. This could explain the unexpectedly lower corrosion rates recorded on these films when compared to that deposited at 30 W for the same deposition time in Table 5-6. Comparing pre and post corrosion surface morphology of the films produced at 100 W and 5 minutes (Figures 5-39 & 5-41), suggests a possible stress relaxation parallel the substrate surface during corrosion exposure. Stress relaxation in thin films may lead to cracking or fracture (Ohring 2002).

From Figure 5-41, it is clear that corrosion attack initiated at the grain boundaries, and progressed even under the ruthenium films. The films produced at 30 W, 3 minutes experienced the least damage. Round flat deposits were observed on the surface of this sample. These precipitates were too small and too sparsely distributed to be meaningfully analysed by EDS. However, it was assumed that they consisted of ferrous sulphate, similar to those deposited on ion implanted 304L stainless steel samples shown in Figure 5-13 and 5-14. These precipitates were not observed on the other

sputter-coated samples, and could have contributed to the low corrosion rates in Table 5-6. Further analysis of the ruthenium coated 304L stainless steel was limited to samples prepared at 30 W.

5.3.3 Effect of deposition time

Figure 5-42 shows that film thickness as measured by X-ray reflectivity (XRR) increased with increase in deposition time. It was therefore anticipated that increasing deposition time the protection efficiency of the ruthenium films. Table 5-6 and Figure 5-41 gave the impression that increasing deposition time caused a decrease in the corrosion performance of the ruthenium films. However, further study was required to verify this trend. As such, more films were prepared at 30 W and deposition times ranging from 3 to 30 minutes.

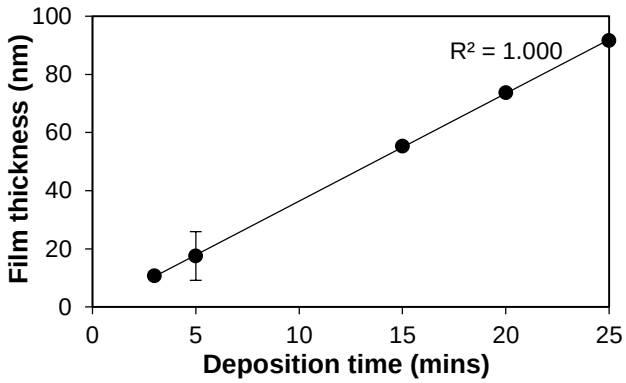

Figure 5- 42 *Influence of deposition time on the thickness of ruthenium films deposited on 304L stainless steel by RF sputtering*

Pre corrosion examination of the deposited films was done using FESEM and AFM. The images obtained are presented in Figure 5-43. In all the cases studied, the surface morphology did not seem influenced by deposition time: the films remained continuous, smooth and mostly featureless. Round hillocks were observed on the films via AFM, the density of which decreased with increase in deposition time. The size of the hillocks increased with longer deposition times. D´heurle (1970) showed that the presence and density of hillocks on RF sputtered films decreased with high deposition rates, and increase in film thickness. These hillocks were not expected to pose any problems in the corrosion performance of the ruthenium films.

XRD measurements were done on the films and the results are presented in Figure 5-44. The Bragg position of the (111) and (200) peaks of 304L stainless steel did not change with increase in deposition time. This implies that any stresses generated in the ruthenium films were not transferred to the stainless steel substrate consistent with the observations made in Figure 5-37.

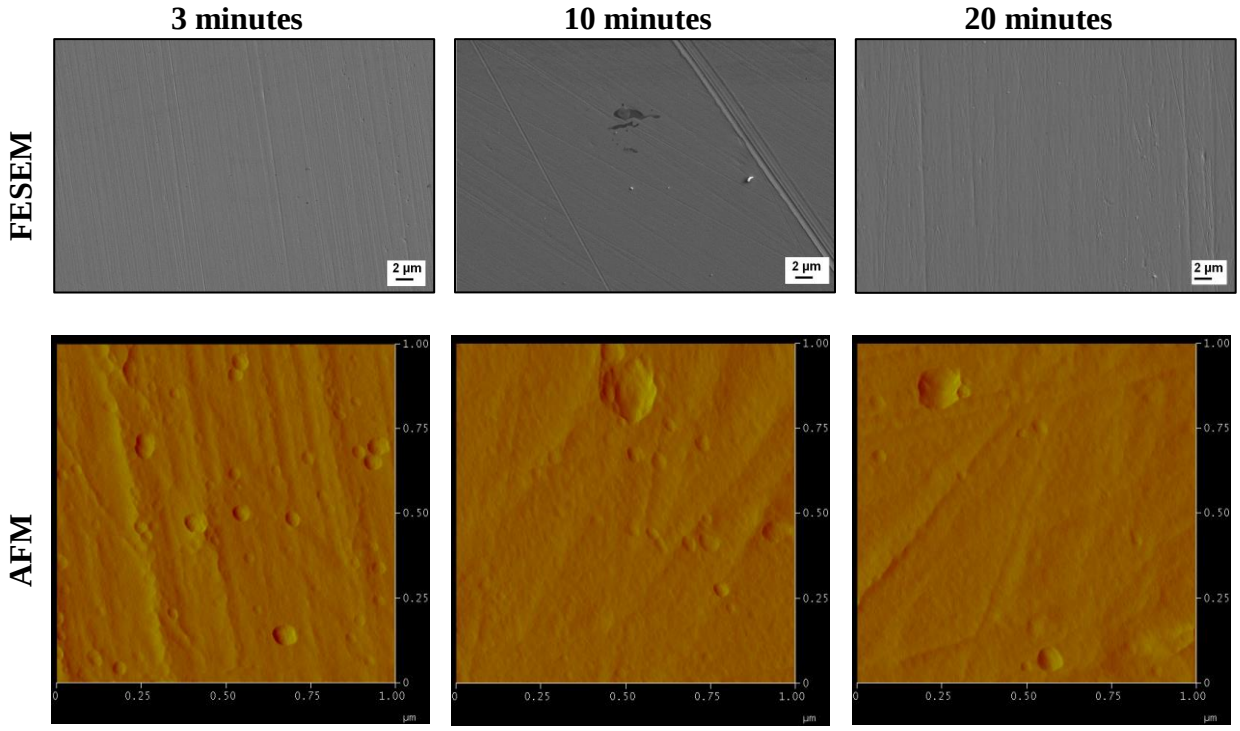

Figure 5- 43 *FESEM and AFM of ruthenium films deposited on 304L stainless steel at 30 W and different deposition times.*

In Figure 5-44, two ruthenium peaks were observed at 2θ ≈ 44.7 and 49.2°, and corresponded to the (1000) and (0022) peaks respectively (PDF 00 006 0663). The (0022) peak appeared after 10 minutes of deposition, and even then, it was poorly defined and unresolvable for meaningful analysis. The appearance and increase in intensity of the ruthenium peaks with increase in deposition time was consistent with increase in film thickness. Naturally, the larger the thickness of the film, the larger the electron interaction volume or scatter volume, and hence the larger the intensity of the ruthenium peaks. It seemed that crystals of the films deposited at lower deposition times were preferentially oriented, while those prepared at times ≥ 20 minutes were more randomly oriented.

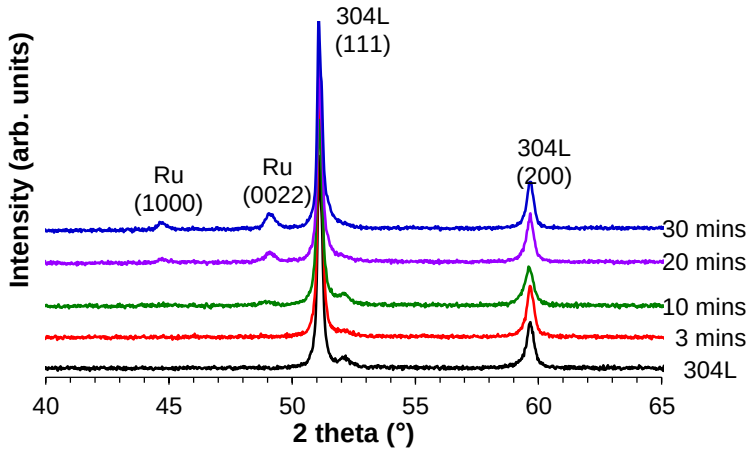

Figure 5- 44 *Influence of deposition time on the Bragg angle of ruthenium coated 304L stainless steel. Deposition power = 30 W.*

In Figure 5-44, two ruthenium peaks were observed at 2θ ≈ 44.7 and 49.2°, and corresponded to the (1000) and (0022) peaks respectively (PDF 00 006 0663). The (0022) peak appeared after 10 minutes of deposition, and even then, it was poorly defined and unresolvable for meaningful analysis. The appearance and increase in intensity of the ruthenium peaks with increase in deposition time was consistent with increase in film thickness. Naturally, the larger the thickness of the film, the larger the electron interaction volume or scatter volume, and hence the larger the intensity of the ruthenium peaks. It seemed that crystals of the films deposited at lower deposition times were preferentially oriented, while those prepared at times ≥ 20 minutes were more randomly oriented.

After XRD analysis, the films were exposed to 1 M sulphuric acid for up to 48 hours at ≈ 25°C. The performance of the ruthenium films was assessed via potentiodynamic polarisation and EIS, and the results obtained are presented in Figures 5-45 to 5-49.

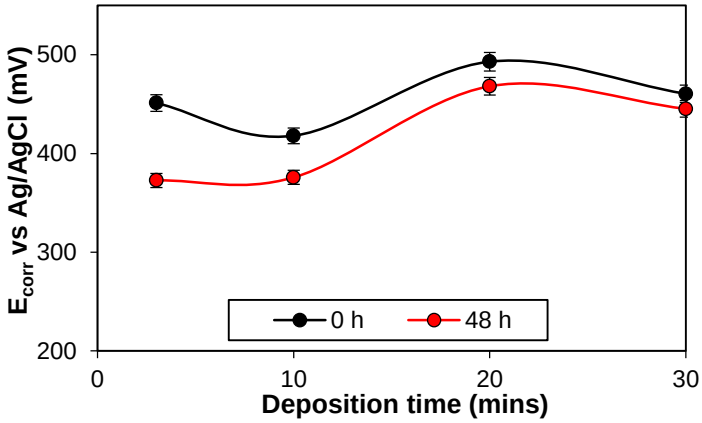

(a)

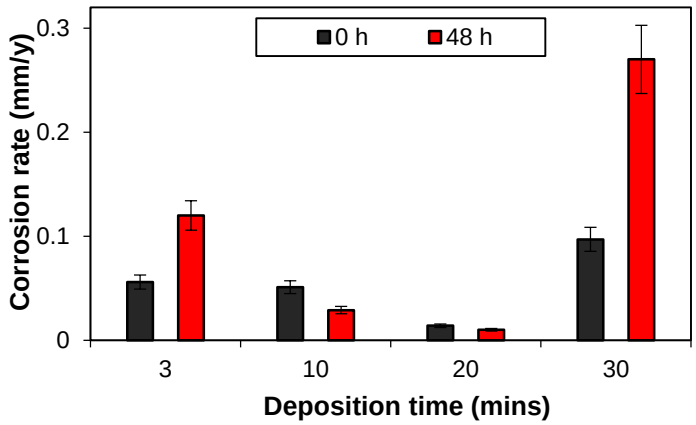

(b)

Figure 5- 45 *Influence of deposition and exposure time on (a) corrosion potential, and (b) corrosion rate of ruthenium coated 304L stainless steel in 1 M sulphuric acid. Deposition power = 30 W*

In Figure 5-45(a), E_{corr} initially decreased, and then increased with increase in deposition time. The initial decrease observed when deposition time was increased from 3 to 10 minutes was consistent with the decrease reported in Table 5-6, and could be due to intrinsic stresses generated in the films as a result of increased film thickness. Increasing deposition time increased E_{corr} to 493 mV at 20 minutes from 418 mV at 10 minutes. The increase in E_{corr} was unexpected and was attributed to a possible change in the structure of the film suggested by the XRD diffractograms in Figure 5-44. It is likely that the different crystal orientation presented more surfaces for cathodic activity, increasing cathodic efficiency and shifting E_{corr} values to much nobler potentials.

A decrease in E_{corr} was observed after 48 hours of exposure to the sulphuric acid. The decrease was much larger for the films produced at lower deposition time. For instance,

the E_{corr} recorded on the film deposited from 3 minutes decreased by 17%, whereas a 5% decrease was associated with those produced for 20 minutes. This trend could be attributed to the higher amount ruthenium on thicker films: the higher the amount of ruthenium, the greater the effect of cathodic modification due to the PGM.

Figure 5-45(b) shows the influence of deposition time on corrosion rate of the ruthenium coated 304L stainless steel. In all cases, the corrosion rates were several magnitudes lower than that of the unmodified 304L stainless steel (Figure 3-5). Initial corrosion rates decreased with an increase in deposition time up to 20 minutes, but increased for higher deposition times. After 48 hours, corrosion performance of the films produced over 3 and 30 minutes deteriorated, with corrosion rates increasing by as much as 17%. The films produced for 10 and 20 minutes exhibited improved performance with increase in immersion time, with corrosion rates of the ruthenium coated stainless steel substrate decreasing by a factor of ≈ 1.7 and 1.4 respectively.

Analysis of the EIS measurements was done using Bode phase plots presented in Figure 5-46. In the early stages of immersion (Figure 5-46(a)), the Bode plots exhibited a single time constant: typical of relatively protective coatings. However, in all but one cases, the phase angle at both low and high frequencies tended towards zero, indicative of a reactive configuration (Orazem & Tribollet 2008). The phase angle recorded on the films deposited for 20 minutes was much closer to |90°|, and remained nearly constant over the test frequency spectrum, varying between |68| and |83°|. This points to a configuration with better protective abilities, and corroborates the results in Figure 5-45.

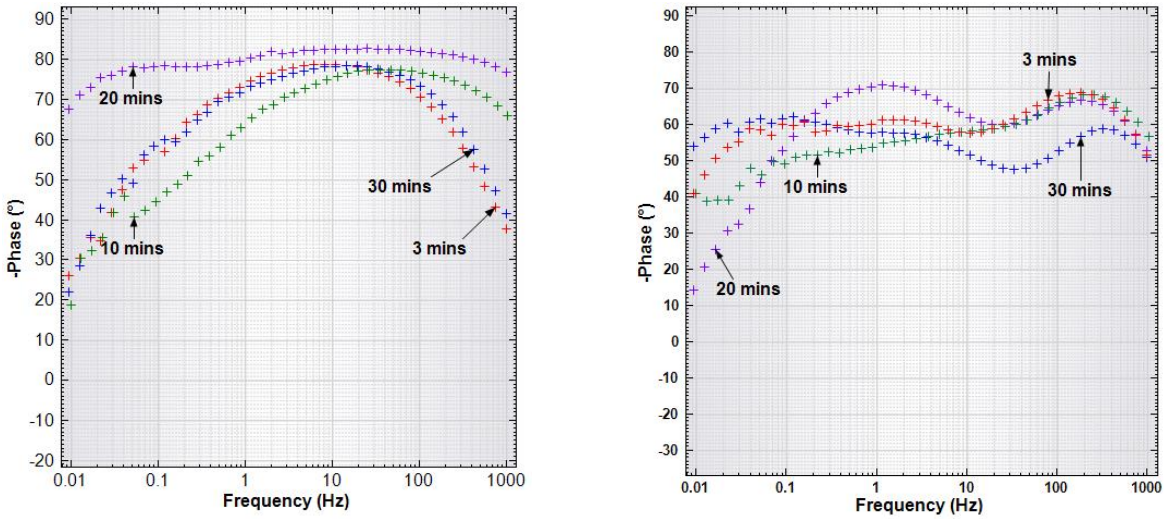

Figure 5- 46 *Bode phase plots for ruthenium coated 304L stainless steel in 1 M sulphuric acid (a) immediately upon exposure, and (b) after 48 hours of exposure.*

As can be seen in Figure 5-46(b), further exposure to 1 M sulphuric acid, caused the curves to resolve into two time constants. This behaviour suggests that discontinuities were developed on the ruthenium sputtered films during long-term immersion in sulphuric acid. Evident from Figure 5-46(b) is an increase in the phase angle at low and high frequencies for most of the films tested, implying improved protection efficiency. This apparent contradiction suggests the possibility of two protection mechanisms: (1) the ruthenium film, which isolates the substrate from the acid, and (2) a chromium oxide film formed at the favourable thermodynamic conditions induced by cathodic modification.

Visual examination of the coated samples post corrosion revealed that the ruthenium films were completely removed during corrosion exposure. This is shown in the images presented in Figure 5-47. Save for the samples prepared for 10 minutes, all the samples exhibited severe surface damage. Both grains and grain boundaries were attacked indiscriminately, giving the corroded samples a gouged appearance. Closer examination of the images in Figure 5-48 shows some remnant of the ruthenium films suggesting that the films did not dissolve, but fractured and chipped off the substrate. The images in Figure 5-47 corroborate the results of the EIS tests. However, they are seemingly inconsistent with the low corrosion rates reported in Figure 5-45(b). These observations

also support the possibility of more than one mechanism of corrosion protection as suggested earlier.

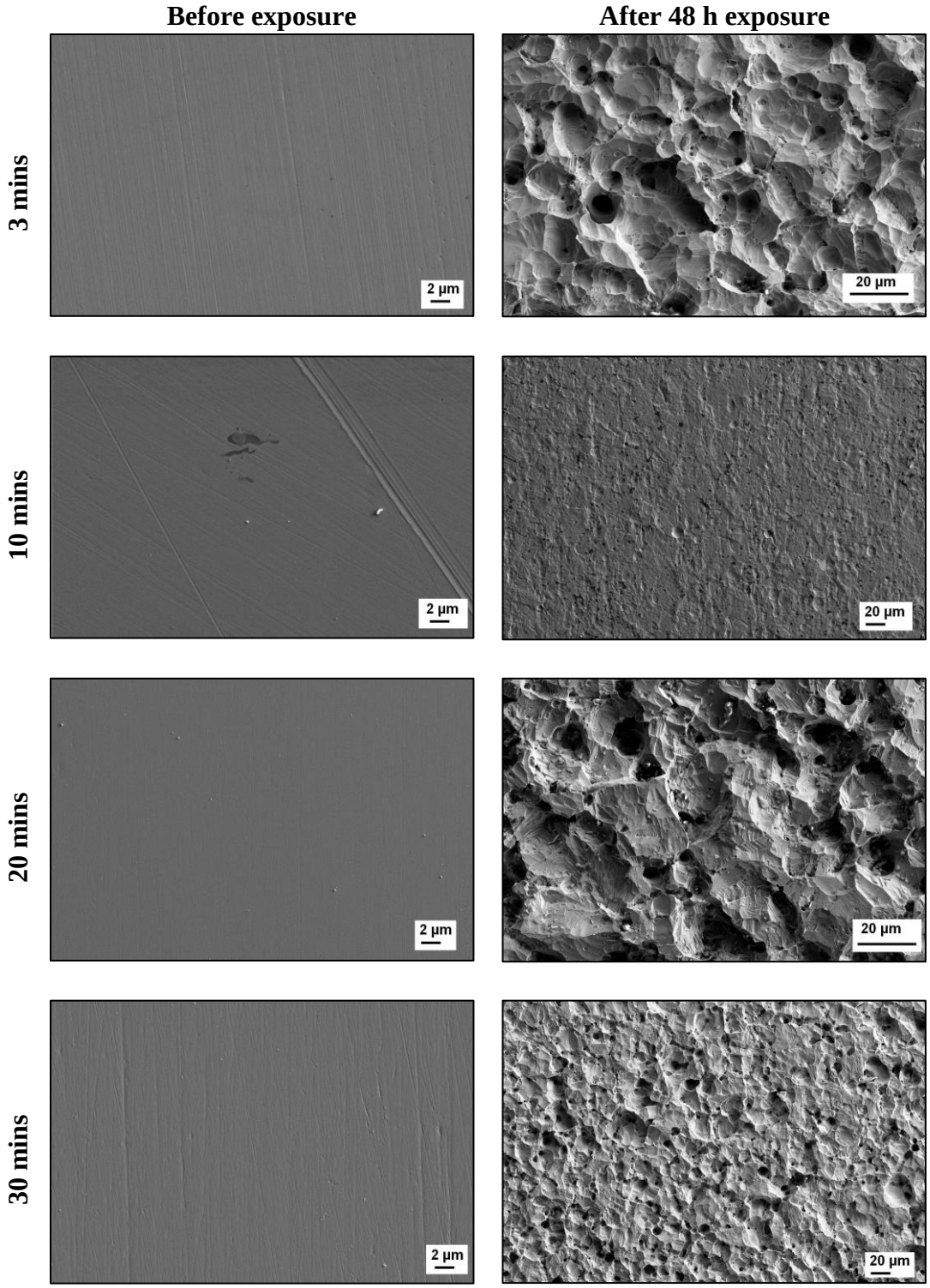

Figure 5- 47 *FESEM-SE images of ruthenium coated 304L stainless steel before and after 48 hours of exposure to 1 M sulphuric acid.*

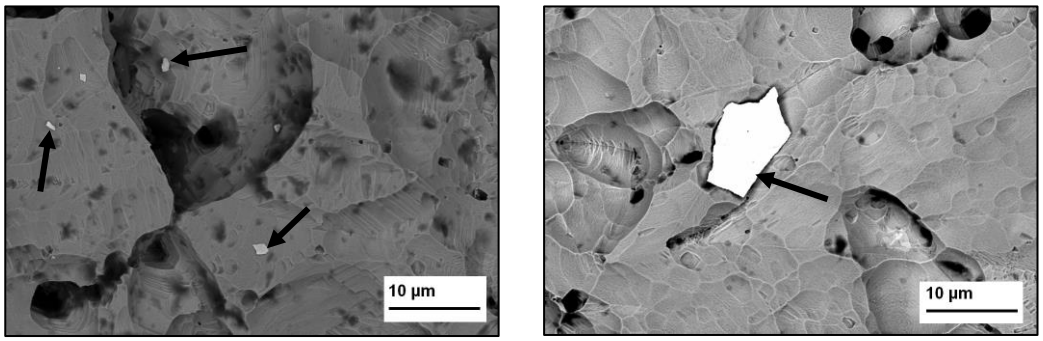

Figure 5- 48 *FESEM-BS images showing remnants of the ruthenium films on 304L stainless steel after 48 hours of exposure to 1 M sulphuric acid.*

Figure 5-49 presents the ion composition of the corrosion solutions. Consistent with Figures 5-45(b) and 5-47, the results show that low metal loss was experienced on the sample sputter coated for 10 minutes. Despite the notably low corrosion rates noted in Figure 5-45(b), the sample prepared for 20 minutes experienced significant metal loss, and exhibited severe surface damage in Figure 5-47. In fact, the amount of metal loss for most of the samples was at least 31 ppm, and in all cases, nickel was the least dissolved metal.

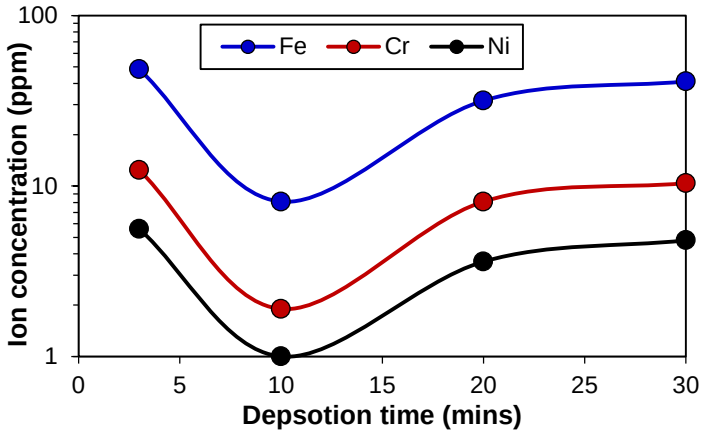

Figure 5- 49 *Metal loss from ruthenium sputter coated 304L stainless steel as a function of deposition time after 48 hours exposure in 1 M sulphuric acid.*

Despite the low corrosion rates recorded in the presence of ruthenium sputtered films, the films were of little practical importance as is. An effective protective barrier should

remain bonded to the substrate for the required exposure period. This was not achieved here. As such, further study was focused on improving the adhesion of the ruthenium films to the 304L stainless steel substrate.

5.3.4 Improving adhesion

Three approaches were used to improve the adhesion of the ruthenium films. These were (1) surface roughening, (2) pulsing deposition pressure, and (3) titanium seeding. The titanium seed layer was produced as described in Section 3.3.2. For each approach, two sets of samples were prepared, one of which was annealed as described in Section 3.3 The objective was to improve adhesive strength, reduce film stress, or achieve both.

Stress analysis

Visual examination of the films by FESEM showed surfaces that were smooth, and similar to those in Figures 5-43. XRD diffractograms obtained on the films are presented in Figure 5-50. Although focus in this section was on films deposited for 10 minutes, theier XRD peaks were mostly poorly defined for meaningful analysis. As such, XRD analysis done on films deposited for 20 minutes instead. In all the cases, the diffractograms of the film deposited on polished 304L stainless steel surfaces was used as the reference. The XRD patterns in the figure show that all the ruthenium films produced for this set of experiments preferentially grew along the (1000) plane. No (0022) reflections were observed, unlike in previous accounts (Figures 5-37 & 5-44). This observation points to poor film reproducibility.

Surface roughening has the effect of increasing interfacial contact, and increasing the adhesive strength of the film-substrate interface. Figure 5-50(a) shows that the surface finish of the substrate did not influence the Bragg position of the ruthenium (1000) peak. The Bragg position of the peak remained at $2\theta \approx 44.9°$. This means that the stresses in the film were not influenced by manner of surface preparation.

It was postulated that annealing would relieve any stresses induced during sputtering. Annealing of the RF sputtered films shifted both the ruthenium and 304L stainless steel peaks to higher Bragg angles towards those of the unstressed state (Figure 5-50(b)). The

ruthenium (1000) peak became narrower after annealing, suggesting grain coarsening with annealing. Notably, no new peaks were shown, confirming that the process of annealing did not cause the formation of new compounds or intermetallics.

Cuthrell and colleagues (1988) proposed that pulsing deposition pressure had the effect of reducing overall film stresses by creating alternating layers of different stresses. Decreasing pressure develops tensile stress, and further decrease in pressure results in a change to compressive stresses (Alagoz et al. 2009). In the present work, working pressure of argon was pulsed between 10 and 23 Sccm. The results are presented in Figure 5-50(c). The ruthenium peak was not visible on the sample, suggesting that the films were very thin. Deposition rate depends on the transportation of sputtered material across the plasma to the substrate, which is a function of sputter and background pressure. It is likely that pulsing pressure reduced the deposition rate so much that film thickness typical of 20 minutes deposition times was no achieved.

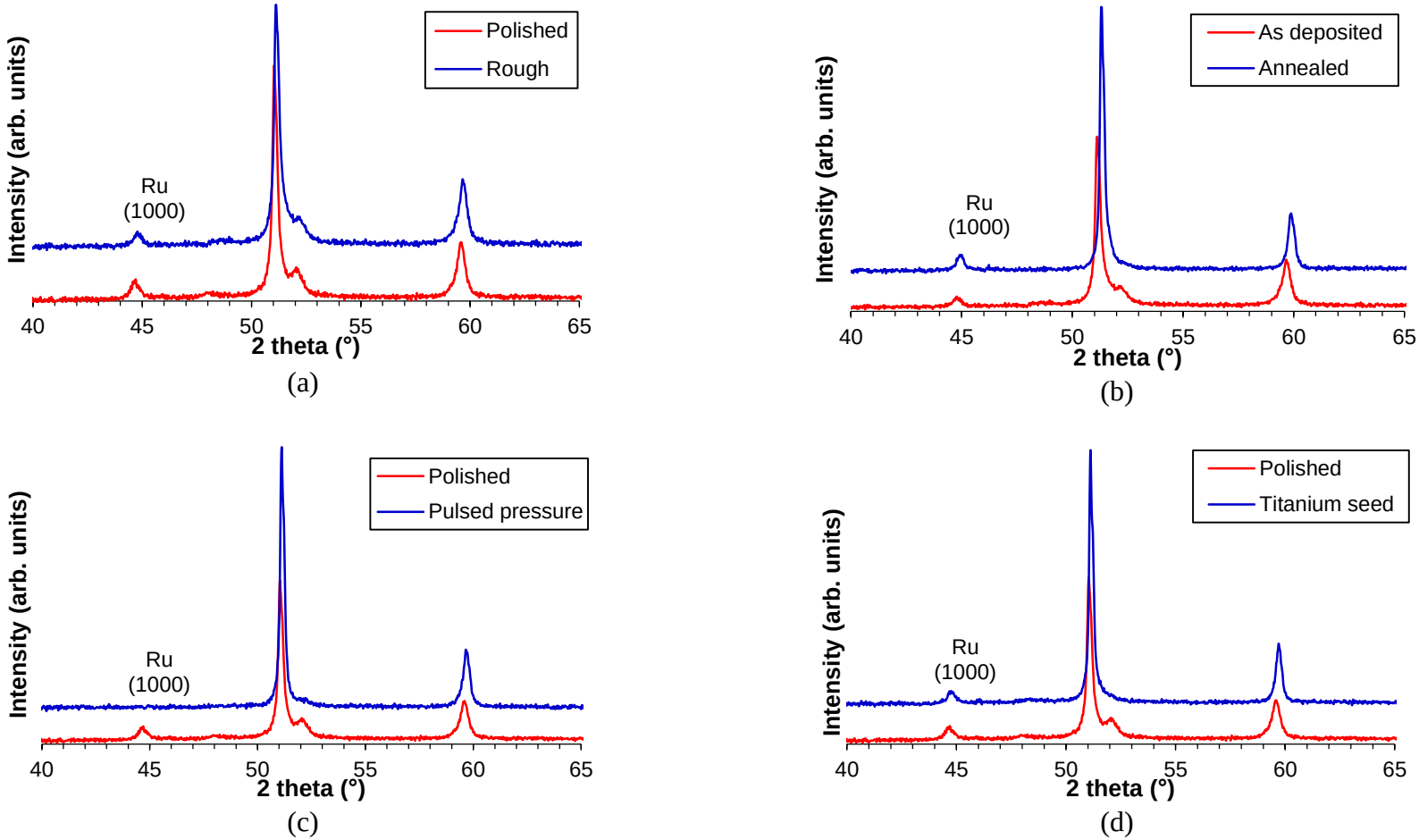

Figure 5- 50 *Influence of (a) surface roughness, (b) annealing, (c) pulsing pressure, and (d) titanium seeding on the Bragg angle of ruthenium sputter coated 304L stainless steel.*

Stainless steel forms a native chromium oxide layer on the surfaces, which may compromise film adhesion. One way of minimising the effect of native oxides is to apply an intermediate layer of an element with a high affinity for oxygen to react with the native oxide (Mattox 1973). In this work, a titanium seed layer was used, and prepared as described in Section 3.3.2. An added advantage of the titanium seed layer was that it provided sites for film nucleation. Figure 5-50(d) shows that no titanium peaks were detected. This was expected since the titanium layer was predicted to be less than 2 nm (Vasu et al. 2014). In addition, no new compounds or intermetallics were detected. The presence of a titanium seed layer did not influence the stress state of the sputtered films; the ruthenium (1000) was still detected at $2\theta \approx 44.9°$.

Corrosion characterisation before annealing

Corrosion performance of the ruthenium films was analysed in 1 M sulphuric acid using EIS at OCP, and then examined by FESEM. Figure 5-51 to 5-55 present the results obtained.

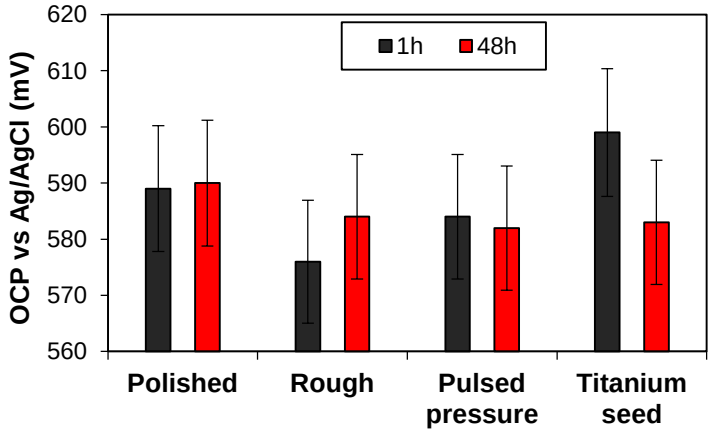

Figure 5- 51 *Variation of OCP of RF sputtered ruthenium films with exposure time in 1 M sulphuric acid. Deposition time = 10 minutes.*

In all the cases studied, the ruthenium film raised the OCP of the 304L stainless steel to values greater than 565 mV (Figure 5-51), consistent with the high values reported in Table 5-6. The highest OCP value of almost 600 mV was associated with the film deposited on the titanium seed layer after 1 hour of exposure, whereas the film prepared

on the polished 304L stainless steel substrate exhibited better stability with its OCP remaining nearly constant at ≈ 590 mV over the 48 hours of exposure.

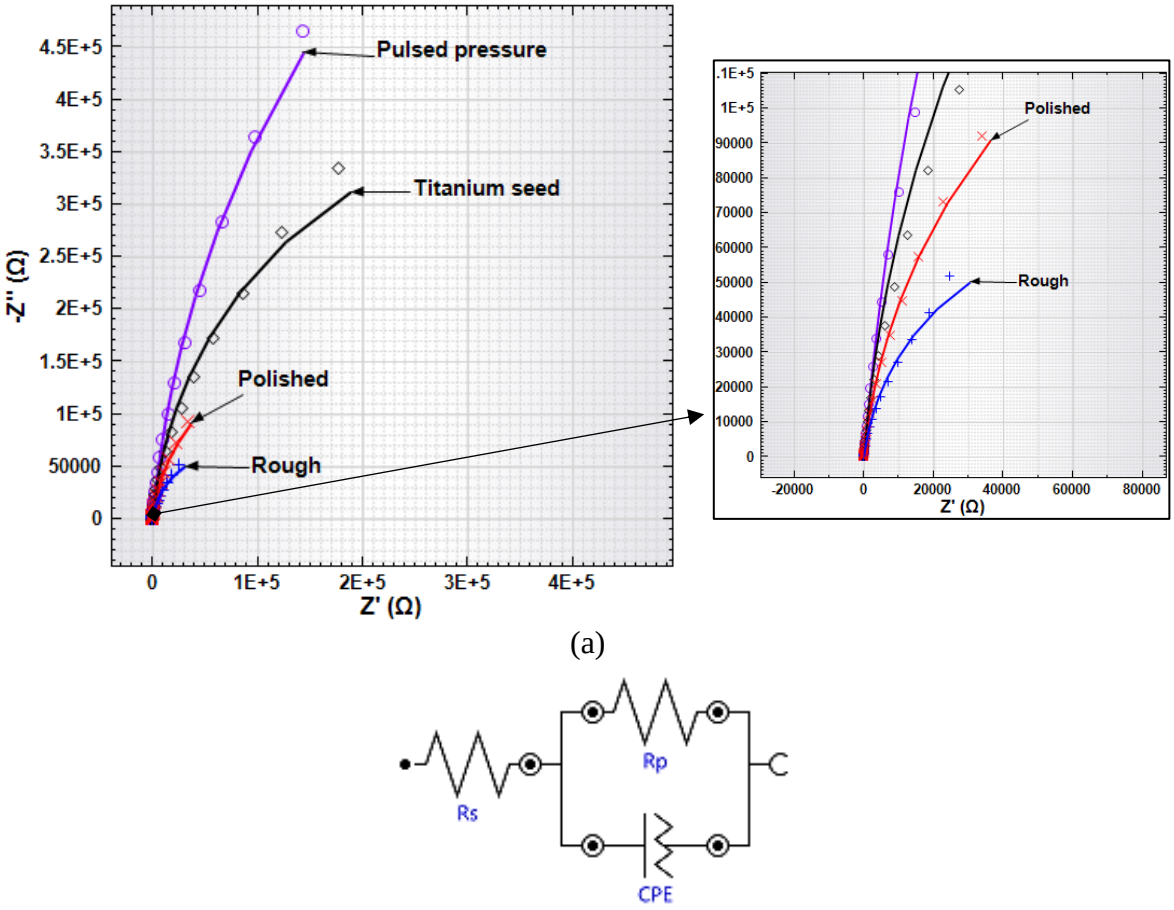

(a)

(b)

Figure 5- 52 *Nyquist plots of the ruthenium sputter coated 304L stainless steel after 48hours of exposure in 1 M sulphuric acid and measured at OCP. Simulation of data was done using the equivalent circuit in (b). (R_p = R_f)*

Nyquist plots obtained on the sputter coated 304L stainless steels after 48 hours of exposure are shown in Figure 5-52(a), where the solid lines are fittings obtained by simulating the EIS data using the equivalent circuit in Figure 5-52(b). The plots were semi-circular in shape, which is distinctive of charge transfer limited corrosion processes. The implication of this observation is that the ruthenium films had a dense equiaxed microstructure, and not columnar one as was observed by other researchers working with sputtered ruthenium films (Morrow et al. 2006; Alagoz et al. 2009). Columnar grains provide a direct diffusion path for the corrosion media, and are

therefore typically associated with diffusion-limited processes. Such processes exhibit Nyquist plots with a linear part of ≈ 45° at low frequencies.

Also evident from Figure 5-52(a) is the dependence of the Nyquist radius on the film preparation condition. The shortest radius was reported on the films deposited on rough surfaces, while the longest was recorded on the film produced by pulsed pressure. In fact, the radii increased in the order: rough < polished < titanium seed < pulsed pressure. The length of a Nyquist radius is indicative of film resistance. The longer the radius, the larger the resistance of the film to corrosion attack as shown in Figure 5-53.

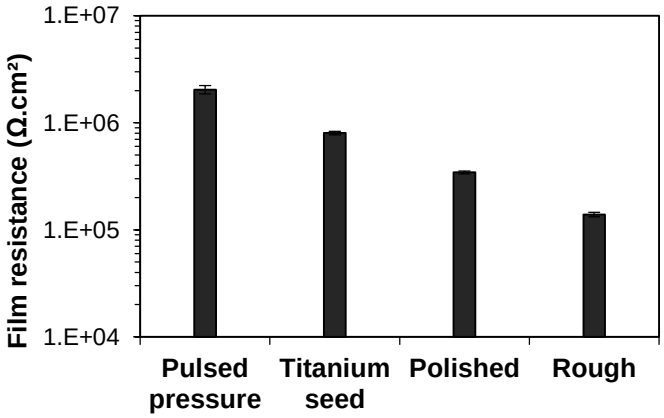

Figure 5- 53 *Resistance of the ruthenium sputtered films as a function of preparation technique. Errors are fitting errors.*

Bode phase plots were used to study the stability of the ruthenium films over the period of exposure. The results are presented in Figure 5-54. Evidence in Figure 5-54(a) suggests that all, but the film deposited by pulsing pressure, failed within 1 hour of immersion in 1 M sulphuric acid. In most cases, the phase angle at low frequencies was far less than |90°|. This is consistent with a non-blocking film configuration (Orazem & Tribollet 2008). However, as with the results presented in Figure 5-46, the phase angle at low frequencies increased with an increase in exposure time (Figure 5-54(b)), implying improved protection efficiency. This, and the observations in Figure 5-51 that OCP values did not decrease to active potentials after 48 hours of exposure, corroborates the possibility of two protection mechanisms suggested in Section 5.3.3.

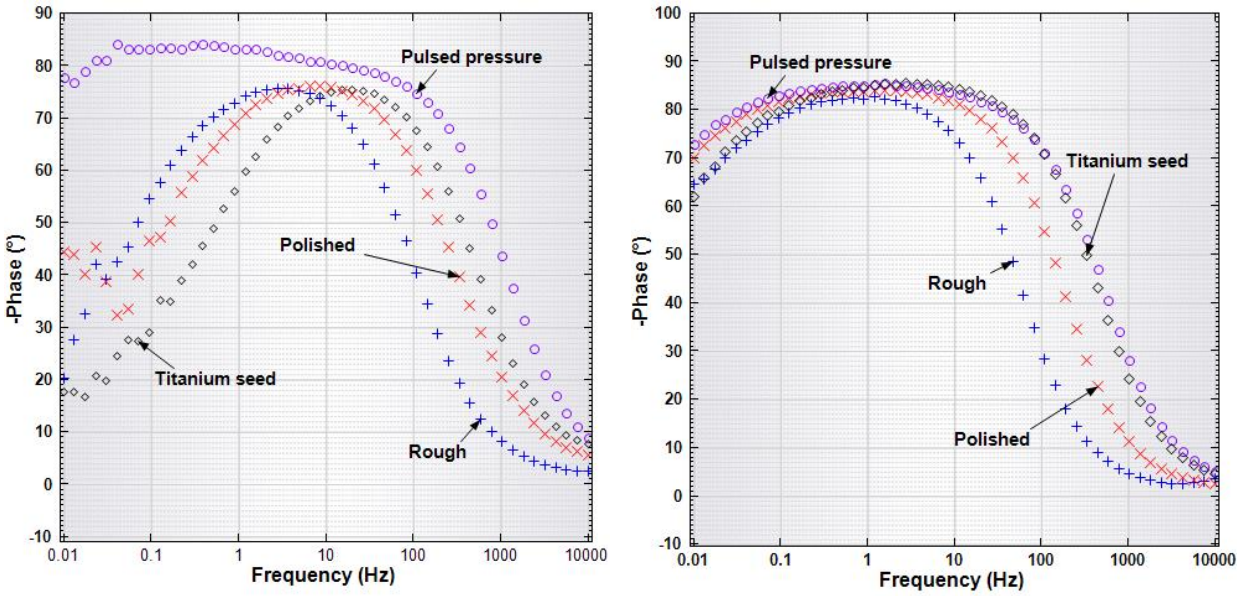

Figure 5- 54 *Bode phase plots of the ruthenium films after exposure to 1 M sulphuric acid for (a) 1 hour, and (b) 48 hours. Deposition time = 10 minutes.*

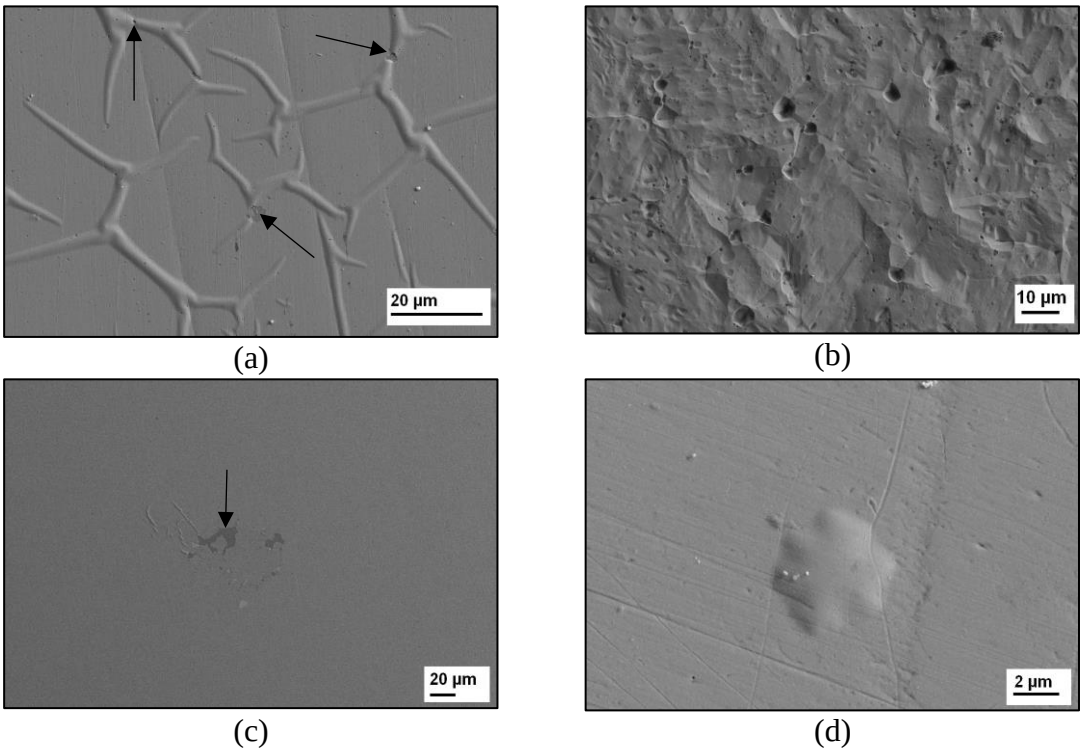

Figure 5- 55 *FESEM post corrosion examination of the RF sputtered films after exposure to 1 M sulphuric acid for 48 hours: (a) polished,(b) rough, (c) pulsed pressure, and (d) titanium seeding. Deposition time = 10 minutes, and power = 30 W*

The low frequency phase angle of the film deposited by pulsing pressure was initially high; at least |76°|, and as high as |84°|. This indicates good protective properties of the film, and suggests that it remained intact during the first hour of immersion. After 48 hours, the phase angle for this film decreased to ≈ |70°|, possibly because of defects developing on the films. Figure 5-55(c) confirms this conclusion. It shows that the film produced by pulsing pressure fractured and peeled off. Film wrinkling was associated with these defects.

Film wrinkling was also observed on the films deposited on polished surfaces (Figure 5-55(a)). The arrows show areas where the film fractured and peeled off. While it is plausible that these defects developed during corrosion exposure, it was not clear if film wrinkling preceded film facture, or otherwise. Film wrinkling is associated with compressive stresses, while fracture in films is a consequence of tensile stresses (Cuthrell et al. 1988; Ohring 2002).

The ruthenium film deposited on the titanium seed layer, and presented in Figure 5-55(d) exhibited signs of blistering. Blisters are indicative of localised loss of adhesion, and may be associated with permeable coatings. However, no cracks were detected on the film to support the possibility of sulphuric acid ingress into the film. Neither did the Nyquist plots in Figure 5-52(a) present evidence of diffusion processes, which are typical of permeable films (Hu et al. 2003).

Figure 5-55(b) shows that the ruthenium film deposited on the rough 304L stainless steel substrate was completely removed during corrosion exposure. This was the only film to exhibit such behaviour. While the Nyquist plots in Figure 5-52(a) and results in Figure 5-53 correctly indicated that this surface had the least film resistance, the Bode phase plots did not present such evidence. In fact, at low frequencies, the plots corresponding to the films deposited on the rough surface was indistinguishable from the other films that were not as severely damaged (Figure 5-54). In addition, the OCP values of this film increased with exposure time. This again confirms that the ruthenium films provided corrosion protection in more than one way.

Corrosion characterisation after annealing

After annealing, the ruthenium sputter coated 304L stainless steel were exposed to 1 M sulphuric acid for 48 hours. EIS at OCP were used to study the corrosion performance of the films.

As can be seen in Figure 5-56, the least measured OCP was ≈ 546 mV vs Ag/AgCl, and was associated with the films deposited on the polished surfaces and on the titanium seed layer. The highest value of OCP was measured on the films deposited on the rough surface, and was almost 590 mV. These results show that, on overall annealing had no effect on the OCP of the films; potentials remained in the region where chromium (III) species are thermodynamically stable.

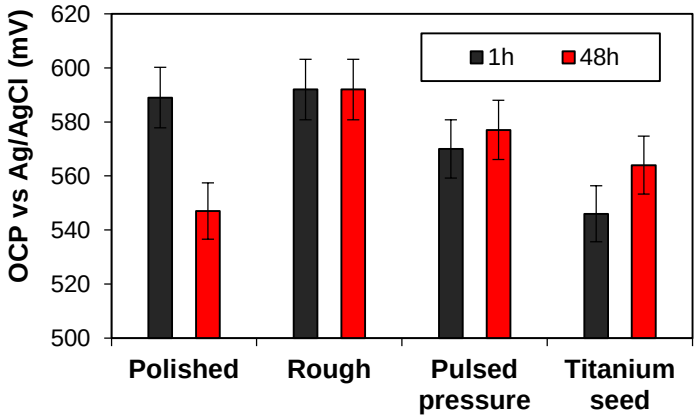

Figure 5- 56 *Variation of OCP of RF sputtered films with exposure time in 1 M sulphuric acid post annealing. Deposition time = 10 minutes.*

Bode phase plots obtained from the EIS measurements are presented in Figure 5-57. It is apparent that annealing was most beneficial to the film deposited on the titanium seed layer. Low frequency phase angle was almost |80°| for this film. The phase angle of the films increased with increase in exposure time, similar to the previous cases (Figures 5-46 & 5-54). These results pointed to improve protection capabilities.

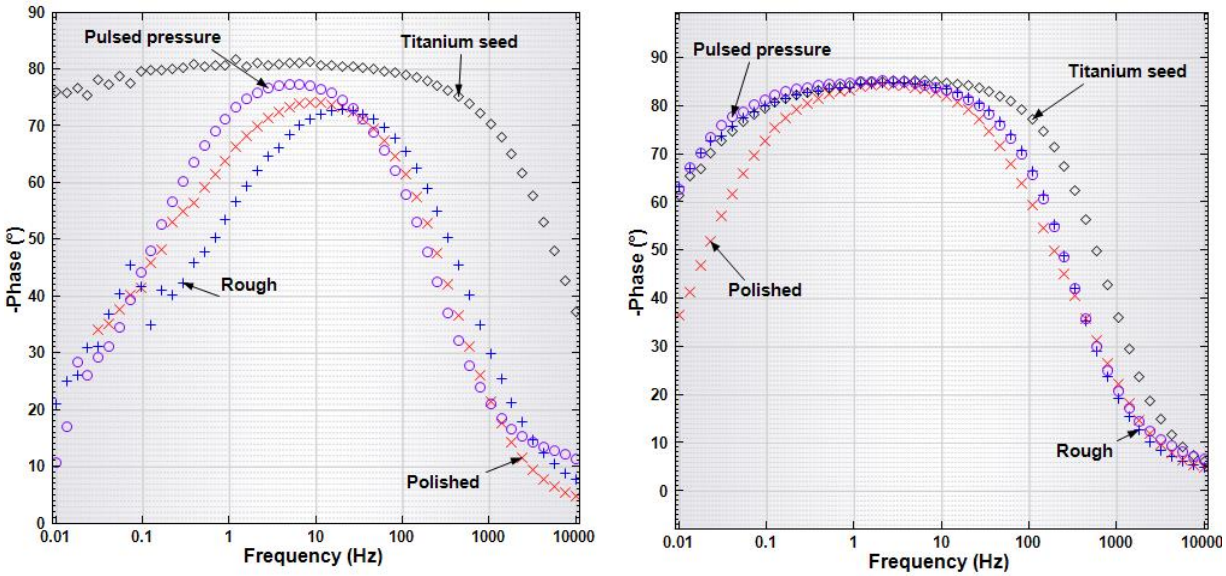

Figure 5- 57 *Bode phase plots of the ruthenium films post annealing, after exposure to 1 M sulphuric acid for (a) 1 hour, and (b) 48 hours.*

Post corrosion examination of the films was done using FESEM. The images presented in Figure 5-58 are consistent with the results recorded in Figure 5-57(a), which shows that the ruthenium films failed within the first hour of exposure. Figure 5-58 shows that the film on the polished surface was completely removed within the first hour, with remnants of the film still visible (shown by arrows). In addition, the film on the rough sample appeared to have failed by both blistering and fracturing.

Figure 5-59 presents the images of the films deposited by pulsed pressure, and that prepared on titanium seed layer at different magnifications. The film produced using pulsed pressure was characterised by film wrinkling and cracks. Light coloured matter seemed to ooze from most of the cracks. This matter was too small to be successfully analysed by EDS, but it was speculated to be corrosion products. They seemed to plug the cracks, and possibly inhibited ingress of the corrosion media into the film. Although the ruthenium film deposited on the titanium seed layer was mostly continuous, it had numerous submicron-sized blisters. These blisters however, presented points of weakness susceptible to fracture as shown at higher magnification. The blister observed in this film could have been a consequence of annealing, as they were not observed in Figure 5-55 at such densities.

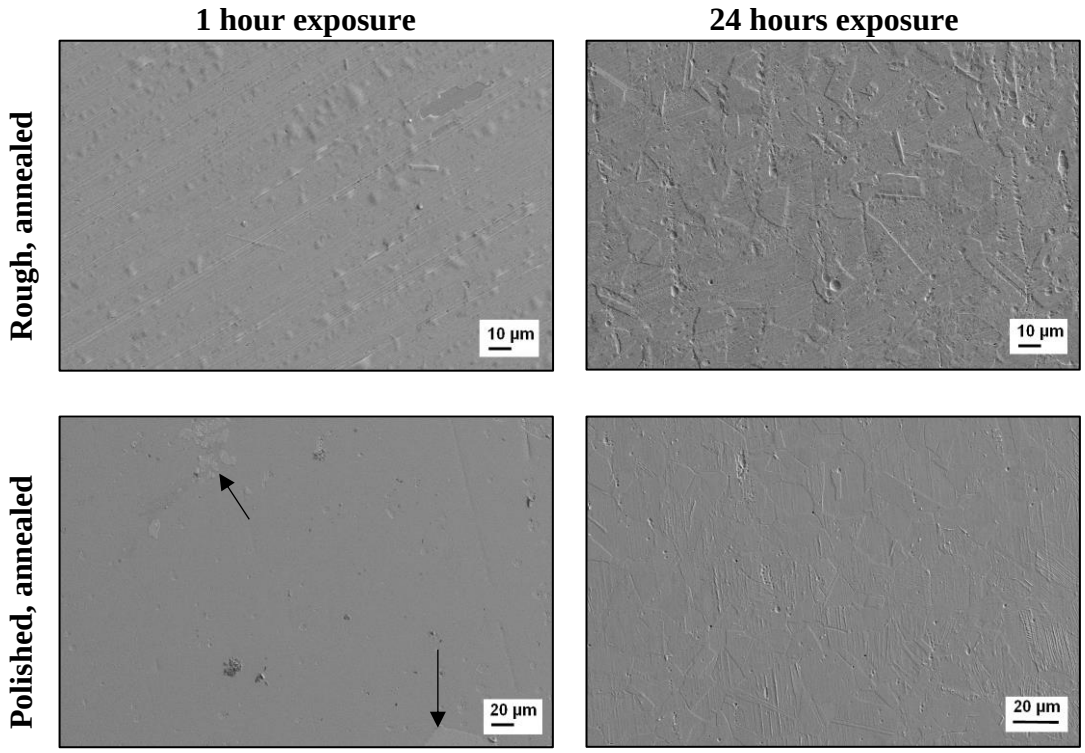

Figure 5- 58 *FESEM post corrosion examination of annealed RF sputtered films deposited on 304L stainless steel after exposure to 1 M sulphuric acid for 48 hours.*

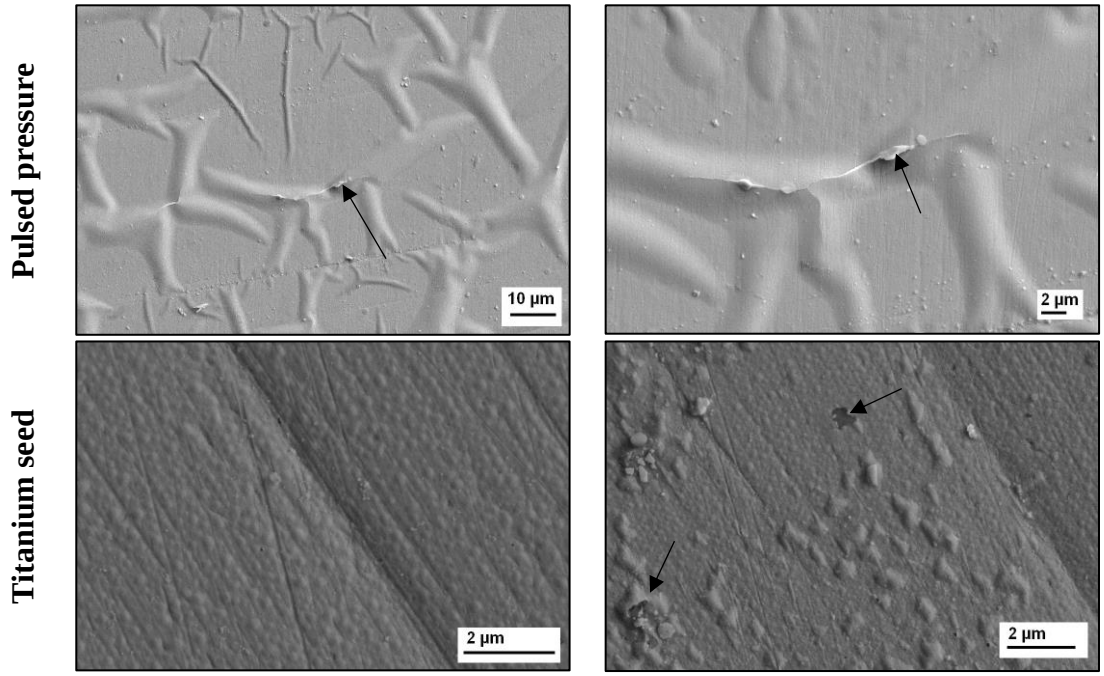

Figure 5- 59 *FESEM post corrosion examination of RF sputtered ruthenium films deposited by pulsed pressure and on titanium seed after exposure to 1 M sulphuric acid for 48 hours. All films were annealed prior to exposure.*

5.3.5 Effects of potential

Films deposited on polished surface for 10 minutes and 30 W were held at potentials ranging from -100 to 800 mV vs Ag/AgCl. The objective was to understand effect of potential on the stability of the film, and possibly the mechanism of film failure. EIS measurements were used in studying the films in 1 M sulphuric acid. Bode phase plots obtained from EIS are presented in Figure 5-60, and film resistance obtained from Bode modulus plots by assuming zero solution resistance as per Equations 2-22 and 2-23, are given in Figure 5-61.

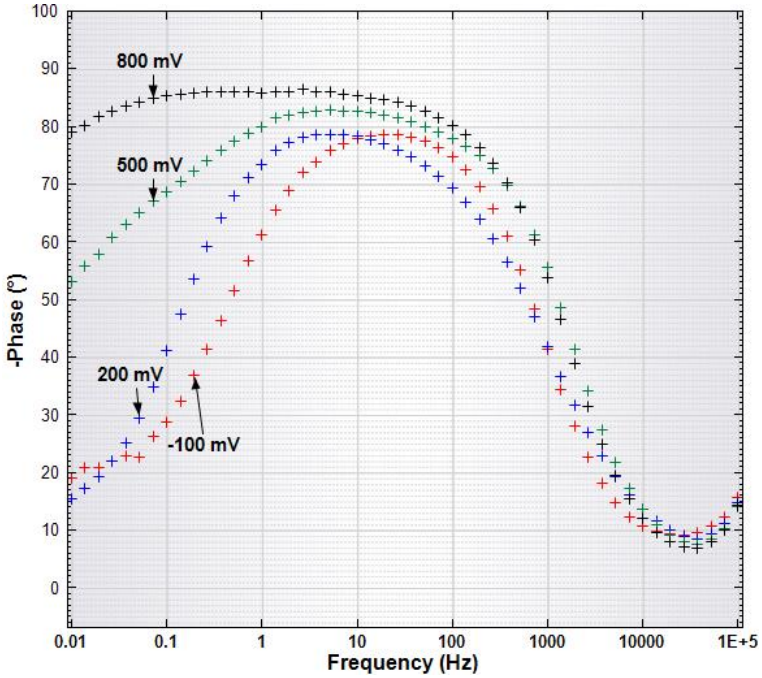

Figure 5- 60 *Effect of potential on the Bode phase plots for ruthenium coated 304L stainless steel exposed to 1 M sulphuric acid. Exposure time = 2 hours.*

It is clear that at potentials ≈ -100 and 200 mV, the ruthenium films exhibited low film resistance, with both low-frequency angle and |Z| tending towards zero. Increasing potential increased the stability, and resistance of the films. At potentials ≈ 800 mV the low frequency phase angle was almost |80°|, and was as high as |87°|. This is indicative of a good protective film. As can be seen in Figure 5-62(d), this film was defect free.

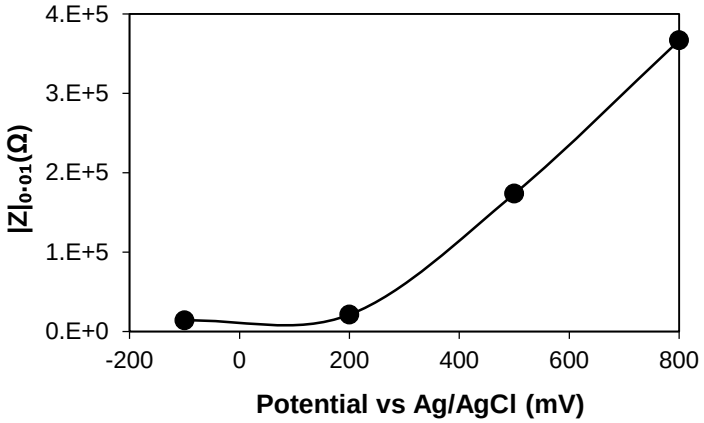

Figure 5- 61 *Effect of potential on resistance of ruthenium sputtered films after 2 hours of exposure in 1 M sulphuric acid. Resistance recorded at 0.01 Hz.*

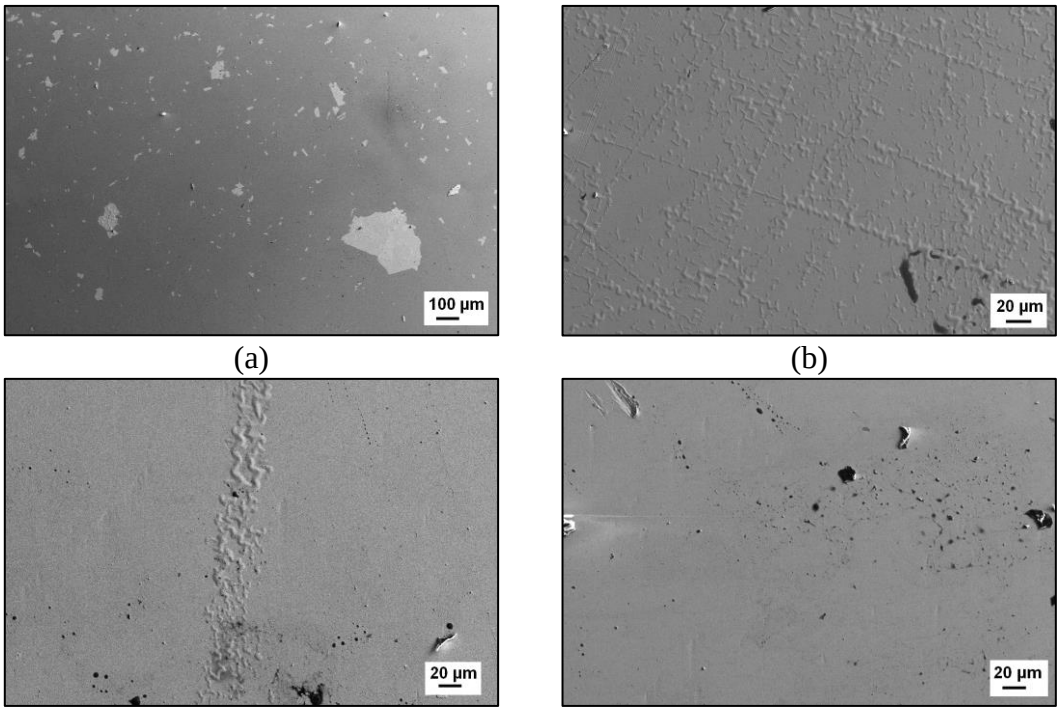

(a) (b)

(c) (d)

Figure 5- 62 *Effect of potential on the adhesion of ruthenium sputtered films. Films were held in 1 M sulphuric acid at (a) -100 mV, (b) 200 mV, (c) 500 mV and (d) 800 mV.*

Figure 5-62 shows the images obtained after FESEM examination of the corroded films. Consistent with the EIS results in Figure 5-60 and 5-61, the films exposed at ≈ 100 mV (Figure 5-62(a)) fractured severely and peeled off. At these potentials, the dominant reaction is the evolution of hydrogen by Equation 2-2. It is likely that the ballistic effect

of the collapsing hydrogen bubbles increased the stresses in the film and caused them to fracture.

Increasing potentials to 500 mV caused films to wrinkle. Film wrinkling is typically associated with compressive stresses. From Figures 5-62(b) and (c), it can be seen that the density of the wrinkles decreased significantly with increase in potentials. This seems to imply; (1) that the stresses induced by the corrosion process in sulphuric acid were compressive in nature and (2) that the magnitude of these stresses decreased with increase in potential. Consistent with this supposition, the films exposed at 800 mV, and presented in Figure 5-62(d) did not show any signs of damage.

5.4 Results: Pulsed electrodeposition

The following section seeks to present, and describe the results of the synthesis of the ruthenium surface alloys via pulsed electrodeposition (PED).

5.4.1 Design of experiments

A 2^4 factorial design for four independent parameters was done to study their effect on the corrosion performance of ruthenium films deposited on 304L stainless steel by PED. These parameters were pulse on time (T_{on}), pulse off time (T_{off}), plating current (i_p) and surface roughness. Table 5-7 lists the parameters studied, their levels and ranges. After synthesis, the films were visually examined using FESEM, and then exposed to 1 M sulphuric acid.

Table 5- 7 *Experimental conditions used for the 2^4 factorial DOE.*

Symbol	Parameter	Low level (-)	High level (+)
A	T_{on} (s)	3	10
B	T_{off} (s)	1	50
C	i_p (A)	1.2	2
D	Surface roughness	Polished	Rough

Visual examination

Prior to corrosion exposure, the films were examined using FESEM. The films deposited on the polished 304L stainless steel are presented in Figures 5-63 and 5-66, where inserts were used to emphasise characteristic features of the films. It was clear from the figures that film morphology showed a strong dependence on T_{off}. At low T_{off}, the films were severely chapped and curled, indicating that they had high residual stresses. This was consistent regardless of T_{on} or i_p.

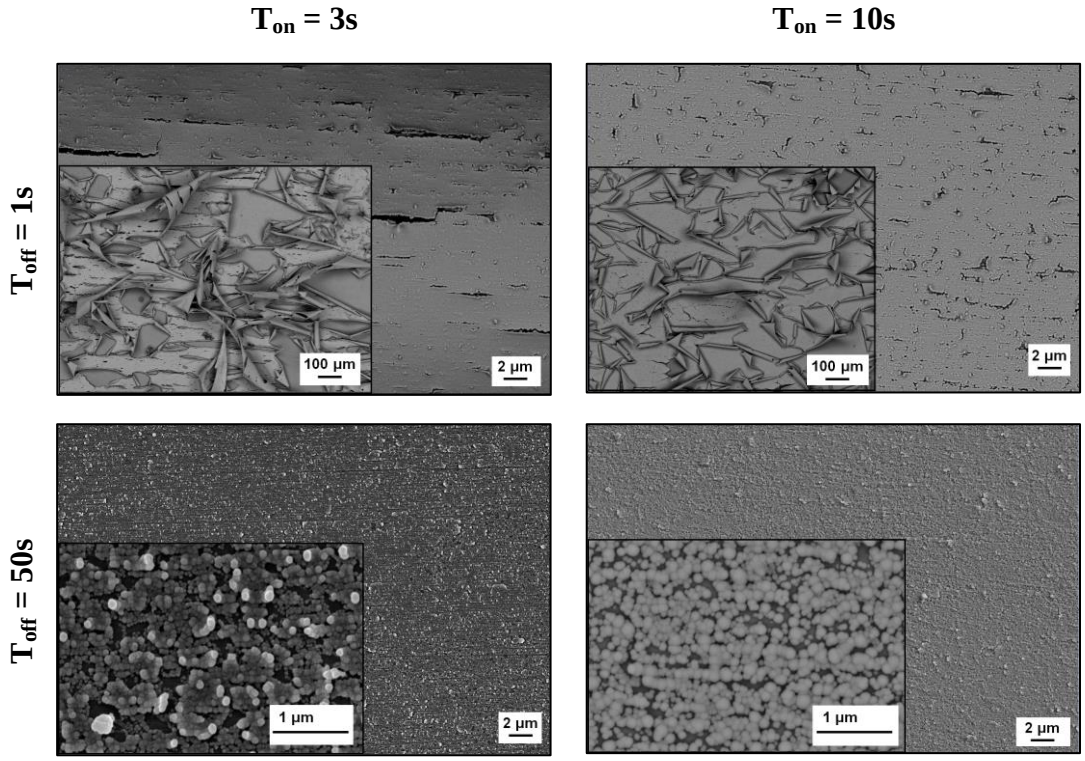

Figure 5- 63 *Influence of T_{on} and T_{off} on surface morphology of ruthenium films deposited on polished 304L stainless steel samples, i_p = 1.2 A (≈ 0.4 A/cm^2).*

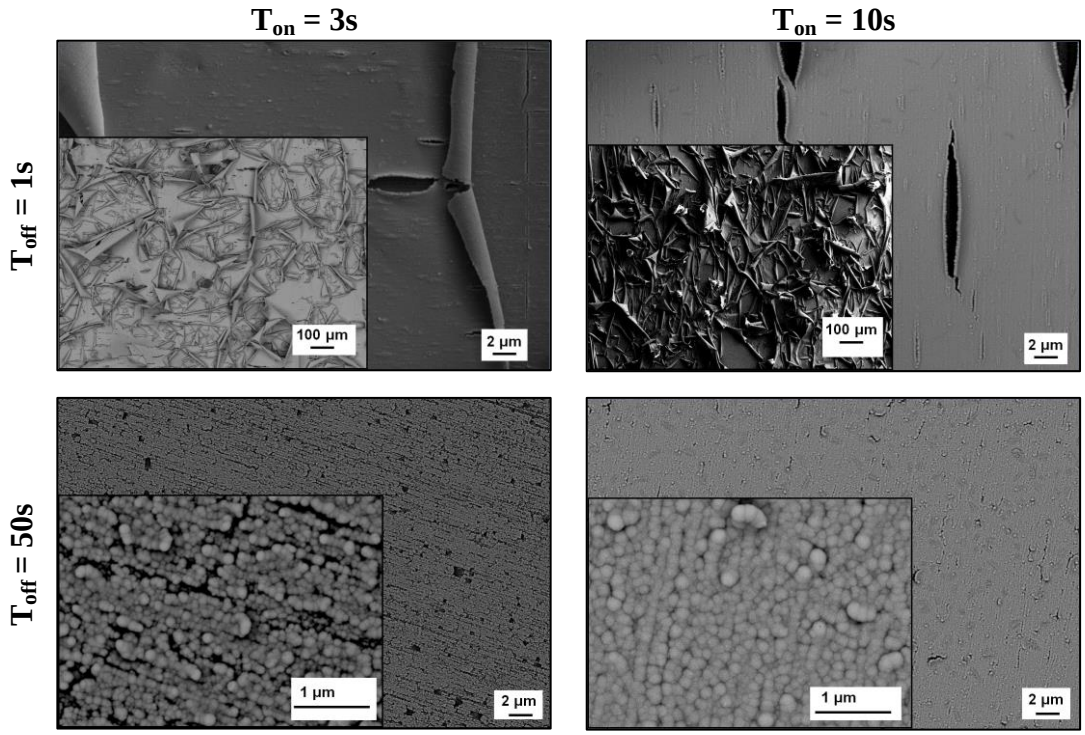

Figure 5- 64 *Influence of T_{on} and T_{off} on surface morphology of ruthenium films deposited on polished 304L stainless steel samples, i_p = 2 A (≈ 0.7 A/cm^2).*

As can be seen in Figure 5-63 and Figure 5-64, the films produced at higher T_{off} (50 s) were relatively smoother. Most of these films, however, were sparsely distributed, and exhibited evidence of incomplete surface coverage. Films produced at high $T_{off,}$ high i_p and high T_{on} (Figure 5-64), appeared compact, more continuous and stress free; probably better suited for corrosion applications.

The morphology of the films deposited on the rough surfaces was notably influenced by the three parameters: T_{off}, T_{on} and i_p. As evident from Figures 5-65 and 5-66, increasing i_p from 1.2 to 2 A appeared to increase the stresses in the films. The films became increasingly chapped with an increase in plating current. In addition, increasing i_p evidently increased the density and surface coverage of the films. Comparing the films deposited at T_{on} = 10 s and T_{off} = 1 s in Figures 5-65 and 5-66, for instance, shows that the films became more compact and dense at 2 A. This is consistent with the expectation that increasing current increases throwing power, and hence the amount deposited.

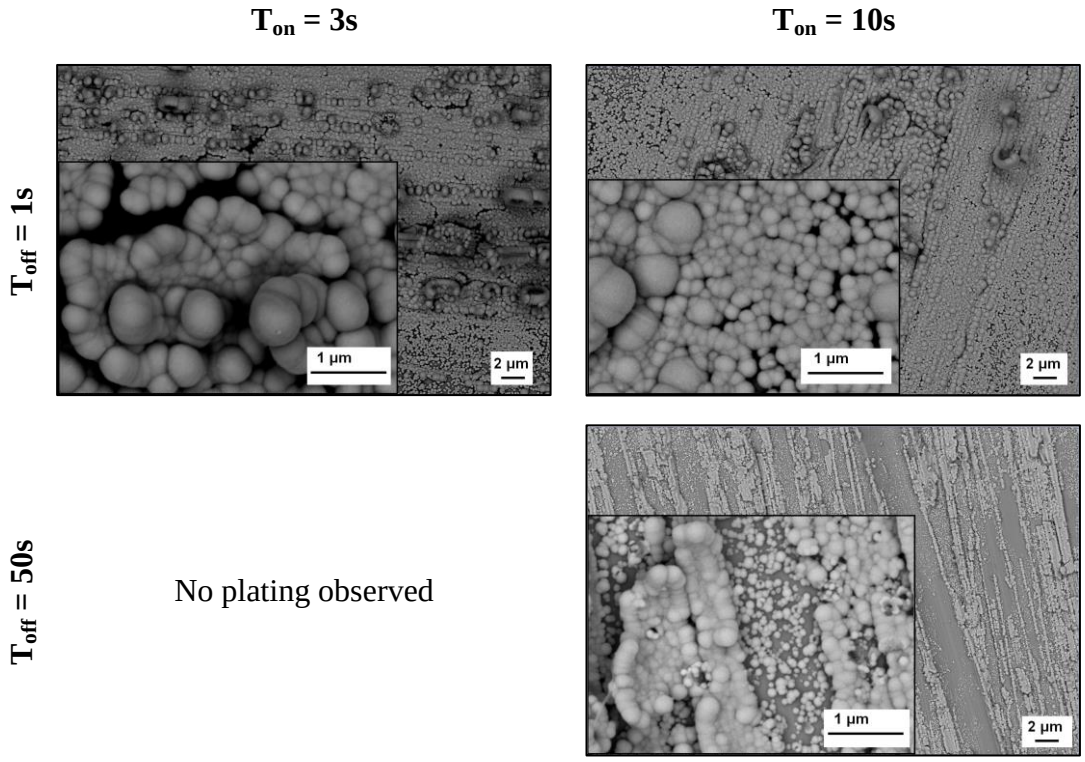

Figure 5- 65 *Influence of T_{on} and T_{off} on surface morphology of ruthenium films deposited on rough 304L stainless steel samples, i_p = 1.2 A (≈ 0.4 A/cm^2).*

Deposits prepared on rough surfaces at high T_{off} (50 s) were strongly affected by T_{on}. At both, high and low i_p, no films were observed on the 304L stainless steel at low T_{on} even at high magnification, suggesting that no deposition occurred under these plating conditions. Since ruthenium films were successfully deposited on polished samples under similar conditions (Figures 5-63 & 5-64), these observations present compelling evidence that pulsed electrodeposition of ruthenium is dependent on pre deposition surface finish. It is possible that the protrusions on the rough surfaces led to non-uniform current distribution, and consequently poor or no deposition.

Increasing T_{on} from 3 to 10 s increased opportunities for electrodeposition as observed in Figures 5-65 and 5-66. From the film deposited at high T_{off}, high T_{on} in Figure 5-65, it can be seen that electrodeposition preferentially initiated in the grooves or protrusions created during surface preparation. This evidently led to non-uniform film growth with some areas being more compact, and some more stressed and chapped than others.

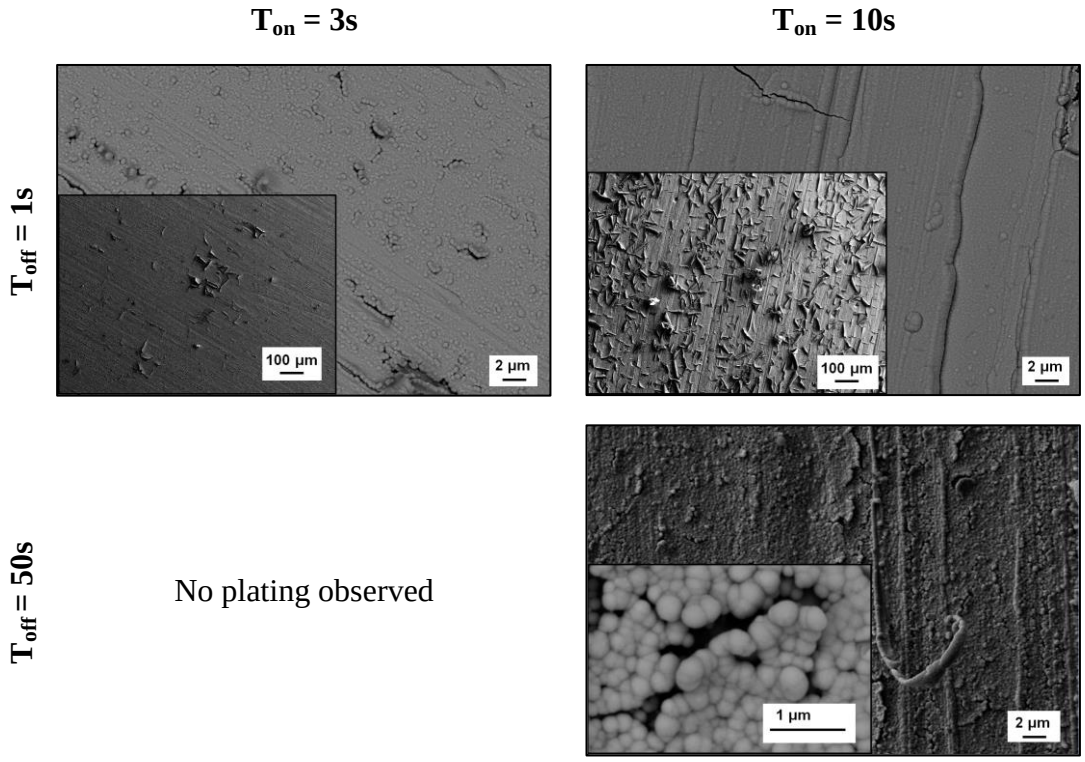

Figure 5- 66 *Influence of T_{on} and T_{off} on surface morphology of ruthenium films deposited on rough 304L stainless steel samples, i_p = 2 A (≈ 0.7 A/cm^2).*

Corrosion characterisation

The ruthenium coated 304L stainless steel samples were then exposed to 1 M sulphuric acid at ≈ 25°C. Results obtained from this exercise are presented in Table 5-8 and Figure 5-67.

In all the cases studied, the presence of the ruthenium film markedly improved the corrosion resistance of 304L stainless steel. Corrosion rates as low as 0.002 mm/y were recorded, corresponding to ≈ 99.7% improvement in corrosion resistance. It is evident from both Table 5-8 and Figure 5-67 that the lowest corrosion rates measured were associated with high T_{off}, regardless of T_{on}, i_p or surface preparation. Corrosion rates of films produced at high T_{off} ranged from 0.002 to a maximum of 0.03 mm/y, compared to 0.04 and a maximum of 0.2 mm/y at low T_{off}. These results were contrary to expectation. At high T_{off}, the films produced were sparsely distributed (Figures 5-63 – 5-66), and it was logical to expect increased accessibility of the sulphuric acid to the 304L stainless steel substrate, and therefore increased dissolution rates.

Table 5- 8 *Corrosion rate (mm/y) results from the 2^4 DOE, calculated by LPR method. *Bold italics present average corrosion rate. Values expressed to 3 d.p.*

				A: T_{on} (s)			
				(-1)		(+1)	
				C: i_p (A)		C: i_p (A)	
				(-1)	(+1)	(-1)	(+1)
B: T_{off} (s)	(-1)	D: Surface roughness	(-1)	0.195	0.073	0.170	0.174
				0.048	0.113	0.071	0.251
				0.051	0.078	0.046	0.103
				0.098*	***0.088***	***0.095***	***0.176***
			(+1)	0.092	0.103	0.103	0.096
				0.011	0.048	0.008	0.007
				0.018	0.040	0.025	0.052
				0.040	***0.063***	***0.045***	***0.052***
	(+1)	D: Surface roughness	(-1)	0.002	0.048	0.028	0.001
				0.003	0.029	0.005	0.009
				0.002	0.025	0.008	0.007
				0.002	***0.034***	***0.014***	***0.006***
			(+1)	0.029	0.068	0.079	0.048
				0.001	0.004	0.009	0.016
				0.007	0.004	0.016	0.009
				0.012	***0.025***	***0.034***	***0.028***

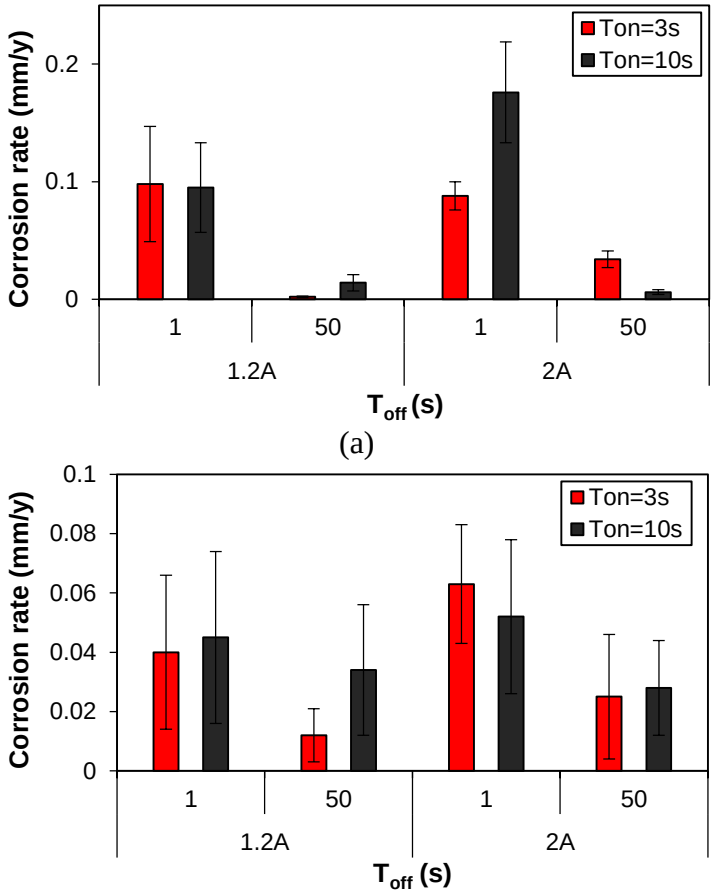

Figure 5- 67 *Influence of T_{off}, T_{on} and i_p on the corrosion rate of ruthenium coated 304L stainless steel in 1 M sulphuric acid. Surfaces were (a) polished and (b) rough.*

Post corrosion examination of the corroded surfaces was done by FESEM. The EDS mapping of the surfaces is presented in Figure 5-68, which shows that the films produced at low T_{off} peeled off during exposure. This could be attributed to high residual stresses, which possibly caused numerous cracks and increased propensity to delamination during corrosion exposure. On the other hand, films produced at high T_{off} remained largely intact during exposure, consistent with the low corrosion rates reported in Table 5-8 and Figure 5-67.

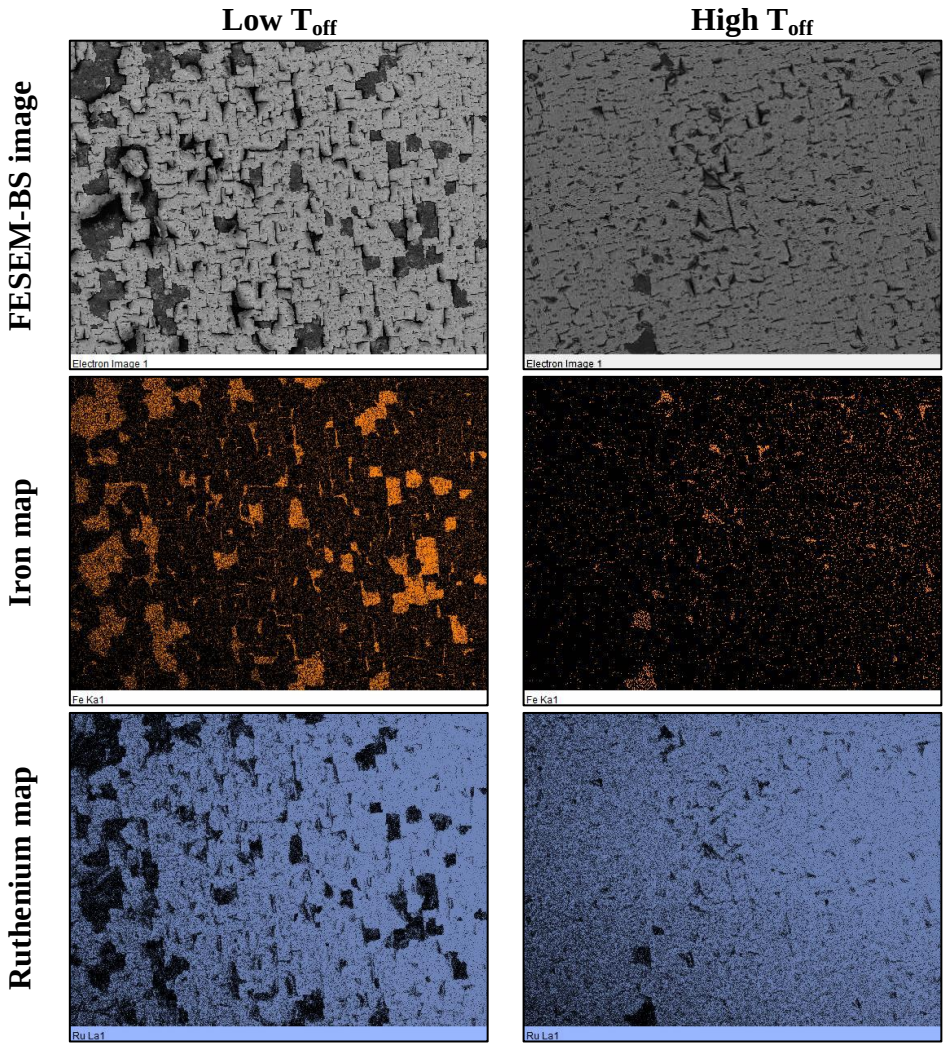

Figure 5- 68 *Images of ruthenium coated 304L stainless steel after exposure to 1 M sulphuric acid, showing effect of* T_{off}.

Table 5- 9 *Effect of Ton (A), Toff (B), ip (C), and surface roughness (D) and their interactions on corrosion of ruthenium plated 304L in 1 M sulphuric acid. *S2 = variance, and values expressed to 3 d.p.*

Sample	A	B	C	D	AB	AC	BC	AD	BD	CD	ABC	ABD	BCD	ACD	ABCD	$\bar{Y}$	S^2
1	(+)	(+)	(+)	(+)	(+)	(+)	(+)	(+)	(+)	(+)	(+)	(+)	(+)	(+)	(+)	0.028	0.028
2	(+)	(+)	(+)	(-)	(+)	(+)	(+)	(-)	(-)	(-)	(+)	(-)	(-)	(-)	(-)	0.006	0.004
3	(+)	(+)	(-)	(-)	(+)	(-)	(-)	(-)	(-)	(+)	(-)	(-)	(+)	(+)	(+)	0.014	0.013
4	(+)	(-)	(-)	(-)	(-)	(-)	(+)	(-)	(+)	(+)	(+)	(+)	(-)	(+)	(-)	0.095	0.065
5	(-)	(-)	(-)	(-)	(+)	(+)	(+)	(+)	(+)	(+)	(-)	(-)	(-)	(-)	(+)	0.098	0.084
6	(-)	(+)	(+)	(+)	(-)	(-)	(+)	(-)	(+)	(+)	(-)	(-)	(+)	(-)	(-)	0.025	0.037
7	(-)	(-)	(+)	(+)	(+)	(-)	(-)	(-)	(-)	(+)	(+)	(+)	(-)	(-)	(+)	0.064	0.034
8	(-)	(-)	(-)	(+)	(+)	(+)	(+)	(-)	(-)	(-)	(-)	(+)	(+)	(+)	(-)	0.040	0.045
9	(-)	(+)	(-)	(-)	(-)	(+)	(-)	(+)	(-)	(+)	(+)	(+)	(+)	(-)	(-)	0.002	0.001
10	(-)	(+)	(+)	(-)	(-)	(-)	(+)	(+)	(-)	(-)	(-)	(+)	(-)	(+)	(+)	0.034	0.013
11	(-)	(-)	(+)	(-)	(+)	(-)	(-)	(+)	(+)	(-)	(+)	(-)	(+)	(+)	(-)	0.088	0.021
12	(+)	(-)	(-)	(+)	(-)	(-)	(+)	(+)	(-)	(-)	(+)	(-)	(+)	(-)	(+)	0.045	0.050
13	(+)	(-)	(+)	(+)	(-)	(+)	(-)	(+)	(-)	(+)	(-)	(-)	(-)	(+)	(-)	0.052	0.045
14	(+)	(-)	(+)	(-)	(-)	(+)	(-)	(-)	(+)	(-)	(-)	(+)	(+)	(-)	(+)	0.176	0.074
15	(-)	(+)	(-)	(+)	(-)	(+)	(-)	(-)	(+)	(-)	(+)	(-)	(-)	(+)	(+)	0.012	0.015
16	(+)	(+)	(-)	(+)	(+)	(-)	(-)	(+)	(+)	(-)	(-)	(+)	(-)	(-)	(-)	0.034	0.039
$\sum\bar{Y}_+$	0.451	0.157	0.474	0.302	0.372	0.415	0.373	0.382	0.558	0.378	0.341	0.475	0.419	0.364	0.471		
$\sum\bar{Y}_-$	0.364	0.659	0.342	0.514	0.443	0.400	0.442	0.433	0.257	0.437	0.474	0.340	0.396	0.451	0.344		
$\bar{Y}_+$	0.056	0.020	0.059	0.038	0.047	0.052	0.047	0.048	0.070	0.047	0.043	0.059	0.052	0.046	0.059		
$\bar{Y}_-$	0.046	0.082	0.043	0.064	0.055	0.050	0.055	0.054	0.032	0.055	0.059	0.043	0.049	0.056	0.043		
Effects	**0.011**	**-0.063**	**0.016**	**-0.026**	**-0.009**	**0.002**	**-0.009**	**-0.006**	**0.038**	**-0.007**	**-0.017**	**0.017**	**0.003**	**-0.011**	**0.016**		

Statistical analysis

Table 5-9 shows the effects of T_{on}, T_{off} plating current and surface roughness on the corrosion rates of ruthenium plated 304L stainless steel. These were calculated as per Section 3.4, and their significance plotted in Figure 5-69.

The probability plot in Figure 5-69 shows that the effects of T_{on} (A), and plating current (C), their interaction with each other (AC), and with T_{off} and surface roughness ((AB), (AD), (BC), (CD), (ABC), (ABD), (BCD), (ACD), (ABCD)) fell on a straight line. This means that these parameters were statistically unimportant to this work. T_{off} (B), surface roughness (D) and their interaction (BD) on the other hand, were statistically significant. As shown in Figure 5-69, their effects on the corrosion rates of pulse plated 304L stainless steel did not fit reasonably well on a straight line. These effects were further analysed in Figure 5-70

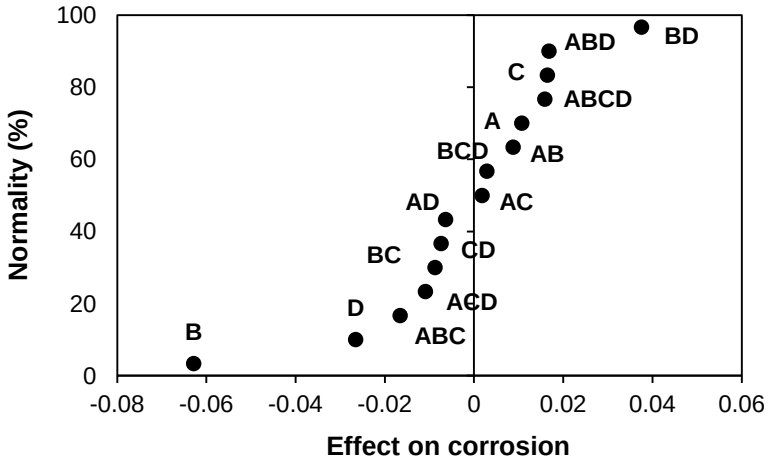

Figure 5- 69 *Normal probability plot of the main and interaction effects on the corrosion of ruthenium plated 304L stainless steel in 1 M sulphuric acid, determined from the 2^4 factorial DOE.*

From Figure 5-70(a) it can be seen that increasing T_{off} from 1 s (coded -1) to 50 s (coded +1) caused a decrease in corrosion rates. This was consistent with the expectation that increasing T_{off} allows for desorption of hydrogen to reduce stresses in the films, and desorption of impurities increasing film chemical purity. Contrary to expectation, increasing surface roughness was associated with increase in corrosion resistance (Figure 5-70(b)). T_{off} played a more significant effect than surface roughness as can be seen by comparing Figures 5-70(a) and

(b). Increasing T_{off} improved corrosion resistance by at least 76%, whereas the effect of increasing surface roughness on corrosion resistance was only ≈ 41%.

Interaction of T_{off} and surface roughness in Figure 5-70(c) however, takes precedence over the individual effects of T_{off} (B) and surface roughness (D) (Barrentine 1999). The disordinal nature of the interaction suggests that the effect of T_{off} on the corrosion resistance of ruthenium plated 304L stainless steel was dependent on the surface finish of the substrate; rough surfaces were beneficial on low T_{off}, whereas polished surfaces performed better when plated at high T_{off}.

The lowest corrosion rates were achievable under conditions of low surface roughness and high T_{off}. Examination of Figure 5-70(c) suggests that the additional step of polishing did not cause a significant change in corrosion rate. In fact, polishing the 304L stainless steel substrate further reduced corrosion by a factor of less than two. However, deposition on rough surface increased the risk of sparse deposition or no deposition.

An extract of Table 5-9 in Figure 5-71 shows the combinations that satisfied the conditions for the least achievable corrosion rate. Samples 2, 3, 9 and 10 were deposited on polished surfaces using high T_{off}. Of these, sample 9 exhibited the lowest average corrosion rate of ≈ 0.002 mm/y in 1 M sulphuric acid, conforming to the targets set in Figure 5-1. This sample was prepared under conditions of low T_{on}, high T_{off}, low surface roughness, and low plating current. Hence, further study was focused on understanding the effects of T_{off}, and surface roughness, and optimisation of these for best corrosion resistance.

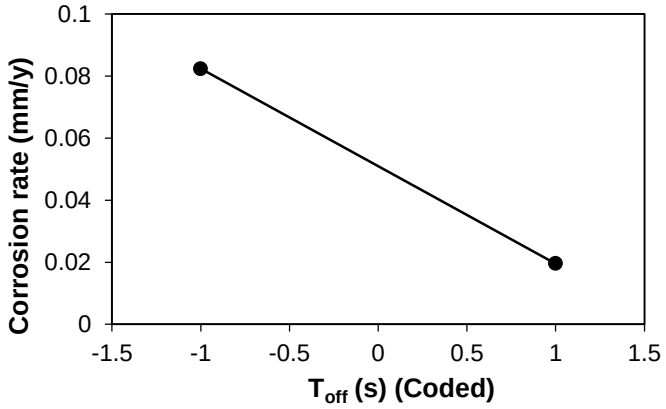

(a)

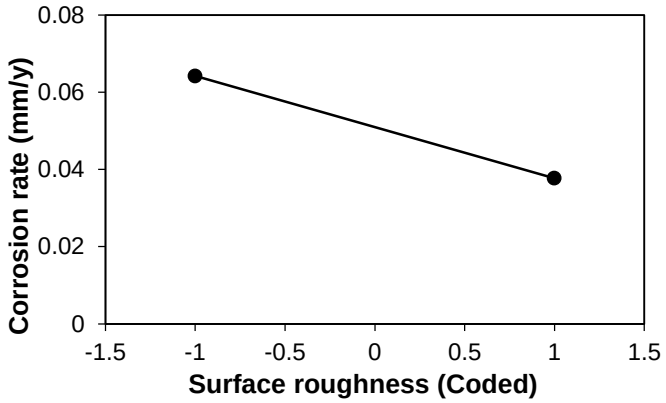

(b)

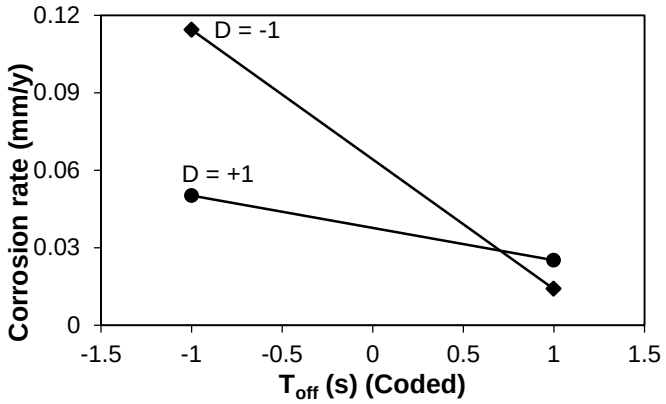

(c)

Figure 5- 70 *Effects of (a) T_{off} (B), (b) surface roughness (D), and (c) their interaction (BD) on the corrosion rate of ruthenium plated 304L stainless steel in 1 M sulphuric acid.*

Sample	A	B	C	D
1	(+)	(+)	(+)	(+)
2	(+)	(+) ✓	(+)	(-) ✓
3	(+)	(+) ✓	(-)	(-) ✓
4	(+)	(-)	(-)	(-)
5	(-)	(-)	(-)	(-)
6	(-)	(+)	(+)	(+)
7	(-)	(-)	(+)	(+)
8	(-)	(-)	(-)	(+)
9	(-)	(+) ✓	(-)	(-) ✓
10	(-)	(+) ✓	(+)	(-) ✓
11	(-)	(-)	(+)	(-)
12	(+)	(-)	(-)	(+)
13	(+)	(-)	(+)	(+)
14	(+)	(-)	(+)	(-)
15	(-)	(+)	(-)	(+)
16	(+)	(+)	(-)	(+)

Figure 5- 71 *Combinations of the conditions that can give the lowest corrosion rates of ruthenium plated 304L stainless steel in 1 M sulphuric acid.*

5.4.2 Effect of T_{off}

Ruthenium films were deposited on polished 304L stainless steel samples using T_{off} values ranging from 1 to 50 s. T_{on} and i_p were kept at 3 s and 1.2 A respectively. Total plating time was 1800 s in all cases.

Ruthenium plating bath

Post electrodeposition, the temperature, pH, and ruthenium content of the plating solutions were analysed, and the observations are presented in Figures 5-72 and 5-73.

The temperature of the bath increased during electrodeposition: bath temperature increased by as much as 11.5°C (Figure 5-72(a)). This suggests that the plating process was exothermic. Abys (2010) reported similar observations, where the release of occluded hydrogen from plated palladium released sufficient heat to turn the coupons red hot, and generated enough stress to twist the film into a cylindrical shape. Examination of the figure shows that the rise in bath temperature was largest at low T_{off} than at high T_{off}. In fact, temperature increase was ≈ 57% at T_{off} = 1 s, while it was about 11% at T_{off} =45 s.

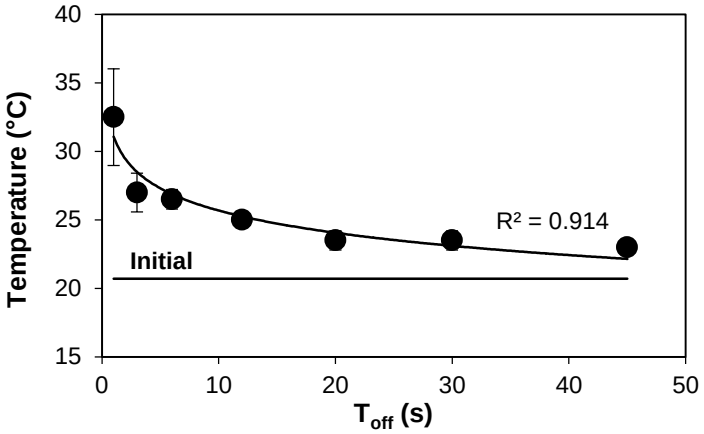

(a)

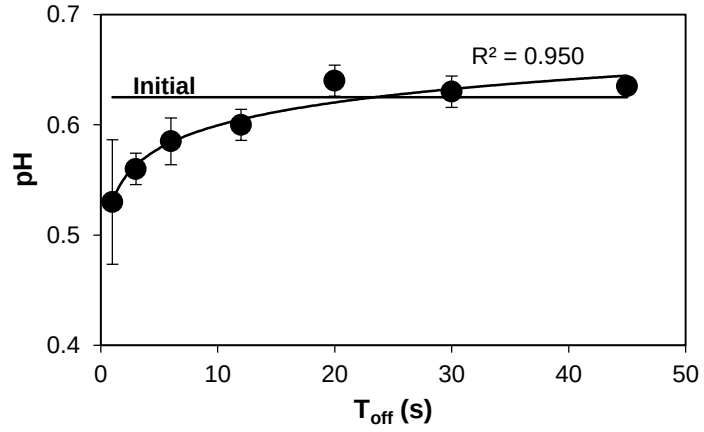

(b)

Figure 5- 72 *Effect of T_{off} on (a) temperature, and (b) pH of the ruthenium plating bath. Initial temperature ≈ 21°C, and pH ≈ 0.63*

The initial pH of the ruthenium plating solution was 0.63. Plating at T_{off} =1 s reduced the pH to about 0.53, but pH remained almost constant at around 0.63 for $T_{off} \geq 20$ s. The decrease in pH suggests an increase in hydrogen ions in the solution. Reduction of hydrogen ions is accompanied by hydrogen evolution, which may be responsible for the chapped films reported in Figures 5-63 to 5-66, and the raise in temperature in Figure 5-72(a). During plating, high effervescence was noted when plating with low T_{off} values.

After plating, the solutions were analysed for ruthenium content, and the results obtained are given in Figure 5-73. They reveal that ruthenium content decreased with increase in T_{off}, but increased for $T_{off} > 8$ s. The decrease in ruthenium

content suggests an increase in deposition rates with increase in T_{off}. For example, deposition rates when T_{off} =1 s were approximately 21 μg/s, and increased significantly to ≈ 507 μg/s at T_{off} =6 s. Plating with T_{off} larger than 8 s apparently led to reduced deposition rates. This is consistent with low film densities associated it T_{off} = 50 s in Figures 5-63 to 5-66. Increasing T_{off} reduces the time dedicated to actuals electrodeposition per pulse period (T_{on} + T_{off}). For instance, 20% of the total plating time was dedicated to ruthenium deposition when T_{off} = 12 s, compared to 50% when T_{off} = 3 s.

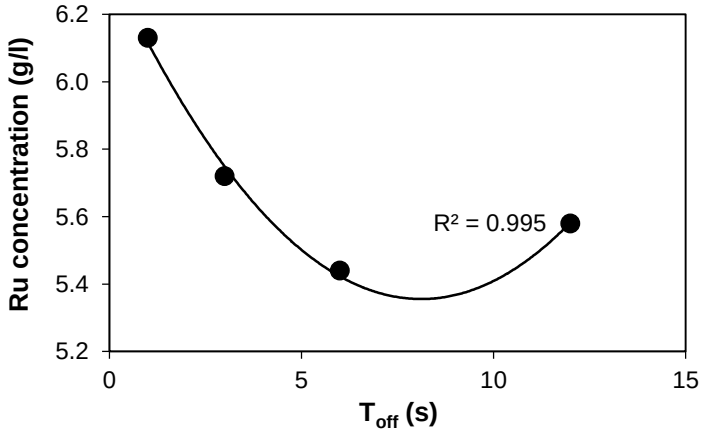

Figure 5- 73 *Variation of the ruthenium concentration with T_{off} as measured by ICP. Initial concentration ≈ 6.2 g/l, and T_{on} = 3 s.*

Stress analysis

XRD analysis done on the ruthenium electrodeposited films revealed a single ruthenium peak at 2θ ≈ 44.7°. The peak was identified as the (1000) reflection from ruthenium HCP crystal (PDF 00 006 0663), and was only observed on the films deposited at low T_{off}. This suggests that film thickness decreased with increase in T_{off}, consistent with the images in Figures 5-63 to 5-66.

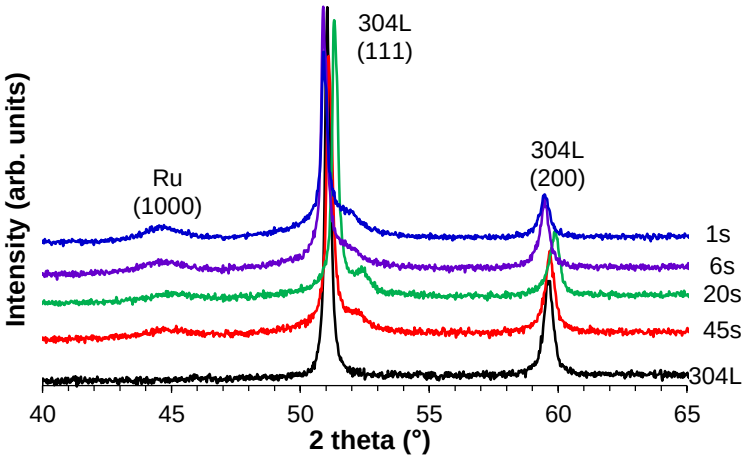

(a)

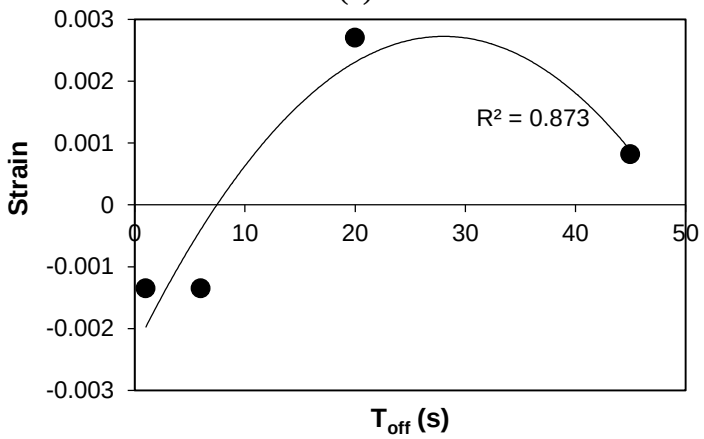

(b)

Figure 5- 74 *Influence of T_{off} on (a) Bragg angle, and (b) strain induced in ruthenium plated 304L stainless steel. T_{on} =3 s.*

As can be seen in Figure 5-74(a), the Bragg angle of the (111) and (200) peaks corresponding to 304L stainless steel shifted from typical 2θ positions. This suggests that any stresses generated in the films during electroplating were transferred to the stainless steel substrate. Since the peaks corresponding to ruthenium were either too small for reasonable analysis, or non-existent, stresses generated during PED were calculated using the (200) 304L stainless steel peaks. The results presented in Figure 5-74(b), indicate that stresses in the films evolved with increase in T_{off}. At low T_{off}, stresses were mostly compressive, but became tensile with higher T_{off}. Further increase in T_{off} (> 27 s) changed the nature of stresses: stresses became more compressive. A possible source of stresses is the ballistic effect of hydrogen bubbles collapsing on the surface.

Corrosion characterisation

Stainless steel samples electroplated with ruthenium were exposed to 1 M sulphuric acid and polarised potentiodynamically at 0.5 mV/s. The results obtained ate presented in Figure 5-75.

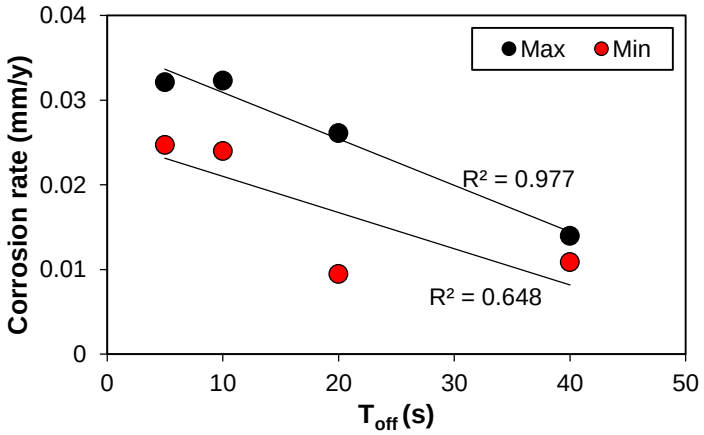

Figure 5- 75 *Variation of corrosion rate of ruthenium plated 304L with T_{off}. Total deposition time was 1800s, and samples were exposed to 1 M sulphuric acid.*

Figure 5-75 shows that corrosion rate decrease with increase in T_{off}. The least corrosion rates measured were between 0.011 and 0.014 mm/y, and were associated with the films prepared at T_{off} = 40 s. These results are consistent with those presented in Figure 5-70.

5.4.3 Effect of surface roughness

The effect of surface roughness on the morphology of the ruthenium film produced by PED is presented in Figure 5-76. Immediately evident from the figure is that film density of the ruthenium films was strongly dependent on surface roughness. No electrodeposition occurred on the roughest samples (120 grit), while the densest film was obtained on the polished surface. The film deposited on the surface ground to 500 grit was not uniform, with some area compact and dense, and others sparsely distributed. On these surfaces, bare spots were observed (shown by ellipse). This uneven film growth is possibly due to uneven current distribution on the surface.

At first glance, the film deposited on the polished surface appeared also sparsely distributed. However, closer examination of the surface revealed very fine deposits on these seemingly bare spots (shown by arrow). This points to uneven film growth, though the effect was not as detrimental as on the rougher surfaces.

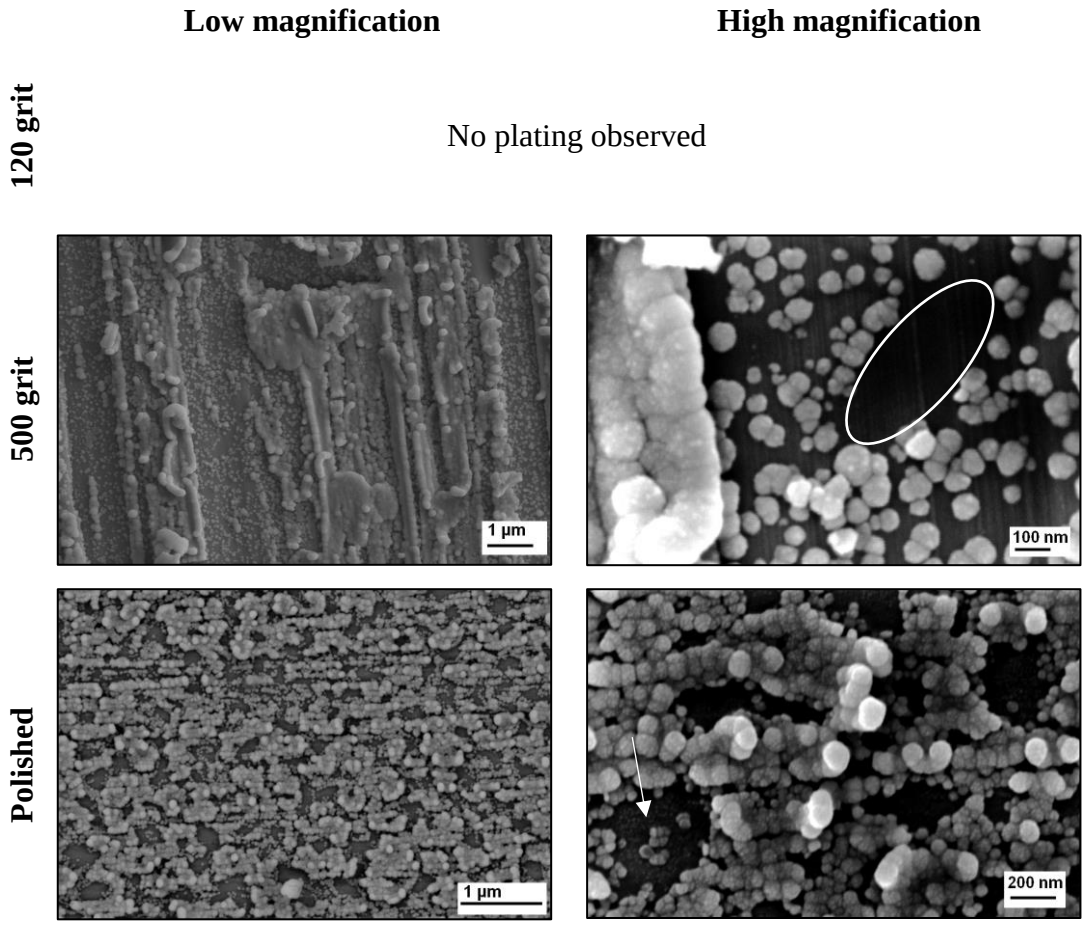

Figure 5- 76 *Influence of surface roughness on film morphology.* T_{on}*= 3 s,* T_{off} *=50 s.*

From the images in Figure 5-76, it is not clear how surface finish could possibly influence stress distribution in the films. However, comparing Figures 5-63 to 5-66 shows that films deposited on polished surfaces were much more chapped and curled than those prepared on rough surfaces under same conditions. This could be due to the high nucleation rates that seem to be associated with polished surfaces.

Corrosion performance of the ruthenium plated 304L stainless steel also exhibited a strong dependence on pre plating surface preparation (Figure 5-77). Overall,

corrosion rates were quite low: less than 0.1 mm/y consistent with ≈ 88% improvement in corrosion resistance. However, the best corrosion rates were recorded on the polished surfaces. These results are in agreement with the findings in Figure 5-70 that at high T_{off}, polished surfaces displayed better corrosion resistance than rough ones.

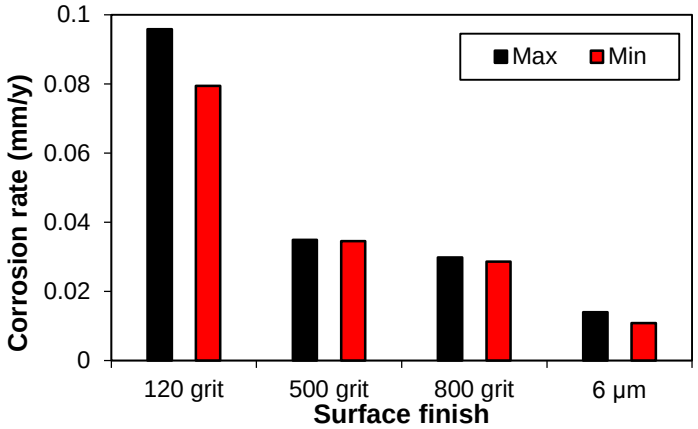

Figure 5- 77 *Variation of corrosion rate of ruthenium plated 304L with T_{off}. Total deposition time was 1800 s, and samples were exposed to 1 M sulphuric acid. All surfaces were polished.*

5.4.4 Effect of plating time

Increasing plating time was expected to increase film thickness and therefore the protection efficiency of the ruthenium films. To verify this, films were prepared using plating times ranging from 1800 to 5400 s. Film morphology, and corrosion performance was analysed using FESEM, and potentiodynamic polarisation. The results are presented in Figures 5-78 and 5-79.

Figure 5-78 shows that increasing T_{off} caused the deposition of smoother films, consistent with observations made in Figure 5-63 and 5-64. Increasing plating time at both T_{off} = 20 s and 40 s increased film stresses. This was indicated by the increased tendency of the films to chap and curl. The behaviour was especially pronounced at lower T_{off}.

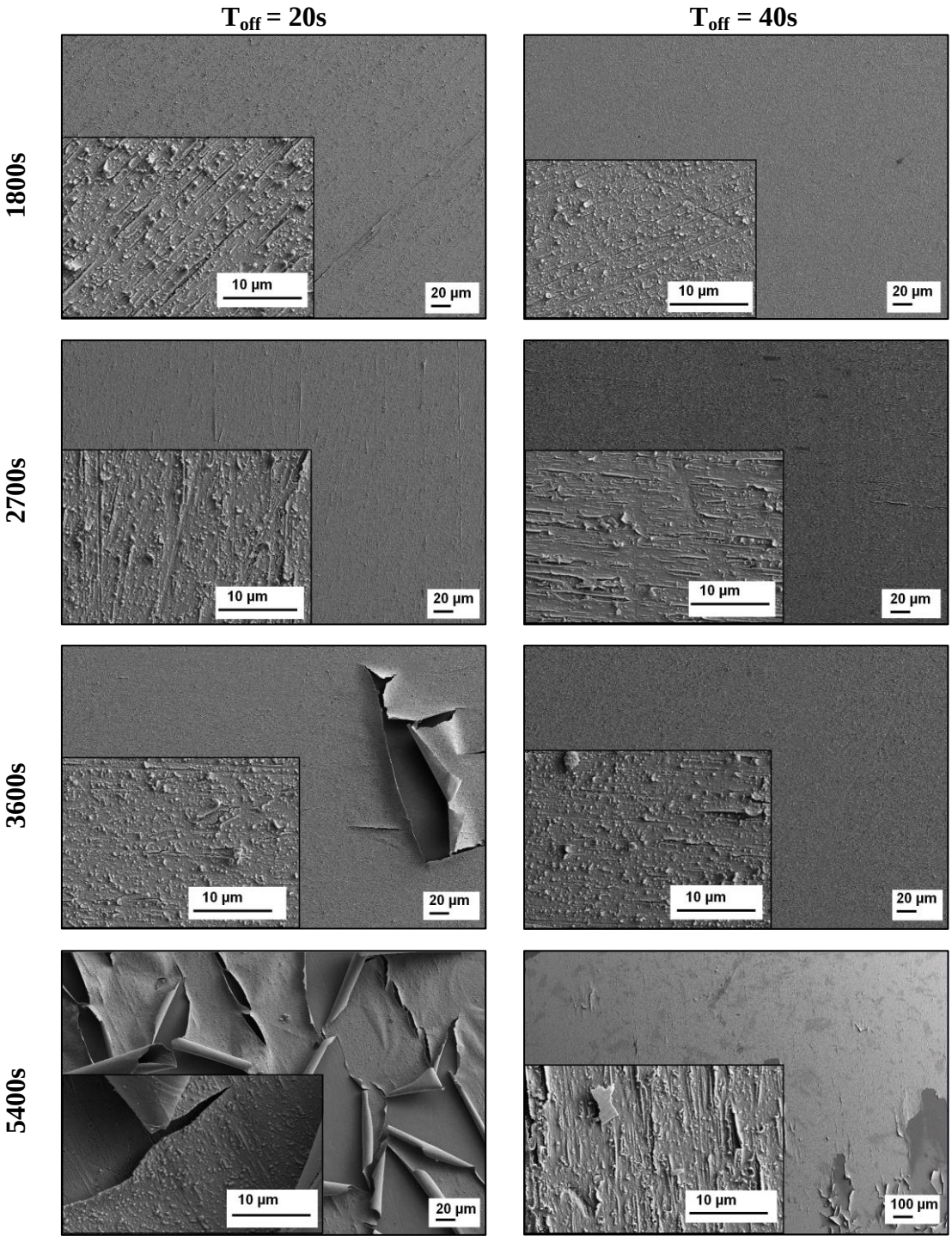

Figure 5- 78 *FESEM-SE images showing the influence of T_{off} and deposition on the morphology of ruthenum prepared by PED.*

Corrosion rates of the ruthenium plated 304L stainless steel reported in Figure 5-79 were consistent with the findings in Figure 5-70 and 5-75: they decreased with increase in T_{off}. The figure also shows that corrosion rates increased with increase

in plating time. These findings were attributed to the increase in film stresses with increase in plating time reported in Figure 5-78. However, the rate of increase was more drastic for the films prepared using T_{off} = 20 s. For instance, increasing deposition time from 3600 to 5400 s increased corrosion rates by 100%, and ≈ 37% for the films deposited at T_{off} = 20 and 40 s respectively. The least corrosion rates were reported on films deposited for 1800 s regardless of the value of T_{off}.

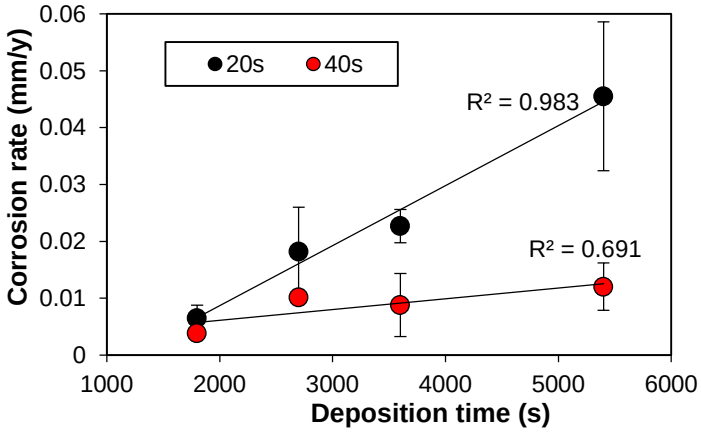

Figure 5- 79 *Effect of deposition time and T_{off} on the corrosion rate of ruthenium 304L stainless steel exposed to 1 M sulphuric acid.*

Films for further analysis were prepared according to the conditions in Table 5-10.

Table 5- 10 *Synthesis conditions for ruthenium plated 304L stainless steel by PED.*

Surface finish	**T_{off}**	**T_{on}**	**i_p**	**Plating time**
Polished	40 s	3 s	-1.2 A	1800 s

5.4.5 Long term exposure

Practical applicability of the ruthenium-plated films hinges on the adhesion of the films before and during corrosion exposure. Samples were prepared as per conditions in Table 5-10. Adhesion of the films pre- corrosion was analysed by the tape test outlined in ASTM D3359-09 using scotch tape from 3M. For repeatability, three samples were tested, and two of these are presented in Figure 5-80. As can be seen from this figure, the tape was clean, the edges of the cuts

were smooth, and none of the squares detached. The adhesion of the films was classified 5B as per ASTM 3959-09, which means they exhibited good adhesion.

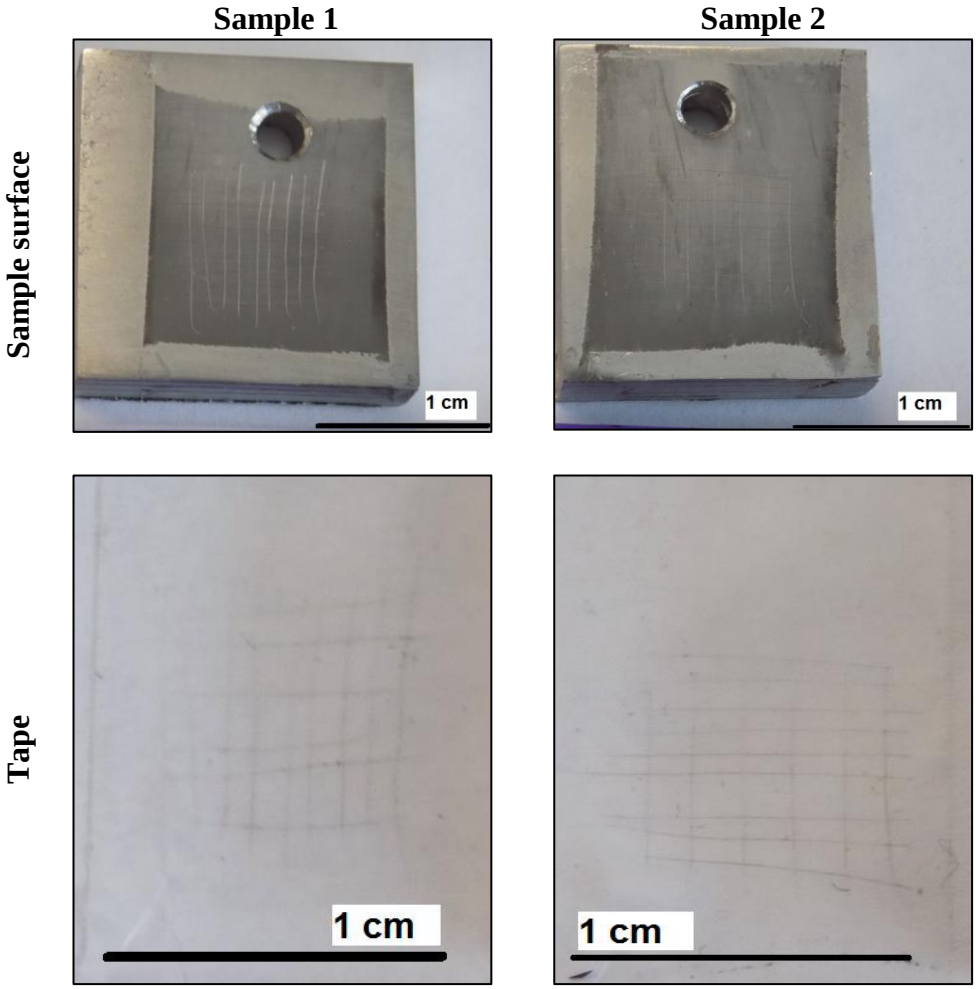

Figure 5- 80 *Adhesion of ruthenium films deposited on 304L stainless steel by PED.*

The films were exposed to 1 M sulphuric acid for 48 hours. They were studied via potentiodynamic polarisation and EIS at OCP. The results obtained are presented in Figure 5-81 and 5-82.

Figure 5-81 shows that the corrosion potential of plated 304L stainless steel was > 680 mV, and increased with increase in exposure time. These potentials were in the transpassive region (Figure 2-3), where the thermodynamic stability of protective chromium (III) species is severely compromise. At these high potentials, metals experience high dissolution rates.

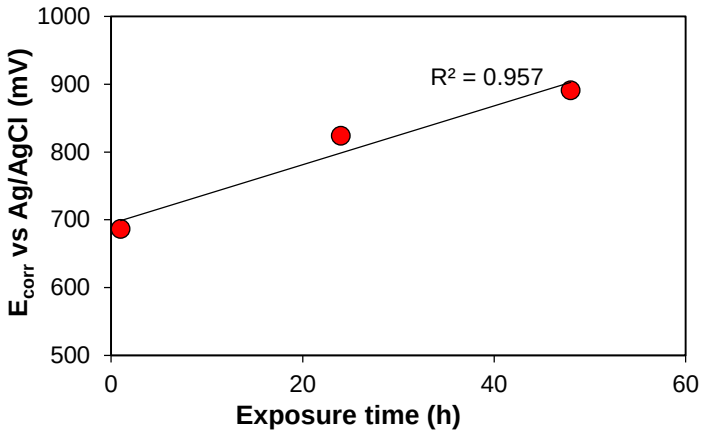

Figure 5- 81 *Variation of corrosion potential of ruthenium plated 304L stainless steel with exposure time in 1 M sulphuric acid.*

Bode phase plots in Figure 5-82(a) show that the ruthenium plated films failed within an hour of application. The phase angle tended towards zero at both ends of the frequency spectrum, suggestive of a defective non-protective film. Increasing exposure time notably resolved the curves into at least two time constants. Bode phase plots with more than one time constant are typical of more than one process occurring on the surface (Orazem & Tribollet 2008). Nyquist plots in Figure 5-82(b) confirm the possibility of multiple processes. The inductive loops on these curves suggest adsorption, and desorption processes, possibly because of the oxidative dissolution of passive films on the surface (Sherif & Park 2006). This could be associated with desorption of oxidised material from the surface. In addition, the radii of the plots decrease with exposure time, consistent with a decrease in film resistance. These results correlate with the observed changes in corrosion potentials in Figure 5-81.

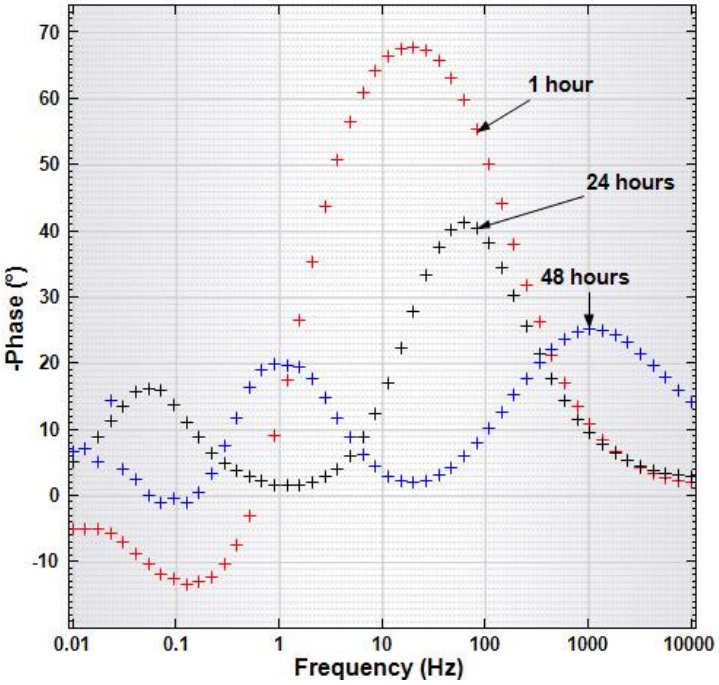

(a)

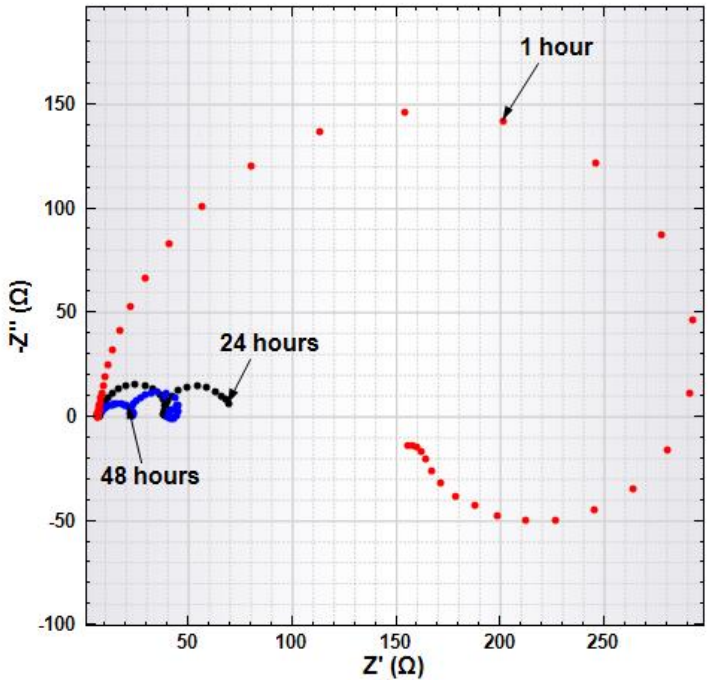

(b)

Figure 5- 82*(a) Bode phase plots, and (b) Nyquist plots of ruthenium plated 304L stainless steel in 1M sulphuric acid.*

Post corrosion examination of the corroded samples in Figure 5-83 confirmed the EIS findings presented in Figure 5-82. The ruthenium films were completely removed from the surface within one hour of corrosion exposure. Random pits, and sparsely sulphate deposits (shown by arrow) were observed on the samples after one hour of exposure. Samples exposed for 48 hours exhibited signs of intergranular corrosion. This is typical of transpassive corrosion.

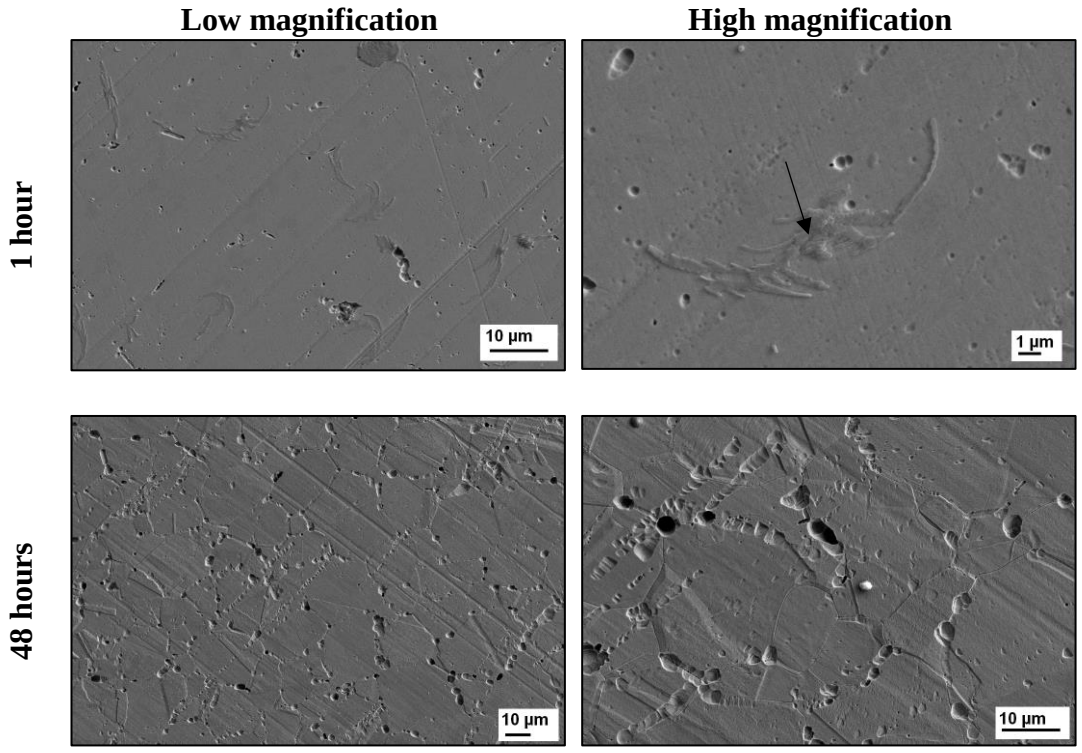

Figure 5- 83 *FESEM-SE images of the corroded ruthenium plated 304L stainless steel after 1 and 48 hours in 1 M sulphuric acid.*

5.5 Discussion

The focus of the study in this chapter was to synthesise ruthenium surface alloys via ion implantation, RF sputtering and PED. These alloys were characterised using a suite of techniques including XRD analysis, FESEM and potentiodynamic polarisation. Preceding sections presented and described the results obtained via these techniques. The present section seeks to discuss, interpret and offer possible implications of these results.

5.5.1 Ion implantation

Ion implantation of ruthenium into 304L stainless steel was done using a Varian 350D implanter. A full 2^k factorial design was used to determine implantation parameters that would give the best corrosion resistance in 1 M sulphuric acid. Three independent parameters, namely dose, energy and surface roughness were considered at two levels: low and high. The levels were as follows: (1) 50 and 160 keV for energy, (2) 10^{12} and 10^{14} Ru/cm^2 for dose, and (3) polished and rough for surface roughness.

In most of the cases studied, introducing ruthenium by ion implantation improved corrosion resistance of the substrate in 1 M sulphuric acid. Tjong and Chu (2007) observed similar effects when they exposed ruthenium implanted Fe-24Cr ferritic stainless to 0.5 M sulphuric acid. The improvement in corrosion resistance was the consequence of cathodic modification as seen by the corrosion potential shift towards more noble values in Figure 5-12(a).

The effect of implantation dose and energy on the corrosion rates of the ruthenium implanted 304L stainless steel exhibited a strong dependence on pre-implantation surface finish. Increasing implantation dose had a detrimental effect on polished surfaces, while increasing energy did not seem to alter corrosion resistance. This was contrary to expectation and documented literature (Wang et al. 1994; Feng et al. 2012): corrosion rates should decrease with increase in implantation dose, and increase with increase in implantation energy. Rough stainless steel surfaces on the other hand, conformed to this typical behaviour.

SRIM simulation in Figure 5-2 predicted that implantation at 160 keV placed the peak ruthenium concentration 34 nm below the surface, compared to 13 nm at lower implantation energy. During corrosion exposure, it is postulated that selective dissolution of the base alloy leads to surface enrichment of the active cathode (Pickering 1983), and the rate of this surface enrichment is a function of the concentration of the active cathode. Hence, for samples with a deeper distribution of ruthenium, the rate of surface enrichment would be low, and the effectiveness of cathodic modification reduced. This accounts for the reduction in corrosion resistance with increase in implantation energy.

The variation of corrosion rate of the polished samples with energy reported in Figure 5-12(b) however, suggests that the depth of ruthenium distribution was the same regardless of implantation energy. Increasing implantation energy from 50 to 160 keV caused a marginal decrease of about 11% in corrosion rate irrespective of implantation dose. One of the challenges associated with ion implantation of polycrystalline substrates such as 304L stainless steel is channelling. Channelling results in a deeper than predicted dopant distribution, and reduces its concentration near the surface (Nastasi & Mayer 2007). Amorphisation of the substrate surface can limit the effects of channelling, and one of the simplest ways of achieving a nearly amorphous surface in through roughening. As can be seen in Figure 4-9, the rough surfaces exhibited a more disordered state, whereas the polished surfaces were homogeneous, with preferentially oriented crystallographic arrangement.

Material loss due to sputtering is typical during ion implantation, and is the reason why a surface alloy concentration of 100% is not achievable with the process (Bunker & Armini 1994). Sputtering is caused by the erosive effect of impinging ions, which also generates dislocations and defects in the lattice structure. Lattice defects present as regions of high energy, susceptible to anodic dissolution. AFM results in Sections 5.2.3 and 5.2.4 show that the amount of sputtered material from polished surfaces was larger when implantation dose was increased than when energy was increased. It is therefore more plausible to expect a higher defect concentration with increasing dose than with increasing energy. Hence, the trend in Figure 5-12(b) where corrosion rates on polished samples increased more with dose than with energy. Paine and Speriosu (1987) did report increased radiation damage with an increase in implantation dose.

Figures 5-13 to 5-15 and 5-35 show that at times the corrosion of the ruthenium implanted stainless steel in 1 M sulphuric acid occurred by intergranular attack. Sputtering preferentially occurs along grain boundaries (Picard et al. 2001; Riviere et al. 2002), and this could be the reason for the observed corrosion form. Other researchers (Covino et al. 1978; Feng et al. 2012) reported similar corrosion behaviour. However, a closer look at these figures revealed that in all but one cases, intergranular corrosion was limited to polished samples. Yet sputtering was

also observed on the rough samples. In fact, the mean sputtered depth was largest on rough samples (Figures 5-26 & 5-31). Ruthenium ion implantation had a smoothening effect on the rough samples, rather than a roughening effect as observed on polished samples. This suggests that material loss from rough surface was from asperities, and not localised at grain boundaries as illustrated in the schematic in Figure 5-84.

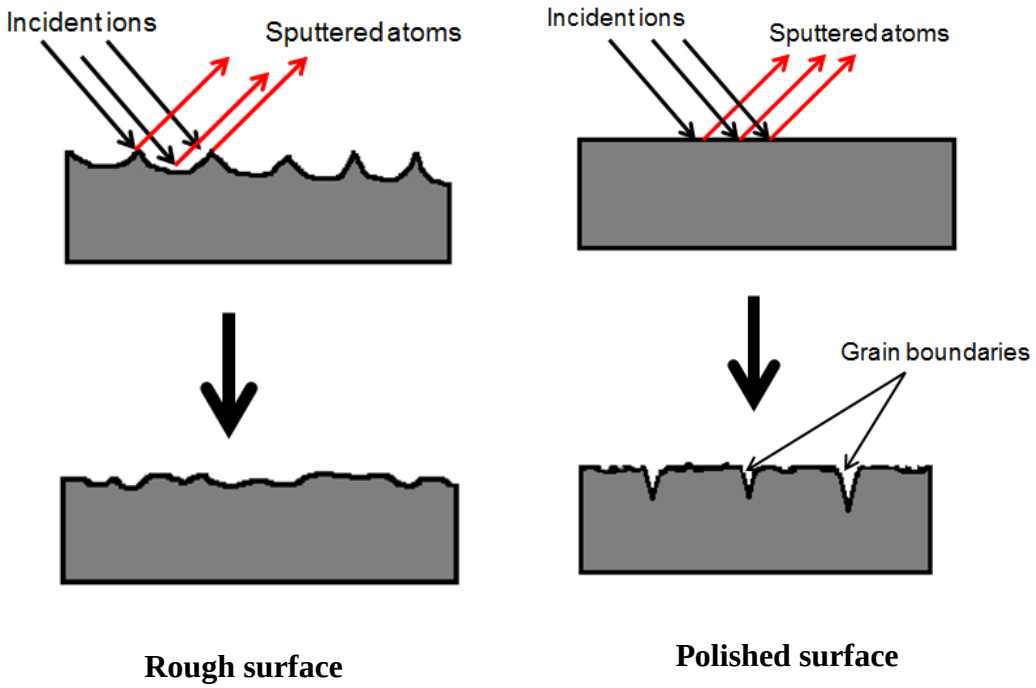

Figure 5- 84 *Schematic illustrating the possible dependence of sputtering on surface finish of the 304L stainless steel substrate.*

XRD analysis of ruthenium implanted 304L stainless steel shows that the Bragg angle shifted more to lower values for rough samples, indicative of larger compressive stresses. Compressive stresses in ion implantation arise mainly from interstitial atoms (Paine & Speriosu 1987), consequently causing volume expansion of the lattice. Schubert et al. (1984) showed that the expansion of a niobium crystal lattice was linearly proportional to the concentration of nitrogen implanted in it. Similar results are reported in Figure 5-28 and Table 5-4. Although the quantities of ruthenium implanted were too small to be successfully detected by EDS, auger electron spectroscopy (AES) or TEM (Appendix D), it was plausible to conclude from the XRD measurements that larger concentrations

of ruthenium were implanted into rough samples than polished samples. This conclusion is corroborated by the low corrosion rates on some of these rough samples. In fact, analysis of 2^k DOE revealed that the best corrosion resistance on 304L stainless steel was achievable on rough samples implanted at low energy, and high implantation dose.

Further experimentation was done on samples prepared under these conditions: rough samples, low implantation energy and high implantation does. Efforts to increase surface roughness by sandblasting did not necessarily increase the benefits of ruthenium ion implantation. On the other hand, increasing implantation dose from 10^{14} to 10^{16} Ru/cm^2 caused a marked improvement in corrosion resistance of the ruthenium-implanted stainless steel (Figure 5-32). However, the same figure shows that the change was smaller than increasing does from 10^{12} to 10^{14} Ru/cm^2. This is consistent with the report by Bunker and Armini (1994) that for high doses, the rate of material sputtering matches the rate of ion implantation, and further increase in dose would not be necessarily beneficial.

Final samples were synthesised as per condition listed in Table 5-11, and exposed to various corrosive environments in Chapter 6.

Table 5- 11 *Synthesis condition for ion implanted 304L stainless steel.*

Surface finish	Energy	Dose	Sample orientation
Ground to 120 grit	50 keV	10^{16} Ru/cm^2	0°

5.5.2 RF sputtering

Thin ruthenium films were deposited on 304L stainless steel using RF sputtering. To determine sputtering parameters that would give films with the best corrosion performance in 1 M sulphuric acid, a one-factor-at-a-time approach was used. Two parameters considered were deposition power and deposition time. These were varied between 30 and 200 W and 3 to 30 minutes respectively.

The presence of the ruthenium films anchored the OCP of the stainless steel in the region where protective chromium (III) species are thermodynamically stable, and reduced corrosion rates of 304L stainless steel by as much as 99%. Potgieter et al. (1992) reported similar improvement (≈ 80%) when they exposed ruthenium

coated 2202 duplex to 10% sulphuric acid. Corrosion improvement was attributed primarily to the ruthenium film physically isolating the substrate from the sulphuric acid. Despite the low corrosion rates reported on these coated 304L stainless steel samples, the ruthenium films failed during corrosion exposure.

Corrosion performance of the ruthenium films was dependent on the deposition power. Films deposited at 100 W performed poorly compared to those prepared at 30 W. Examination of these films pre-corrosion (Figures 5-39 & 5-40) revealed that films deposited at 100 W were characterised by wrinkling. Wrinkling is a consequence of high compressive stresses in the film (Cuthrell et al. 1988), and low adhesion energies at the film-substrate interface. This feature was not observed on the films produced at 30 W, consistent with the expectation that film stresses increase with increase in deposition power. Hence, the poor corrosion performance of the films deposited at higher power was attributed to film stresses.

Increasing deposition time influenced corrosion rate twofold: it decreased corrosion rates, but increased corrosion rates when the deposition time was extended beyond 20 minutes. In fact, the lowest corrosion rates were recorded on the films produced for 10 and 20 minutes. The initial decrease in corrosion rate was attributed to the increase in film thickness with increase in deposition time. A further increase in thickness could have possibly induced larger stresses, consistent with observations by Sheeja and co-workers (2002), who showed that increasing the thickness of diamond-like-carbon films from 3 to 50 nm increased compressive stresses from 2 to 8 GPa.

In addition, films deposited for 30 minutes seemed to be more randomly oriented than the films deposited using lower times. As shown in Figure 5-44, the XRD pattern for the film was characterised by two peaks, suggestive of a film with randomly oriented crystals. It was postulated that change in orientation influenced stress distribution in the film and reduced the corrosion performance of the ruthenium film.

To improve the adhesion of the ruthenium films, four approaches were used. These were surface roughening, pulsing deposition pressure, using a titanium seed layer, and annealing. Films produced by pulsing pressure and using a titanium

seed layer preformed relatively well compared to those produced on rough and polished surfaces. In all the cases studied, these films remained on the substrate for the whole 48 hours of immersion (Figure 5-55 & 5-58). Nonetheless, the films experienced some form of failure during corrosion exposure.

The most prevalent form of failure observed on the ruthenium films were wrinkling and blistering. These indicate a localised loss of adhesion, which severely compromised the corrosion performance of the films. Results presented in Figures 5-55 and 5-62 show that wrinkling and blistering were not necessarily preceded by film fracture, confirming that these were probably caused by stresses in the films. The primary source of stress in the ruthenium films was probably residual stresses due to the sputter coating process. Ballistic effects of ions and atoms during film condensation could have induced compressive stresses in the produced film (Cuthrell et al. 1988; Detor et al. 2009). Another source of stress could be hydrogen gas released during corrosion processes, which is forceful and has been associated with stresses ranging from 20 to 200 MPa (Wampler et al. 1976; Nakahara & Okinaka 1983).

XRD diffractograms obtained on all the ruthenium films did not present evidence of intermetallics, compounds, or new phases. This means that the interaction between the ruthenium film and the 304L stainless steel substrate was only physical. It is likely therefore that stresses induced in the films, during manufacturing or application could not be transferred to the tough ductile 304L stainless steel. This is confirmed by the XRD results in Figures 5-44 and 5-50, which show that the peaks corresponding to 304L did not shift from the unmodified Bragg positions. Ruthenium is quite brittle, and any stresses induced in the film are likely to have damaged it.

Despite the remarkably low corrosion rates measured on ruthenium sputtered coated 304L stainless steel, failure of the films in 1 M sulphuric acid compromised their long-term applicability. Hence, the ruthenium films produced by RF sputtering were not considered for further testing in Chapter 6.

5.5.3 Pulsed electrodeposition

Thin ruthenium films were deposited on 304L stainless steel via pulsed electrodeposition using the Metrohm PGSTAT 302 Autolab in Figure 3-4. A full 2^k factorial design was used to determine plating parameters that would give the best corrosion protection in 1 M sulphuric acid. Four parameters were considered, and these were pulse on time (T_{on}), pulse off time (T_{off}), plating current (i_p) and surface roughness. The parameters were considered at two levels as follows: (1) 3 and 10 s for T_{on}, (2) 1 and 50 s for T_{off}, (3) 1.2 and 2 A for i_p, and (4) polished and rough for surface roughness.

Corrosion rates recorded on these plated stainless steel were mostly less than 0.2 mm/y and as low as 0.002 mm/y. This corresponds to improvements of at least 77%. Improvement in corrosion resistance was attributed to, (1) the ruthenium films physically isolating the substrate from the sulphuric acid, and (2) cathodic modification. The latter justifies the low corrosion rates record on rough surfaces despite the films on these surfaces being sparsely distributed (Figure 5-65, 5-66 & 5-76), and echo the findings of Chernova et al. (1981), who also showed that palladium films on stainless steel need not be continuous to provide effective corrosion protection.

DOE results showed that T_{off} was most influential on the corrosion rate of ruthenium plated 304L stainless steel: corrosion rates in 1 M sulphuric acid decreased with increase in $T_{off.}$ However, the effect was more beneficial on polished surfaces then on rough ones. Films deposited on rough surface at high T_{off} were sparsely distributed as can be seen in Figure 5-63 to 5-66. Current distribution on rough surfaces in non-uniform as illustrated in Figure 5-85. If the height of the protrusions on rough surface (h) is less than the width of the diffusion layer (δN), then the current distribution is given by Equation 5-4 (Wong et al. 1999).

$$i = \frac{zFD(C_O - C_S)}{\delta N - h} \qquad \textbf{\textit{Equation 5-4}}$$

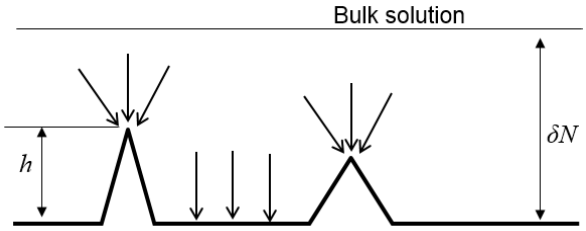

Figure 5- 85 *Effect of protrusions on current distribution (adapted from Wong et al. 1999)*

In contrast, the current density on a flat surface is given by Equation 5-5. It is clear from these two equations that current density is much lower on the protrusions than in the valleys of the surface, leading to uneven current distributions. On rough surfaces where the value of *h* approaches the size of δN, it is likely that current density would be so low that there is insufficient energy for electrodeposition. This could explain the lack of plating on rough surfaces in Figure 5-76.

$$i = \frac{zFD(C_O - C_S)}{\delta N} \qquad \textbf{\textit{Equation 5-5}}$$

Increasing T_{off} apparently had a twofold effect on the deposition rate of ruthenium. Figure 5-73 suggested that plating rates increased with T_{off}, and then decreased with further increase in T_{off}. Increasing T_{off} during PED has the effect of increasing cation concentration at the surface. From Equation 2-15, this causes an increase in the concentration overpotential, and hence nucleation rate. However, a further increase in T_{off} lead to reduced nucleation rates as less time per pulse period is dedicated to the actual plating process. The consequence is low film density reported in Figures 5-63 to 5-66.

T_{off} also had a significant effect on the stresses in the ruthenium films. From Figure 5-74 it can be seen that the nature of stresses in the films evolved with T_{off}: at low T_{off} stresses were largely compressive, and became tensile at high T_{off}. Film stresses in this work were approximated from the stresses in the 304L stainless steel substrate. Figure 5-86 shows the possible effect of substrate stress on the films, assuming that stresses generated in the film were balanced by opposite stresses in the films.

Although the stresses were insufficient to bend the 6 mm stainless steel plates (Figure 5-86(b)), they did cause the ruthenium to deform. At low T_{off} values the compressive stresses are likely to have caused the films to curl as observed in Figures 5-63, 5-64 and 5-86(a). This stress state increased the tendency of the films to peel off during corrosion exposure (Figure 5-68), leading to poorer corrosion rates associated with these films.

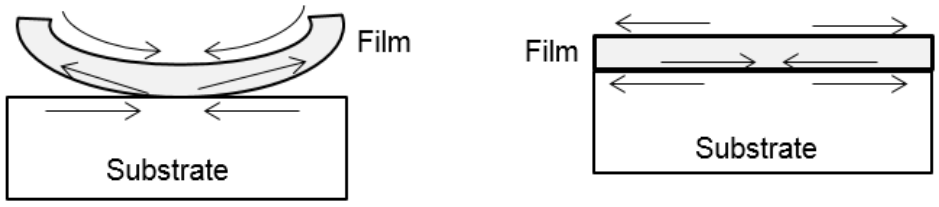

(a) (b)

Figure 5- 86 *Stress state in ruthenium films when substrate stresses were (a) compressive, and (b) tensile.*

One possible source of stresses in the ruthenium films is the hydrogen adsorbed into the surface. Electrodeposition of the ruthenium film is accompanied by co-deposition of hydrogen according to Equation 2-2, which is subsequently adsorbed into the film. Release of this occluded hydrogen is a forceful exothermic reaction shown here, and in previous work (Abys 2010), to cause extensive damage to the plated films. Increasing T_{off} reduced the damaging effect of this process, and smoother films were produced.

Increasing plating time did not necessarily increase corrosion resistance of the 304L stainless steel. This was contrary to expectation since it was supposed that increasing film thickness would increase surface coverage, and hence protection efficiency. As can be seen in Figure 5-78, increasing plating time had the consequence of increasing film stresses, indicated by the increased tendency of the film to crack, curl and peel off. These findings were consistent with the direct relationship between film stress and film thickness (Ohring 2002). The best corrosion resistance was recorded on films deposited for 1800 s.

Despite low corrosion rates, and good adhesion properties, (Figure 5-80) the ruthenium-electrodeposited films performed poorly in the long term. They failed

within one hour of exposure. The corrosion potentials of the plated 304L stainless steel samples were quite high, and increased with exposure time. They were anchored in the transpassive region, suggesting that the failure of the ruthenium was most likely associated with oxidative dissolution chromium (III) species.

Due to the failure of the films over long-term exposure, these films were not considered for further testing in Chapter 6.

5.5.4 Comparison

Three ruthenium surface alloys were produced in this work using ion implantation, RF sputtering and PED. Their corrosion performance was studied in 1 M sulphuric acid at ≈ 25°C. This section of the chapter seeks to compare the behaviour of these surface alloys.

Protection efficiency (PE) is one way of qualifying the effectiveness of alloy addition in improving corrosion resistance (Sherif et al. 2009a). It is defined by the expression in Equation 5-6, where CR_{304L} is the corrosion rate of pristine 304L stainless steel, and $CR_{alloyed}$ is that of the ruthenium alloyed stainless steel. Figure 5-87 compares the PE of each surface alloy studied in this work.

$$PE = \frac{CR_{304L} - CR_{alloyed}}{CR_{304L}} \times 100 \qquad \textbf{\textit{Equation 5-6}}$$

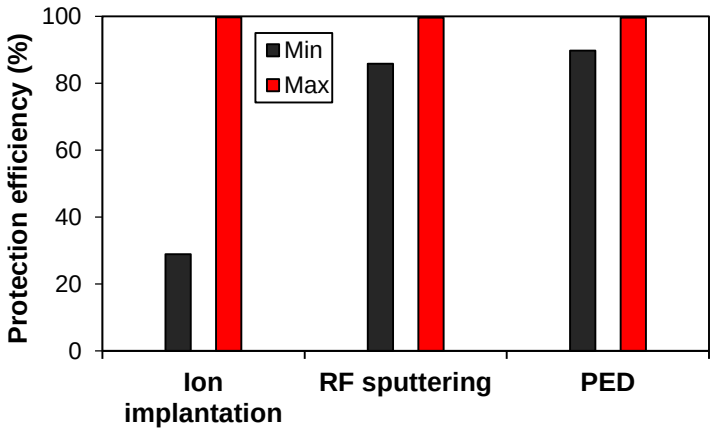

Figure 5- 87 *Protection efficiency of ruthenium surface alloys.CR_{304L} Max = 1.9 and CR_{304L} Min = 0.5 mm/y.*

The ruthenium surface alloys were effective in controlling corrosion rates of 304L stainless steel in 1 M sulphuric acid. In all cases, corrosion rates were less than that reported on the unmodified alloy (Figure 3-5), as seen by the positive values of PE in Figure 5-87. The least PE was associated with ion-implanted stainless steel. Type I ruthenium alloys exhibited very high PE of at least 85%. However, the delamination of these surface alloys compromises their practical applicability.

Improvement in corrosion resistance was primarily attributed to cathodic modification due to the presence of ruthenium. The effect of ruthenium was to increase the corrosion potential of the 304L stainless steel into regions where protective chromium (III) species are thermodynamically stable. As illustrated in Figure 5-88, the increase of corrosion potential was much more marked on Type I ruthenium surface alloys. It is likely that the increase was due to an increase in ruthenium concentration on the surface. Several researchers (Potgieter & Brookes 1995; Sherif et al. 2009a) noted a direct relationship between ruthenium concentration in stainless steel and E_{corr}. In the case of PED ruthenium films, potentials increased to as high as 890 mV. From Figure 4-11, these high potentials correspond to potentials when 304L stainless steel begins to experience transpassive corrosion.

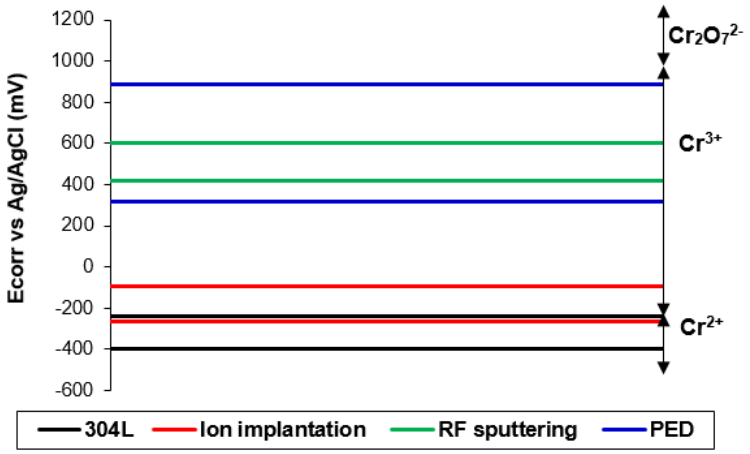

Figure 5- 88 *Effects of ruthenium surface alloying on the corrosion potential of 304L stainless steel.*

Type I ruthenium alloys apparently afforded 304L stainless steel dual corrosion protection. They provided a physical barrier to isolate the metal from the

sulphuric acid. Once broken, the alloys provided protection via cathodic modification. This was mostly observed on the RF sputtered films. Only the Type II surface alloy exhibited the tendency to form surface films during corrosion exposure, which possibly augmented the corrosion protection.

The production of the surface alloys was accompanied by generation of stress. Stresses induced during RF sputtering were compressive. This was attributed to the peening effect of impinging ions and atoms associated with the film manufacturing process. Stresses induced via PED evolved, changing from compressive to tensile with increase in T_{off}. Regardless of the stress state of the films, they all failed during exposure to 1 M sulphuric acid, and in most cases within an hour of application. This suggests that the failure of the films was due to stresses generated during exposure rather than during manufacturing. In addition, stresses generated during PED were transferred to the 304L stainless steel, but this was not observed on the RF sputtered films.

Pre-manufacture surface preparation influenced the corrosion performance of all the surface alloys produced. Rough surfaces were beneficial in ion implantation, whereas polished surfaces were important for best corrosion performance for alloys produced by RF sputtering and PED.

5.6 Summary

The objective of the study in this chapter was to produce ruthenium surface alloys that would improve the corrosion resistance of 304L stainless steel. The surface alloys were produced via ion implantation, RF sputtering, and PED and their corrosion performance qualified in 1 M sulphuric acid. It was important that the surface alloys satisfied the following conditions:

1. They were intact and continuous prior to corrosion exposure,
2. They remained intact and continuous during and after corrosion exposure,
3. Their corrosion rate in 1 M sulphuric acid is less than 0.1 mm/y.

Corrosion rates as low as 0.002 mm/y were recorded on all the surface alloys. However, the films made by RF sputtering and PED failed during corrosion

exposure rendering them unsuitable for corrosion application. Only the surface alloy produced by ion implantation satisfied the three conditions listed earlier. The best corrosion resistance on the ruthenium implanted 304L stainless steel was achievable on rough sample implanted with 10^{16} Ru/cm^2 at 50 keV. Further analysis was limited to this surface alloy.

Chapter 6
Corrosion characterisation

6.1 Introduction

Results presented in the previous chapter demonstrated that the ruthenium surface alloys prepared via ion implantation performed satisfactorily in 1 M sulphuric acid. These surface alloys maintained structural integrity before and after corrosion exposure, and recorded corrosion rates less than 0.1 mm/y. The current chapter presents the corrosion behaviour of the alloys as characterised in various solutions including hydrochloric acid, and simulated fuel cell media. Characterisation was frequently done by electrochemical tests namely potentiodynamic polarisation and chronoamperometry. In most cases, unmodified 304L stainless steel was used as the control. Typical samples used for these experiments are presented in Figure 6-1.

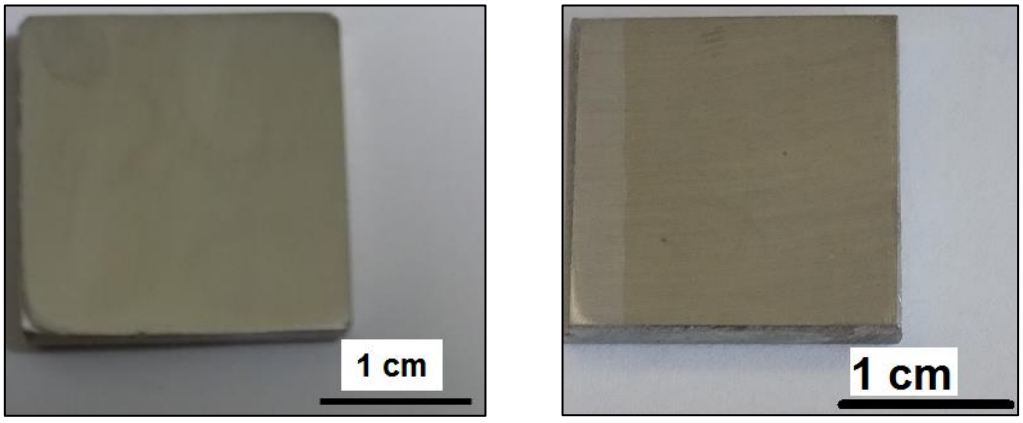

(a) (b)

Figure 6- 1 *Samples used in corrosion characterisation: (a) unmodified, and (b) ruthenium implanted 304L stainless steel.*

6.2 Results: Corrosion in reducing acids

This section of the chapter seeks to present, and describe the results obtained when the ruthenium implanted samples were exposed to sulphuric acid and hydrochloric acid.

6.2.1 Sulphuric acid

Potentiodynamic polarisation curves obtained on unmodified and ruthenium implanted 304L stainless steel in 1 M sulphuric acid are compared in Figure 6-2.

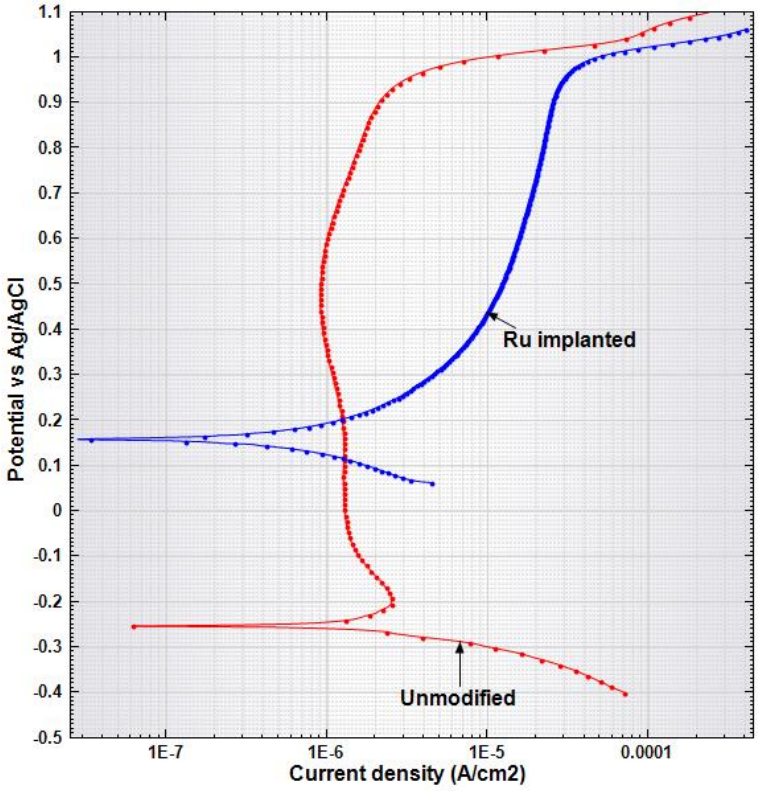

Figure 6- 2 *Potentiodynamic polarisation curves of unmodified and ruthenium implanted 304L stainless steel in 1 M sulphuric acid at ≈ 25°C.*

Introducing ruthenium shifted the corrosion potential to nobler values, typical of cathodic modification, and reduced corrosion current densities to < 1 μA/cm^2. This is consistent with reduction in corrosion rates. Notably, the polarisation curve corresponding to the ruthenium implanted stainless steel did not exhibit the anodic peak commonly observed on active-passive alloys such as 304L stainless steel. The absence of the peak is consistent with spontaneous passivation, and was also observed by previous researchers on ruthenium bulk alloyed stainless steel (Tjong 1990a; Potgieter et al. 1996; Olubambi et al. 2009).

Effects of acid concentration

The stainless steel samples were exposed to sulphuric acid solutions with concentrations ranging from 0.5 to 4 M. All tests were carried out at ≈ 25°C, and the results obtained are presented in Figures 6-3 to 6-9.

Figures 6-3 and 6-4 show the OCP variation on the stainless steel samples with time and sulphuric acid concentration. As can be seen in Figures 6-3(a) and 6-4(a), increasing acid concentration shifted the OCP to increasingly negative values on pristine 304L stainless steel. OCP measured in 0.5 M was ≈ 68 mV, and decreased markedly to almost -320 mV in 4 M sulphuric acid. Comparing these potentials to Figure 2-3, this is consistent with moving from passive potentials where chromium (III) species are stable, to active potentials where non-protective chromium (II) species are predominant, with increase in sulphuric acid concentration. This trend points to an increased tendency for 304L stainless steel to dissolve with increase in acid concentration, and is in agreement with results presented by Phelps and Vreeland (1957).

Examination of Figures 6-3(b) and 6-4(b) reveals that OCP measured on ruthenium implanted 304L stainless steel tended towards nobler values with increase in sulphuric acid concentration. Increasing acid concentration from 0.5 to 4 M increased OCP from ≈ 5 to 470 mV. This was contrary to expectation and observations by other researchers on bulk ruthenium alloyed stainless steel (Olubambi et al. 2009). The trend observed implies that the ruthenium implanted stainless steel exhibited an increased ability to form stable protective chromium (III) films with increase in acid concentration.

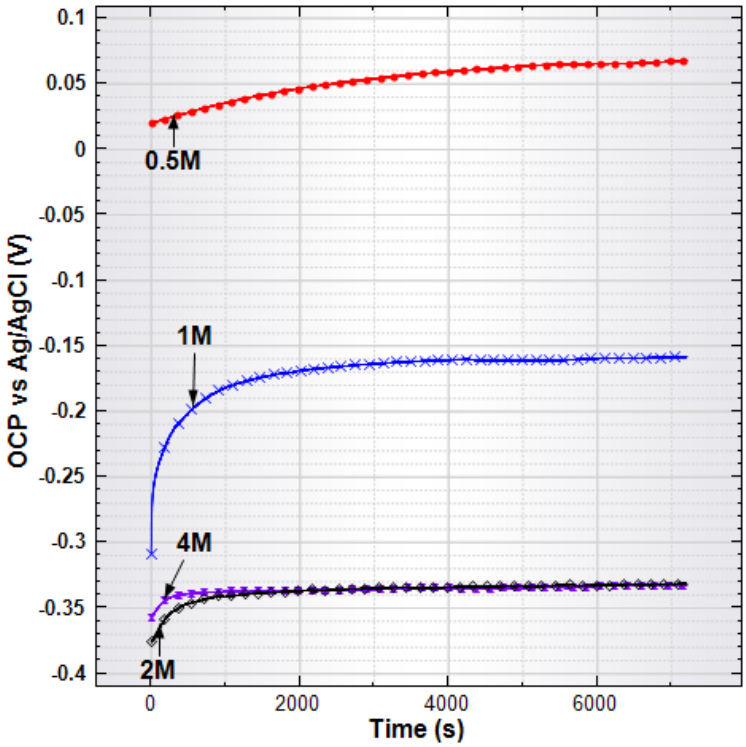

(a)

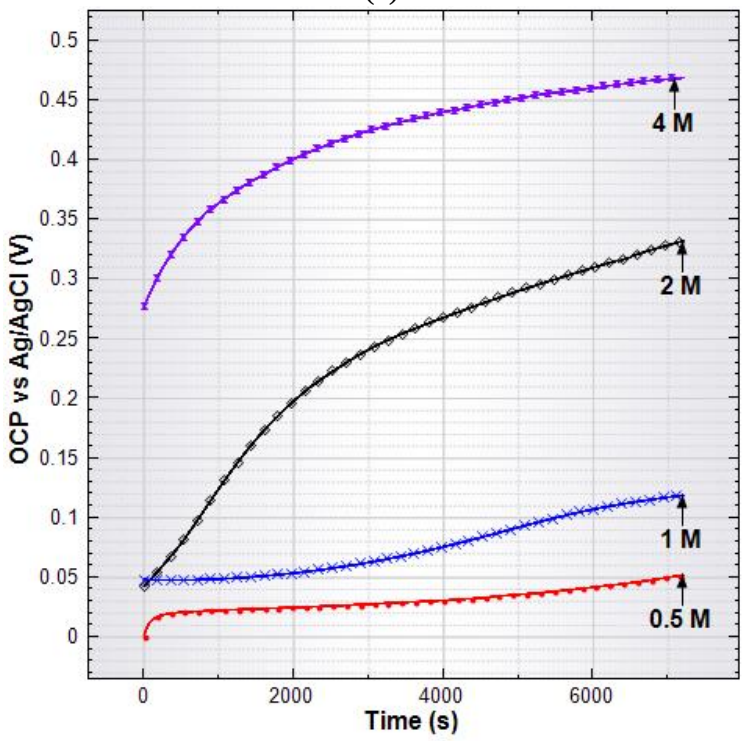

(b)

Figure 6- 3 *OCP-time curve of (a) unmodified and (b) ruthenium implanted 304L stainless steel in sulphuric acid of different concentrations at ≈ 25°C.*

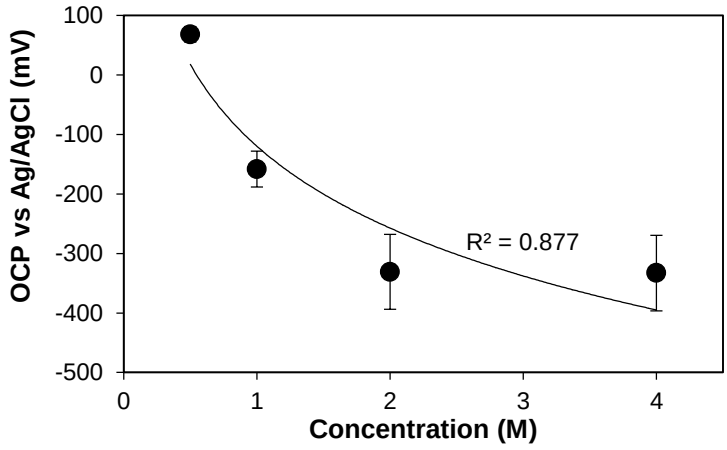

(a)

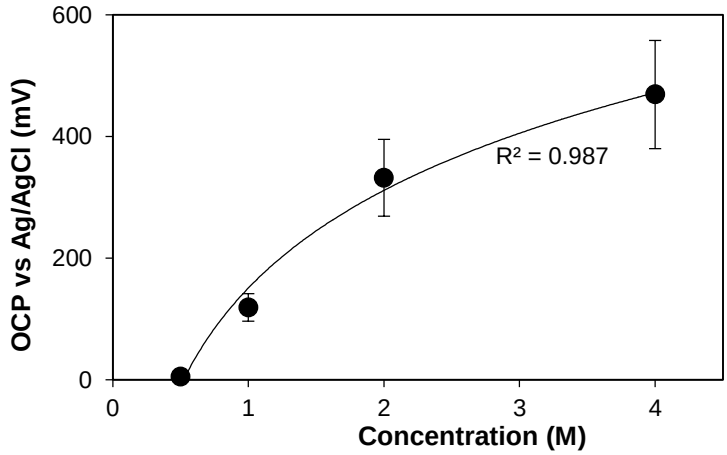

(b)

Figure 6- 4 *Variation of OCP with sulphuric acid concentration for (a) unmodified, and (b) ruthenium implanted 304L stainless steel.*

Based on the results presented in in Figures 6-3 and 6-4, it was expected that corrosion rates of ruthenium implanted stainless steel would decrease with increase in sulphuric acid concentration. This is confirmed in Figure 6-5 where the polarisation curves recorded on the modified stainless steel shifted to lower current densities with increase in sulphuric acid concentration. The corrosion current density in 0.5 M sulphuric acid was typically 0.8 μA/cm^2, and increasing concentration to 4 M decreased the value to an average of 0.4 μA/cm^2.

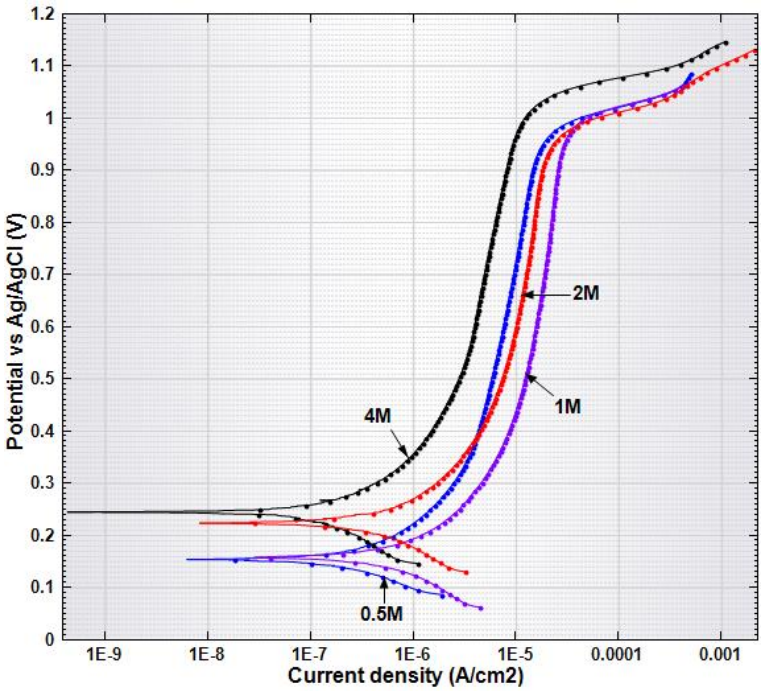

Figure 6- 5 *Effect of sulphuric acid concentration on the potentiodynamic polarisation curve obtained on ruthenium implanted 304L stainless steel after 2 hours of exposure.*

Figure 6-6 compares the corrosion rates measured on pristine and ruthenium implanted 304L stainless steel in sulphuric acid at different concentrations. Consistent with observations in Figures 6-3 and 6-4, corrosion rates of unmodified stainless steel increased with sulphuric acid concentration, but decreased for the ruthenium implanted samples. Corrosion rate of the stainless steel in 4 M sulphuric acid was at least 5 mm/y compared to about 0.004 mm/y measured on ruthenium implanted stainless steel in the same tests conditions. Interestingly, the corrosion rate of ruthenium implanted samples in 1 M sulphuric acid was larger than in 0.5 M. In fact, dissolution rates increased by at least 30% when acid concentration was increased to 1 M.

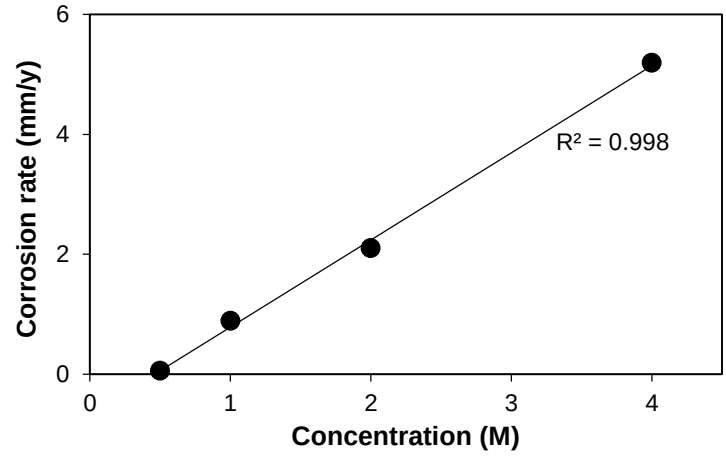

(a)

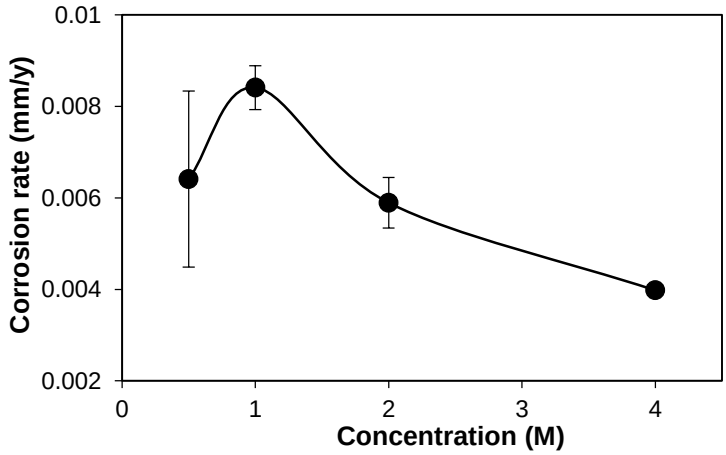

(b)

Figure 6- 6 *Influence of sulphuric acid concentration on corrosion rate of (a) unmodified, and (b) ruthenium implanted 304L stainless steel.*

Further analysis was by EIS at OCP, and the results obtained are presented in Figures 6-7 and 6-8 as well as Table 6-1. Fitting of the EIS data was done using the equivalent circuit in Figure 4-12(b). Figure 6-7(a) shows Nyquist plots that are semi-circular in shape, distinctive of charge transfer limited corrosion processes. Comparing these curves and that presented in Figure 4-12(b) suggests a change in reaction mechanism with introducing ruthenium. In 1 M sulphuric acid, the corrosion of 304L stainless steel was by both diffusion and charge transfer controlled but changed to entirely charge transfer control in the presence of ruthenium.

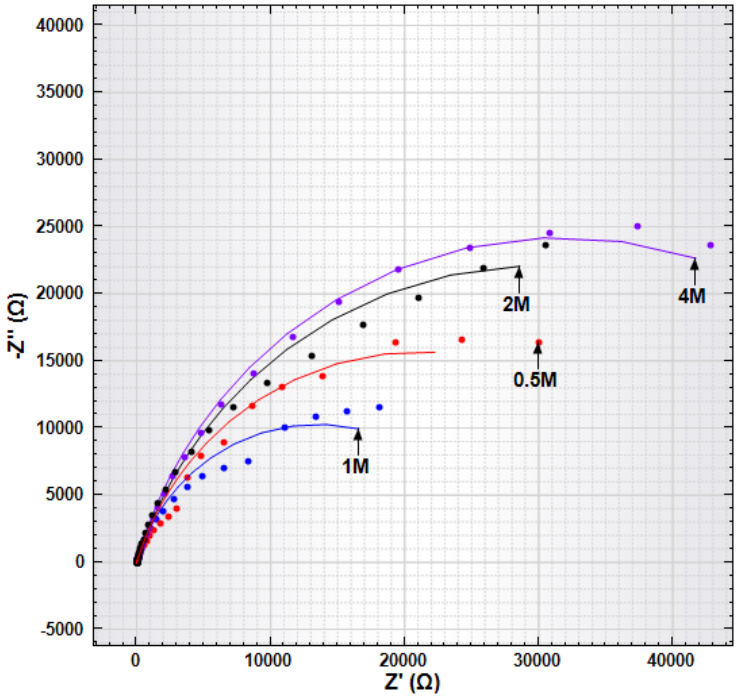

(a)

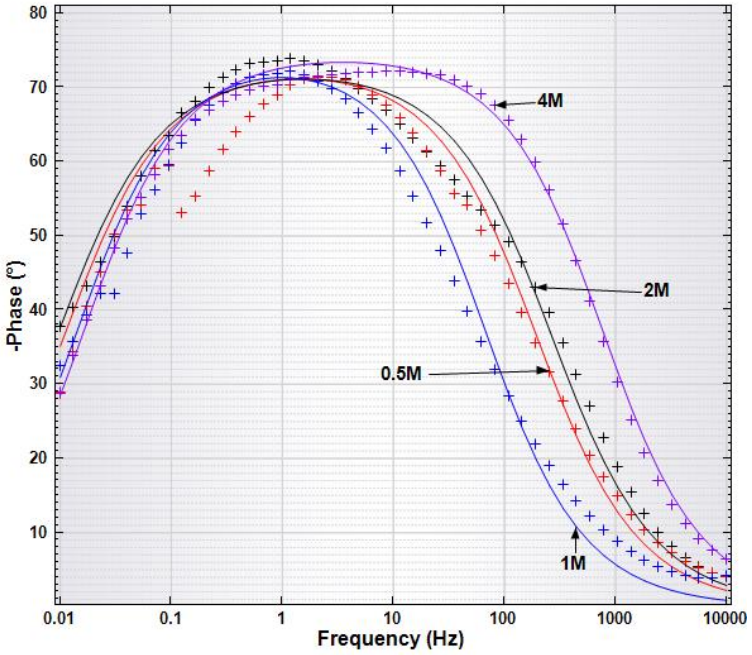

(b)

Figure 6- 7 *Influence of sulphuric acid concentration on (a) Nyquist, and (b) Bode phase plots measured on ruthenium implanted 304L stainless steel.*

The radii of the Nyquist plots in Figure 6-7(a) increased with increase in sulphuric acid concentration, consistent with an increase in polarisation resistance. Polarisation resistance increased from about 42 kΩ.cm^2 to 63 kΩ.cm^2 when acid

concentration was increased from 0.5 to 4 M (Table 6-1). These values are several magnitudes greater than the polarisation resistances reported on pristine 304L stainless in 1 M sulphuric acid (≈ 0.7 kΩ.cm^2). Polarisation resistance can be increased by the presence of passive films on the surface. Figure 6-8 shows that increasing sulphuric acid concentration increased the thickness of the passive films formed on the ruthenium implanted stainless steels. This observation is consistent with the expectation that passive films formed at high potentials are thicker (Olefjord & Elfstrom 1982; Olsson & Landlot 2003).

Table 6- 1 *Electrochemical parameters obtained from EIS tests. *Estimated error in fitting equivalent circuit to data.*

Concentration (M)	n	R_p (Ω.cm^2)	CPE (µF.cm)	C (µF)
0.5	0.813	42 236	210	346
	**0.861*	*9.907*	*2.669*	
1	0.829	26 971	274	414
	0.754	*6.788*	*2.085*	
2	0.809	59 869	166	286
	0.608	*7.955*	*1.922*	
4	0.830	63 458	104	152
	0.203	*2.221*	*0.77*	

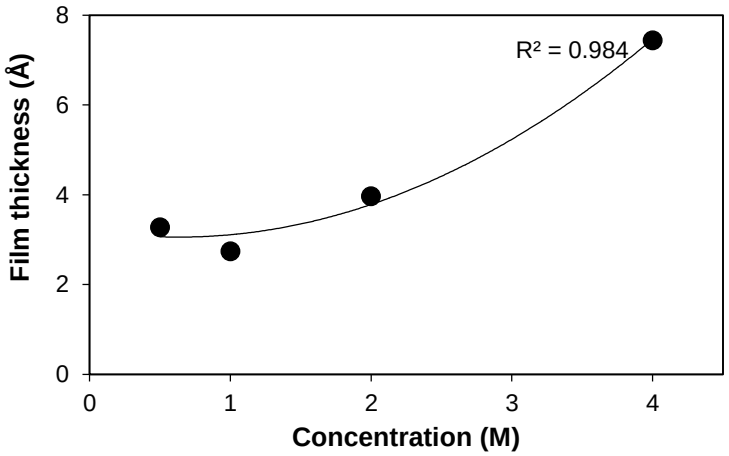

Figure 6- 8 *Influence of sulphuric acid concentration on the thickness of films grown on ruthenium implanted 304L stainless steel. Thickness estimated from Equation 2-24.*

The surfaces of the ruthenium alloyed 304L stainless steel were examined by FESEM after exposure to sulphuric acid, and the images obtained are presented in Figure 6-9. No evidence of corrosion damage was observed on the surfaces. Except for the grooves generated during surface preparation, the surfaces were essentially featureless. These surfaces are in stark contrast to the images obtained on unalloyed 304L stainless and displayed in Figure 4-14, but are consistent with the very low dissolution rates reported in Figure 6-6.

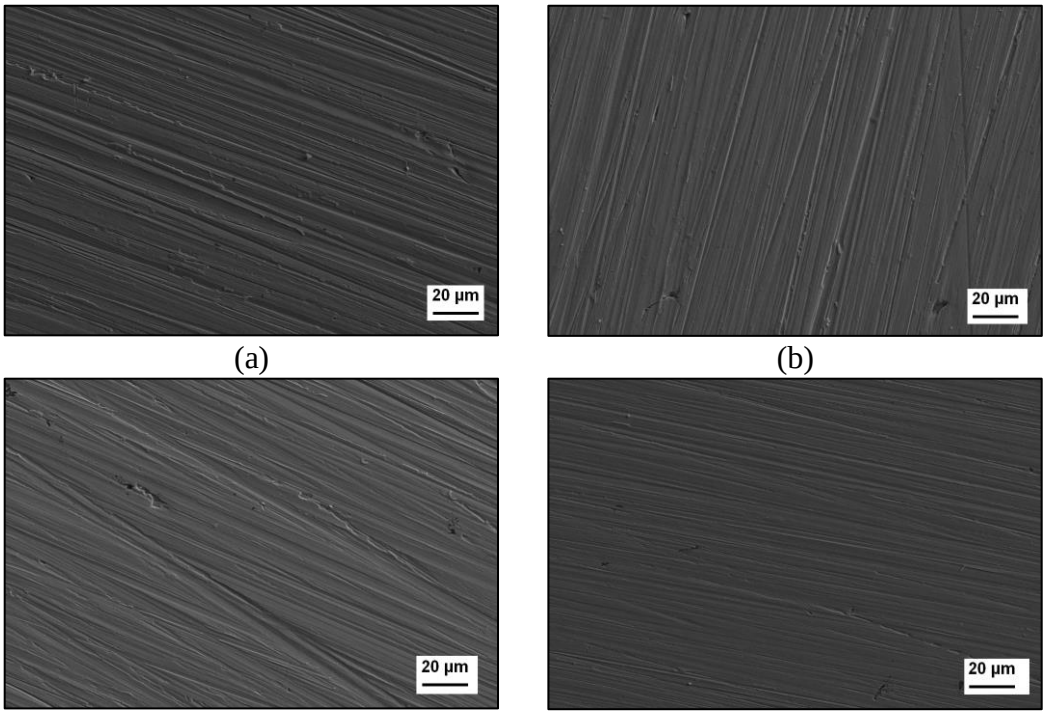

Figure 6- 9 *FESEM-SE images of the ruthenium implanted 304L stainless steel after 2 hours exposure at OCP in (a) 0.5 M, (b) 1 M, (c) 2 M, and (d) 4 M sulphuric acid.*

In Figure 6-7, the phase angle at low frequencies was between |29°| and |38°|. Ideally, the phase angle should tend towards |90°| for a good protective film (Orazem & Tribollet 2008). The observations in Figure 6-7(b) present the likelihood of reduced corrosion resistance with time. Figure 6-10 shows the results obtained when the ruthenium implanted 304L stainless steel was exposed to 0.5 and 4 M sulphuric acid for 54 hours.

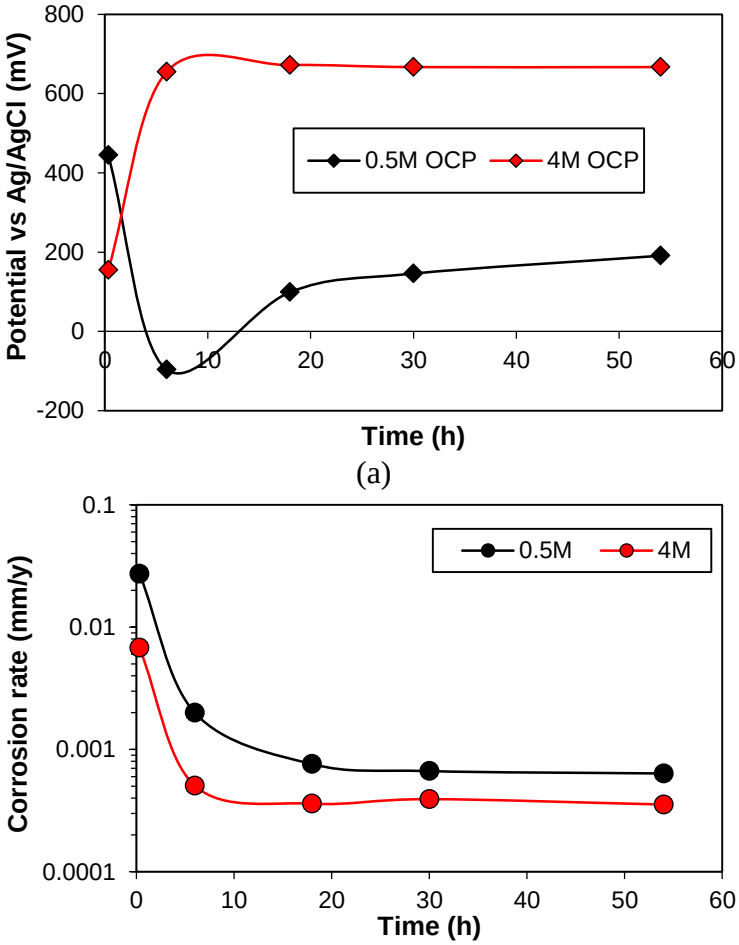

Figure 6- 10 *Effect of exposure time and concentration on (a) OCP, and (b) corrosion rate of ruthenium implanted 304L stainless steel in 0.5 and 4 M sulphuric acid.*

It is clear from Figure 6-10(a) that OCP values measured in 4 M were nobler than in 0.5 M, consistent with the findings presented in Figure 6-4(b). In 4 M sulphuric acid, the OCP of ruthenium implanted stainless steel was ≈ 160 mV, increased to about 642 mV in 6 hours, and remained nearly constant at ≈ 640 mV throughout the exposure period. The OCP in 0.5 M deceased to negative values in the first 6 hours of exposure, possibly due to the dissolution of air formed chromium oxide in the reducing acid (Sherif et al. 2009b). However, OCP values increased with further exposure to regions where chromium (III) species are thermodynamically stable. In this solution, OCP values were almost 140 mV at the end of the 54 hours.

Corrosion rates of the alloyed 304L stainless steel in 4 M sulphuric acid were lower than in 0.5 M as can be seen in Figure 6-10(b), and consistent with results presented in Figure 6-6(b). For much of the exposure period, corrosion rates were stable at ≈ 0.0007 and 0.0004 mm/y in 0.5 and 4 M respectively. These observations suggest that the films formed in the sulphuric acid solutions were stable, and afforded the stainless steel steady corrosion protection over the period of exposure.

Effect of temperature

To understand the effect of temperature on the corrosion behaviour of ruthenium implanted 304L stainless steel, additional tests were carried out at 50°C. The results are presented in Figures 6-11 to 6-14.

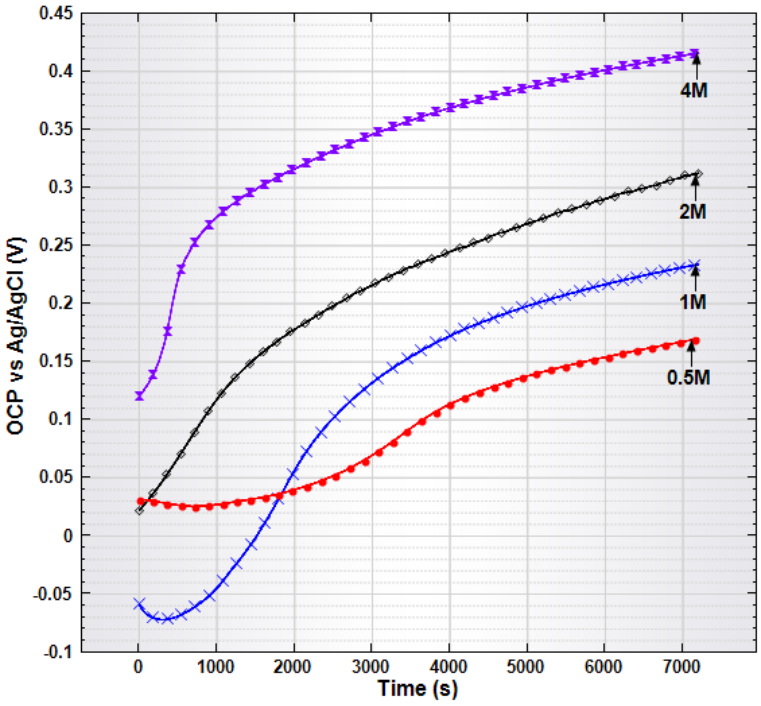

Figure 6- 11 *OCP-time curve of ruthenium implanted 304L stainless steel in sulphuric acid of different concentrations at 50°C.*

The variation of OCP for ruthenium implanted 304L stainless steel with time at 50°C is presented in Figure 6-11. In all the cases studied, increasing sulphuric acid concentration shifted potentials to nobler values: a behaviour also observed at

lower temperatures (Figure 6-3). The effect of increasing temperature was apparently dependent on the concentration of the sulphuric acid. Figure 6-12(b), which compares the OCP recorded at 25 and 50°C, reveals that increasing temperature had a more notable effect in lower acid concentrations. For instance, increasing exposure temperature to 50°C increased OCP measured in 0.5 M acid by a factor of 28.4, whereas the same temperature adjustment in 2 M sulphuric acid increased OCP by only a factor of 1.2.

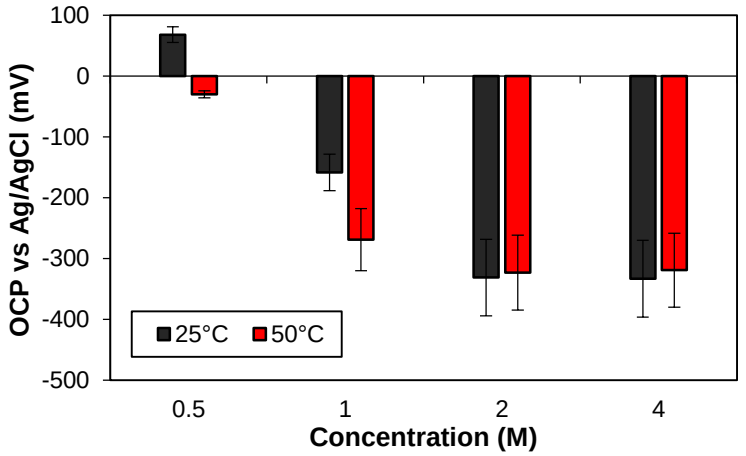

(a)

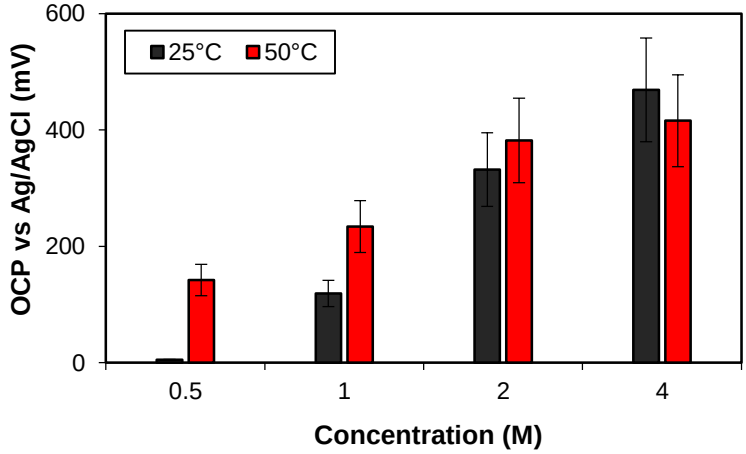

(b)

Figure 6- 12 *OCP of (a) unmodified, and (b) ruthenium implanted 304L stainless steel in sulphuric acid of different concentrations at 25 and 50°C.*

Similar behaviour was observed on unalloyed 304L stainless steel (Figure 6-12(a)). Increasing temperature from 25 to 50°C caused a more significant shift in OCP in acid solutions of low concentrations. However, the shift was towards more active potentials, suggesting increased tendency to corrode with increase in

temperature. This was confirmed in Figure 6-13(a) where increasing temperature generally increased the corrosion rate of 304L stainless steel in acid of different concentrations.

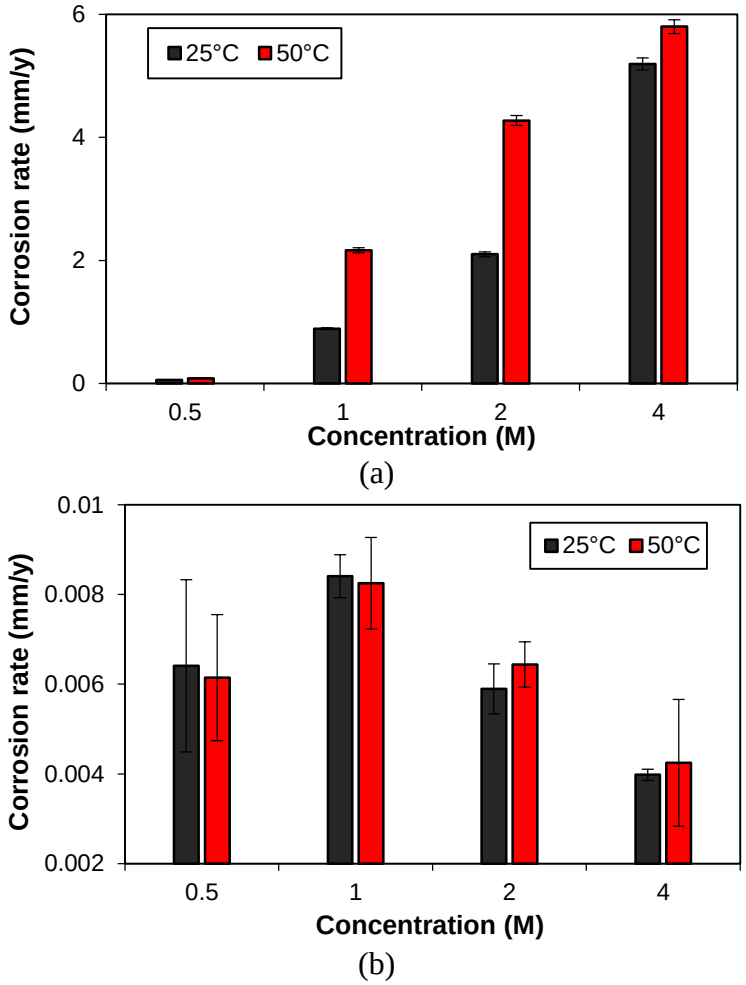

Figure 6- 13 *Effect of temperature on the corrosion rate of (a) unmodified, and (b) ruthenium implanted 304L stainless steel exposed to sulphuric acid.*

Despite the trend observed in Figure 6-12(b), changing temperature did not significantly affect corrosion rate of ruthenium implanted 304L stainless steel. This is shown in Figure 6-13(b). The trend observed at 50°C was similar to that observed at 25°C: corrosion rates initially increased when concentration was increased from 0.5 to 1 M, and eventually decreased at higher concentrations.

Consistent with the findings in Figure 6-13(b), post corrosion examination did not reveal obvious signs of corrosion damage. In fact, the surfaces presented in Figure 6-14 were indistinguishable from those presented in Figure 6-9.

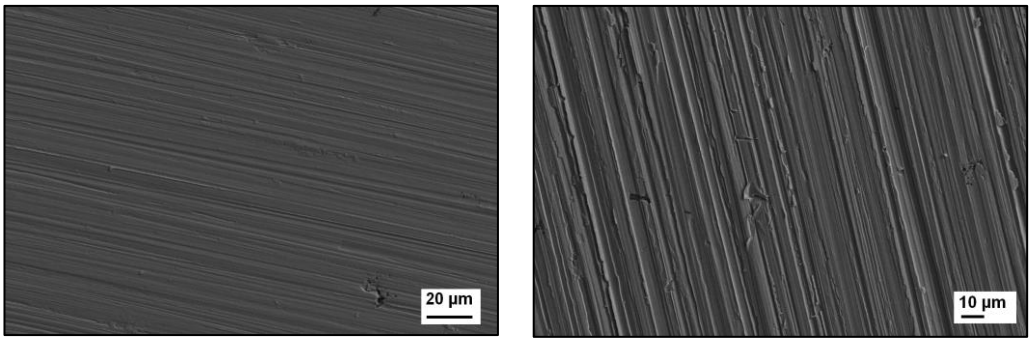

(a) (b)

Figure 6- 14 *Typical FESEM-SE images of ruthenium implanted after exposure to sulphuric acid at 50°C. Acid concentration was (a) 1 M, and (b) 4 M.*

Effect of agitation

Unmodified and ruthenium implanted 304L stainless steel samples were exposed to 1 M sulphuric acid, which was agitated at 900 rpm. The samples were tested under potentiodynamic and potentiostatic conditions at 25°C, and the results obtained are presented in Figures 6-15 to 6-17.

Figure 6-15 shows that for unmodified 304L stainless steel, agitating the corrosion medium resulted in three E_{corr} values at -310, -172, and 178 mV. This suggests that the cathodic curve intersected the anodic curve at three different potentials, and is consistent with increased corrosion rates (Perry et al. 1999). The shape of the potentiodynamic polarisation curve corresponding to ruthenium implanted 304L stainless steel was not significantly affected by agitation: the curve still exhibited evidence of spontaneous passivation, with a single corrosion potential. However, when this curve was compared to that recorded under static conditions (Figure 6-2 & 6-5), it was noted that agitation increased i_{corr} from ≈ 0.77 to 5.54 μA/cm^2, indicative of increased corrosion rates with agitation.

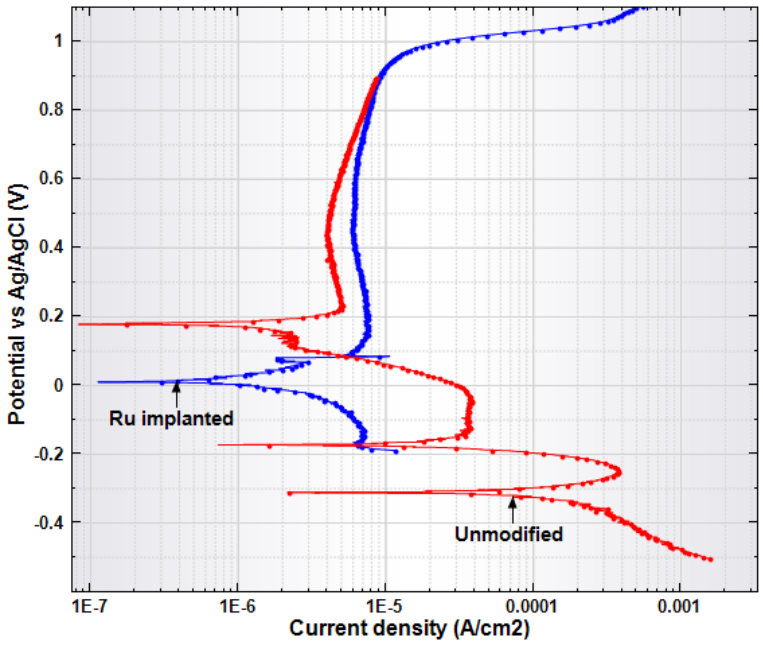

Figure 6- 15 *Effect of agitation on the potentiodynamic polarisation curves for unmodified and ruthenium implanted 304L stainless steel in 1 M sulphuric acid.*

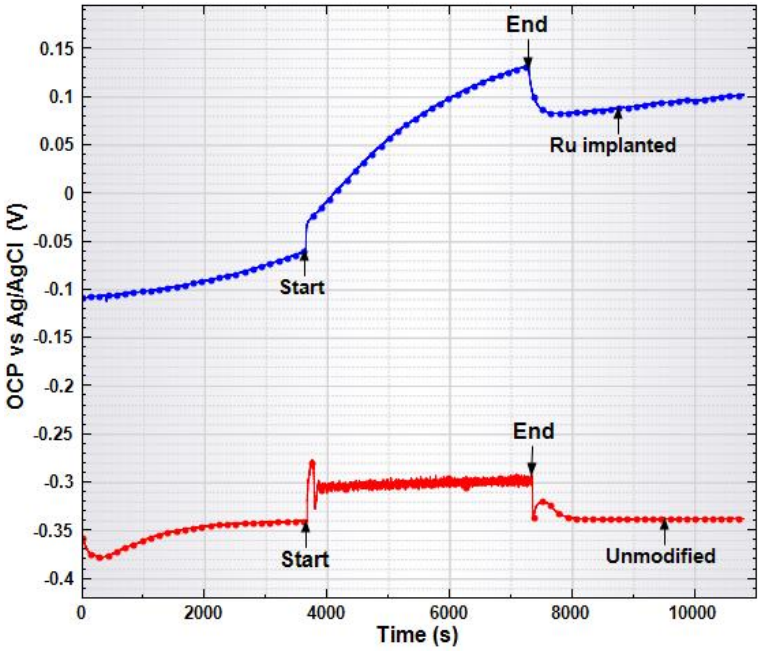

Figure 6- 16 *Influence of agitation on OCP-time curves for unmodified and ruthenium implanted 304L stainless steel in 1 M sulphuric acid over 3 hours.*

The response of OCP to agitation is shown in Figure 6-16. For both samples, agitation caused an increase in OCP towards nobler potentials. In the case of

unmodified 304L stainless steel, agitation increased OCP values to about -300 mV (≈ 100 mV vs SHE). Comparing with Figure 2-3, this corresponds to potentials where non-protective chromium (II) species are thermodynamically stable. The OCP values recorded on the unalloyed stainless steel fluctuated throughout the period of agitation, consistent with competitive film formation and film dissolution processes.

Agitation served to increase the rate of OCP increase for the ruthenium implanted 304L stainless steel in 1 M sulphuric acid. Rate of increase prior to agitation was ≈ 0.014 mV/s, and increased to 0.044 mV/s during agitation. All the while, OCP values remained in the potential range where chromium (III) are thermodynamically stable, and spontaneous passivation possible.

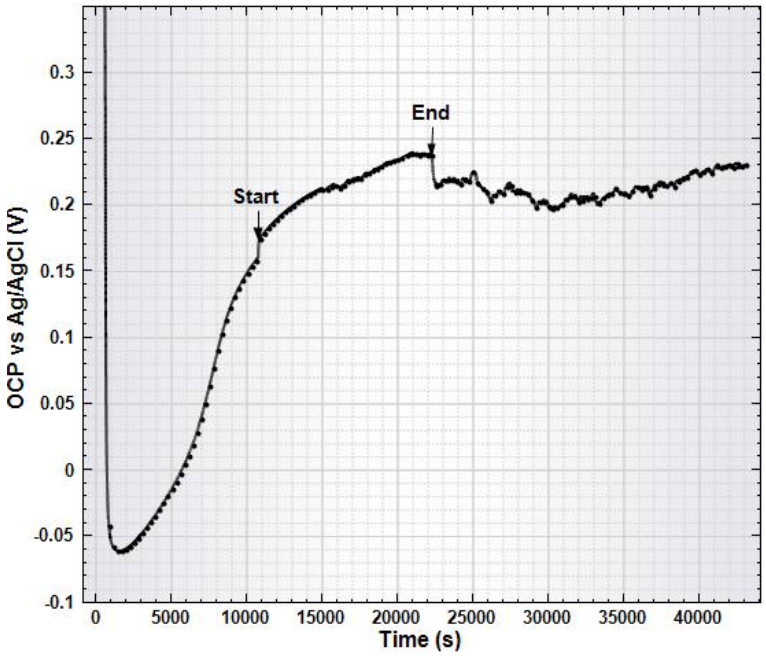

Figure 6- 17 *Effect of agitation on OCP-time curve for ruthenium implanted 304L stainless steel in 1 M sulphuric acid over 12 hours.*

In Figure 6-16, the OCP recorded on the ruthenium implanted 304L stainless steel decreased upon termination of agitation, and seemed to increase thereafter. It was therefore important to understand the effect of agitation long term. Figure 6-17 shows results obtained over a period of 12 hour. Before agitation was initiated, the OCP-time curve was smooth, pointing to steady film growth. After agitation was

stopped, variation of OCP suggests film dissolution and repair processes. This implies that the long term stability of the films grown on the ruthenium implanted stainless steel could be compromised by stirring.

Effect of salt contamination

About 2750 ppm sodium chloride were added to 1 M sulphuric acid, and the corrosion behaviour of ruthenium implanted 304L stainless steel in the solution studied by potentiodynamic polarisation. The results obtained are presented in Figure 6-18 and Table 6-2.

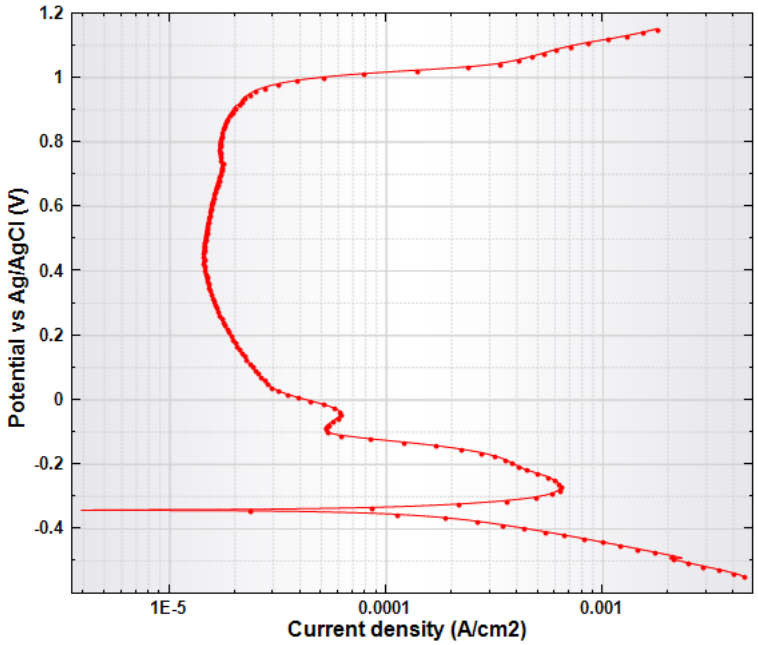

Figure 6- 18 *Potentiodynamic polarisation curve of ruthenium implanted 304L stainless steel exposed to 1 M sulphuric acid with ≈ 2750 ppm sodium chloride*

Comparing the curves corresponding to ruthenium implanted 304L stainless steel in Figure 6-2 and 6-18 shows that the presence of the salt contaminant lowered E_{corr} values to negative potentials, and shifted i_{corr} to higher values. In fact, E_{corr} values in the contaminated solution were anchored in the region where non-productive chromium (II) species are thermodynamically stable, and active corrosion likely. Corrosion current densities in all cases studied were > 100 $\mu A/cm^2$, consistent with high corrosion rates as shown in Table 6-2. In addition,

the presence of sodium chloride reintroduced the anodic peak, typical of active-passive behaviour. The i_{crit} was ≈ 628 μA/cm^2, several magnitudes greater than that reported on unmodified 304L in 1 M sulphuric acid (Figure 6-2).

Table 6- 2 *Electrochemical parameters obtained from potentiodynamic polarisation of ruthenium implanted 304L stainless steel in different solutions.*

Solution	OCP (mV)	E_{corr} (mV)	i_{crit} (μA/cm^2)	R_p (Ω.cm^2)	Corrosion rate (mm/y)
1 M H_2SO_4	119	115	-	41 848	0.008
1 M H_2SO_4 + 2750 ppm NaCl	-347	-332	628	137	2.449

6.2.2 Hydrochloric acid

Potentiodynamic polarisation curves obtained on unmodified and ruthenium implanted 304L stainless steel in 1 M hydrochloric acid are presented in Figure 6-19.

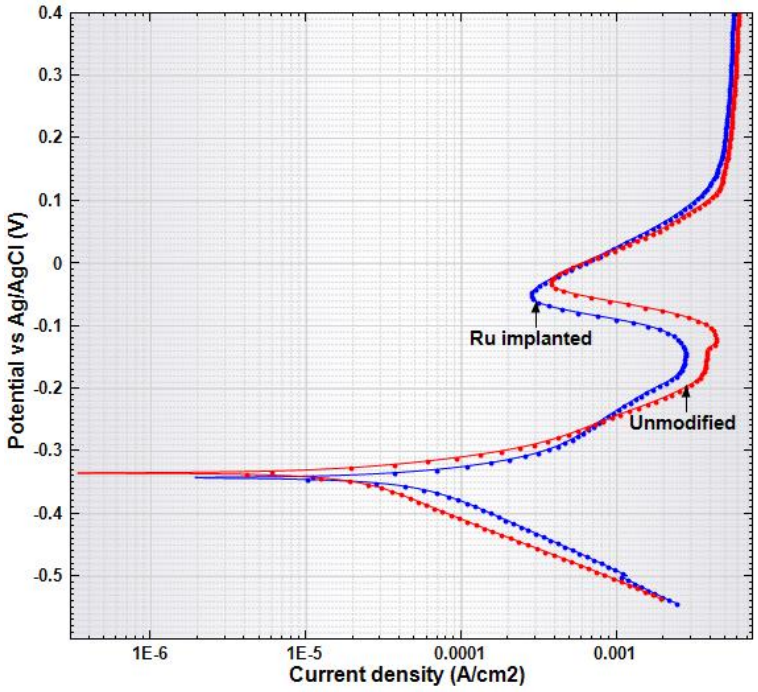

Figure 6- 19 *Potentiodynamic polarisation curves of unmodified and ruthenium implanted 304L stainless steel in 1 M hydrochloric acid at ≈ 25°C.*

As can be seen in Figure 6-19, the shapes of the curves were very similar. In both cases, the polarisation curves were characterised by a broad anodic peak at current densities > 1000 μA/cm^2. A decrease in current density was observed between -100 and 0 mV, followed by a rapid increase. The decrease in current density could have been associated with a weakly protective surface film. At higher potentials, pseudo passivity was observed, suggesting the growth of relatively protective surface film at potentials > 100 mV.

Introducing ruthenium shifted the i_{corr} to higher values, consistent with increase in corrosion rates of the surface alloyed stainless steel. The results observed here are however contrary to those noted by Sherif et al. (2009a), who showed that addition of at least 0.14% ruthenium improved corrosion resistance in hydrochloric acid solutions.

Effect of concentration

Unmodified and ruthenium implanted 304L stainless steel samples were exposed to hydrochloric acid ranging from 0.5 to 2 M. The results obtained are presented in Figures 6-20 to 6-23. All tests were done at ≈ 25°C.

OCP-time curves in Figure 6-20 show that in all cases, potentials increased to more negative values upon immersion. This was probably due to the dissolution of the native chromium oxide films that formed on the stainless steel in air (Sherif et al. 2009b). Increasing immersion time shifted the potentials to more positive values, but these remained below -300 mV where non-protective chromium (II) specie are thermodynamically stable. It is unlikely therefore that the increase in potential was due to the formation of chromium (III) or iron (II) species (Figure 2-3).

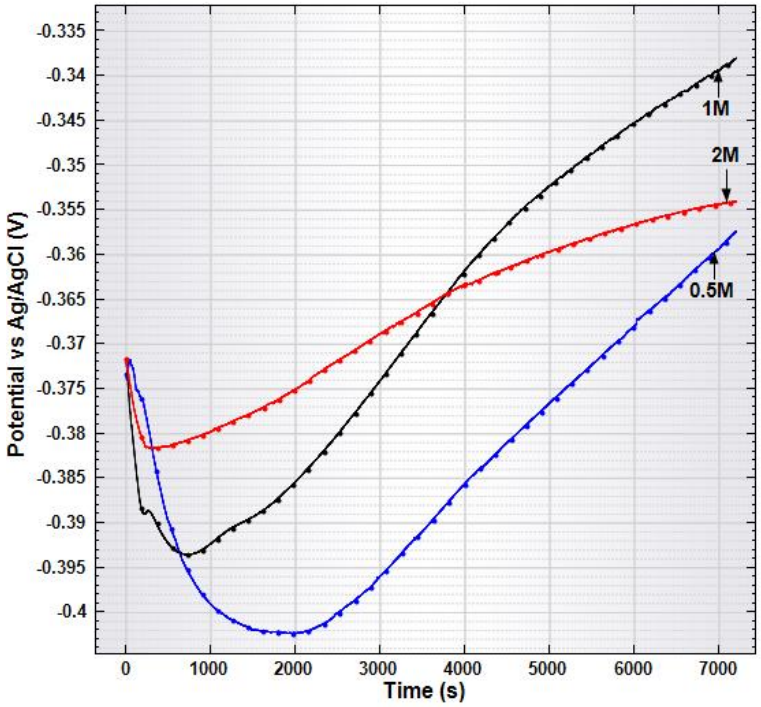

(a)

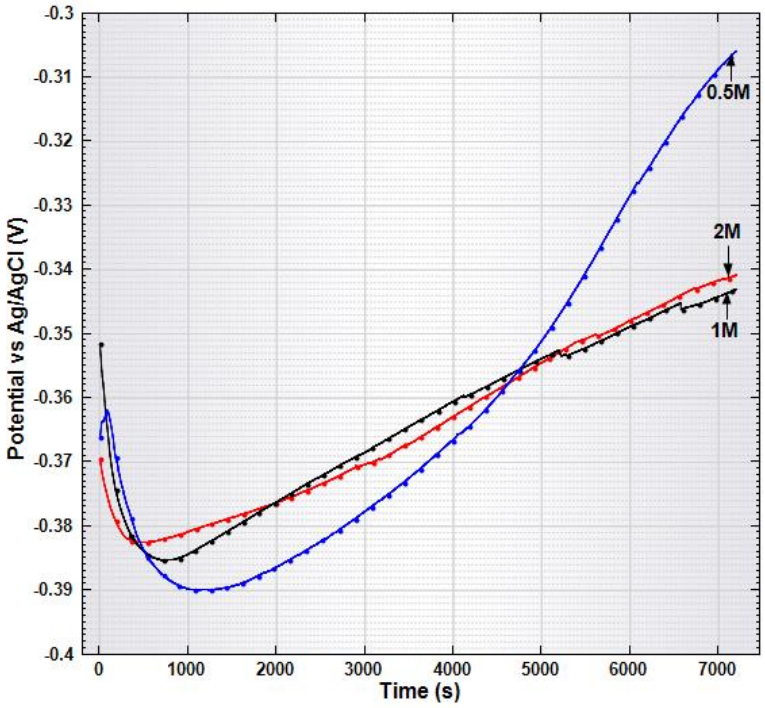

(b)

Figure 6- 20 *OCP-time curves for (a) unmodified, and (b) ruthenium implanted 304L stainless steel in hydrochloric acid of different concentrations at 25°C.*

In Figure 6-20(a), it can be seen that the time taken for the potential to increase to more positive values varied with hydrochloric acid concentration. In fact, it

decreased in the order 0.5 M > 1 M > 2 M. In 0.5 M hydrochloric acid, it took just over 30 minutes, while in 2 M it took less than 500s. Since this dip in OCP is associated with the dissolution of air formed chromium oxide, these observations suggest that the oxide film dissolved much more rapidly in 2 M than in lower acid concentrations. Hence, corrosion rates of unmodified 304L stainless steel would be expected to be faster in 2 M than in 0.5 M hydrochloric acid.

Introducing ruthenium did not alter the trend observed in Figure 6-20(a): time taken for the potential to turn decreased in the order 0.5 M > 1 M > 2 M. However, the time taken to dissolve the native chromium oxide in 0.5 M decreased by almost 50% as illustrated in Figure 6-20(b). This suggests that adding ruthenium by ion implantation increased the propensity of the native oxide layer to dissolve in hydrochloric acid.

Notably, the rate of potential increase was higher on ruthenium implanted than on pristine 304L stainless steel. The potential in all concentrations after 2 hours of immersion was > -345 mV on the ruthenium implanted samples, and > -360 mV on the unmodified stainless steel after the same period of immersion. Figure 6-19 demonstrated that neither unmodified nor ruthenium implanted 304L stainless steel samples passivated in hydrochloric acid. Hence the rapid increase in potential could point to marked increase in the thermodynamic tendency to corrode.

Figure 6-21 compares the polarisation curves obtained when pristine and ruthenium alloyed 304L stainless steels were exposed to hydrochloric acid solutions of different concentrations. It is immediately clear from this figure that the general shapes of the curves were not altered by the presence of ruthenium. In both cases (Figures 6-21(a) & (b)), the anodic curves in 0.5 M and 1 M hydrochloric were characterised by an anodic peak and a passive region. The passive region was narrowed with increase in concentration, and in 0.5 M hydrochloric acid it widened with the addition of ruthenium.

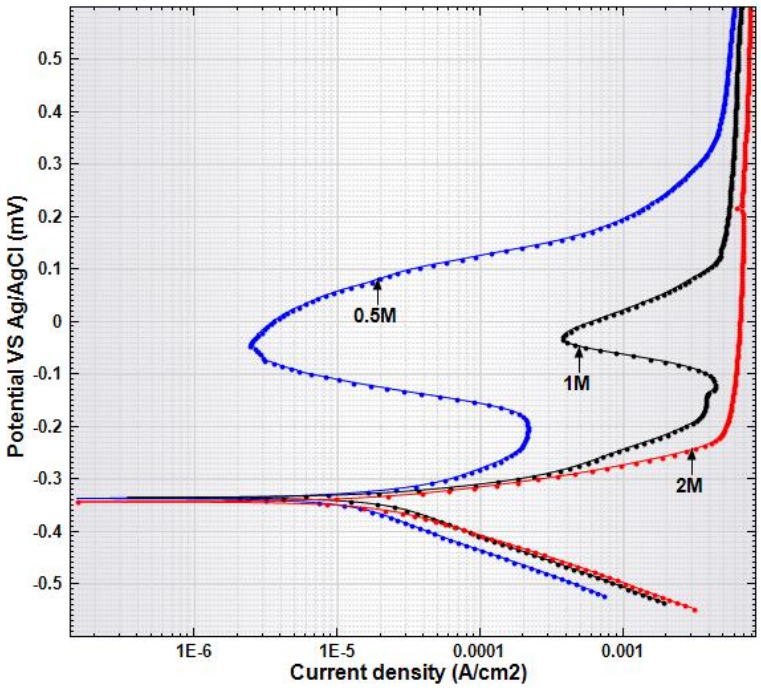

(a)

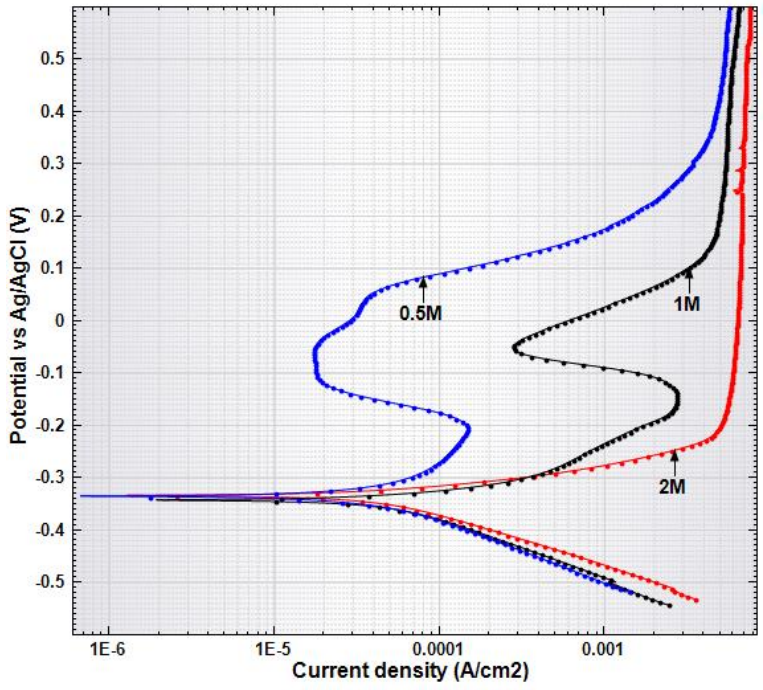

(b)

Figure 6- 21 *Effects of hydrochloric acid concentration on the potentiodynamic polarisation curves obtained on (a) unmodified and (b) ruthenium implanted 304L stainless steel after 2 hours of exposure.*

One of the indicators of successful cathodic modification of stainless steel is an increase in E_{corr} towards nobler potentials. Close examination of Figure 6-21

revealed that introducing ruthenium did not significantly increase E_{corr}. E_{corr} measured on pristine 304L stainless steel was between -335 and -358 mV, and increased marginally to between -325 and -341 mV when ruthenium was added via ion implantation. This suggests that cathodic modification by ruthenium was not successful in hydrochloric acid, which is contrary to reports by previous authors on duplex and superferritic stainless steel in hydrochloric acid (Olubambi et al. 2009; Sherif et al. 2009a). There was no clear relationship between E_{corr} and hydrochloric acid as can be seen in Figure 6-22(a).

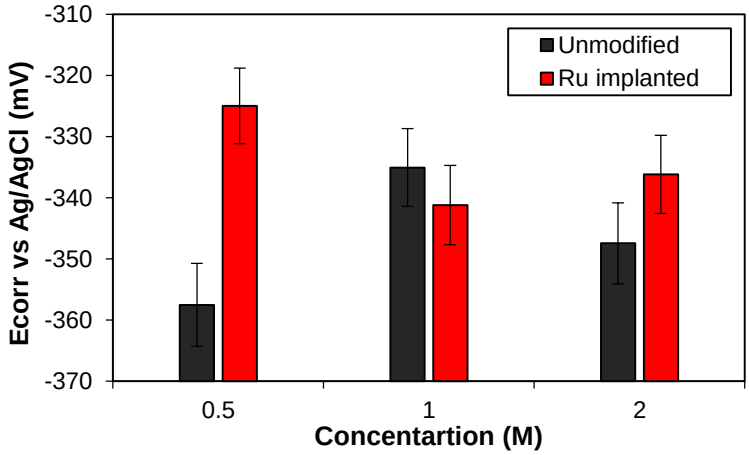

(a)

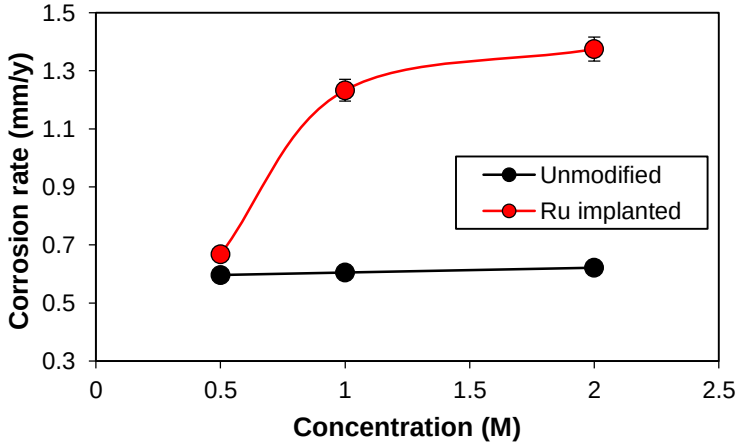

(b)

Figure 6- 22 *Influence of concentration on (a) E_{corr}, and (b) corrosion rates of unmodified and ruthenium implanted 304L stainless steel exposed to hydrochloric acid.*

Comparing Figures 6-21(a) and (b), it can be seen that introducing ruthenium shifted the polarisation curves to high current densities. For instance, i_{corr} for

unalloyed and ruthenium alloyed 304L stainless steel in 2 M was ≈ 57 and 126 $\mu A/cm^2$ respectively. This shift is synonymous with an increase in corrosion rate with addition of ruthenium as shown in Figure 6-22(b). In Figure 6-22(b), it was noted that change in acid concentration did not significantly alter corrosion rates of pristine stainless steel: average corrosion rates in 0.5 M was ≈ 0.60 mm/y and increased to just 0.62 mm/y in 2 M hydrochloric acid. In contrast, ruthenium implantation seemed more detrimental in hydrochloric acid solutions of higher concentrations. Corrosion rates in these media increased by a factor > 2.

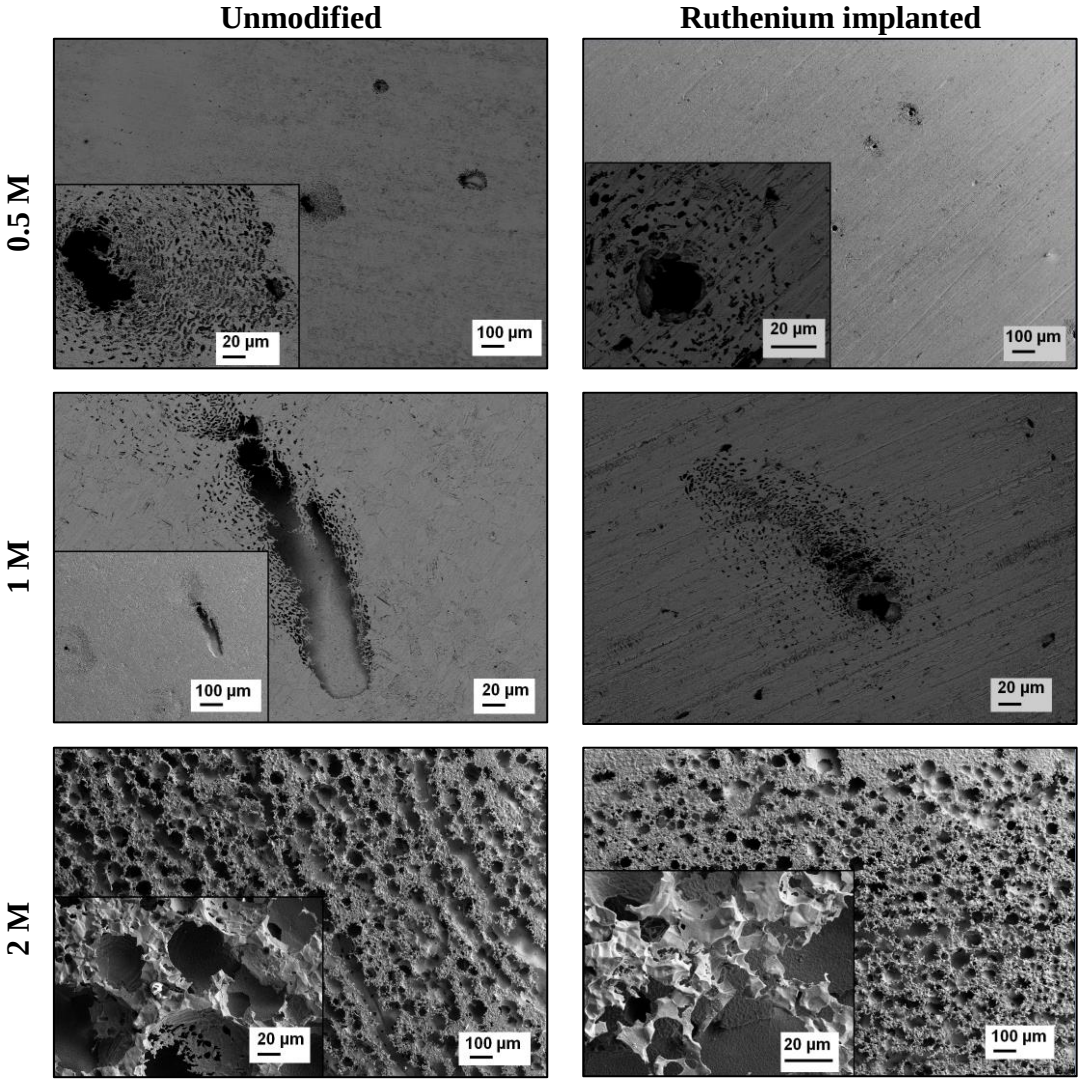

Figure 6- 23 *FESEM images of unmodified and ruthenium implanted 304L stainless steel after 2 hours exposure in hydrochloric acid.*

Images of the corroded surfaces obtained via FESEM are presented in Figure 6-23. The surface morphologies of unalloyed and alloyed 304L stainless steel were similar in each of the test solutions, and exhibited extensive damage with increase in concentration. In 0.5 M hydrochloric acid, the samples were characterised by round pits with lacy coverings, consistent with pits that grew under the surface (Ernst et al. 1997). The pits became more circular, and the lacy covering coarser for ruthenium implanted 304L stainless steel.

In 1 M hydrochloric acid, the pits became elongated. Most of the pits grown on pristine 304L stainless steel were shallow and uncovered, while most of those on ruthenium implanted stainless steel were covered. Corrosion in 2 M hydrochloric acid resulted in severely perforated surfaces with a sponge-like appearance. Dissolution of both pristine and ruthenium implanted 304L stainless steel left a 'skeleton' of the subsurface layers. EDS analysis of the 'skeleton' revealed that it was indistinguishable from the base metal. Hence, it was not clear why this metal structure remained undissolved.

Effects of temperature

Additional tests were carried out at 50°C with the objective of studying the effect of temperature on the corrosion of the ruthenium implanted 304L stainless steel in hydrochloric acid. The results obtained are given in Figure 6-24 to 6-26.

The polarisation curves in Figure 6-24 show that increasing temperature did not markedly influence E_{corr}, but shifted i_{corr} towards higher values. This is consistent with an increase in corrosion rates with increase in exposure temperature. The anodic peak in 1 M hydrochloric acid (Figure 6-24(a)) widened at 50°C, while the passive region narrowed.

Increasing temperature to 50°C increased the corrosion rates of both unmodified and ruthenium implanted 304L stainless steel as shown in Figure 6-25. Corrosion rates reported on pristine 304L stainless steel in 2 M hydrochloric acid at 50°C were as high as 3 mm/y, and increased to about 4.3 mm/y after ruthenium implantation.

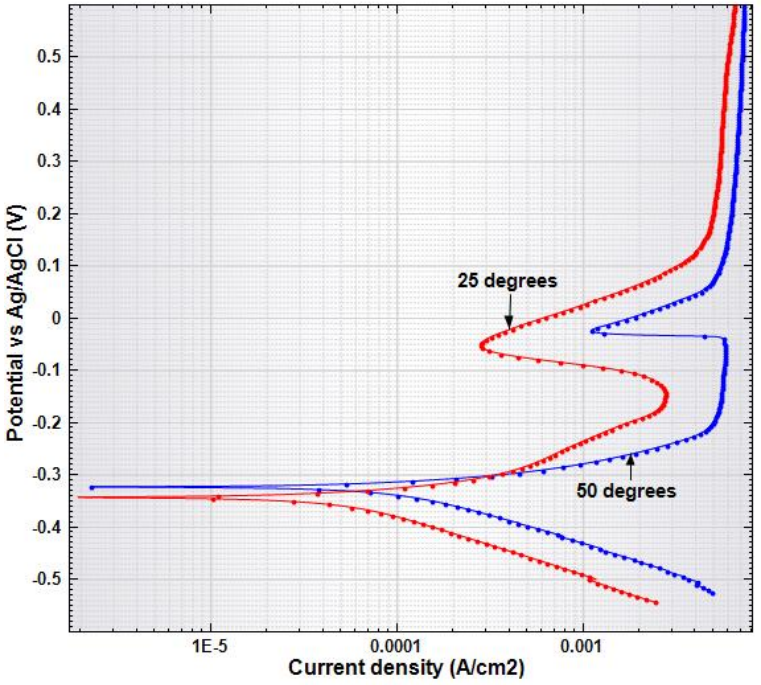

(a)

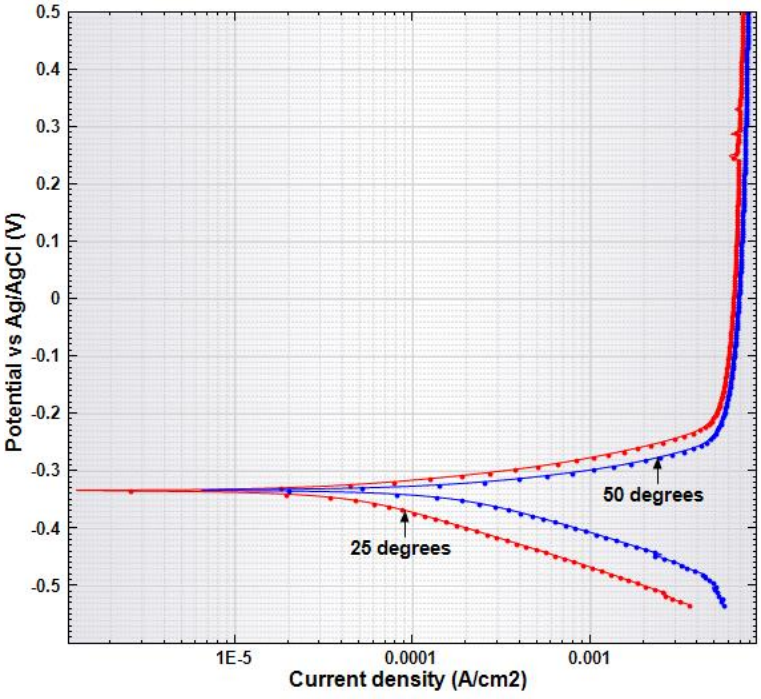

(b)

Figure 6- 24 *Effect of temperature on the potentiodynamic polarisation curves for ruthenium implanted 304L stainless steel after 2 hours of exposure in (a) 1 M, and (b) 2 M hydrochloric acid.*

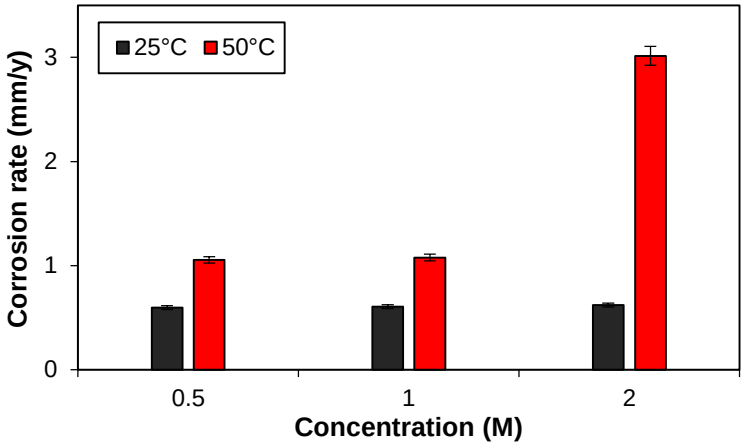

(a)

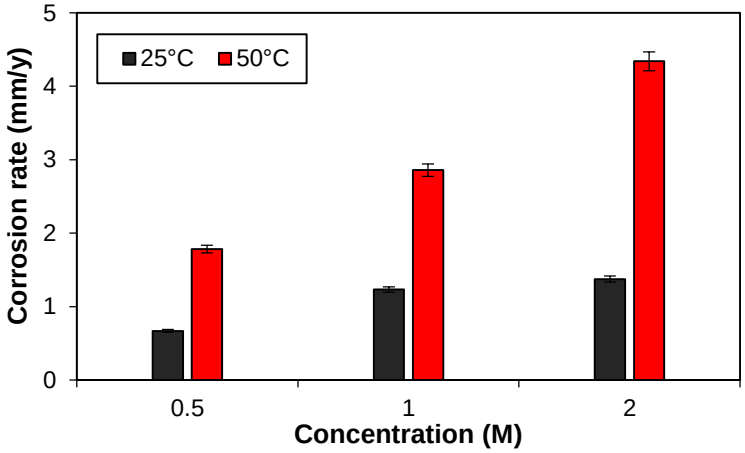

(b)

Figure 6- 25 *Influence of temperature and concentration on the corrosion rates of (a) unmodified, and (b) ruthenium implanted 304L stainless steel.*

Images obtained post corrosion are presented in Figure 6-26. Comparing Figure 6-23 and 6-26, it is immediately clear that increasing temperature increased the severity of corrosion damage. In 0.5 M for instance, external pit size increased by as much as 180% on pristine 304L stainless steel, and by up to 610% on introducing ruthenium. Although pit density in this solution seemed to decrease with increase in temperature, the pit sizes under the surface appeared much larger as indicated by the ellipse in Figure 6-26.

As at 25°C, increasing hydrochloric acid concentration played an influential role on the surface morphology of the corroded samples. In 1 M hydrochloric acid, corrosion of pristine 304L stainless steel was quite insidious, progressing mostly under the surface. Adding ruthenium resulted in a peculiar pit growth mechanism,

with a pit morphology characterised by a layered dissolution of the metal. Corrosion in 2 M hydrochloric acid was less localised, with complete removal of the surface layers.

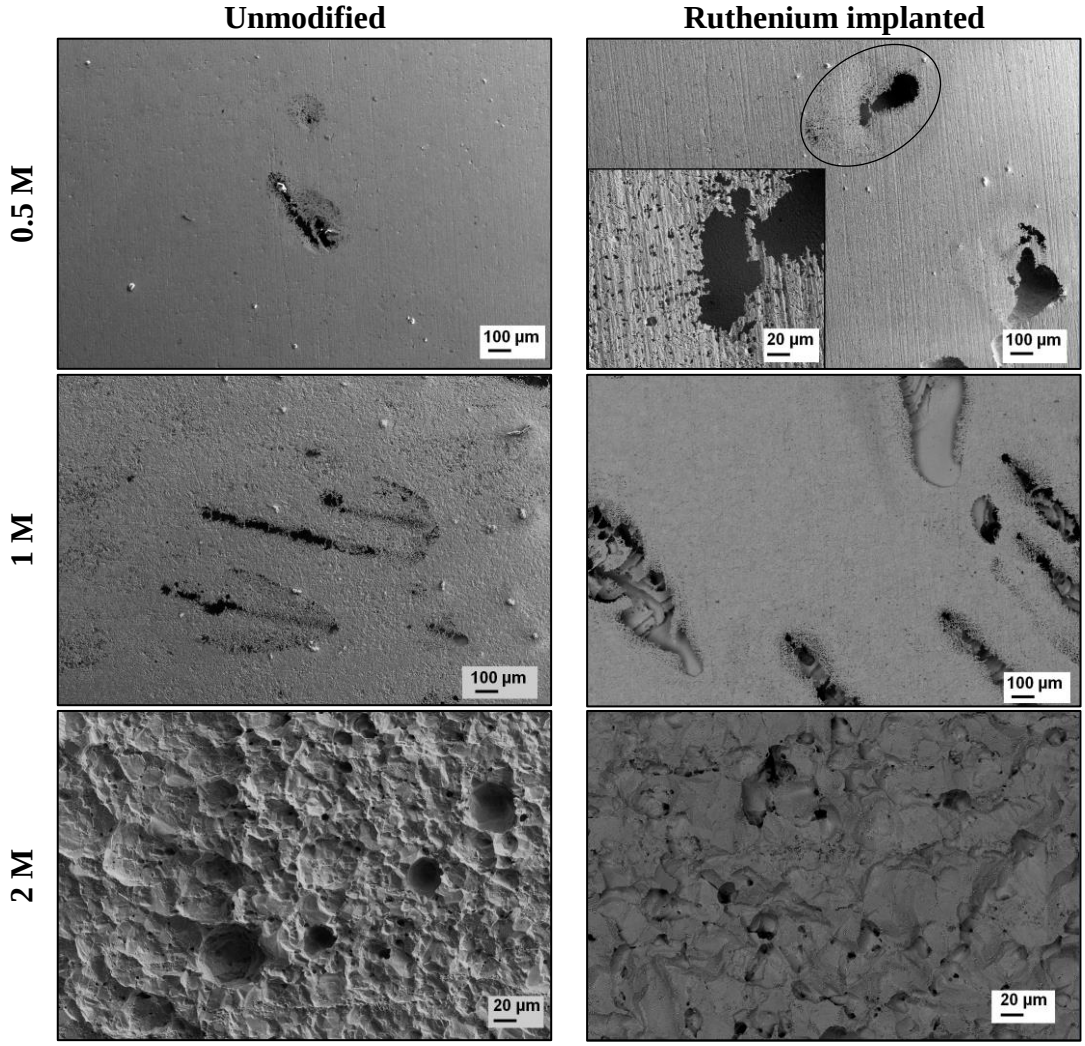

Figure 6- 26 *FESEM images of unmodified and ruthenium implanted after 2 hours exposure at OCP in hydrochloric acid of different concentrations at 50°C.*

6.3 Results: Corrosion in chloride solutions

This section of the chapter presents and describes the results obtained when alloyed and unalloyed 304L stainless steels were exposed to chloride solutions.

6.3.1 Sodium chloride

Figure 6-27 compares the typical potentiodynamic polarisation curves obtained on unmodified 304L stainless steel to that recorded on the ruthenium implanted stainless steel.

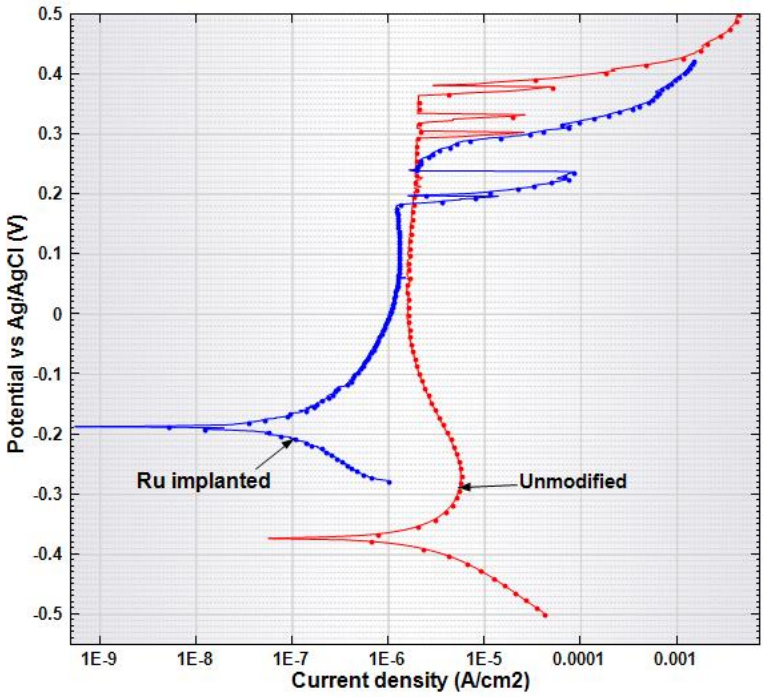

Figure 6- 27 *Potentiodynamic polarisation curves of unmodified and ruthenium implanted 304L stainless steel in 3.5 wt% sodium chloride at ≈ 25°C.*

On both stainless steel samples, the onset of transpassive corrosion was way below the oxygen reduction potentials, typical of pitting corrosion. Pitting potential (E_{pit}) was ≈ 380 mV on pristine 304L stainless steel, but decreased to almost 330 mV with addition of ruthenium via ion implantation. This is consistent with an increased tendency to pitting corrosion. Introducing ruthenium notably shifted i_{corr} to lower values.

Effect of concentration

Both unalloyed and ruthenium implanted 304L stainless steels were exposed to sodium chloride solutions with concentrations ranging from 1 to 5 wt%. All tests were carried out at 25°C, and the results are given in Figures 6-28 to 6-30.

The effect of sodium chloride concentration on the corrosion performance of ruthenium implanted 304L stainless steel is presented in Figure 6-28. It is immediately clear that increasing the concentration of sodium chloride reduced the E_{pit} of the ruthenium implanted stainless steel samples. This indicates that increasing concentration of sodium chloride increased the susceptibility of the stainless steel to pitting, and was consistent with observations by other researchers (Chaofang et al. 2011).

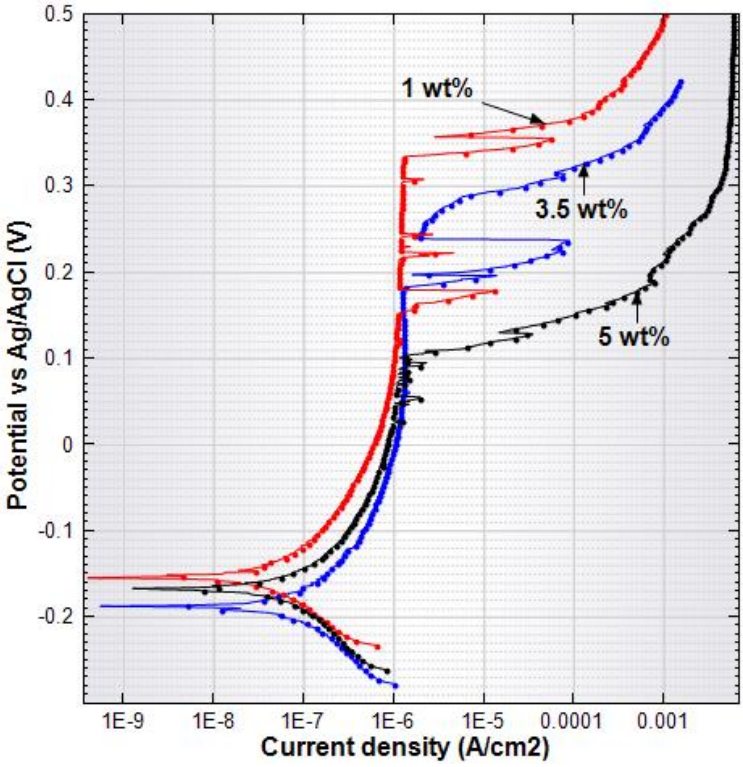

Figure 6- 28 *Influence of sodium chloride concentration on polarisation curves of ruthenium implanted 304L stainless steel. Temperature ≈ 25°C.*

Figure 6-29 compares the E_{corr} and E_{pit} of unmodified and ruthenium implanted 304L stainless steel in different sodium chloride solutions. Increasing sodium chloride concentration had a much more significant effect on unalloyed 304L stainless steel. E_{corr} values increased negatively from ≈ -15 mV to about -288 mV with increasing concentration from 1 to 3.5 wt% as can be seen in Figure 6-29(a). For the ruthenium implanted stainless steel, E_{corr} values remained nearly constant over the studied concentration at around -169 mV.

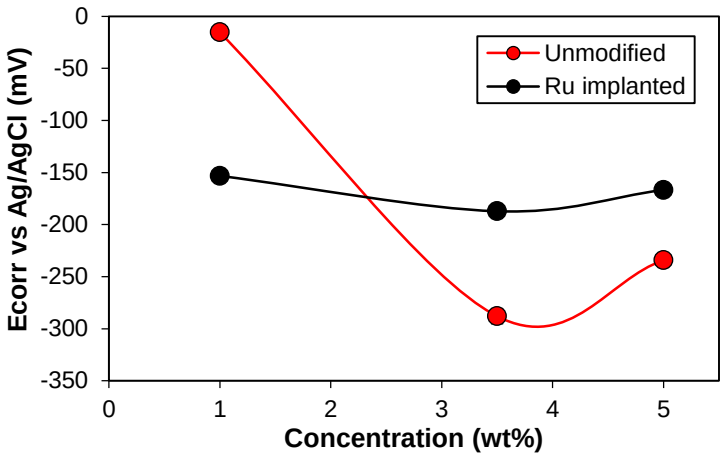

(a)

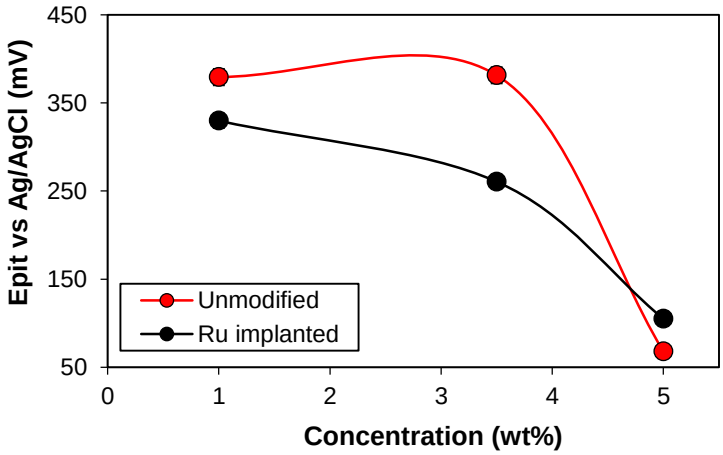

(b)

Figure 6- 29 *Effect of sodium chloride concentration and exposure temperature on (a) E_{corr}, and (b) E_{pit} of unmodified and ruthenium implanted 304L stainless steel.*

Introducing ruthenium decreased E_{pit} as illustrated in Figure 6-29(b). The results presented in this figure are contrary to observations by Sherif et al. (2009), who demonstrated that the presence of ruthenium shifted both E_{pit} and E_{corr} to more positive values.

FESEM examination of the ruthenium implanted 304L stainless steel after exposure at 200 mV vs OCP gave the images presented in Figure 6-30. Introducing ruthenium significantly changed pit morphology. Pits grown on the unmodified were elongated and irregular (Figure 4-18), but became round and much smaller with the addition of ruthenium. In addition, pit morphology in

Figure 6-30 did not seem dependent of the manganese stringers unlike for unmodified 304L stainless steel (Figure 4-18).

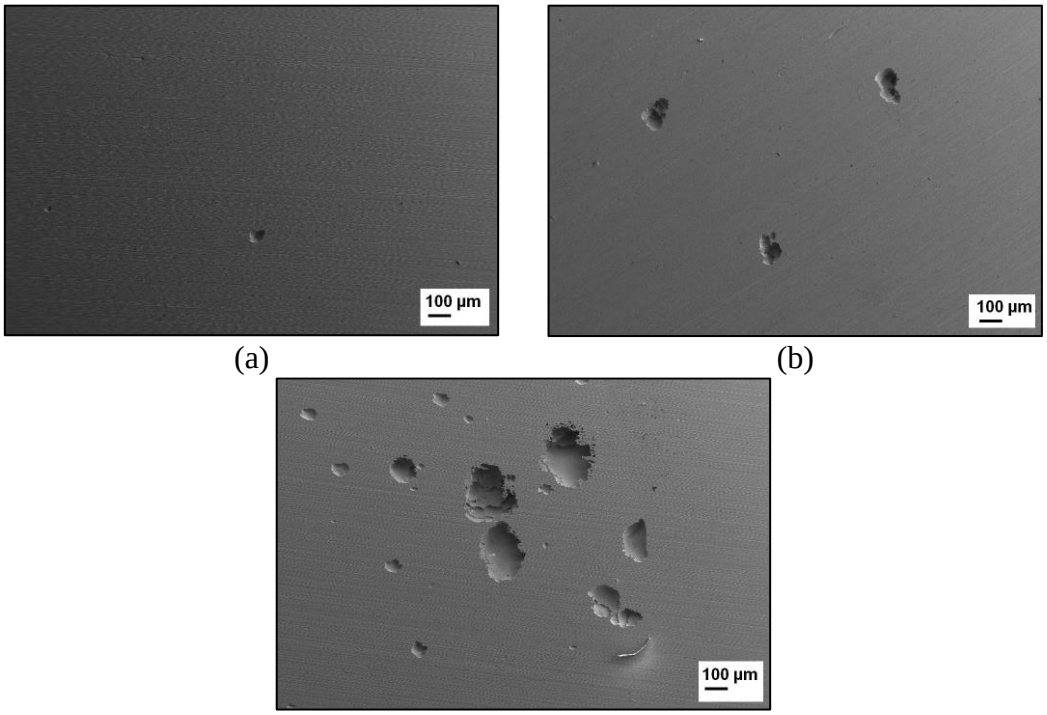

(a) (b)

(c)

Figure 6- 30 *FESEM images of ruthenium implanted 304L stainless steel after exposure at 200 mV vs OCP (a) 1 wt%, (b) 3.5 wt%, and (c) 5 wt% sodium chloride at 25°C.*

Consistent with expectation, pit density, pit size and pit depth on ruthenium implanted increased with increase in sodium chloride. In 1 wt%, the pits were typically 54 µm, but increased to as much as 303 µm in 5 wt% sodium chloride. Measurements were done on the longest diameter of the pits.

Effect of temperature

Further testing in sodium chloride was done at 50°C. The results obtained are presented in Figures 6-31 to 6-34.

Polarisation curves in Figure 6-31 show that increasing sodium chloride concentration reduced E_{pit}. This trend is consistent with that observed at 25°C in Figures 6-28 and 6-29(b). Two things are clear from comparing Figure 6-31 with

Figure 6-28. Firstly, increasing temperature did not markedly change the E_{corr} values of the ruthenium implanted stainless steel; E_{corr} values remained between -150 and -190 mV. Secondly, E_{pit} decreased with increase in exposure temperature. This is better illustrated in Figure 6-32. The decrease in E_{pit} suggests that adding ruthenium increased propensity to pitting. Results presented in Figures 6-33 and 6-34 confirm this.

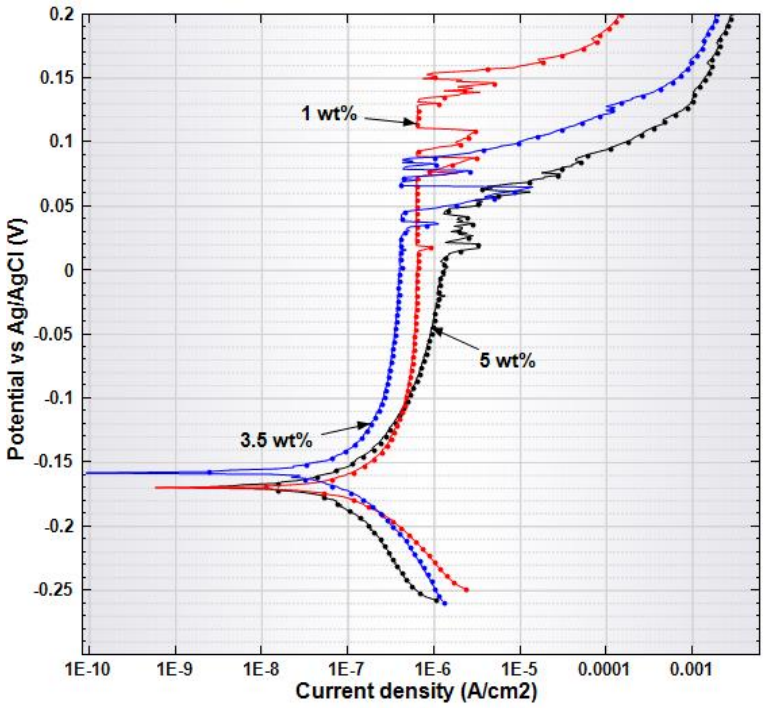

Figure 6- 31 *Potentiodynamic polarisation curves of ruthenium implanted 304L stainless steel in different concentrations of sodium chloride at 50°C.*

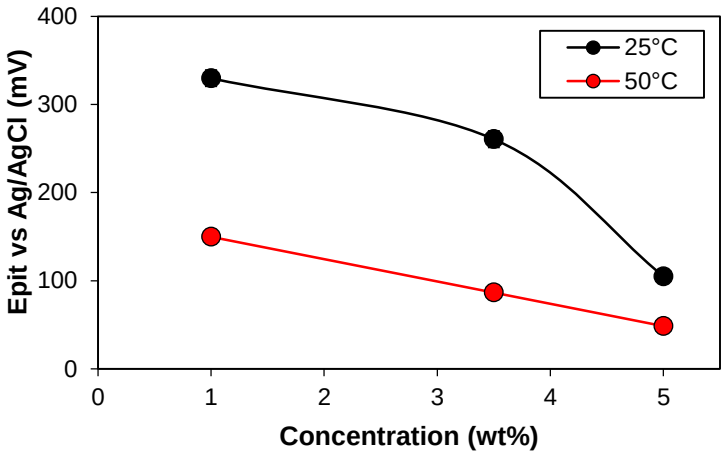

Figure 6- 32 *Effect of temperature on E_{pit} of ruthenium implanted 304L stainless steel in different concentrations of sodium chloride.*

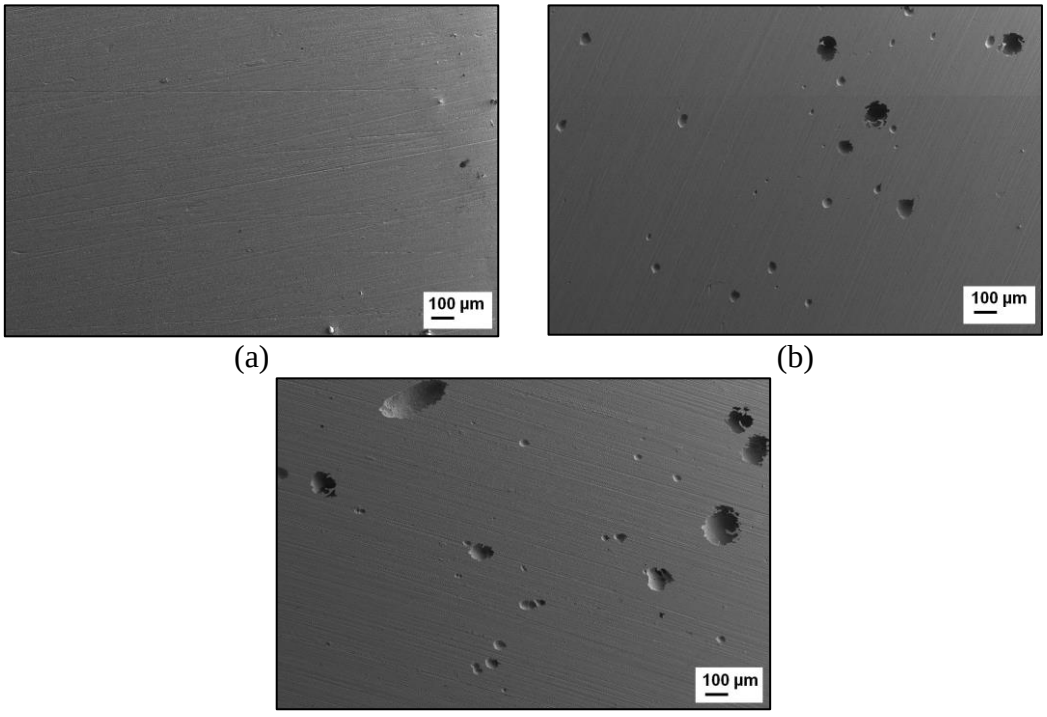

(a) (b)

(c)

Figure 6- 33 *FESEEM images of ruthenium implanted 304L stainless after exposure in (a) 1 wt%, (b) 3.5 wt%, and (c) 5 wt% sodium chloride at 50°C.*

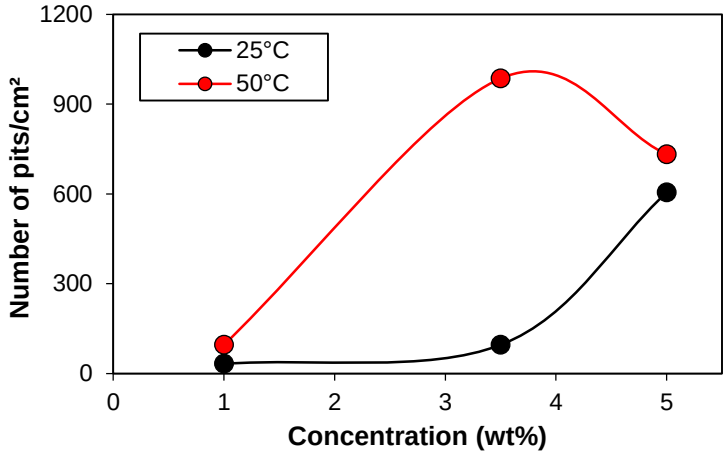

Figure 6- 34 *Effect of temperature and sodium chloride concentration on pit density on ruthenium implanted 304L stainless steel.*

In Figure 6-33, pit density increased with increase in sodium chloride; maximum density was recorded on the sample exposed to 3.5 wt%. Pits grown in this solution were numerous, but most were smaller than those grown in 5 wt% sodium chloride. It is likely that the smaller pits coalesced to give larger anf fewer pits in the 5 wt% solution.

Effect of pH

The effect of pH on the pitting behaviour of ruthenium implanted 304L stainless steel was studied in 3.5 wt% sodium chloride. pH adjustments were achieved by adding either sulphuric acid or sodium hydroxide. The results obtained are presented in Figures 6-35 and 6-36.

Potentiodynamic polarisation curves given in Figure 6-35 show that adjusting solution pH influenced both E_{pit} and E_{corr} of the ruthenium implanted 304L stainless steel. Reducing pH to 1 increased E_{pit} from about 261 to ≈ 350 mV, and E_{corr} to values greater than zero. The increase in E_{pit} suggests a reduced tendency for the alloy to pit in acidic sodium chloride. Current transients typical of metastable pitting (Figure 2-3(b)) were minimal in this solution, confirming the reduced tendency of the ruthenium implanted stainless steel to pit. However, decreasing pH to 1 increased i_{corr} by more than 50%, synonymous with increased dissolution rates.

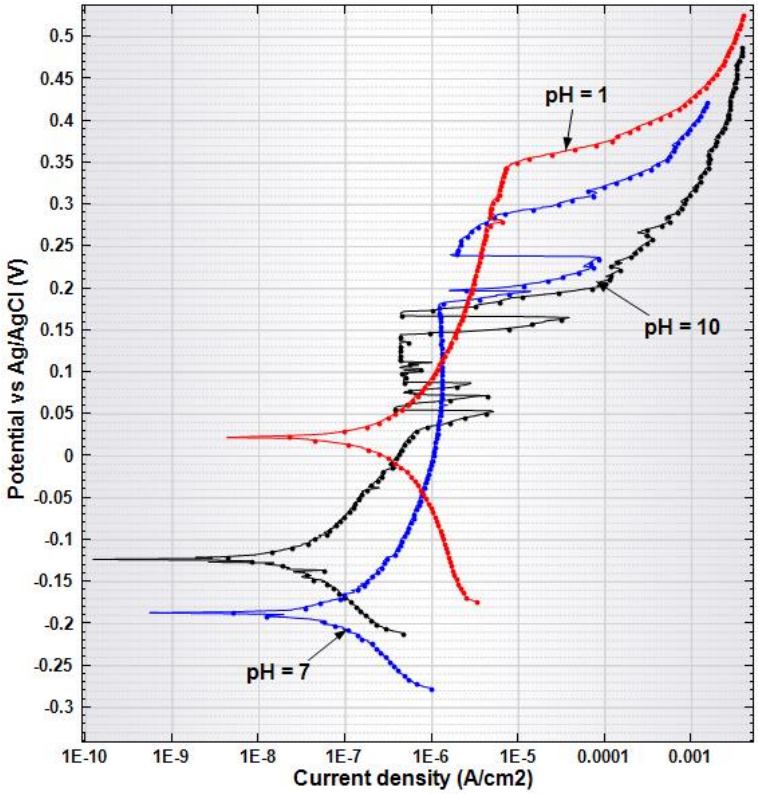

Figure 6- 35 *Effect of pH on the potentiodynamic polarisation curves for ruthenium implanted 304L stainless steel exposed to 3.5 wt% sodium chloride at ≈ 25°C.*

Increasing pH to 10 reduced E_{pit} by almost 35%, but increased E_{corr} towards nobler potentials. i_{corr} values were lower at pH 10; 0.07 μA/cm^2 compared to 0.2 μA/cm^2 at pH 7, indicating lower dissolution rates. The lower E_{pit} values suggest that pitting resistance at high pH was reduced, and is consistent with the high current fluctuations recorded in the solution. As can be seen in Figure 6-36(a), no E_{pit} was recorded in solutions of pH = 13. This indicates that ruthenium implanted 304L stainless steel was not susceptible to pitting in alkaline salt solutions.

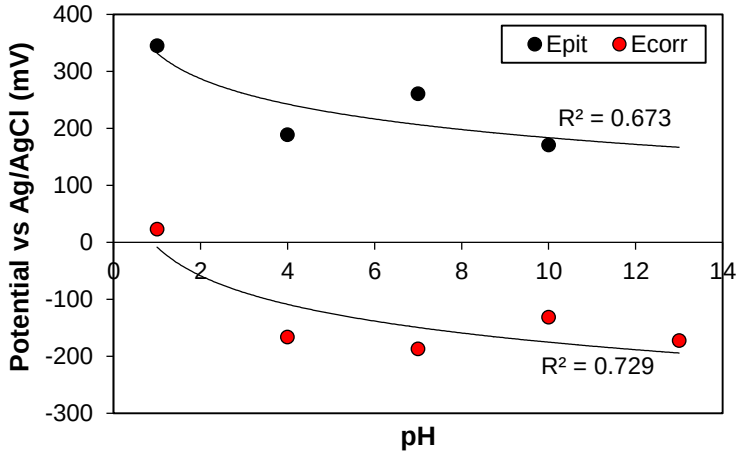

(a)

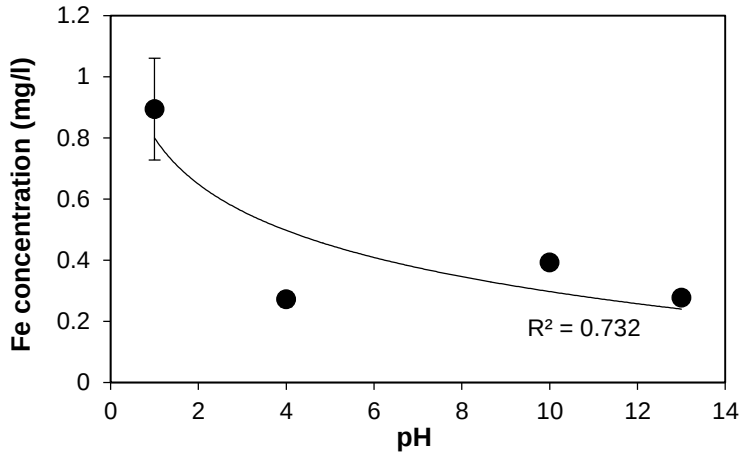

(b)

Figure 6- 36 *Variation of (a) E_{corr} and E_{pit}, and (b) dissolved iron with pH of 3.5 wt% sodium chloride.*

Figure 6-36(b) shows that the amount of iron dissolved from the ruthenium implanted 304L stainless steel decreased with increase in pH, consistent with a decrease in dissolution rates.

6.3.2 Magnesium chloride

The unalloyed and ruthenium implanted 304L stainless steel was exposed to 3.5 wt% magnesium chloride, and the results obtained are presented in Figure 6-37 and 6-39.

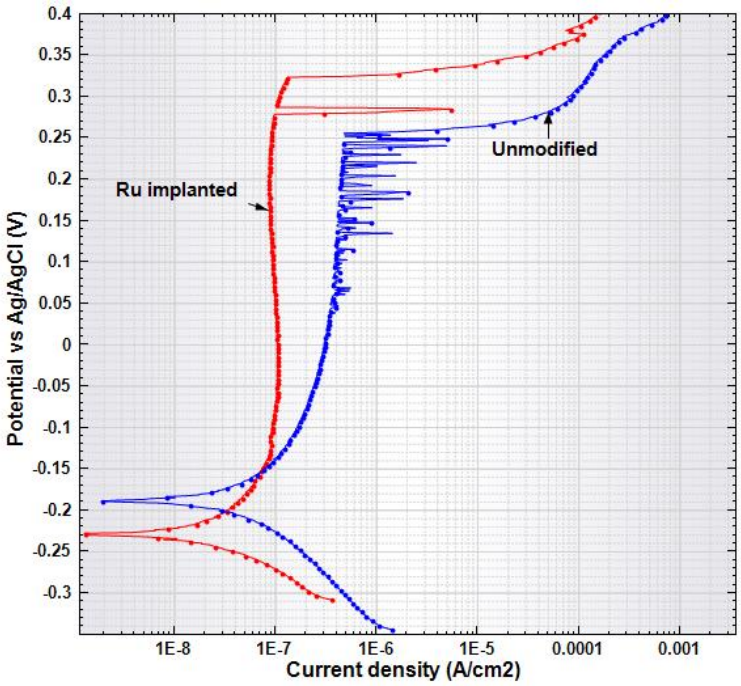

Figure 6- 37 *Potentiodynamic polarisation curves for unmodified and ruthenium implanted 304L stainless steel in 3.5 wt% magnesium chloride.*

In Figure 6-37, the curve corresponding to unmodified 304L stainless steel was characterised by intense current fluctuations at high potentials. This is consistent with high incidents of metastable pitting. Introducing ruthenium reduced the frequency of these fluctuations, and raised E_{pit} from about 251 to 320 mV. These two observations imply that introducing ruthenium improved pitting resistance of 304L stainless steel in 3.5 wt% magnesium chloride. Although alloying with ruthenium shifted E_{corr} values towards negative potentials, it also sifted i_{corr} to lower values, consistent with reduced dissolution rates.

Increasing exposure temperature to 50°C shifted E_{corr} to nobler potentials, increased i_{corr} and significantly lowered E_{pit} as can be seen in Figure 6-38. These are indications that high temperatures increased the tendency for ruthenium implanted 304L stainless steel to pit, and corrode faster in 3.5 wt% magnesium chloride. The images in Figure 6-39 corroborate this, and show that increasing temperature increased pit density on the alloyed stainless steel.

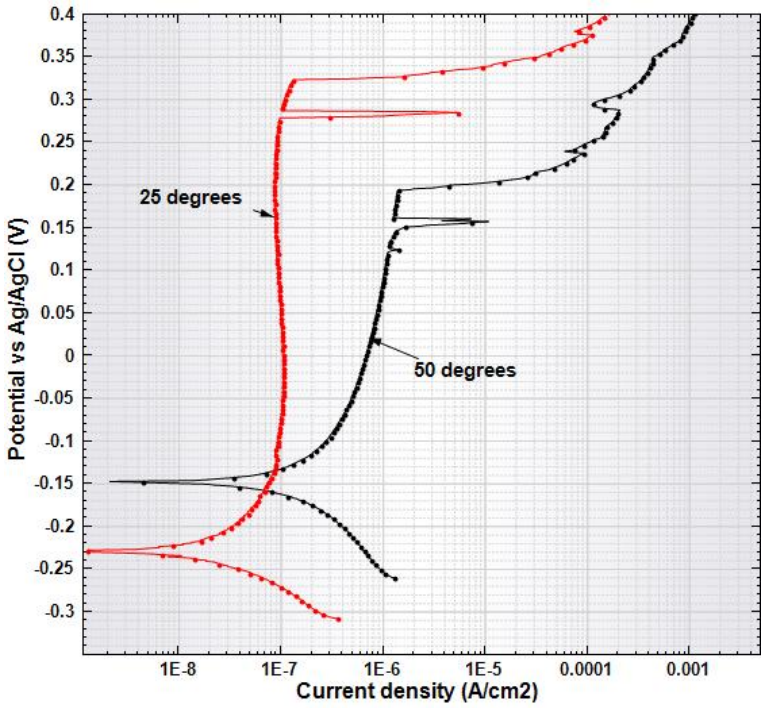

Figure 6- 38 *Effect of temperature on the polarisation of ruthenium implanted 304L stainless steel in 3.5 wt% magnesium chloride.*

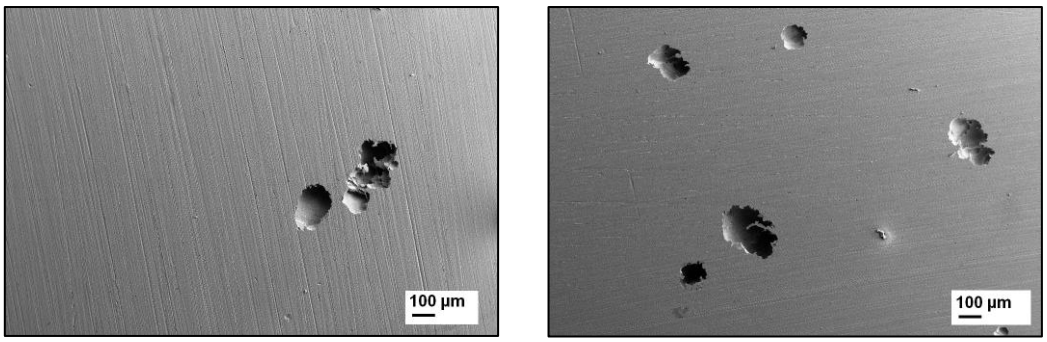

(a) (b)

Figure 6- 39 *FESEM image of ruthenium implanted 304L stainless steel after 2 hours exposure in 3.5 wt% magnesium chloride at (a) 25, and (b) 50°C.*

6.4 Results: Corrosion in simulated fuel cell solution

Two solutions were used to simulate the environment in polymer electrode membrane fuel cells (PEMFCs). Electrolyte 1 consisted of 10^{-4} M sulphuric acid and 0.5 M sodium sulphate at pH 4.8 (Kim et al. 2002), and Electrolyte 2 was made of 0.01 M hydrochloric acid and 0.01 M sodium sulphate (Li et al. 2004).

All tests were carried out at 60°C. The results obtained are given in Figures 6-40 to 6-44.

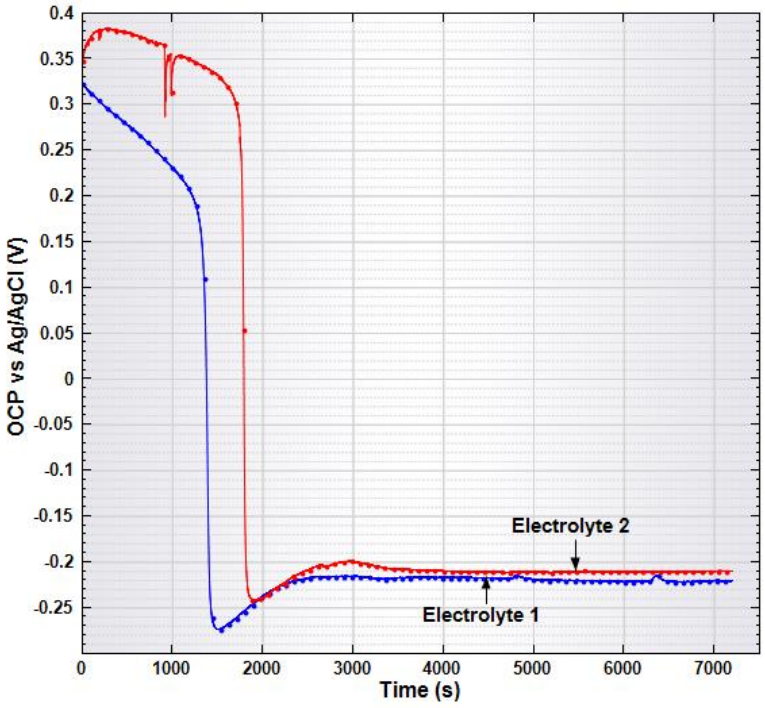

(a)

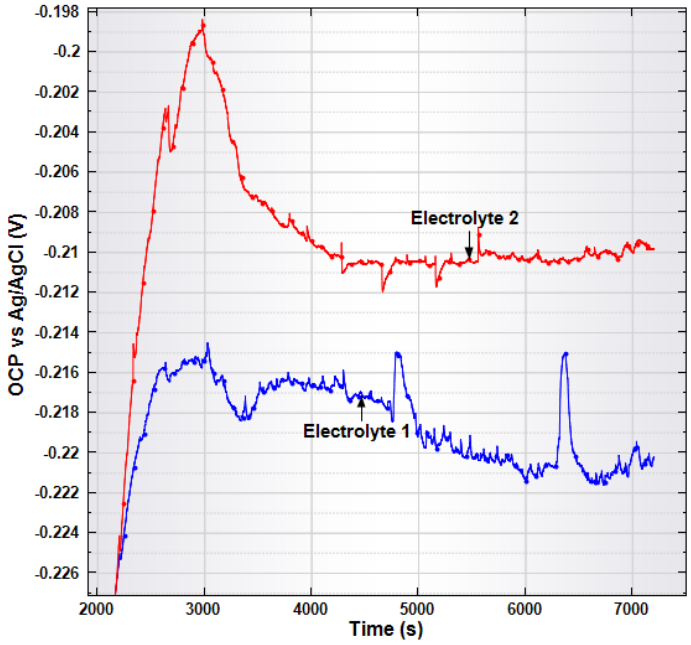

(b)

Figure 6- 40 *OCP-time curves for ruthenium implanted 304L stainless steel in simulated fuel cell solutions. (b) amplifies exposure period between 2000 and 7200s in (a).*

In both test solutions, the OCP of the implanted stainless steel decreased rapidly in the first 2000s from ≈ 350 mV to just below -200 mV (Figure 6-40). This OCP drop could have been due to the dissolution of the air-formed passive oxide on the ruthenium implanted stainless steel. The OCP values eventually stabilised between -209 and -222 mV. Figure 6-40(b) shows the section of the curve in Figure 6-40(a) between 2000 and 7200s. It is clear from this figure that OCP values were not consistent, but fluctuated over the period of exposure. This points to competing passivation and film dissolution processes, and is consistent with the expectation that passive films are not rigid structures, but evolve with time (Schumki 2002).

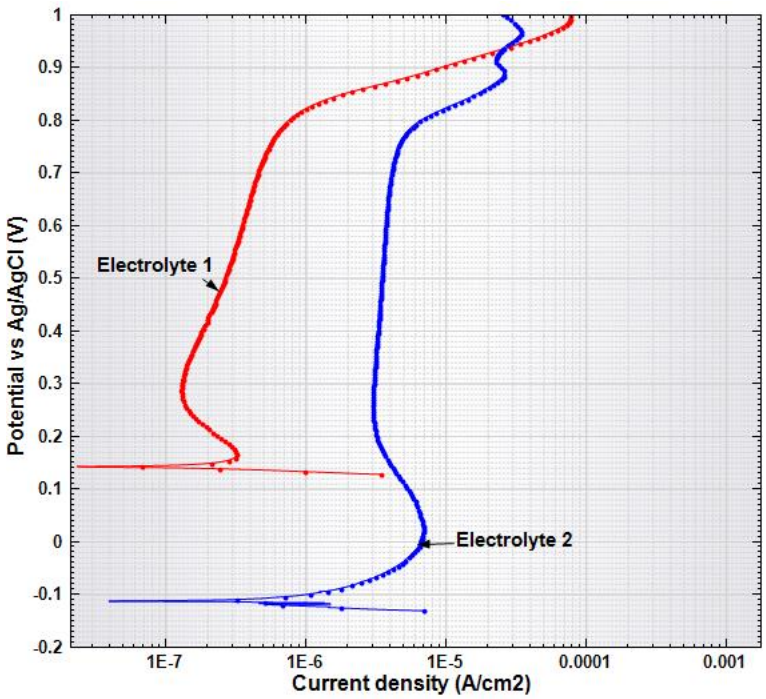

Figure 6- 41 *Potentiodynamic polarisation curves for ruthenium implanted 304L stainless steel in simulated fuel cell solutions after 2 hours exposure.*

Potentiodynamic polarisation curves in Figure 6-41 suggest that the ruthenium implanted 304L stainless steel performed better in Electrolyte 1 than in Electrolyte 2. Ruthenium implanted 304L stainless steel exhibited typical active-passive behaviour in both solutions. The anodic nose was wider in Electrolyte 2, with i_{crit} close to 7 μA/cm^2, suggesting increased difficulty to passivate in this solution than in Electrolyte 2. In both cases though, i_{corr} was typically less than 16

μA/cm^2, which is the target corrosion rate for PEMFCs (Brett & Brandon 2007) as shown in Figure 6-42. In addition, E_{corr} of ruthenium implanted 304L stainless steel was greater than -195 mV (≈ 240 mV vs SCE) the operation potential of the anode environment of PEMFCs (Li et al. 2004). This means that the ruthenium surface alloy would be corrosion resistant in the anodic environment of the fuel cell.

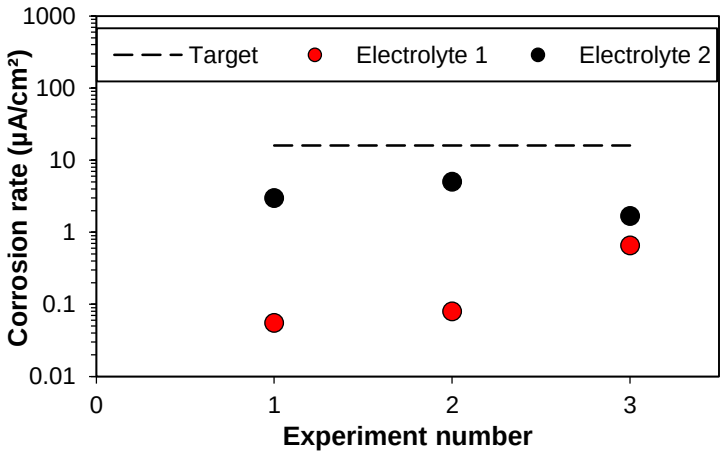

Figure 6- 42 *Comparison of corrosion rates for ruthenium implanted 304L stainless steel in simulated fuel cell solutions. Target corrosion rate is 16 μA/cm^2.*

Figure 6-43 show chronoamperometric curves for the ruthenium implanted 304L stainless steel at 645 mV (≈ 600 mV vs SCE), the operation potential of the cathodic environment of the PEMFC (Li et al. 2004). The current density in Electrolyte 1 (Figure 6-43(a)) was mostly below 1 μA/cm^2, and was about 0.08 μA/cm^2 at the end of the test period. Figure 6-43(b) shows that current densities for the ruthenium alloyed stainless steel at 645 mV were quite high; at the end of the 24 hours current densities were almost 1200 μA/cm^2. Comparing these results with the curve corresponding to exposure in Electrolyte 2 in Figure 6-41, where current density at 645 mV was ≈ 3.8 μA/cm^2, it may be concluded that the corrosion performance of the alloy in the electrolyte deteriorated with increase in exposure time.

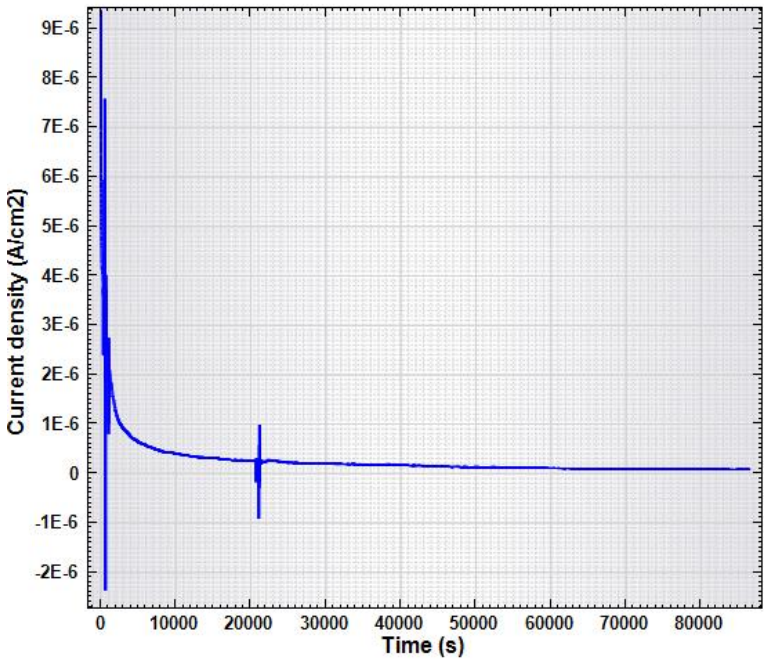

(a)

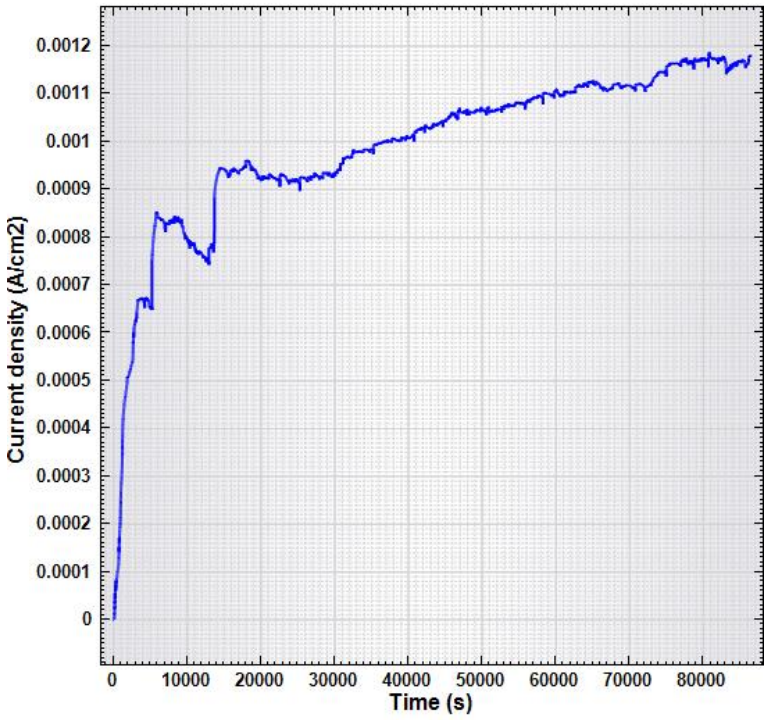

(b)

Figure 6- 43 *Time variation of current density at 645 mV for ruthenium implanted 304L stainless steel exposed for 24 hours in (a) Electrolyte 1, and (b) Electrolyte 2.*

The stability of the film formed in Electrolyte 1 was studied by agitating the solution, and the results obtained are presented in Figure 6-44. Agitation was

initiated after about 1 hour of exposure, and stopped after an additional hour. From Figure 6-44 it can be seen that initiating agitation increased current density, suggesting an increase in corrosion rate. However, the increase was slight: current densities never exceeded 0.3 μA/cm^2, and tended to decrease during agitation.

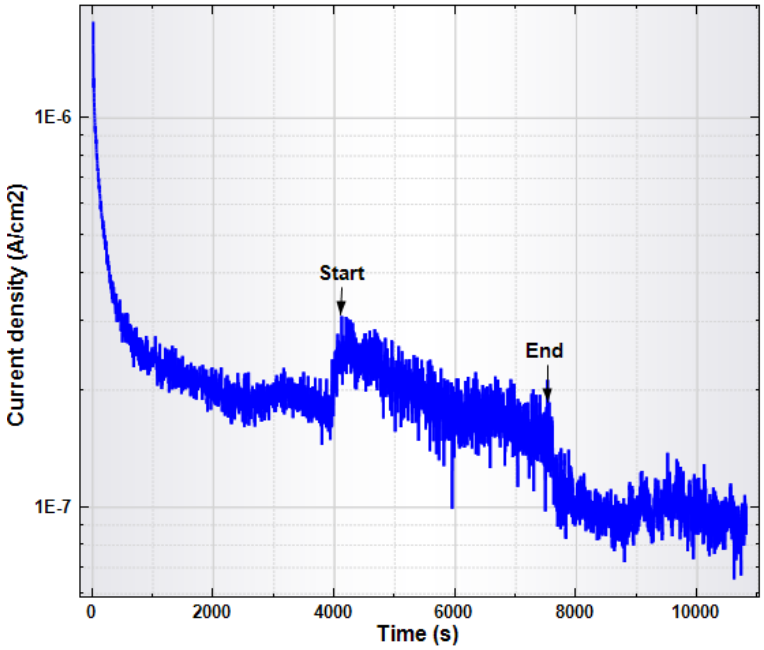

Figure 6- 44 *Effect of stirring on current density of ruthenium implanted 304L stainless steel at 645 mV in Electrolyte 1.*

6.5 Discussion

Ruthenium implanted 304L stainless steel produced in Chapter 5 was exposed to different corrosive media and conditions. The aim was to understand the corrosion behaviour of these surface modified alloys. Corrosion behaviour was mostly characterised by potentiodynamic polarisation, and where possible, compared to that of unalloyed 304L stainless steel. Preceding sections presented and described the results obtained. The present section seeks to discuss, interpret and offer possible implications of these results.

6.5.1 Corrosion in sulphuric acid

The ruthenium implanted stainless steel samples were exposed to sulphuric acid solutions of concentrations ranging from 0.5 to 4 M at 25 and 50°C. Exposure was done under both stagnant and stirred conditions.

It was found that adding ruthenium significantly improved corrosion resistance of 304L stainless steel in all sulphuric acid concentrations studied. Corrosion improvement was attributed to cathodic modification by ruthenium as indicated by the increase in free corrosion potential (OCP) in Figure 6-4. The improvement was consistent with reports by previous researchers (Potgieter et al. 1992; Tjong & Chu 2007) who noted improved corrosion resistance of stainless steels with ruthenium surface alloys when exposed to sulphuric acid.

Increasing acid concentration had the general effect of increasing the corrosion resistance of ruthenium implanted stainless steel. This is atypical since increasing acid concentration should reduce corrosion resistance as observed on pristine 304L stainless steel in Figure 6-6(a), and as presented by other authors (Phelps & Vreeland 1957; Olubambi et al. 2009). Figures 6-3(b) and 6-4(b) demonstrated that increasing sulphuric acid concentration shifted OCP to more positive values, suggesting that the efficiency of cathodic modification by ruthenium increased with acid concentration.

Hydrogen evolution by Equation 2-2 is the primary cathodic reaction in sulphuric acid. According to the rate law, the higher the concentration of the acid, the faster the rate of hydrogen evolution. The rate or exchange current density (i_o) (Section 2.1.2) of this reaction plays a significant role in the corrosion rate of metals. Increasing i_o for the hydrogen reaction would cause an increase in i_{corr}, and hence corrosion rate as illustrated in Figure 2-2. This explains the typical effect of increasing acid concentration on corrosion resistance of metals. In the case of the ruthenium implanted stainless steel, increasing i_o by increasing acid concentration possibly shifted corrosion potentials to nobler values as shown in Figure 6-45, thus increasing corrosion resistance.

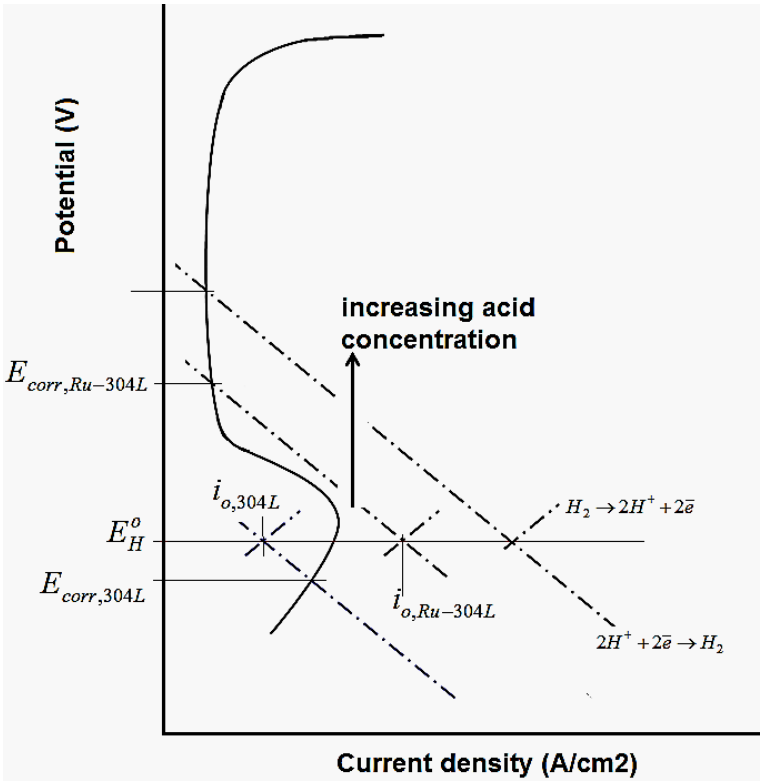

Figure 6- 45 *Schematic illustrating possible effect of sulphuric acid concentration on ruthenium implanted 304L stainless steel.*

Olubambi and co-workers (2009) studied the effect of sulphuric acid concentration on ruthenium alloyed superferritic stainless steel. They found that increasing concentration from 0.5 to 2 M shifted E_{corr} to more negative values and significantly increased corrosion rates. The difference in the response of ruthenium alloying could stem from the processes used to manufacture these alloys. In the present study, the ruthenium surface alloys were prepared via ion implantation, a process known to create amorphous surface layers (Tjong & Wong 1993; Rautray et al. 2011). In addition, ion implantation on the 304L stainless steel was done on roughened surfaces, which presents nearly amorphic surfaces. Grain boundaries are high energy regions that are prone to anodic dissolution, and corrosion initiation may be minimised by amorphisation. Comparing Figure 4-14 and 6-9 confirms the reduced tendency to undergo intergranular attack or selective leaching with introducing ruthenium via ion implantation.

Figure 6-46 shows schematically the effect of sulphuric acid concentration on the corrosion rate of 304L stainless steel. Corrosion rates initially increase, reach a

maximum, and then decrease. The increase is caused by large amounts of hydrogen ions as acid concentration is increased, while the decrease is due to the fact that at very high concentrations sulphuric acid is essentially free of water, and ionisation is reduced (Fontana 1986; Richardson 2010). The peak corrosion rate of 304 stainless steels typically occurs at ≈ 9-11 M (about 50-65%) sulphuric acid (Figure 2-6). Introducing ruthenium via ion implantation shifted this peak to 1 M acid. This remarkable shift expands the application spectrum for 304L stainless steel.

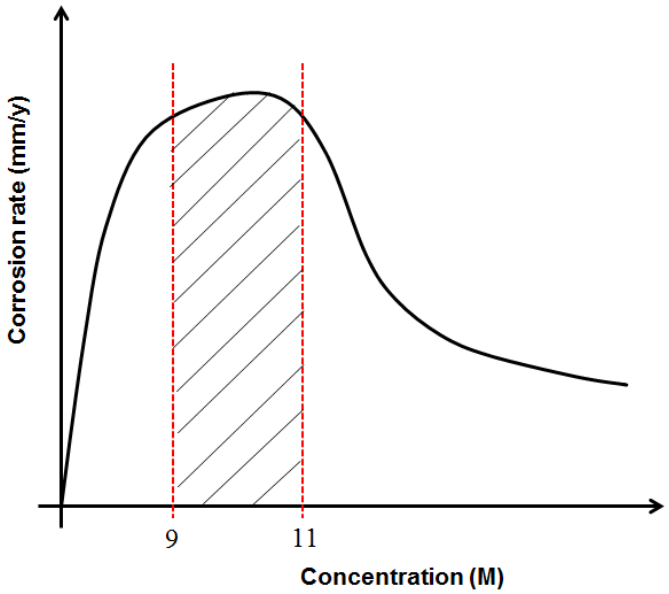

Figure 6- 46 *Schematic illustrating the typical effect of sulphuric acid concentration on the corrosion of 304 stainless steels (adapted from Phelps & Vreeland 1957; Fontana 1986). Schematic is not to scale.*

Nyquist plots in Figure 6-7(a) suggest that the corrosion of ruthenium implanted stainless steel in sulphuric acid is charge transfer controlled, i.e. the corrosion reaction is controlled by a slow step in a reaction sequence (Fontana 1986). The step could be any of those listed in Equations 2-7 to 2-9. Similar results were obtained by Sherif (2011) on ruthenium bulk alloyed duplex stainless steel exposed to 10% sulphuric acid. Typically, charge transfer controlled corrosion processes are insensitive to agitation.

However, results presented in Figures 6-15 to 6-17 show that the electrochemical processes on ruthenium implanted stainless steel were affected by solution

agitation: OCP increased when agitation was initiated. This implies that the corrosion process on ruthenium implanted 304L stainless steel may also be influenced by mass transport effects, possibly of oxygen to the surface. The increase in OCP observed upon agitation is consistent with the increase in resistance as the potential is shifted to regions where protective chromium (III) species are thermodynamically stable.

Increasing temperature increases the aggressiveness of a corrosion media, and frequently results in increased corrosion rates. This was observed on pristine 304L stainless steel in Figure 6-13(a), and was also noted by Olubambi et al. (2009) on ruthenium alloyed stainless steel. However, increasing temperature did not have an effect on the corrosion rate of the ruthenium implanted 304L stainless steel in sulphuric acid. In fact, corrosion rates and corroded surfaces obtained at 50°C were indistinguishable from those recorded at 25°C. This anti-Arrhenius behaviour suggests that ruthenium was such an effective catalyst that the increase in reaction rate due to increase in temperature was negligible.

6.5.2 Corrosion in hydrochloric acid

Corrosion performance of the ruthenium implanted 304L stainless steel was characterised in 0.5 and 2 M hydrochloric acid at 25 and 50°C. In all tests, exposure was done under stagnant conditions.

Previous workers (Olubambi et al. 2009; Sherif et al. 2009a; Sherif 2012) demonstrated that adding ruthenium to stainless steel alloys improved corrosion rates in hydrochloric acid solutions with concentrations ranging from 0.5 to 2 M. Introducing ruthenium via ion implantation however had a detrimental effect on the corrosion rate of 304L stainless steel in hydrochloric acid. In all cases studied, corrosion rates were higher than those reported on pristine 304L stainless steel.

Images obtained on both unmodified and ruthenium implanted 304L stainless steel post corrosion exposure were indistinguishable, suggesting that introducing ruthenium did not alter corrosion mechanism in hydrochloric acid. Polarisation curves in Figure 6-21 corroborate this. With or without ruthenium, the stainless

steel corroded by pitting typical in hydrochloric acid solutions (Wang et al. 2003). The severity of pitting attack was mostly influenced by concentration and temperature, and to a much lesser extent by the presence of ruthenium.

Corrosion in hydrochloric acid is supported by the combined effect of hydrogen and chloride ions. These two ions have high diffusivity (Table 2-1), are severely intrusive, and can penetrate passive films formed on stainless steel with ease (Galvele 1981; Ibrahim et al. 2009). Increasing concentration increases the amount of hydrogen and chloride ions and their potency to break down the passive films as shown in Figure 6-20. Furthermore, increasing temperature increases the diffusivity of the ions, and hence the ease with which they penetrate, and breakdown any protective films on the stainless steel surfaces.

Addition of ruthenium did not significantly increase either E_{corr} or OCP of 304L stainless steel. The implication is that implanted ruthenium did not successfully induce cathodic modification in hydrochloric acid. Examination of the polarisation curves measured on 304L stainless steel (Figure 6-21(a)) shows that where passivation was achieved, the passivation region was too narrow and the value of i_{crit} too high for effective cathodic modification to occur.

A study by Sherif et al. (2009a), reported that i_{corr} of ruthenium alloyed 2205 duplex stainless steel, and exposed to 2 M hydrochloric acid decreased with increase in the percent composition of ruthenium in the alloy. It is possible that the amount of ruthenium introduced via ion implantation was too little to successfully improve the corrosion resistance on 304L stainless steel in hydrochloric acid. this is consistent with Figures 6-19 and 6-21, where addition of ruthenium had no or very little effect on the polarisation curves.

6.5.3 Corrosion in sodium chloride

Corrosion of ruthenium implanted stainless steel was characterised in sodium chloride solutions with concentration ranging from 1 to 5 wt% at 25 and 50°C. The tests were carried out in stagnant conditions.

The presence of ruthenium promoted spontaneous passivation in sodium chloride solutions of all concentrations. Similar results were reported by other authors (Sherif et al. 2009b; Banda 2013), where ruthenium alloying induced spontaneous passivation, and reduced tendency to pitting. However, adding ruthenium via ion implantation had the effect of reducing E_{pit} and hence resistance to pitting. Adding ruthenium changed pit morphology from elongated to round (Figures 4-18, 6-30 & 6-33). Pit growth on 304L stainless steel seemed associated with elongated manganese sulphide stringers observed on Figures 4-1(c) and 4-2. Several workers (Wranglén 1974; Stewart & William 1992; Baker & Castle 1993; Böhni et al. 1995) have reported pit initiation and growth around manganese sulphide inclusions in stainless steel alloys. However, the influence of these manganese sulphides seemed to diminish with ruthenium ion implantation.

Pitting associated with manganese sulphide inclusions is postulated to initiate in the sulphur-rich matrix near the inclusions as illustrated in Figure 6-47. Hydrolysis of manganese sulphide by Equation 6-1 (Lott & Alkire 1989) creates a localised drop in pH, and the sulphide inclusion acts as a cathodic site, supporting hydrogen evolution as shown in Figure 6-47. Pitting this way is autocatalytic, and will stop when the sulphide inclusion is undermined and fall away. Ruthenium is believed to minimise corrosion by blocking anodic sites in the crystal lattice (Tomashov et al. 1984). It is likely therefore that ruthenium implanted into 304L stainless steel block matrix dissolution as described in Figure 6-47, and minimised pit initiation at manganese sulphide stringers.

$$2MnS + 3H_2O \rightarrow 2Mn^{2+} + S_2O_3^{2-} + 6H^+ + 8\bar{e} \qquad \textbf{\textit{Equation 6-1}}$$

Increasing exposure temperature from 25 to 50°C did not significantly influence i_{corr}, suggesting that dissolution rates of ruthenium implanted 304L stainless steel in sodium chloride were not affected by change in temperature. In both temperatures, the alloyed samples exhibited spontaneous passivation, confirming that temperature had no influence on dissolution rates of the samples. However, E_{pit} values decreased with increase in temperature, and incidents of metastable pitting increased, pointing to reduced pitting resistance. This was consistent with the expectation that at high temperature the diffusivity and hence intrusive ability

would increase. Reports by Chaofang et al. (2011) also showed that increasing temperature increased the tendency for 2205 duplex stainless steel to pit in sodium chloride solutions of concentrations ranging from 0.01 to 4 M.

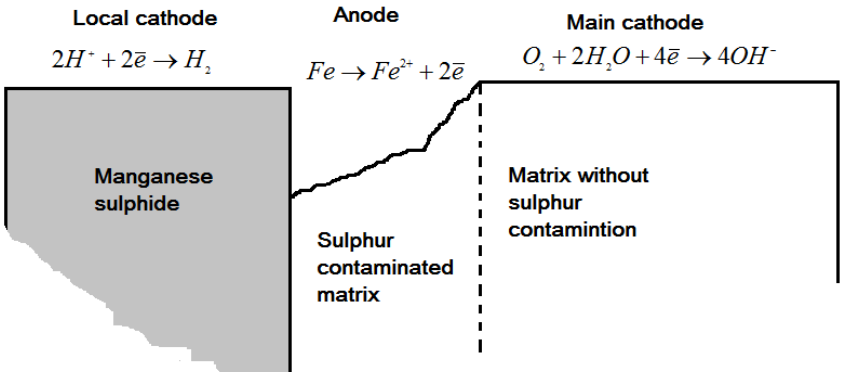

Figure 6- 47 *Schematic illustrating pit initiation on the matrix close to a manganese sulphide inclusion (adapted from Wranglén 1974).*

Reducing the pH of 3.5 wt% sodium chloride markedly increased E_{pit}, and reduced tendency to pitting corrosion. In neutral sodium chloride, the cathodic reaction is the reduction of oxygen as per Equation 2-3. Increasing the acidity of the chloride solution adds a second cathodic reaction; the evolution of hydrogen by Equation 2-2, whose catalysed reaction on ruthenium sites was possibly responsible for the rise in E_{corr} and E_{pit} in Figures 6-35 and 6-36(a). However, the presence of two cathodic reactions increases the demand for electrons, and causes increased anodic dissolution (Fontana 1986). As can be seen in Figure 6-36(b), the amount of iron dissolved from ruthenium implanted 304L stainless steel in acidic sodium chloride solutions was very high.

6.5.4 Corrosion in magnesium chloride

Corrosion in magnesium chloride was studied at 25 and 50°C. The concentration of the chloride was maintained at 3.5 wt%.

Adding ruthenium via ion implantation had two effects: (1) it increased the value of E_{pit}, and (2) reduced the current transients typically associated with incidents of metastable pitting. The cathodic reaction in magnesium is the reduction of oxygen coupled with hydrogen evolution as per Equations 2-2 and 2-3 (Dillion 1986). It is

likely that the catalysed hydrogen evolution on ruthenium caused the upward shift of E_{pit} in magnesium chloride, and reduced susceptibility to pitting.

Increasing temperature inevitably increased the potency of both hydrogen and chloride ions, and hence susceptibility of the ruthenium implanted stainless steel to pitting. This was corroborated by a reduction in E_{pit} values in Figure 6-38. The same figure shows that increasing temperature significantly shifted E_{corr} values to nobler potentials. It is likely that this shift was caused by the synergistic effects of increasing temperature, and the catalytic activity of ruthenium on the rate of the hydrogen evolution reaction.

6.5.5 Corrosion in simulated fuel solutions

Two solutions were used to simulate the environment in PEMFCs. Electrolyte 1 consisted of 10^{-4} M sulphuric acid and 0.5 M sodium sulphate, while Electrolyte 2 had 0.01 M hydrochloric acid and 0.01 M sodium sulphate. All tests were done at 60°C.

In both electrolytes, the ruthenium implanted 304L stainless steel exhibited satisfactory corrosion rates: rates were < 16 μA/cm^2, the target corrosion rate for bipolar plates used in PEMFCs. However, the alloyed stainless steel underwent active-passive behaviour in both solutions. This means that at noble potentials, the alloyed stainless steel would passivate, but actively corrode at lower potentials.

Figure 6-48 presents a simplified schematic of a bipolar plate in PEMFCs. The reactions that occur in the anodic environment are supported by the oxidation of hydrogen, while the reactions in the cathodic environment of the cell are supported by reduction of hydrogen ions to form water. Operation potentials in the cathodic environment are ≈ 645 mV vs Ag/AgCl. From Figure 6-41, this potential lies in the passive region where chromium (III) species are thermodynamically stable. Potentiostatic tests at this potential (Figure 6-43) showed the passive film on ruthenium implanted stainless steel was prone to anodic dissolution in Electrolyte 2.

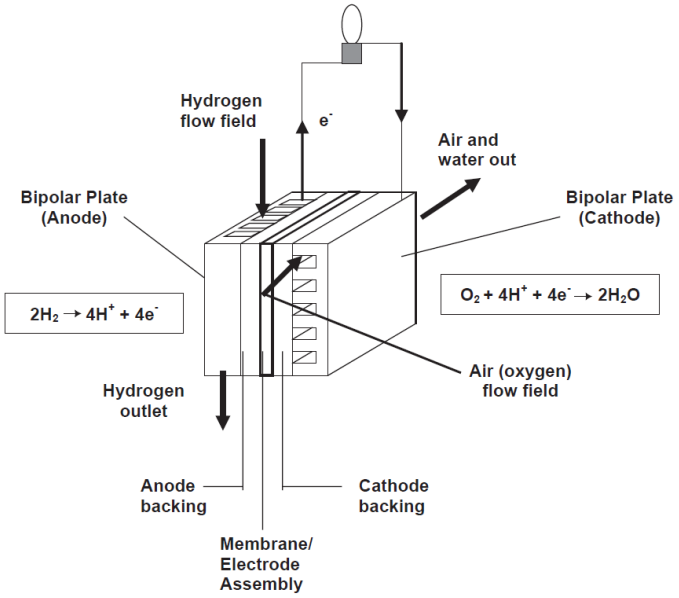

Figure 6- 48 *Schematic diagram of a PEMFC (Hermann et al. 2005).*

The different responses recorded in Figure 6-43 were due to the different solutions used. Electrolyte 2 contained chloride ions, which damage the ruthenium implanted stainless steel. The alloyed stainless steel was quite stable in the chloride free electrolyte.

6.5.6 Comparison

Corrosion behaviour of the ruthenium implanted 304L stainless steel was characterised in sulphuric acid, hydrochloric acid, sodium chloride, magnesium chloride and PEMFC simulation solutions. This section of the chapter seeks to compare the performance of the alloyed stainless steel in these media.

The corrosion of ruthenium-implanted stainless steel in these media was apparently influenced by three factors. These are (1) the passive behaviour of the pristine 304L stainless steel in the media, (2) the presence of chloride ions, and (3) the presence of a hydrogen evolution cathodic reaction.

Corrosion in the reducing acids sulphuric acid and hydrochloric acid is supported by hydrogen evolution according to Equation 2-2. The catalysis of this reaction on ruthenium is responsible for cathodic modification, which is seen as an increase in

E_{corr}. This typical behaviour was observed in sulphuric acid solutions where it had the beneficial effect of reducing corrosion rates of ruthenium implanted 304L stainless steel. However, cathodic modification in hydrochloric acid was not as successful. In fact adding ruthenium via ion implantation increased corrosion rates by as much as 120%.

Pristine 304L stainless steel exhibited active-passive behaviour in sulphuric acid, and to much lesser extent in hydrochloric acid (Figures 6-2 & 6-19). The width of passive region was determined by Equation 6-2 as done previously (Thanjekwayo 2009). In sulphuric acid, the size of the passive range was 1000 mV, and the widest measured in hydrochloric acid was barely 164 mV. i_{crit} values recorded on hydrochloric were quite high, typically > 150 µA/cm^2, compared to 2.5 µA/cm^2 in sulphuric acid. The vast differences in passive behaviour of pristine 304L stainless steel in the two reducing acids are responsible for the opposing responses to ruthenium alloying.

$$Passive\,range = E_{trans} - E_{pass} \qquad \textbf{Equation 6-2}$$

Adding chloride ions to 1 M sulphuric acid increased corrosion rates of ruthenium implanted 304L stainless steel from ≈ 0.008 to almost 3.2 mm/y. The alloyed stainless steel also experienced higher corrosion rates in the PEMFC simulation solutions with chloride ion (Figure 6-41). Chloride ions are known to compromise the corrosion resistance of stainless steels (Tomashov 1964; Frankel 1998). Chloride ions tend to interfere with passivation processes on the stainless steel alloys as described in Section 2.2.1, thereby reducing corrosion resistance.

Pitting resistance in chloride salt solutions due to alloying can be measured by changes in E_{pit}. Elements that improve pitting resistance will tend to shift E_{pit} to values that are more positive. Ruthenium introduced to 304L stainless steel notably lowered E_{pit} in sodium chloride, implying increased susceptibility to pitting. However, the presence of a hydrogen evolution cathodic reaction increased E_{pit}. The results summarised in Figure 6-49 emphasise the prerequisite for a hydrogen evolution reaction for cathodic modification to be successful in chloride solution.

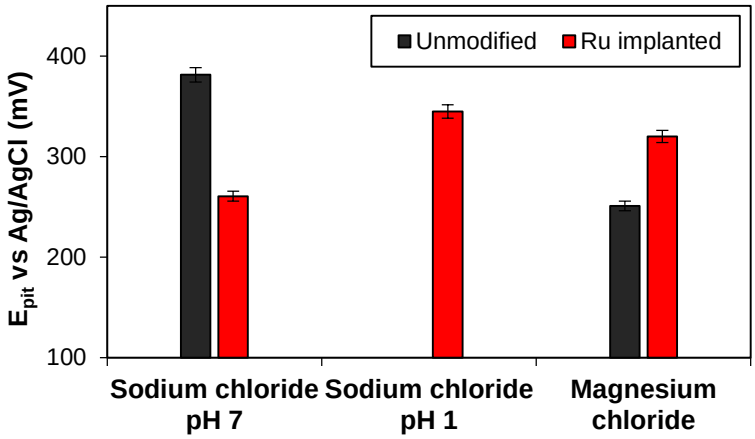

Figure 6- 49 *Effect of ruthenium implantation on E_{pit} of 304L stainless steel in sodium and magnesium chloride solutions. Concentration = 3.5 wt%.*

6.6 Summary

The objective of the study in this chapter was to characterise the corrosion performance of the ruthenium implanted 304L stainless steel in various corrosive media such as sulphuric acid, magnesium chloride, and simulated fuel cell solutions. Characterisation was done mainly via electrochemical means, and where possible, corrosion performance was compared to unalloyed 304L stainless steel.

It was found that implanted stainless steel exhibited the best corrosion performance in chloride free solutions. Remarkable improvement in corrosion rate was observed in sulphuric acid, where corrosion rates as low as 0.004 mm/y were measured. In addition, increasing concentration of sulphuric acid increased the corrosion resistance of the ruthenium implanted stainless steel.

Chapter 7
Conclusions and recommendations

7.1 Introduction

The aim of this research project was to modify the surface properties of austenitic stainless steel using ruthenium for improved corrosion resistance in reducing acids and in chloride media. Ruthenium surface alloys were synthesised on 304L stainless steel using three non-thermal techniques, namely, RF magnetron sputtering, ion implantation, and pulsed electrodeposition (PED). The surface alloys were characterised using a suite of techniques such as XRD, FESEM, EIS, and potentiodynamic polarisation. This chapter therefore highlights the findings made via these techniques, and to present recommendations for future research.

7.2 Conclusions

This section presents the findings and conclusions drawn from the experimental work done to fulfil the aim of the research project.

7.2.1 General conclusions

Alloy synthesis

During alloy synthesis, corrosion performance was studied in 1 M sulphuric acid at 25°C, and the following conclusions were drawn:

1. Surface alloying can successfully reduce corrosion rates of austenitic stainless steel. All ruthenium surface alloys produced via RF sputtering, ion implantation, and PED reduced corrosion rates of 304L stainless steel by up to 99.7%. This was attributed to cathodic modification induced by ruthenium.
2. Type II ruthenium surface alloys are more reliable than Type I alloys for long-term corrosion applications. Surface alloys prepared by ion

implantation performed better than those prepared by PED and RF sputtering, which spalled during long-term corrosion exposure.

Corrosion characterisation

Corrosion characterisation was limited to ruthenium surface alloys prepared via ion implantation. The following conclusions were drawn from the experimental work:

1. Corrosion resistance of the ruthenium implanted stainless steel is best in chloride-free solutions. Corrosion rates in sulphuric acid were less than 0.01 mm/y, and none of the samples studied exhibited evidence of corrosion attack upon post-corrosion examination.
2. Increasing temperature from 25 to 50°C has no effect on the corrosion rate of ruthenium implanted stainless steel in all concentrations of sulphuric acid studied. The non-Arrhenius behaviour was attributed to the effectiveness of cathodic modification in the acid.
3. Adding ruthenium via ion implantation may not necessarily improve pitting resistance in sodium chloride. In all the cases studied, ruthenium implanted 304L stainless steel had E_{pit} values lower than those recorded on pristine stainless steel when exposed to sodium chloride solutions, pointing to increased susceptibility to pitting.
4. Ruthenium ion implantation could alter the pitting morphologies in sodium chloride solutions. Pits on pristine 304L stainless steel were elongated and their growth seemed influenced by manganese sulphide stringers in the stainless steel. Introducing ruthenium changed the pit shape from elongated to round, and there was no evidence of the influence of manganese sulphide stringers.

7.2.2 Research highlights

This section presents findings from the research project that have been seldom reported by other authors. These findings are:

1. It is common practise to polish samples prior to ion implantation for corrosion application. However, this work demonstrated that the best corrosion performance was on rough samples. In addition, the rough samples exhibited reduced susceptibility to intergranular corrosion.
2. In PED, researchers often vary duty cycle ($\frac{T_{on}}{T_{on}+T_{off}}$), frequency ($\frac{T}{T_{on}+T_{off}}$), or pulse charge ($i_p \times T_{on}$) to alter the quality of deposited films. This work demonstrated that T_{off} (pulse off time) played a much more significant role in films deposited for corrosion application. Increasing T_{off} produced the best corrosion resistance.
3. Increasing sulphuric acid concentration typically increases corrosion rates of metallic alloys. This work demonstrated that corrosion rates on ruthenium implanted 304L stainless steel decreased with increase in sulphuric acid concentration. Furthermore, adding ruthenium via ion implantation reduced that peak for maximum corrosion rate from about 10 M to 1 M.
4. Very little work has been done on the effect of cathodic modification in acidic chloride solutions. The present study demonstrated that ruthenium alloying was more beneficial in magnesium chloride an acidic chloride salt than in sodium chloride a neutral salt.

7.3 Validation of hypotheses

Hypothesis 1:

Corrosion is a surface dependent degradation mode. As such, the corrosion resistance of austenitic stainless steel in chloride and reducing acidic media can be increased by only enriching the surface with ruthenium.

This hypothesis was confirmed in sulphuric acid and magnesium chloride. Ruthenium surface alloys reduced corrosion rates in sulphuric acid by up to 99%, and reduced propensity to pitting in magnesium chloride. However, ruthenium surface alloying via ion implantation was not beneficial in hydrochloric acid and sodium chloride solutions.

Hypothesis 2:

Since cathodic modification provides sites that kinetically favour the cathodic process, the corrosion resistance of the surface alloys on austenitic stainless steel will not be compromised by discontinuities in the films prepared by RF magnetron sputtering or PED.

This hypothesis was confirmed on films prepared by both RF magnetron sputtering and PED. Some of the films prepared via these techniques were discontinuous. However, corrosion rates measured on these discontinuous films were as low as 0.002 mm/y, corresponding to > 99% improvement in corrosion resistance.

Hypothesis 3:

During synthesis of the surface alloys, the initial interaction between ruthenium and the austenitic stainless steel is on the surface. Hence, the nature of surface preparation would play an important role on the properties of the ruthenium surface alloys and therefore influence their corrosion behaviour.

This hypothesis was confirmed on all the ruthenium surface alloys studied. The effect of implantation dose and implantation energy on corrosion resistance exhibited a strong dependence on surface roughness, while the best corrosion performance on the films deposited by PED was recorded on polished surfaces and at high T_{off}. Films deposited by RF sputtering on rough surfaces exhibited the least corrosion resistance.

7.4 Recommendations

Although the results obtained in this research project were remarkable and encouraging, more work is necessary to maximize the benefits of ruthenium surface alloys on austenitic stainless steels. The following may be considered for future study:

1. The ruthenium implanted 304L stainless steel has potential as a candidate material for bipolar plate production for use in PEMFCs. In the two fuel

cell simulation solutions studied, the corrosion rate of the ruthenium surface alloys was < 16 μA/cm^2, which is the target corrosion rate for PEMFCs application. This potential application should be explored using other simulation electrolytes. Other properties such as interfacial contact resistance, and electronic conductivity should be investigated.

2. The results presented here provide compelling evidence that rough ruthenium implanted stainless steel out-performed polished ruthenium implanted samples. This was attributed to such phenomena as channelling, sputtering and amorphisation. However, the underlying cause of this behaviour remains to be experimentally determined.
3. The corrosion rate of ruthenium implanted 304L stainless steel was found to decrease with increase in sulphuric acid concentration. These results are encouraging and present an opportunity to expand the application spectrum for both 304L stainless steel and ruthenium. Future work should focus on validating these results using more samples, and a wider range of concentrations, and exposure times. The effect of chloride should also be investigated further.
4. Ruthenium surface alloys prepared by RF sputtering and PED exhibited remarkably low concentration rates: at least 85% improvement in corrosion resistance was noted with the introduction of these surface films. However, the films spalled during corrosion exposure making them unsuitable for long-term application. It would be beneficial to improve the adhesion strength of these films, and a starting point would be studying the interfacial region by means such as Rutherford backscattering spectrometry (RBS) or Glow discharge optical emission spectroscopy (GD-OES).

Bibliography

Abouzari, M.R.S., Berkemeier, F., Schmitz, G. & Wilmer, D., 2009, 'On the physical interpretation of constant phase elements', *Solid State Ionics*, 180, 922-927.

Abreu, C.M., Cristóbal, M.J., Nóvoa, X.R., Pena, G., Pérez, M.C. & Rodríguez, R.J., 2002a, 'Modification of the stainless steel passive film induced by cerium implantation, *Surface and Coatings Technology,* 158-159, 582-587.

Abreu, C.M., Cristóbal, M.J., Nóvoa, X.R., Pena, G. & Pérez, M.C., 2002b, 'Characterisation of the electrochemical behaviour of cerium implanted stainless steels', *Electrochimica Acta,* 47, 2215-2222.

Abreu, C.M., Cristóbal, M.J., Losad, R., Nóvoa, X.R., Pena, G. & Pérez, M.C., 2004, 'High frequency impedance spectroscopy study of passive films formed on AISI 316 stainless steel in alkaline medium', *Journal of Electroanalytical Chemistry*, 572, 335-345.

Abreu, C.M., Cristóbal, M.J., Losada, R., Nóvoa, X.R., Pena, G. & Pérez, M.C., 2006, 'The effect of Ni in the electrochemical properties of oxide layers grown on stainless steels', *Electrochimica Acta*, 51, 2991-3000.

Abreu, C.M., Cristóbal, M.J., Merino, P., Nóvoa, X.R., Pena, G. & Pérez, M.C., 2008, 'Electrochemical behaviour of an AISI 304L stainless steel implanted with nitrogen', *Electrochimica Acta*, 53, 6000-6007.

Abys, J.A., 2010, Palladium electroplating, in Modern Electroplating, Schlesinger, M. & Pannovic, M., (Eds.), 5th Ed., John Wiley & Sons Inc., New Jersey, USA, p. 335.

Agarwala, V.S. & Biefer, G.J., 1972, 'Corrosion of Type 430 stainless steel: Effects of Mo-Pd and other addition pairs,' *Corrosion*, 28(2), 64-74.

Akgün, O.V., Ürgen, M. & Çakir, A.F., 1995, 'The effect of heat treatment on corrosion behaviour of laser surface melted 304L stainless steel,' *Materials Science and Engineering*, A203, 324-331.

Alagoz, A.S., Kamminga, J.-D., Grackev, S.Y., Lu, T.-M. & Karabacak, T., 2009, 'Residual stress reduction in sputter deposited thin films by density modulation,' 2009 MRS fall meeting, Manuscript ID 1224-FF05-22.R1, 1-6.

Alfonso, E., Olaya, J. & Cubillos, G., 2012, 'Thin film growth through sputtering technique and its application', Chapter 15, in Crystalline-Science and Technology, M. Andreeta (Ed.), InTech, DOI: 10.5772/35844, pp. 397-432accessed on 15 February 2016 from http://www.intechopen.com

Anderoglu, O., 2004, 'Residual stress measurements using X-ray diffraction,' MSc dissertation, Faculty of Engineering, Texas A&M University, Texas.

Angerer, P., Neubauer, E., Yu, L.G. & Khor, K.A., 2009, 'Determination of the residual stress depth profile of uniaxial compacted ruthenium powder samples by X-ray diffraction', *International Journal of Refractory Metals and Hard Materials*, 27, 1004-1008.

Antunnes, R.A., Oliveira, M.C.L., Ett, G. & Ett, V., 2010, 'Corrosion of metal bipolar plates for PEM fuel cells: A review,' *International Journal of Hydrogen Energy*, 35, 3632-3647.

Arblaster, J.W., 2013, 'Crystallographic properties of ruthenium,' *Platinum Metals Review*, 57(2), 127-136.

ASM Handbook, 1985, Volume 9, Metallography and microstructures, Mills, K. (vol. Ed.), 9th Ed., American Society for Metals, Ohio, USA.

ASTM A240/A 240M-05a, Standard specification for chromium and chromium-nickel stainless steel plate, sheet, and strip for pressure vessels and for general applications, ASTM, West Conshohocken, USA, 2005.

ASTM D907-15 Standard terminology of adhesives, ASTM, West Conshohocken, USA, 2015.

ASTM D3359-09, Standard test method for measuring adhesion by tape test, ASTM, West Conshohocken, USA, 2009.

ASTM E407-07, Standard practice for microetching metals and alloys, ASTM, West Conshohocken, USA, 2007.

ASTM G1-03, Standard practise for preparing, cleaning and evaluating corrosion test specimens, ASTM, West Conshohocken, USA, 2003.

ASTM G3-89, Standard practise for conventions applicable to electrochemical measurements in corrosion testing, ASTM, West Conshohocken, USA, 2010.

.ASTM G5-94, Standard reference test method for making potentiostatic and potentiodynamic anodic polarisation measurements, ASTM, West Conshohocken, USA, 2010.

ASTM G16-95, Standard guide for applying statistics to analysis to corrosion data, ASTM, West Conshohocken, USA, 2010.

ASTM G102-89, Standard practise for calculating of corrosion rats and related information from electrochemical measurements, ASTM, West Conshohocken, USA, 2010.

Atashin, S., Pakshir, M. & Yazdani, A., 2011, 'Synergistic investigation into the marine parameters' effect on the corrosion rate of AISI 316 stainless steel,' *Materials and Design*, 32, 1315-1324.

Bagotsky, V.S., 2006, Fundamentals of electrochemistry, 2nd Ed, The electrochemical Society Series, John Wiley & Sons Inc. Publication, New Jersey.

Banda, S.C.K., 2013, 'The effect of small additions of ruthenium on the pitting corrosion resistance of LDX 2101 duplex stainless steel,' MSc dissertation, Faculty of Engineering, University of the Witwatersrand, Johannesburg, accessed on 16 August 2013 from www.wiredspace.wits.ac.za

Bandy, R. & Jones, D.A., 1976, 'Analysis of errors in measuring corrosion rates by linear polarisation,' *Corrosion*, 32(4), 126-134.

Banerjee, I., Kumari, N., Singh, A.K., Kumar, M., Laha, P., Panda, A.B., Pabi, S.K., Barhai, P.K. & Mahapatra, S.K., 2010, 'Influence of RF power on the electrical and mechanical properties of nanostructural carbon nitride thin films deposited by RF magnetron sputtering', *Thin Solid Films*, 518, 7240-7244.

Barker, M.A. & Castle, J.E., 1993, 'The initiation of pitting corrosion at MnS inclusions,' *Corrosion Science*, 34(4), 667-682.

Barrentine, L.B., 1999, An introduction to design of experiments: A simplified approach, ASQ, Milwaukee, Wisconsin.

Barson, S.D., Skeldon, P., Thompson, G.E., Piekoszewski, J., Chmielewski, A.G., Werner, Z., Grötzschel, R. & Wieser, E., 2000, 'Corrosion protection of titanium by pulse plasma deposition of palladium,' *Corrosion Science*, 42, 1213-1234.

Bhatt, V., Chandra, S., Kumar, S., Rauhan, C.M.S. & Dixit, P.N., 2007, 'Stress evaluation of RF sputtered silicon dioxide films for MEM', *Indian Journal of Pure and Applied Physics*, 45, 377-381.

Bierwagen, G., Tallman, D., Li, J., He, J. & Jeffcoate, C., 2003, 'EIS studies of coated metals in accelerated exposure,' *Progress in Organic Coatings*, 46, 148-157.

Böhni, H., Suter, T. & Schreyer, A., 1995, 'Micro- and nanotechniques to study localised corrosion,' *Electrochimica Acta*, 40(10), 1361-1368.

Bojinov, M., Betova, I., Frabricius, G., Laitinen, T., Raicheff, R. & Saario, T., 1999, 'The stability of the passive state of iron-chromium alloys in sulphuric acid solution', *Corrosion Science*, 41, 1557-1584.

Braceras, I., Briz, N., Garcia, F., Munoz, R., Viviente, J.L. & Onate, J.I., 2007, 'Effects of ion implantation on nano-topographic properties,' *Surface and Coatings Technology*, 201, 8511-8515.

Brett, D.J.L. & Brandon, N.P., 2007, 'Review of materials and characterisation methods for polymer electrolyte fuel cell flow-field plate,' *Journal of Fuel Cell Science and Technology*, 4, 29-44.

Bunker, S.N. & Armini, A.J., 1994, 'Technique for the growth of metal coatings by ion implantation', *Surface and Coatings Technology,* 66, 30-44.

Canli, S., 2010, 'Thickness analysis of thin films by energy dispersive X-ray spectroscopy,' MSc dissertation, Graduate School of Natural and Applied Sciences, Middle East Technical University, Ankara, accessed on 17 March 2017 from https://etd.lib.metu.edu.tr

Cano, E, Martínez, L., Simancas, J., Pérez-Trujillo, F.J., Gómez, C. & Bastidas, J.M., 2006, 'Influence of N, Ar, Si ion implantation on the passive layer and corrosion behaviour of AISI 304 and 430 stainless steels', *Surface and Coatings Technology,* 200, 5123-5131.

Chandrasekar, M.S. & Pushpavanam, M., 2008, 'Pulse and pulse reverse plating-Conceptual, advantages and application', *Eectrochimica Acta,* 53, 3313-3322.

Chang, B. & Ameen, M., 2011, High mass molecule ion implantation, crystalline silicon- properties and uses, Basu, S. (Ed), InTech, DOI: 10.5772/24194, pp. 81-104, accessed on 10 September 2016 from http://www.intechopen.com

Chaofang, D., Hung, L., Kui, X., Ting, S., Qian, L. & Xiaogan, L., 2011, 'Effect of temperature and Cl^- concentration on pitting of 2205 Duplex stainless steel,' Journal of Wuhan University of Technology- Materials Science, August Edition, 641-647.

Chaoumead, A., Sung, Y-M. & Kwak, D-J., 2012, 'The effects of RF sputtering power and gas pressure on structural and electrical properties of ITiO thin film', *Advances in Condensed Matter Physics,* 2012, 1-7.

Chapin, J.S., 1979, *Sputtering process and apparatus,* US Patent 4,166,018.

Chernova, G.P., Fedoseeva, T.A., Kornienko, L.P. & Tomashov, N.D., 1981, 'Increasing the passivation ability and corrosion resistance of chromium steel by surface alloying with palladium,' *Surface Technology,* 13, 241-256.

Chou, W-J., Yu, G-P. & Huang, J-H., 2001, 'Corrosion behaviour of TiN coated 304 stainless steel', *Corrosion Science,* 43, 2023-2035.

Clark, P.J., 1971, *Sputtering apparatus*, US Patent 3,616,450.

Codd, L.W., Dijkhoff, K., Fearon, J.H., Van Oss, C.J., Robernsen, H.C., Stanford, E.G. & Van Thoor, T.J.W. (Ed.), 1970, *Metals and Ores*, Materials and Technology, vol. 3, Longman, USA, pp. 791-795.

Cohen, M., 1953, 'Interpretation and significance of potentials of metals in aqueous solutions,' *Corrosion*, 9, 372-379.

Collins, G.A., Hutchings, R. & Tendys, J., 1991, 'Plasma immersion ion implantation of steels,' *Materials Science and Engineering*, A139, 171-178.

Collins, G.A., Hutchings, R., Tendys, J. & Samandi, M., 1994, 'Advanced surface treatments by plasma ion implantation', *Surface and Coatings Technology* 68/69, 285-293.

Covino, B.S., Sartwell, B.D. & Needham, P.B. Jr, 1978, 'Anodic polarisation behaviour of Fe-Cr surface alloys formed by ion implantation,' *Journal of the Electrochemical Society: Electrochemical Science and Technology*, 125(3), 366-369.

Crosby, J.N., 1978, *Electrodeposition of ruthenium*, US patent 4,082,625.

Crosby, J.N., 1981, *Ruthenium electroplating and bath and compositions therefor*, US Patent 4,297,178.

Cuthrell, R.E., Matox, D.M., Peeples, C.R., Dreike, P.L. & Lampa, K.P., 1988, 'Residual stress anisotropy, stress control, and resistivity in post cathode magnetron sputter deposited molybdenum films', *Journal of Vacuum Science Technology A*, 6(5), 2914-2920.

Dagielski, J., Piatkowska, A., Aubert, P., Thomé, L., Turos, A. & Kaber, A.A., 2006, 'Ion implantation for surface modification of biomaterials', *Surface and Coatings Technology*, 200, 6355-6361.

Dawson, J.L. & Ferreira, M.G.S., 1986, 'Electrochemical studies of the pitting of austenitic stainless steel,' *Corrosion Science*, 26(12), 1009-1026.

Deiter, G.E. 1986, Mechanical metallurgy, McGraw Hill Book Company (UK) Limited, UK, pp. 132-133.

Delport, W.E. & Roux, J.P., 1986, 'The surface segregation and oxidation of chromium and palladium in high chromium stainless steel', *Corrosion Science*, 26(6), 407-417.

Detor, A.J., Hodge, A.M., Chason, E., Wang, Y., Xu, H., Conyers, M., Nikroo, A. & Hamza, A., 2009, 'Stress and microstructure in thick sputtered films,' *Acta Materialia*, 57, 2055-2065.

Devaraj, G., Guruviah, S. Seshadri, S.K., 1990, 'Pulse plating,' *Materials Chemistry and Physics*, 25, 439-461.

D'heurle, F.M., 1970, 'Aluminium films deposited by rf sputtering,' *Metallurgical Transactions*, 1, 725-732.

Dillion, C.P., 1986, Corrosion control in the chemical process industries, McGraw-Hill Book Company, USA, pp. 99-102.

Dudognon, J., Vayer, M., Pienan, A. & Erre, R., 2008, 'Mo and Ag ion implantation in austenitic, ferritic and duplex stainless steels: A comparative study,' *Surface and Coatings Technology*, 203, 180-185.

Dumerval, M., Perrin, S., Marchetti, L., Sennour, M., Jomard, F., Vaubaillion, S. & Wouters, Y., 2016, 'Effect of implantation defects on the corrosion of 316L stainless steels in primary medium pressurized water reactors,' *Corrosion Science*, 107, 1-8.

EN 10088-2, Technical delivery conditions for sheet/plate and strip for general purposes, British Standards Institution, London, 2014.

Ensinger, W., 1998, 'Modification of mechanical and chemical surface properties of metals by plasma immersion ion implantation,' *Surface and Coatings Technology*, 100-101, 341-352.

Ernst, P., Laycock, N.J., Moayed, M.A. & Newman, R.C., 1997, 'The mechanism of lacy cover formation in pitting,' *Corrosion Science*, 39(6), 1133-1136.

Escalada, L., Lutz, J., Brühl, S.P., Fazoio, M., Márquez, A., Mändl, S., Manova, D. & Simison, S.N., 2013, 'Microstructure and corrosion behaviour of AISI 36L duplex treated by means of ion nitriding and plasma based on implantation and deposition', *Surface and Coating Technology*, 223, 41-46.

Ezaki, H., Morinaga, M. & Watanabe, S., 1993, 'Hydrogen overpotential for transition metals and alloys, and its interpretation using an electronic model', *Electrochimica Acta*, 38(4), 557-564.

Feng, K., Cai, X., Li, Z. & Chu, P.K., 2012, 'Improved corrosion resistance of stainless steel 316L by Ti ion implantation,' *Materials Letters*, 68, 450-452.

Fletcher, S., 1994, 'Tables of degenerate electrical networks for use in the equivalent-circuit analysis of electrochemical systems', *Journal of the Electrochemical Society*, 141(7), 1823-1826.

Flis, J. & Kuczynska, M., 2004, 'Effects of low-temperature plasma nitriding on corrosion of 304L stainless steel in sulfate and chloride solutions, *Journal of the Electrochemical Society*, 151(11), B573-B580.

Flitt, H.J. & Schweinsburg, D.P., 2005a, 'Evaluation of corrosion rate from polarisation curves not exhibiting a Tafel region', *Corrosion Science*, 47, 3034-3052.

Flitt, H.J. & Schweinsberg, D.P., 2005b, 'A guide to polarisation curve interpretation: deconstruction of experimental curves typical of the $Fe/H_2O/H^+/O_2$ corrosion system,' *Corrosion Science*, 47, 2125-2156.

Fontana, M.G., 1986, Corrosion engineering, 3rd Ed., McGraw-Hill Book Company, New York, USA.

Forghani, S.M., Ghazali, M.J., Muchtar, A., Daud, A.R., Yusoff, N.H.N. & Azhari, C.H., 2013, 'Effects of plasma spray parameters on TiO_2-coated mild steel using design of experimental (DoE) approach,' *Ceramics International*, 39, 312-3127.

Fossati, A., Borgioli, F., Galvanetto, E. & Bacci, T., 2006, 'Corrosion resistance properties of glow discharge nitride AISI 316L austenitic stainless steel NaCl solutions', *Corrosion Science,* 48, 1513-1527.

Frankel, G.S., 1998, 'Pitting corrosion of metals: A review of the critical factors,' *Journal of the Electrochemical Society*, 145(6), 2186-2198.

Frankel, G.S., 2008, 'Electrochemical techniques in corrosion: Status, limitations and needs', *Journal of ASTM International,* 5(2), 1-27.

Galvele, J.R., 1981, 'Transport processes in passivity breakdown-II. Full hydrolysis of the metal ions', *Corrosion Science,* 21(8), 551-579.

Gao, X., Tang. J., Zou, Y., Tang, Y. & Xiong, J., 2009, 'The electroplated palladium-copper alloy film on 316L stainless steel and its corrosion resistance in mixture of acetic acid & formic acid, *Corrosion Science*, 51, 1822-1827.

Gebauer, B.G., 1978, US patent, Electrodeposition of ruthenium, US patent 4,082,622.

Girija, S., Mudali, U.K., Andreev, C., Ninova, L. & Raj, B., 2012, 'Corrosion behaviour of nitrogen-containing stainless steel in nitric acid and chloride environments', *Corrosion,* 68(10), 922-931.

Glasman-Deal, H., Science research writing for non-native speakers of English, 2010, Imperial College Press, London.

Gorji, M.R. & Sanjabi, S., 2012, 'Corrosion behaviour of ion implanted NiTi shape memory alloy thin films', *Materials Letters*, 73, 179-182.

Graham, A.K. (Ed.), 1971, Electroplating engineering handbook, 3rd Ed., Van Nostrand Reinhold Co., New York, pp. xiii.

Greene, N.D. & Fontana, M.G., 1959, 'A critical analysis of pitting corrosion,' *Corrosion*, 15, 41-47.

Haruyama, S., 1990, 'Electrochemical methods in passivity study', *Corrosion Science,* 31, 29-38.

Haupt, S. & Strehblow, H.-H., 1995, 'A combined surface analytical and electrochemical study of the formation of passive layers on Fe/Cr alloys in 0.5 M H_2SO_4', *Corrosion Science,* 37(1), 43-54.

Hermann, A., Chaudhuri, T. & Spagnol, P., 2005, 'Bipolar for PEM fuel cell: A review,' *International Journal of Hydrogen Energy*, 30, 1297-1302.

Hicks, C.R., 1982, Fundamental concepts in the design of experiments, 3rd Ed., CBS College Publishing, New York, USA, pp. 89-120.

Hirschorn, B., Orazem, M.E., Tribollet, B., Vivier, V., Frateur, I. & Musiani, M., 2010, 'Determination of effective capacitance and film thickness from constant-phase-element parameters', *Electrochimica Acta*, 55, 6218-6227.

Hogg, R.V. & Ledolter, J., 1992, Applied statistics of engineers and physical scientists, 2nd Ed., Macmillan, New York, pp. 297-343.

Hoster, H.E., 2013, 'Surface alloys in surface and interface science-Properties of composite surfaces: Alloys, compounds, semiconductors,' Wandelt, K. (Ed.), ISBN: 978-3-527-41157-3, Wiley-VCH Velag GmbH & Co., pp. 329-367 accessed on 5 February 2016 from www.eu.wiley.com

Hoyle, R.A.S. & Taylor, D.E., 1993, 'Effect of chlorinated hydrocarbons on the corrosion resistance of austenitic stainless steels in chloride solutions,' Datta, P.K. & Gray, J.S. (Ed.), Surface Engineering Volume 1: Engineering Applications, Royal Society of Chemistry, Cambridge.

Hu, J.M., Zhang, J.Q. & Cao, C.N., 2003, 'Determination of water uptake and diffusion of Cl^- ion in epoxy primer on aluminium alloys in NaCl solution by electrochemical impedance spectroscopy', *Progress in Organic Coatings,* 46, 273-27.

Hydes, P.C., 1980, 'Electrodeposited ruthenium as an electrical contact material: A review of its properties and economic advantages,' *Platinum Metals Review,* 24(2), 50-55.

Ibl, N., Puippe, J.Cl. & Angerer, H., 1978, 'Electrocrystallisation in pulse electrolysis,' *Surface Technology,* 6, 287-300.

Ibl, N., 1980, 'Some theoretical aspects of pulse electrolysis', *Surface Technology,* 10, 81-104.

Ibrahim, M.A.M., Korablov, S.F. & Yoshimura, M., 2002, 'Corrosion of stainless steel coated with TiN, (TiAl)N and CrN in aqueous environments', *Corrosion Science,* 44, 815-828.

Ibrahim, M.A.M, Abd El Rehim, S.S. & Hamza, M.M., 2009, 'Corrosion behaviour of some austenitic stainless steels in chloride environments', *Materials Chemistry and Physics*, 115, 80-85.

ISO 8044:2015, Corrosion of metals and alloys- Basic terms and definitions, International Organisation for Standardisation, Geneva, 2015.

ISSF 2015, Stainless steel in figures, International Stainless Steel Forum, Brussels.

Jagielski, J., Piatkowska, A., Aubert, P., Thomé, L., Turos, A. & Abdul K.A., 2006, 'Ion implantation for surface modification of biomaterial,' *Surface and Coatings Technology*, 200, 6355-6361.

Jargelius-Petterson, R.F.A. & Pound, B.G., 1998, 'Examination of the role of molybdenum in passivation of stainless steel using AC impedance spectroscopy,' *Journal of Electrochemical Society*, 145(5), 1462-1469.

Johnson Matthey 2016, PGM market report May 206: Summary of platinum supply and demand in 2015, Johson Matthey PLC, accessed on 20 June 2016 from www.platinum.matthey.com

Joi, A., Akolkar, R. & Landau, U., 2013, 'Pulse electrodeposition of copper-manganese alloy for application in interconnect metallization', *Journal of the Electrochemical Society*, 160(12), D3145-D3148.

Jüttner, K., 1990, 'Electrochemical impedance spectroscopy (EIS) of corrosion processes on inhomogeneous surfaces', *Electrochimica Acta*, 35(10), 1501-1508.

Kelly, P.J. & Arnell, R.D., 2000, 'Magnetron sputtering: a review of recent developments and application', *Vacuum,* 56, 159-172.

Kim, J.S., Peelen, W.H.A., Hemmes, K. & Makkus, R.C., 2002, 'Effect of alloying elements on the contact resistance and the passivation behaviour of stainless steel,' *Corrosion Science*, 44, 635-655.

Kim, S-J. & Woo, Y-B., 2010, 'Coating layer and corrosion protection characteristics in sea water with various thermal spray coating materials for STS304', *Surface Review and Letters*, 17(3), 299-305.

Kim, K.M., Kim, J.H., Lee, Y.Y. & Kim, K.Y., 2012 'Electrodeposition of ruthenium oxide on ferritic stainless steel bipolar plate for polymer electrolyte membrane fuel cells', *International Journal of Hydrogen Energy*, 37, 1653-1660.

Kim, W. & Weil, R., 1989, 'Pulse plating effects in nickel electrodeposition,' *Surface and Coatings Technology*, 38, 289-298.

Kolotyrkin, Y.A.M., 1977, 'Professor N.D. Tomashov', *Corrosion*, 33(12) 423-425.

Kumar, T., Jambulingam, P., Gopal, M. & Rajadurai, A., 2002, 'Surface hardening of AISI 304, 316, 304L and 316L SS using cyanide free salt bath Nitriding process', paper presented at the International Symposium of Research Students on Materials Science and Engineering, Indian Institute of Technology, Chennai, 4th December.

Kumar, B.R., Singh, R., Mahato, B., De, P.K., Bandyopadhyay, N.R. & Bhattacharya, D.K., 2005, 'Effect of texture on the corrosion behaviour of AISI 304L stainless steel,' *Materials Characterisation*, 54, 141-147.

Landolt, D. & Marlot, A., 2003, 'Microstructure and composition of pulse-plated metals and alloys,' *Surface and Coatings Technology*, 169-170, 8-13.

Lædre, S., Kongstein, O.E., Oedegaard, A., Seland, F. & Karohussen, H., 2012, 'The effect of pH and halide on the corrosion process of stainless steel bipolar plate for proton exchange membrane fuel cells', *International Journal of Hydrogen Energy*, 37, 18537-18546.

Lefrou, C., Nogneria, P. Huet, F. & Takenouti, H., 2010, Electrochemistry, in Shreir's Corrosion, vol. 1, Richardson, T.J.A. (Ed.), ISBN: 978-0-444-52787-5, Elsevier BV, pp. 13-51, accessed on 5 May 2014 from www.sciencedirect.com

Lei, M.K. & Zhu, X.M., 2005, 'Plasma-based low-energy ion implantation of austenitic stainless steel for improvement in wear and corrosion resistance', *Surface and Coatings Technology*, 193, 22-28.

Lekala, M.B., Van der Merwe, J.W. & Pityana, S.L., 2012, 'Laser surface alloying of 316L stainless steel with Ru and Ni mixtures', *International Journal of Corrosion*, 2012, 1-4.

Li, M., Luo, S., Zeng, C., Shen, J., Liu, H. & Cao, C., 2004, 'Corrosion behaviour of TiN coated type 316 stainless steel in simulated PEMFC environments,' *Corrosion Science*, 46, 1369-1380.

Li, W. & Li, D.Y., 2006, 'Influence of surface morphology on corrosion and electronic behaviour,' *Acta Materialia*, 54, 445-452.

Lide, D.R., 2005, CRC handbook of chemistry and physics, 86th Ed., Taylor and Francis, pp. 2005-2006.

Lieser, M.J. & Xu, J., 2010, Composites and the future of society: preventing a legacy of costly corrosion with modern, brochure, Owens Corning, viewed 12 November 2014 from http://www.owenscorning.com.

Liu, C., Bi, Q., Leyland, A. & Matthews, A., 2003, 'An electrochemical impedance spectroscopy study of the corrosion behaviour of PVD coated steels in 0.5 N NaCl aqueous solution: Part I Establishment of equivalent circuits for EIS data modelling', *Corrosion Science*, 45, 1243-1256.

Llopis, J., Tordesillas, I.M. & Alfayate, J.M., 1966, 'Anodic corrosion of ruthenium in hydrochloric acid solution', *Electrochimica Acta*, 11, 623-632.

Lorenz, W.J. & Mansfeld, F., 1981, 'Determination of corrosion rates by electrochemical DC and AC methods', *Corrosion Science*, 21(9), 647-672.

Lott, S.E. & Alkire, R.C., 1989, 'The role of inclusions on initiation of

Macdonald, J.R., 1992, Impedance spectroscopy, *Annals of Biomedical Engineering*, 20, 289-305

Macsteel, 2009, *Stainless steel and aluminium catalogue*, brochure, Macsteel VRN, South Africa.

Mändl, S., Manova, D., Neumann, H., Pham, M.T., Richter, E. & Rauschenbach, B., 2005, 'Correlation between PIII nitriding parameters and corrosion behaviour of austenitic stainless steels,' *Surface and Coatings Technology*, 200, 104-108.

Manfeld, F., 1990, 'Electrochemical impedance spectroscopy (EIS) as a new tool for investigating methods of corrosion protection,' *Electrochimica Acta*, 35(10), 1533-1544.

Manning, P.E., Duquette, D.J. & Savage, W.F., 1980, 'Technical note: The effect of retained ferrite on localised corrosion in duple 304L stainless steel', *Welding Research Supplement*, 260-262.

Mason, R.L., Guns, R.F. & Hess, J.L., 1989, 'Statistical design and analysis of experiments with application to engineering and science', John Wiley & Sons, New York, pp. 92-116.

Mattox, D.M., 1973, 'Thin film metallization of oxides in microelectronics', *Thin Solid Films*, 18, 173-186.

Mattox, D.M., 1998, Handbook of physical vapour deposition (PVD processing: Film formation, adhesion, surface preparation and contamination control, Noyes Publication, New Jersey.

McGill, I.R., 1990, 'Platinum metals in stainless steels: a review of corrosion and mechanical properties', *Platinum Metals Review*, 34(2), 86-97.

Melchers, R.E. & Jeffery, R., 2004, 'Surface roughness effect on marine immersion corrosion of mild steel,' Corroison, 697-703.

Meng, H., Hu, X. & Neville, A., 2007, 'A systematic erosion-corrosion study of two stainless steels in marine conditions via experimental design,' *Wear*, 263, 355-362.

Meng, L. & dos Santos, M.P., 1999, 'Characterisation of RuO_2 films prepared by rf reactive magnetron sputtering,' *Applied Surface Science*, 147, 94-100.

Mintek, 2011, The high cost of corrosion, accessed on 12 August 2013 from www.mintek.co.za

Mischler, S., Vogel, A., Mathien, H.J. & Landolt, D., 1991, 'The chemical composition of the passive film on Fe-24Cr and Fe-24Cr-11Mo studied by AES, XPS and SIMS', *Corrosion Science*, 32(9), 925-944.

Mitrovic-Scepanovic, V., MacDougall, B. & Graham, M.J., 1987, 'The effect of Cl^- ions on the passivation of Fe-26Cr alloy,' *Corrosion Science*, 27(3), 239-247.

Monnartz, P., 1911, 'Iron-chromium alloys with special consideration of resistance to acids,' *Metallurgie (Halle)*, 7(8), 161-176.

Morrow, P., Tang, F., Karabacak, T., Wang, P.-I, Ye, D.-X, Wang, G.-C. & Lu, T.-M., 2006, 'Texture of ruthenium columns grown by oblique angle sputter deposition,' *Journal of Vacuum Science Technology A*, 24(2), 235-245.

Myburg, G., Varga, K., Barnard, W.O., Baradlai, P., Tomcsányi, L., Potgieter, J.H., Louw, C.W. & van Staden, M.J., 1998, 'Surface composition of Ru containing duplex stainless steel after passivation in non-oxidising media', *Applied Surface Science*, 136, 29-35.

Nakahara, S. & Okinaka, Y., 1983, 'Microstructure and ductility of electroless copper deposits,' *Acta Metallurgica*, 31(5), 713-724.

Nastasi, M. & Mayer, J.W., 2006, Ion implantation and synthesis of materials, Springer-Verlag, Berlin, Germany.

Noyan, I.C. & Cohen, J.B., 1987, Residual stress measurement by diffraction and interpretation, Springer, New York, USA.

Nunogaki, M., Uchinda, M., Kuratomi, Y. & Miyazaki, K., 1989, 'Surface roughness and sputtering yield of heavily ion implanted surfaces,' *Nuclear Instruments and Methods in Physics Research*, B37/38, 325-328.

Ohring, M., 2002, Materials science of thin films: Deposition and structure, Academic Press, San Diego, pp. 152-158, 191-198, 711-781.

Okamoto, G. & Shibata, T., 1970, 'Stability of passive stainless steel in relation to the potentials of passivation treatment,' *Corrosion Science*, 10, 371-378.

Okamoto, N., Wang, F. & Watanabe, T., 2004, 'Adhesion of electrodeposited copper, nickel and silver films on copper, nickel and silver substrates, *Materials Transactions*, 45(12), 3330-3333.

Oke, D., Ndlovu, S. & Sibanda, V., 2014, 'Removal of platinum group metals from dilute process streams: Identification of influential factors using DOE approach,' *Journal of Environmental Chemical Engineering*, 2, 1061-1069.

Oladijo, O.P., Venter, A.M., Cornish, L.A. & Sacks, N., 2012, 'X-ray diffraction measurement of residual stress in WC-Co thermally sprayed coatings onto metal substrates,' *Surface and Coatings Technology*, 206, 4725-4729.

Olaseinde, O.A., van der Merwe, J.W., Cornish, L.A., Chown, L.A. & Olubambi, P.A., 2012, 'Electrochemical studies of Fe-21Cr-1Ni duplex stainless steel with 0.15wt% ruthenium at different temperatures', *The Journal of the Southern African Institute of Mining and Metallurgy*, 7A, 535-538.

Olefjord, I. & Elfstrom, B., 1982, 'The composition of the surface during passivation of stainless steels,' *Corrosion*, 38(1), 46-52.

Olsson, C.-O.A. & Landlot, D., 2003, 'Passive films on stainless steels-chemistry, structure and growth', *Electrochimica Acta*, 48, 1093-1104.

Olubambi, P.A., Potgieter, J.H. & Cornish, L., 2009, 'Corrosion behaviour of super ferritic stainless steels cathodically modified with minor additions of ruthenium in sulphuric and hydrochloric acids', *Materials and Design*, 30, 1451-1457.

Orazem, M.E., 2004, 'A systematic approach toward error structure identification for impedance spectroscopy,' *Journal of Electroanalytical Chemistry*, 572, 317-327.

Orazem, M.E. & Tribollet, B., 2008, Electrochemical impedance spectroscopy, Wiley, New Jesery.

Padhy, N., Ninghen, S., Panigrahi, B.K. & Mudali, U.K., 2010, 'Corrosion behaviour of nitrogen ion implanted AISI type 304L stainless steel in nitric acid medium', *Corrosion Science*, 52, 104-112.

Padhy, N., Mudali, K., Chawla, V., Chandra R. & Raj, B., 2011a, 'Corrosion behaviour of single (Ti) and duplex (Ti-TiO_2) coating on 304L stainless steel in nitric acid medium', *Materials Chemistry and Physics*, 130, 962-972.

Padhy, N., Paul, R., Mudali, U.K. & Raj, B., 2011b, 'Morphological and compositional analysis of passive film on austenitic stainless steel in nitric acid medium,' *Applied Surface Science*, 257, 5088-5097.

Paine, B.M. & Speriosu, V.S., 1987, 'Nonlinear strain effects in ion-implanted GaAs,' *Journal of Applied Physics*, 62(5), 1704-1709.

Pajkossy, T., 2005, 'Impedance spectroscopy at interfaces of metals and aqueous solutions- surface roughness, CPE and related issues,' *Solid State Ionics*, 176, 1997-2003.

Pardo, A., Merino, M.C., Coy, A.E., Viejo, F., Arrabal, R. & Matykina, E., 2008, 'Pitting corrosion behaviour of austenitic stainless steel-combining effects of Mn and Mo additions,' *Corrosion Science*, 50, 1796-1806.

Pasel, C., 1918, *Herstellung von Gegenständen, die hohe Widerstandsfähigkeit gegen den Angriff durch Säuren und hohe Festigkeit erfordern (Gefäße, Rohre, Maschinenteile usw.), nebst thermischem Behandlungsverfahren. [Manufacture of goods which have high resistance, to attack by acids and high strength (vessels, pipes, machine parts, etc.), in addition to thermal treatment methods]*, German patent 304 159.

Pelletier, H., Mille, P., Cornet, A., Grob, J.J., Stoquert, J.P. & Muller, D., 1999, 'Effects of high energy nitrogen implantation on stainless steel microstructure,' *Nuclear Instruments and Methods in Physics Research B*, 148, 824-829.

Pelletier, H., Mille, P., Muller, D., Stoquert, J.P., Cornet, A. & Grob, J.J., 2001, 'Correlation between distribution of nitrogen atoms implanted at high energy and high dose and nanohardness measurements into 316L stainless steel,' *Nuclear Instruments and Methods in Physics Research B*, 178, 319-322.

Perry, R.H., Green, D.W. & Maloney, J.O. (Eds), 1999, Perry's Chemical Engineer's Handbook, 7th Ed., McGraw-Hill, New York, USA.

Phelps, E.H. & Vreeland, D.C., 1957, 'Corrosion of austenitic stainless steels in sulphuric acid,' *Corrosion*, 13, 21-26.

Picard, S., Memet, J.B., Sabot, R., Grosseau-Poussard, J.L., Riviere, J.P. & Meilland, R., 2001, 'Corrosion behaviour, microhardness and surface characterisation of low energy, high current ion implanted austenitic stainless steel,' *Materials Science and Engineering A*, 303, 163-172.

Pickering, H.W., 1983, 'Characteristic features of alloy polarisation curves', *Corrosion Science*, 23(10), 1107-1120.

Piotrowski, T. & Accinno, D.J., 1971, 'The preparation of ruthenium for optical metallography,' *Metallography*, 4, 521-532.

Pons, M., Caillet, M. & Galerie, A., 1986, 'A comparison between ion implantation and laser alloying of iron for oxidation resistance improvement: Part 2 Aluminium alloying,' *Journal of Materials Science*, 21, 4101-4106.

Potgieter, J.H., Heyns, A.M. & Skinner, W., 1990, 'Cathodic modification as a means of improving the corrosion resistance of alloys', *Journal of Applied Electrochemistry*, 20, 711-715.

Potgieter, J.H., 1991, 'Alloys cathodically modified with noble metals', *Journal of Applied Electrochemistry*, 21, 471-482.

Potgieter, J.H. & Kincer, M.U., 1991, 'An electrochemical investigation of the effect of nickel and ruthenium on the dissolution of a high chromium super-ferritic stainless steel in reducing acid media', *South African Journal of Chemistry*, 44(2), 47-50.

Potgieter, J.H., Wentzel, E. & Myburg, G., 1992, 'Effects of vapour deposition and bulk alloyed ruthenium on corrosion resistance of a duplex stainless steel in sulphuric acid', *Surface Engineering,* 8(4), 289-291.

Potgieter, J.H. & Brookes, H.C., 1995, 'Corrosion behaviour of a high-chromium duplex stainless steel with minor additions of ruthenium in sulphuric acid', *Corrosion,* 51(4), 312-320.

Potgieter, J.H., Ellis, P. & van Bennekom, A., 1995, 'Investigation of the active dissolution behaviour of a 22% chromium duplex stainless steel with small ruthenium additions in sulphuric acid', *ISIJ International,* 35(2), 197-202.

Potgieter, J.H., Barnard, W.O., Myburg, G., Varga, K., Baradlai, P. & Tomcsanyi, L., 1996, 'Corrosion behaviour of duplex stainless steels containing minor ruthenium additions in reducing acid media', *Journal of Applied Electrochemistry,* 26, 1103-1110.

Qu, N.S., Zhu, D., Chan, K.C. & Lei, W.N., 2003, 'Pulse electrodeposition of nanocrystalline nickel using ultra narrow pulse width and high peak current density,' *Surface and Coatings Technology*, 168, 123-128.

Quemper, J.-M., Dufor-Gergam, E., Frantz-Rodriguez, N., Gilles, J.-P., Grandchamp, J.-P. & Bosseboeuf, A., 2000, 'Effects of direct and pulse current on copper electrodeposition through photoresist molds,' *Journal of Micromechanics and Microengineering*,' 10, 116-119.

Radjabov, T.D., 1988, 'Improvement of the corrosion performance of metals by ion implantation', *Vacuum*, 38(1), 979-985.

Rautray, T.R., Narayanau, R. & Kim, K.-H., 2011, 'Ion implantation of titanium based biomaterials,' *Progress in Materials Science*, 56, 1137-1177.

Reddy, G.S. & Taimsalu, P., 1971, *Electrodeposition of ruthenium*, US Patent 3,576,724.

Revie, R.W. & Uhlig, H.H., 2008, Corrosion and corrosion control: An introduction to corrosion science and engineering, 4th Ed., Wiley-Interscience, New Jersey, USA.

Richardson, J.A., 2010, Corrosion in sulfuric acid, in Shreir's Corrosion, vol. 2, Richardson, T.J.A. (Ed.), ISBN: 978-0-444-52787-5, Elsevier BV, pp. 1226-1249, accessed on 5 May 2014 from www.sciencedirect.com

Rickerby, D.S., 1988, 'A review of the methods for the measurement of coating-substrate adhesion,' *Surface and Coatings Technology*, 36, 541-557.

Riviere, J.P., Meheust, P., Villain, J.P., Templier, C, Cahoreau, M., Abrasonis, G. & Pranevicius, L., 2002, 'High current density nitrogen implantation of an austenitic stainless steel,' *Surface and Coatings Technology*, 158-159, 99-104

Roberge, P.R., 2000, Handbook of corrosion engineering, McGraw-Hill, New York, USA.

Saad, M. & Kassis, A., 2012, 'Effect of rf power on the properties of rf magnetron sputtered ZnO:Al thin films', *Materials Chemistry and Physics*, 136, 205-209.

Sadeghpour, S., Kermanpur, A. & Najafizadeh, A., 2013, 'Influence of Ti microallying on the formation of nanocrystalline structure in the 201L austenite stainless steel during martensite thermomechanical treatment', *Materials Science and Engineering A*, 584, 177-183.

Saidi, D., Zaid, B., Souami, N., Saoula, N., Siad, M., Si Ahmed, A. & Biberian, JP., 2015, 'AES depth profiles in Mo-coated 304L stainless steel achieved by RF magnetron sputtering and influence of Mo on the corrosion in 3.5% NaCl solution', *Journal of Alloys and Compounds*, 645, 45-50.

Schmuki, P., 2002, 'From Bacon to barriers: a review on the passivity of metals and alloys', *Journal of Solid State Electrochemistry*, 6, 145-164.

Schubert, U., Metzger, H. & Peisl, J., 1984, 'Diffuse x-ray scattering from interstitial nitrogen in niobium: I. Haung diffuse scattering,' *Journal of Physics F: Metal Physics*, 14, 2457-2466.

Schweitzer, P.A., 2007, Corrosion engineering handbook corrosion: Fundamentals of metallic corrosion- Atmospheric and media corrosion of metals, 2nd Ed., Taylor & Francis Group LLC, Florida, USA.

Scully, J.R., 2000, 'Polarisation resistance method for determination of instantaneous corrosion rates', *Corrosion,* 56(2), 199-218.

Sheeja, D., Tay, B.K., Leong, K.W. & Lee, C.H., 2002, 'Effect of film thickness on the stress and adhesion of diamond-like-carbon,' *Diamond and Related Materials,* 11, 1643-1647.

Sherif, E.M, 2011, 'Corrosion behaviour of duplex stainless steel alloy cathodically modified with minor ruthenium additions in concentrated sulphuric acid solutions', *International Journal of Electrochemical Science,* 6, 2284-2298.

Sherif, E.M., 2012, 'Corrosion of duplex stainless steel alloy 2209 in acidic and neutral chloride solutions and its passivation by ruthenium as an alloying element', *International Journal of Electrochemical Science,* 7, 2374-2388.

Sherif, E.M. & Park, S.-M., 2006, 'Effects of 1,4-naphthoquinone on aluminium corrosion in 0.5 M sodium chloride solutions,' *Electrochimica Acta,* 51, 1313-1321.

Sherif, E.M., Potgieter, J.H., Cornish, L., Olubambi, P.A. & Machio, C.N., 2009a, 'Effects of minor additions of ruthenium on the passivation of duplex stainless steel corrosion in concentrated hydrochloric acid solution', *Journal of Applied Electrochemistry,* 39, 1385-1392.

Sherif, E.M., Potgieter, J.H., Comins, J.D., Cornish, L., Olubambi, P.A. & Machio, C.N., 2009b, 'The beneficial effect of ruthenium additions on the passivation of duplex stainless steel corrosion in sodium chloride solution', *Corrosion Science,* 51, 1364-1371.

Simcoe, C.R., 2015, 'Stainless steel: The steel that does not rust-Part 1', *Advanced Materials and Processes,* 38-39.

Smenkowski, V.S., 2000, 'Trends in sputtering,' *Progress in Surface Science,* 64, 1-58.

Snyder, D.D., 2010, Preparation for deposition, in Modern Electroplating, Schlesinger, M. & Paunovic, M. (Ed.), 5th Ed., John Wiley and Sons Inc., pp. 507-512.

Spadoni, A. & Addonizio, M.L., 2015, 'Effect of the RF sputtering power on microstructural, optical and electrical properties of Al doped ZnO thin films', *Thin Solid Films,* 589, 514—520.

Statistics South Africa, 2016, Gross domestic product: Fourth quarter 2015, accessed on 9 March 2016 from www.stassa.gov.za

Stern, M. & Geary, L., 1957, 'Electrochemical polarisation I: A theoretical analysis of the shape of polarisation curves', *Journal of the Electrochemical Society,* 104(1), 56-63.

Stern, M. & Wissenberg, H., 1959, 'The electrochemical behaviour and passivity of titanium,' *Journal of the Electrochemical Society,* 106(9), 755-759.

Stewart, J. & William, D.E., 1992, 'The initiation of pitting corrosion on austenitic stainless steel: On the role and importance of sulphide inclusions,' *Corrosion Science,* 33(3), 457-474.

Stoller, R.E., Toloczko, M.B., Was, G.S., Certain, A.G., Dwaraknath, S. Garner, F.A., 2013, 'On the use of SRIM for computing radiation damage exposure,' *Nuclear Instruments and Methods in Physics Research B,* 310, 75-80.

Streicher, M.A., 1977, 'Alloying stainless steels with platinum metal', *Platinum Metals Review*, 21(2), 51-55.

Stypula, B. & Banás, J., 1993, 'Passivity of chromium in sulphuric acid solutions,' *Electrochimia Acta,* 38(15), 2309-2314.

Subramanian, B., Ananthakumar, R. & Jayachandran, M., 2010, 'Microstructure, mechanical and electrochemical corrosion properties of sputtered titanium-aluminium-nitride films for bio-implants', *Vacuum,* 85, 601-609.

Suda, T., Ohkawa, M., Sawada, S., Watanabe, S., Ohnuki, S. & Nagata, S., 2002, 'Effect of surface modification by ion implantation on hydrogenation property of TiFe alloy,' *Materials Transactions,* 43(11), 2703-2705.

Sudesh, T.L., Wijesinghe, L. & Blackwood, D.J., 2006, 'Characterisation of passive films on 300 series stainless steel', *Applied Surface Science*, 253, 1006-1009.

Taylor, J.R., 1997, *An introduction to error analysis: The study of uncertainties in physical measurements*, 2nd Ed., University Books, Colorado, USA.

Thanjekwayo, N.P., 2009, 'The influence of Ru additions on the corrosion behaviour of WC-Co cemented carbide in corrosive media,' MSc dissertation, Faculty of Engineering, University of the Witwatersrand, Johannesburg, accessed on 14 October 2013 on www.wiredspace.wits.ac.za

Tien, C-L., Yu, K-C., Tsai, T-Y. & Liu, M-C., 2015, 'Effect of RF power on the optical, electrical, mechanical and structural properties of sputtering Ga-doped ZnO thin films', *Applied Surface Science*, 354, 79-84.

Tjong, S.C, 1989, 'Electrochemical and surface characterisation of the passive film on Fe-Cr-Pd alloys', *Surface and Coatings Technology*, 38, 325-338.

Tjong, S.C., 1990a, 'Electrochemical and surface analysis of the Fe-Cr-Ru system in non-oxidising acid solutions', *Applied Surface Science*, 44, 7-15.

Tjong, S.C., 1990b, 'Self-passivation of Fe-Cr-PGM alloys in reducing acids studied by electrochemical and electron spectroscopic techniques,' *Applied Surface Science*, 45, 301-318.

Tjong, S.C. & Wong, M.C., 1993, 'Corrosion behaviour of boron- and phosphorous-implanted Fe-40Cr alloy in reducing acid solutions,' *Applied Surface Science*, 64, 127-132.

Tjong, S.C., Ku, J.S. & Ho, N.J., 1997, 'Laser surface alloying of ferritic Fe-40Cr alloy with ruthenium', *Surface and Coatings Technology*, 90, 203-209.

Tjong, S.C. & Chu, P.K., 2007, 'Corrosion properties of Fe-24Cr stainless alloy modified by plasma immersion ion implantation in 0.5 M sulphuric acid solution', *Surface and Coatings Technology*, 201, 6781-6784.

Tomashov, N.D., 1964, 'Passivity and corrosion resistance of metal systems', *Corrosion Science*, 4, 315-334.

Tomashov, N.D., Chernova, G.P. & Volkov, L.N., 1970, 'Effect of palladium on corrosion and electrochemical; behaviour of 0 KH 25 N 6 T steel,' *Protection of metals*, 6(4), 388-390.

Tomashov, N.D., Chernova, G.P. & Fedoseeva, T.A., 1980, 'Cathodic alloying of the surface of titanium, chromium, and stainless steels as a method of increasing their passivation and corrosion resistance', *Corrosion*, 36(4), 201-207.

Tomashov, N.D., Chernova, G.P. & Ustinsky, E.N., 1984, 'Effects of platinum elements additions on the active dissolution of plastic chromium in sulfuric acid', *Corrosion*, 40(3), 134-138.

Tomlison, W.J. & Carroll, M.W., 1990, 'Substrate roughness, deposition thickness and the corrosion of electroless nickel coatings,' *Journal of Materials Science*, 25, 4972-4976.

Tóth-Kádár, E., Bakonyi, I., Pogány, L. & Cziráki, Á., 1996, 'Microstructure and electrical properties of pulse-plated nanocrystalline nickel electrodeposits,' *Surface and Coatings Technology*, 88, 57-65.

Trompette, J.L. & Massot, L., 2011, 'Chronoamperometric study of the passive behaviour of tantalum in hostile media during water addition,' *Corrosion Science*, 57, 174-181.

Tury, B., Lakatos-Varsányi, M. & Roy, S., 2007, 'Effect of pulse parameters on the passive layer formation on pulse plated Ni-Co alloys,' *Applied Surface Science*, 253, 3103-3108.

Uhlig, H.H., 1979, 'Passivity in metals and alloys,' *Corrosion Science*, 19, 777-791.

Üneri, S., 1969, 'The utility of linear polarisation method for the determination of the corrosion rate', accessed on 22 July 2013 from www.communications.science.ankara.edu.tr

Varga, K., Baradlali, P., Barnard, W.O., Myburg, G., Halmos, P. & Potgieter, J.H., 1997, 'Comparative study of surface properties of austenitic stainless steels in sulphuric and hydrochloric acid solutions,' *Electrochimica Acta*, 42(1), 25-35.

Van der Merwe, J.W. & Tharandt, D., 2015, 'Corrosion resistance of laser-cladded 304L stainless steel enriched with ruthenium additions exposed to sulphuric acid and sodium chloride media', *The Journal of the Southern African Institute of Mining and Metallurgy*, 115, 499-505.

Vasu, K., Krishna, M.G., Padmanabhan, K.A., 2014, 'Nanomechanical behaviour of (100) oriented titanium thin films', *The European Physical Journal of Applied Physic*, 65(30302), 1-5.

Walsh, F.C., Ponce de León, C., Kerr, C. Court, S. & Barker, B.D., 2008, 'Electrochemical characterisation of the porosity and corrosion resistance of electrochemically deposited metal coatings', *Surface and Coatings Technology*, 202, 5092-5102.

Walter, G.W., 1977, 'Problems arising in the determination of accurate corrosion rates from polarisation resistance measurements,' *Corrosion Science*, 17, 983-993.

Wampler, W.R., Schober, T. & Lengeler, B., 1976, 'Precipitation and trapping of hydrogen in copper,' *Philosophical Magazine*, 34(1), 129-141.

Wang, M., Zhang, Q.Y., Shi, W.D., Ma, T.C. & Hou, S.Z., 1994, 'Effects of Mo and Mo+N implantation on corrosion resistance of austenitic stainless steel', *Surface and Coatings Technology*, 65, 171-174.

Wang, S.G., Sun, M., Long, K. & Zhang, Z.D., 2013, 'The electronic structure characterisation of oxide film on bulk nanocrystalline 304 stainless steel in hydrochloric acid solution', *Electrochimica Acta*, 112, 371-377.

Warner, J.C., 1943, 'Thermodynamics considerations in the corrosion of metals', Presented at the 83rd General meeting, Pittsburgh, 10 April, 1943, 319-333.

Whillock, G.O.H. & Worthington, S.E., 2010, Corrosion in nitric acid, in Shreir's Corrosion, vol. 2, Richardson, T.J.A. (Ed.), ISBN: 978-0-444-52787-5, Elsevier BV, pp. 1250-1269, accessed on 5 May 2014 from www.sciencedirect.com

Williamson, G.K. & Hall, W.H., 1953, 'X-ray line broadening from field aluminium and wolfram,' *Acta Metallurgica,* 1, 22-31.

Wong, K.P., Chau, K.C. & Yue, T.M., 1999, 'A study of surface finishing in pulse current electroforming of nickel by utilizing different shaped waveforms,' *Surface and Coatings Technology,* 115, 132-139.

Wranglén, G., 1974, 'Pitting and sulphide inclusions in steel,' *Corrosion Science,* 14, 331-349.

Wright, A., 1877, 'On a new process for the electrical deposition of metals and for constructing metal covered glass specula,' *The American Journal of Science and Arts,* 14, 169-178.

Wolff, I.M., 1999, 'New applications for ruthenium', *South African Journal of Science,* 95, November/December, 539-542.

Xu, R., Yang, X., Jiang, J., Li., P., Wu, G. & Chu, P.K., 2013, 'Effects of chromium ion implantation voltage on the corrosion resistance and cytocompatibility of dual chromium and oxygen plasma-ion-implantation biodegradable magnesium', *Surface and Coatings Technology,* 235, 875-880.

Xuetao, Y., Yu, W., Dongbai, S. & Hongying, Y., 2008, 'Influence of pulse parameters on the microstructure and microhardness of nickel electrodeposits, *Surface and Coating Technology,* 202, 1895-1903.

Yan, Z., Liao, W., Zhang, Y., Xiang, X., Yuan, X. & Zu, X., 2014, 'Optical characterisation and laser damage of fused silica optics after ion beam sputtering,' *Optik,* 125, 756-760.

Yang, S., Wang, Z., Kokawa, H. & Sato, Y.S., 2008, "Reassessment of the effects of laser surface melting on IGC of SUS 304L', *Materials Science Engineering A,* 474, 112-119.

Youssef, Kh.M.S., Koch, C.C. & Fedkiw, P.S., 2004, 'Influence of additives and pulse electrodeposition parameters on production of nanocrystalline zinc chloride electrolytes,' *Journal of the Electrochemical Society,* 151(2), C103-C111.

Zand, R.Z., Verbeken, K. & Adriaen, A., 2012, 'Corrosion resistance performance of cerium doped silica sol-gel coatings on 304L stainless steel', *Progress in Organic Coatings,* 75, 463-473.

Zak, A.K., Abd. Majid, W.H., Abrishami, M.E. & Yousefi, R., 2011, 'X-ray analysis of ZnO nanoparticles by Williamson-Hall and size-strain plot methods,' *Solid State Sciences*, 13, 251-256.

Zhou, X.W., Wadley, H.N.G. & Sainathan, S., 2005, 'Low energy sputtering of nickel by normally incident xenon ions,' *Nuclear Instruments and Methods in Physics Research B,* 24, 441-457.

Appendices

Appendix A: Publications from this and related work

A.1 Peer reviewed articles

1. Fortunate Moyo, Josias W. van der Merwe, Daniel Wamwangi, 2016, 'Corrosion performance of pulse plated ruthenium: Dependence on pulse-off time', *Surface and Coatings Technology* 307, 971-977.

2. Josias van der Merwe, Fortunate Moyo, Emily Phetla, 2017, 'Corrosion behaviour of ruthenium laser alloyed austenitic stainless steel in sulphuric acid and sodium chloride', *Materials and Corrosion*, in press, Manuscript ID: maco.201609343.R2

A.2 Articles submitted or in preparation

1. Fortunate Moyo, Josias van der Merwe, Daniel Wamwangi, Alan Shemi, 'Corrosion of ruthenium implanted 304L stainless steel: determination of influential parameters by 2^k factorial design, submitted to *Surface and Coatings Technology* on 9 March 2017, Manuscript ID SURFCOAT-D-17-00675.

2. Fortunate Moyo, Yonela Mgwebi, Josias van der Merwe, 'Ruthenium application in wet and dry corrosion: A review of recent developments,' *in preparation.*

3. Fortunate Moyo, Josias van der Merwe, Daniel Wamwangi 'Corrosion of ruthenium implanted 304L stainless steel in chloride containing solutions,' *in preparation.*

A.3 Scientific conferences

1. Effects of plating parameter on corrosion behaviour of ruthenium films produced by pulsed electrodeposition, Africorr 2016, 27-29 July, Midrand Conference Centre, Midrand, South Africa
   Fortunate Moyo*, Josias van der Merwe, Daniel Wamwangi

Poster presentation (-*won award for best poster presentation*)

2. Corrosion characterisation of ruthenium films deposited by RF sputtering, Eurocorr 2015, 6-10 September, Graz, Austria.
   Fotunate Moyo*, Josias van der Merwe, Daniel Wamwangi
   Oral presentation

3. Electrochemical behaviour of AISI 304L implanted with ruthenium, 19th International Corrosion Congress 2014, November, Jeju, South Korea.
   Fortunate Moyo*, Josias van de Merwe
   Oral presentation

4. Influence of surface preparation on the precision of electrochemical measurements, Africorr 2014, 26-30 July, Farm Inn, Pretoria, South Africa
   Fortunate Moyo*, Josias van der Merwe
   Oral presentation

Appendix B

Determination of corrosion rates

Corrosion rates were calculated as per Equation B-1 (ASTM G102-89(2010)), K_1 is a constant = 3.27×10^{-3} mm.g/μA.cm.y, ρ is the density of the corroding metal, E_W is equivalent weight, and i_{corr} is the corrosion current density expressed as μA/cm^2.

$$Corrosion\,rate = K_1 \frac{i_{corr}}{\rho} E_W \qquad \textit{Equation B-1}$$

B.1 Equivalent weight

The equivalent weight of 304L stainless steel was calculated using Equation B-2, where n_i is the valence of the ith element in the alloy involved in the corrosion process, w_i is the atomic weight of the ith element in the alloy, and f_i is the mass fraction of the ith element in the alloy. Only the elements with a concentration > 1 wt% were considered. For elements with variable valence, the lowest variance was used. The results are presented in Table B-1, where the calculated value of E_W was compared to that stated in ASTM G102-89(2010).

$$E_W = \frac{1}{\sum \frac{n_i f_i}{w_i}} \qquad \textit{Equation B-2}$$

Table B- 1 *Determination of the equivalent weight of the supplied 304L stainless steel. *based on 1g of the alloy.*

Element	Composition (wt%)	Mass fraction*	Atomic weight	Valence	Electron equivalent
Iron	70.548	0.705	55.845	2	0.0253
Chromium	18.320	0.183	51.996	3	0.0106
Nickel	8.200	0.082	58.693	2	0.0027
Manganese	1.210	0.012	54.938	2	0.004
		E_w of supplied 304L stainless steel			**25.595**
		E_w from ASTM G102-89(2010)			**25.120**

B.2 Density of supplied 304L stainless steel

The density of the supplied 304L stainless steel was calculated as per Equation B-3. The calculated value was 7.668 g/cm^3, and was comparable to that stated in ASTM G1-03 in Table B-2.

Table B- 2 *Calculation of the actual density of the supplied 304L stainless steel. *based on 100g.*

Element	Composition (wt%)	Weight in unit mass*	Theoretical density (Lide, 2005)	Calculated density
C	0.031	3.100E-04	2.857	1.085E-04
Si	0.444	4.440E-03	2.329	1.906E-03
Mn	1.210	1.210E-02	7.300	1.658E-03
P	0.038	3.800E-04	2.227	1.707E-04
S	0.006	6.200E-05	2.070	2.995E-05
Cr	18.320	1.832E-01	7.150	2.562E-02
Ni	8.200	8.200E-02	8.900	9.213E-03
Mo	0.343	3.430E-03	10.200	3.363E-04
Al	0.017	1.700E-04	2.700	6.296E-05
Cu	0.313	3.130E-03	8.960	3.493E-04
Co	0.165	1.650E-03	8.860	1.862E-04
Ti	0.004	4.300E-05	4.506	9.543E-06
Nb	0.008	8.000E-05	8.570	9.335E-06
V	0.087	8.700E-04	6.000	1.450E-04
W	0.078	7.800E-04	19.830	3.933E-05
Sb	0.013	1.300E-04	6.680	1.946E-05
Sn	0.009	8.700E-05	6.517	1.335E-05
As	0.038	3.800E-04	5.750	6.609E-05
Ca	0.001	1.300E-05	1.540	8.442E-06
Se	0.037	3.700E-04	4.493	8.235E-05
N	0.076	7.600E-04	1.145	6.638E-04
Fe	70.600	7.060E-01	7.870	8.971E-02
	Density of supplied 304L stainless steel (g/cm^3)			**7.668**
	Density from ASTM G1-03 (g/cm^3)			**7.940**

The weight of ruthenium in the alloyed 304L stainless steel was assumed negligible, without effect on the density of the stainless steel.

B.3 Corrosion current density

Corrosion current density was determined from polarisation resistance, R_p, and the Stern-Geary constant B as follows:

$$i_{corr} = \frac{B}{R_p} \qquad \textit{Equation B-3}$$

The slope of the graph ± 10 mV vs E_{corr}, as demonstrated from Figure B-1, was used to characterise R_p, and B was taken as 22 mV.

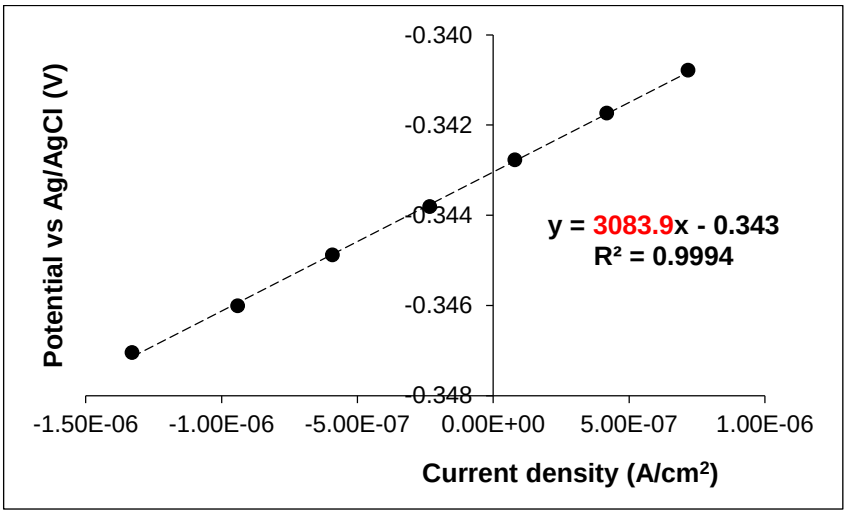

Figure B- 1 *Determination of polarisation resistance from potentiodynamic polarisation curves.*

Appendix C

Chemical assay of ruthenium salt

The assay of the ruthenium nitrosyl salt as supplied by Impala Platinum Refineries is presented in Figure C-1.

IMPALA PLATINUM

IMPALA PLATINUM LIMITED
(INCORPORATED IN THE REPUBLIC OF SOUTH AFRICA)
PLATINUM METALS LABORATORY
CERTIFICATE OF ANALYSIS

Ref no: RU SALT 2014/45DS/1

Purity Ru%: 99.99

Certificate No: RU SALT 2014/45DS/1

Date Received: 08 MAY 2015

PARTS PER MILLION		PARTS PER MILLION	
Pt	17	Pd	2
Au	<1	Rh	9
Ir	<1	Os	3
Ag	2	Ni	2
Cu	<1	Fe	41
Pb	<1	Te	<1
Sb	<1	As	<1
Al	3	Na	1
Ca	8	Si	22
Mg	<1	Zn	<1
Mn	1	Bi	1
Ti	1	Mo	2
Cr	4	Sn	4
Co	1		

Metal content %: 24.07

< = Less Than

DATE: 08 MAY 2015

SENIOR CHEMIST

LABORATORY MANAGER

1. Rounding in accordance with the rounding off method of ASTM Recommended Practice E29
2. This certificate must be reproduced in full and then only if written permission of the Lab Manager has been obtained

Figure C- 1 *A copy of the assay certificate for the ruthenium nitrosyl salt used in this study.*

Appendix D

Supplementary results

D.1 Ruthenium composition on ruthenium implanted 304L stainless steel

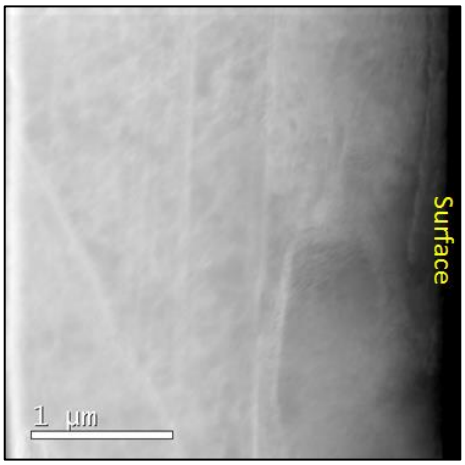

(a)

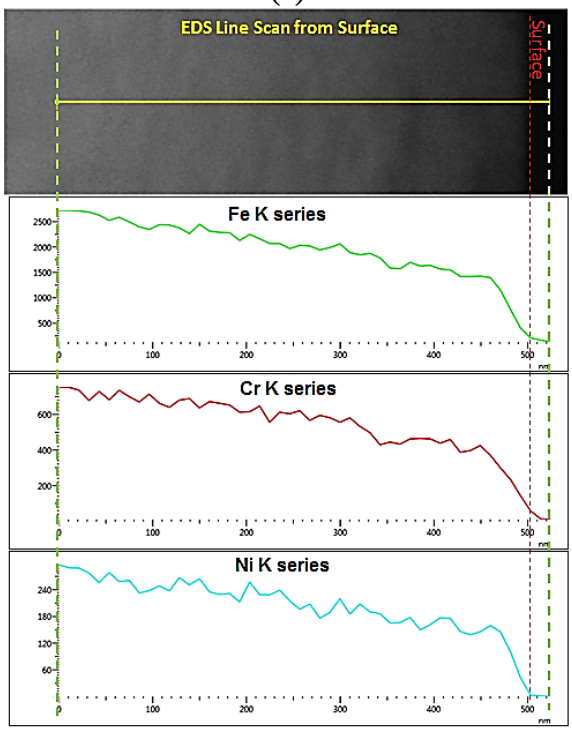

(b)

Figure D- 1*(a) Annular dark field STEM micrograph of the rough ruthenium implanted 304L stainless steel, and (b) EDS line scan of the sample in (a)*

The scanning transmission electron microscope (STEM) micrographs in Figure D-1(a) did not exhibit a clear indication of implantation damage near the surface region on the surface. EDS analysis 500 nm into the surface did not detect the

implanted ruthenium (Figure D-1(b)). The variation in the EDS signal observed in this figure is due to thickness defects: the samples analysed were wedge shaped.

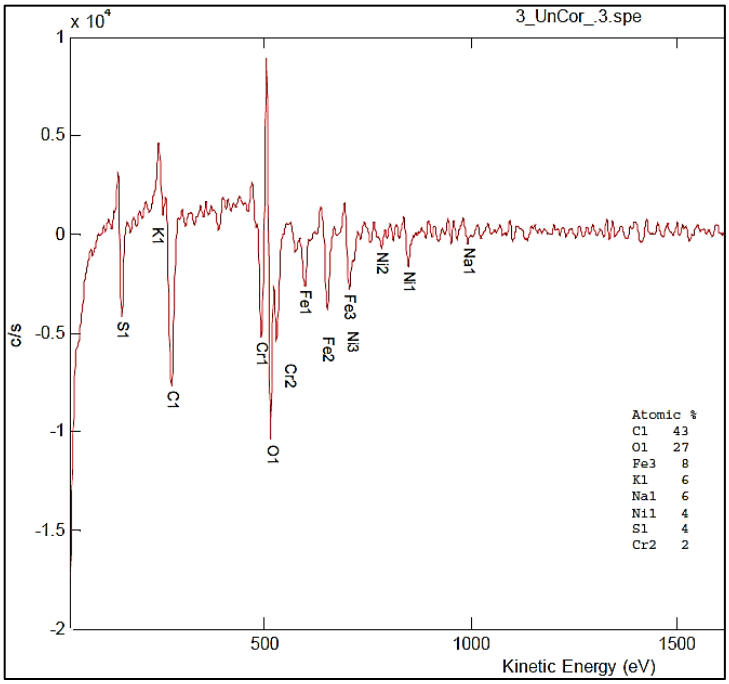

(a)

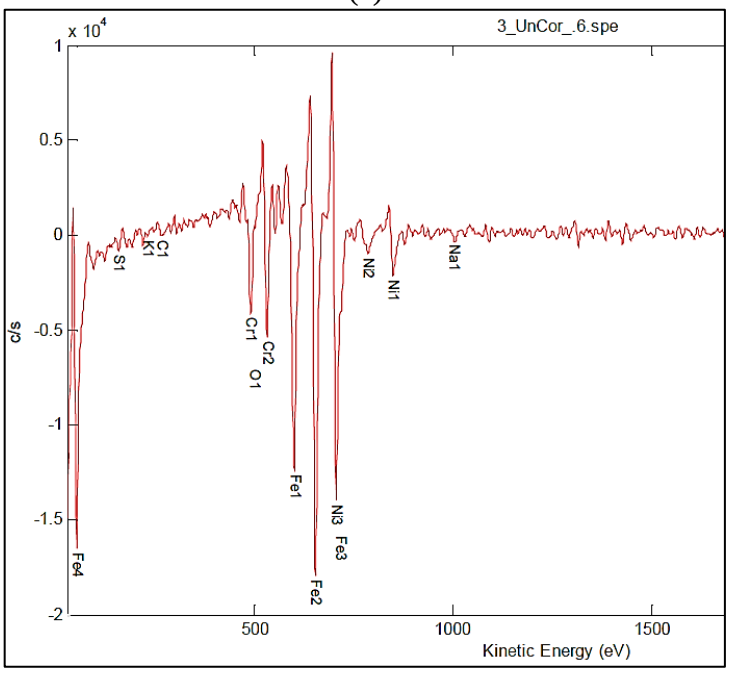

(b)

Figure D- 2 *Typical AES survey of ruthenium implanted 304L stainless steel (a) before, and (b) after 1 minute sputtering at a rate of 15 nm/min.*

In Figure D-2, a ruthenium peak was expected at 271.8 eV. Before sputtering two peaks were observed at around this kinetic energy position. These were resolved, and found to correspond to the positions of carbon and potassium, which were possibly contaminants picked up during sample handling. No peaks corresponding to ruthenium were not detected either before or after sputtering.

D.2 Thickness of ruthenium films deposited by PED

The thickness of the ruthenium films deposited by PED was approximated by Equation D-1, where ρ is the density of ruthenium, and A the area of 304L plated. The results are presented in Figure D-3.

$$Thickness = \frac{mass\ gained}{\rho \times A} \qquad \textbf{\textit{Equation D-1}}$$

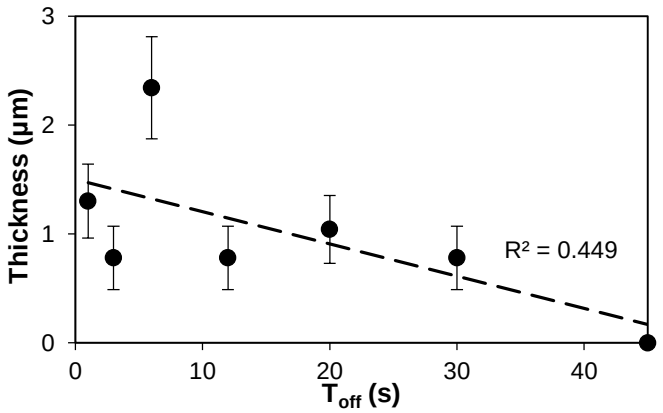

Figure D- 3 *Influence of Toff on the thickness of ruthenium films deposited on 304L stainless steel by PED.*

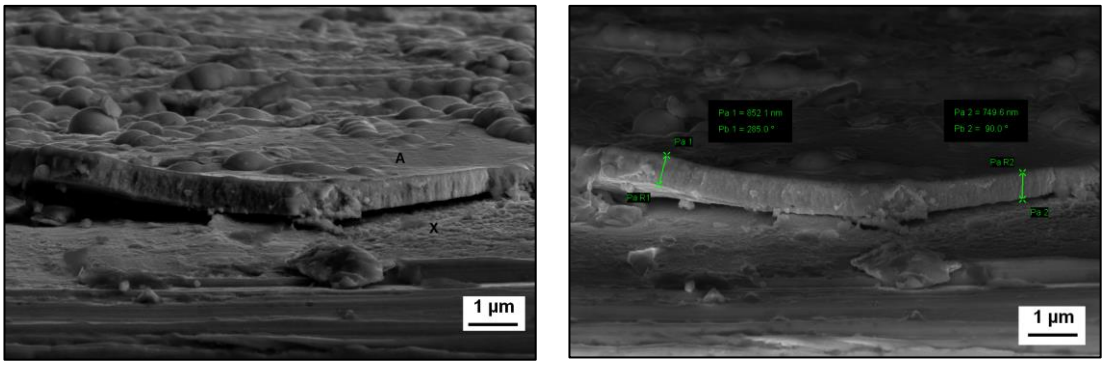

(a) (b)

Figure D- 4 *FESEM images of the ruthenium film deposited on 304L stainless steel by PED in (a) SE mode, and (b) BSD mode.* T_{off} *= 3s.*

FESEM analysis showed that film deposited at T_{off} were typically 860 ± 40 nm. However, the thickness measurements did not take into account the thin layer marked 'X' in Figure D-4(a), which contributed to overall mass gain used to approximate film thickness in Figure D-3.

Appendix E

Equipment

E.1 Analytical instruments

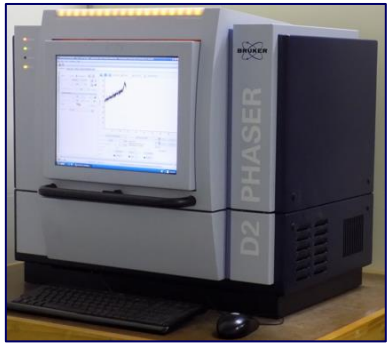

(a)

(b)

(c)

(d)

(e)

Figure E- 1 *Some of the analytical instruments used in this project. (a) Bruker D2 Phaser, (b) Veeco Dimension 3100 AFM, (c) Lecia DM6000 M optical microscope, (d) Carl Zeiss Sigma FESEM, and (e) Agilent 240FS atomic adsorption spectroscope*

E.2 Electrochemical cell

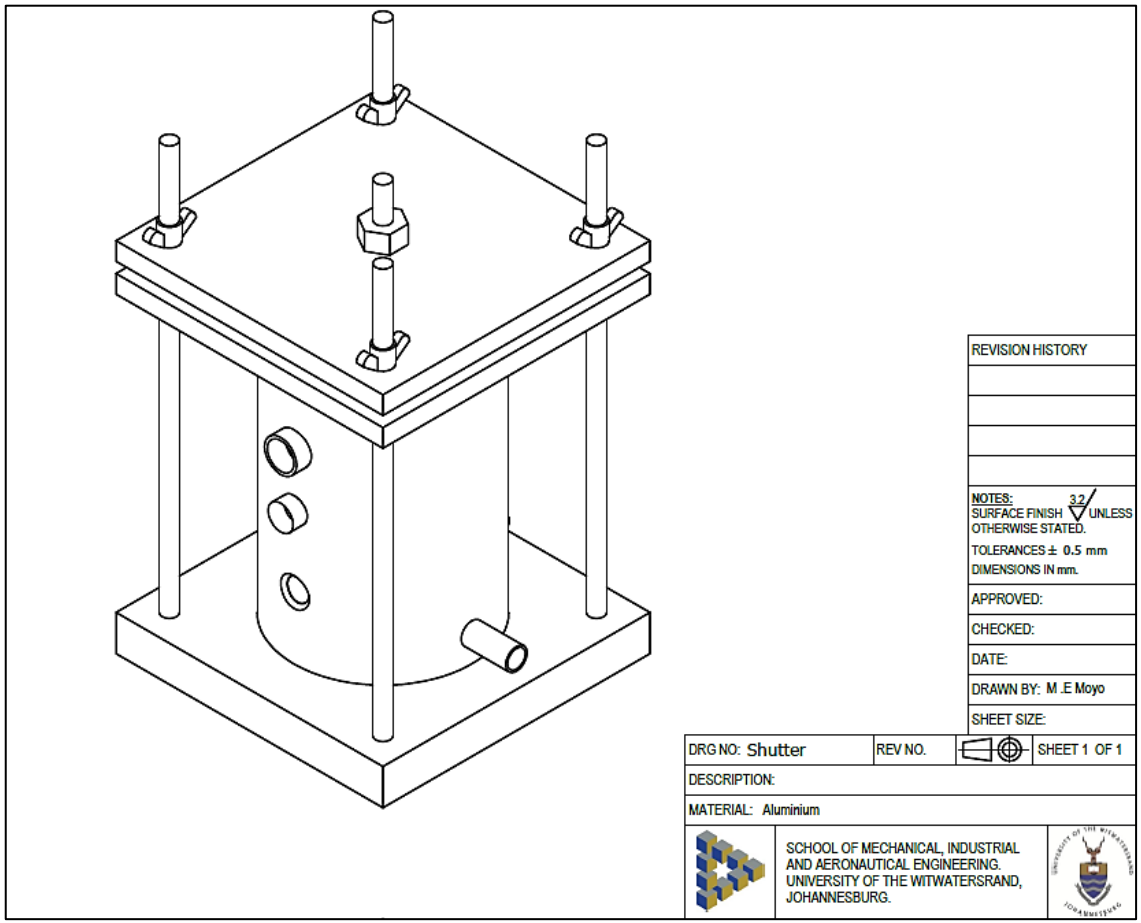

Figure E- 2 *Drawing of the cell used in electrochemical corrosion tests*

E.3 RF sputtering sample holder

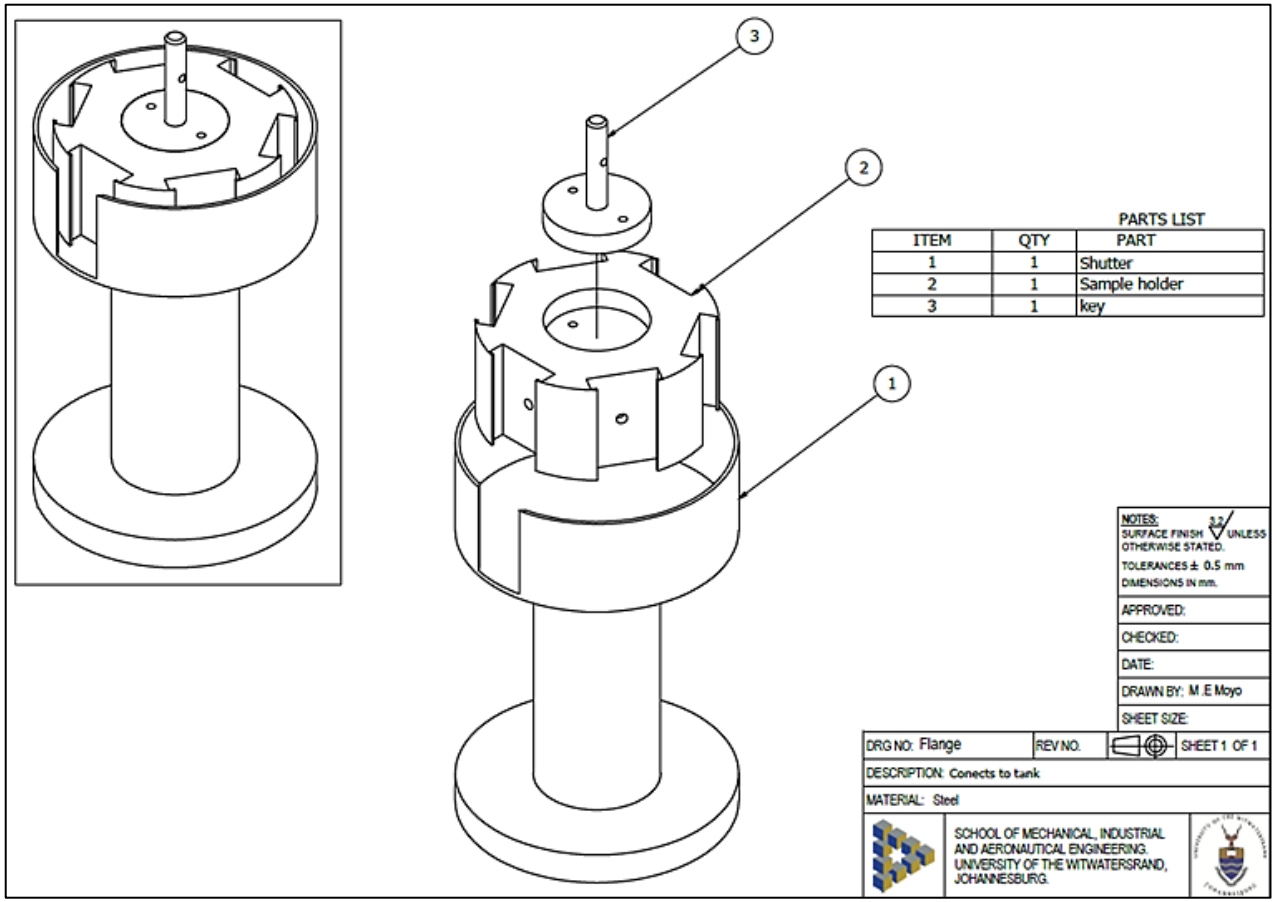

Figure E- 3 *Assembled and exploded views of the sample holder used in RF sputtering.*